IMPLEMENTATION OF STRUCTURAL MONITORING TO ASSESS THE PERFORMANCE AND SERVICEABILITY OF CONCRETE AND STEEL GIRDER BRIDGES

By

ALLA EDDINE ACHELI

Bachelor of Science in Civil Engineering
University of Science and Technology Houari Boumediene
Bab Ezzouar, Algiers, Algeria
2014

Master of Science in Civil Engineering
University of Science and Technology Houari Boumediene
Bab Ezzouar, Algiers, Algeria
2016

Master of Science in Civil Engineering
University of Houston
Houston, Texas,
2018

Submitted to the Faculty of the
Graduate College of the
Oklahoma State University
in partial fulfillment of
the requirements for
the Degree of
DOCTOR OF PHILOSOPHY
May 2023

IMPLEMENTATION OF STRUCTURAL

MONITORING TO ASSESS THE PERFORMANCE

AND SERVICEABILITY OF CONCRETE AND STEEL

GIRDER BRIDGES

Dissertation Approved:

Dr. Bruce W. Russell

Dissertation Adviser

Dr. Mohamed Soliman

Dr. Robert Emerson

Dr. Ning Wang

ACKNOWLEDGEMENTS

First and foremost, I would like to thank my parents (Hakim Acheli and Sakina Laib) that stood behind me since I came to this world. They have pushed me and supported me in all the ways they could to further my studies. I would like to thank Dr. Larbi Sennour that had inspired me to leave my country and pursue my studies in the United States. A special thanks for my brothers (Ahmed Imad Eddine Acheli, and Adel Acheli) that were supporting me with everything they could. I would like to thank my aunts (Acheli Samia, and Laib Karima) that kept encouraging me since the first day I came to the United States. I would like also to thank Dr. Bruce Russell for his guidance and support throughout my Ph.D. program. His expertise and knowledge have inspired me to excel both in academics and in the development of my personal character. It has been an honor and a blessing to be his student. I am thankful to my fellow graduate students: Christopher Filip, Dillon Cochran and Dr. Hema Jayasselan for all their time and hard work in this research program. I also want to thank the team of undergraduate research assistants who contributed to my research. I want to thank my family members for all their support and encouragement.

I am thankful for all my professors for their support and guidance. I gratefully acknowledge the sponsors of this research, Oklahoma Department of Transportation (ODOT) and W&W Steel/AFCO Steel Co.

Name: Alla Eddine Acheli

Date of Degree: MAY 2023

Title of Study: IMPLEMENTATION OF STRUCTURAL MONITORING TO ASSESS THE PERFORMANCE AND SERVICEABILITY OF CONCRETE AND STEEL GIRDER BRIDGES

Major Field: CIVIL ENGINEERING

Abstract: This research focuses on bridges and the development of structural monitoring systems used for both concrete and steel bridges. Parts of two bridges were built with a combination of sensors attached to a data acquisition system powered by a solar panel and battery, where data is transmitted wirelessly through cell phone technology. The research represents the first efforts to develop remote structural monitoring that is robust and reliable to survive through the construction of both concrete and steel bridges and continue to function from the beam fabrication through bridge construction and even now as the bridges have been in service for more than two years.

Prestressed Concrete Bridge Beams were instrumented during beam fabrication. Concrete strains, concrete temperatures, and ambient temperatures are measured continuously from the time immediately before the casting of the beams, through fabrication, including detensioning of prestressing strands, through handling and storage, transportation, and erection, through bridge construction, and now during life-in-service. Sensors capture concrete strains and temperatures from early ages. These data are useful to assess important variables regarding the design and construction of prestressed concrete bridge beams and the bridges made with those beams. Specifically, prestress losses were assessed, and beam cambers were measured. Designs were varied to investigate different design choices to control and limit both prestress losses and cambers.

In-situ load testing was performed on the completed concrete bridge structure. These data are used to investigate design parameters, specifically distribution factors for bridges' design and load rating and the dynamic amplification factor for bridges. Recommendations are made from the research.

Findings from the research demonstrate the effectiveness of including fully tensioned top strands in prestressing strand patterns and mild horizontal steel as part of the primary reinforcement at midspans of bridge beams. The research shows that both of these design choices are effective in limiting prestress losses and beam cambers. These techniques can be employed nationwide and worldwide where precast, prestressed concrete bridge beams are used.

TABLE OF CONTENTS

Chapter Page

Chapter Page

LIST OF TABLES

Table Page

Table Page

LIST OF FIGURES

Figure Page

Figure Page

Figure Page

Figure Page

Figure Page

Figure Page

CHAPTER I

1. INTRODUCTION

The United States highway transportation infrastructure is aging. The National Highway System contains over 617 000 bridges, 42 percent of which are 50 years or older. According to the National Bridge Inventory, 7.5% of the nation's bridges are considered structurally deficient (ASCE, 2021). Therefore, the decision-making concerning bridge repair, rehabilitation, or replacement has clear economic consequences.

Structural Health Monitoring is a new way to assess the condition of bridges. Thanks to advancements in sensors, data acquisition, and networking technologies, complex and accurate systems can now evaluate the performance of both new and existing bridges. This enables more precise evaluations, which help make better bridge repair and rehabilitation decisions with clear economic consequences. (Farrar & Worden, 2007). Bridges are monitored to achieve an optimal assessment.

In this study, our primary focus was to implement structural health monitoring systems for both steel and concrete bridges. The steel bridge selected for the structural monitoring

program is the bridge located on State Highway 4 over the Chikaskia River in Blackwell, Oklahoma, USA. This bridge represents a typical steel bridge rehabilitation in the state.

The bridge is older than 50 years old, and new deck slabs are placed on the existing steel girders. Newly rehabilitated bridges have experienced poor ride quality (Jayaseelan et al., 2019). Instrumentation, data acquisition, and structural monitoring were employed to assess strains, temperatures, and other factors that influence the bridge's performance. The purpose of structural monitoring of the SH 11 bridge is to investigate the causes of poor ride quality and poor elevation control in newly rehabilitated steel bridges. Furthermore, the research aims to improve the understanding of volume changes that contribute to the bridge's early age deflection and cracking. The results of monitoring State Highway 11 are presented in Chapter 3. However, the analysis is not included in this research.

The second bridge selected for a structural health monitoring program is located on State Highway 4 over the North Canadian River in Yukon, Oklahoma, USA. The bridge represents typical new concrete bridge construction. The purpose of the structural monitoring System and instrumentation are deployed to measure concrete strains and temperature for concrete girders during beam fabrication, transportation, erection, bridge construction, and life in service. The results of monitoring the bridge in SH 4 are to investigate prestress. Prestress losses refer to the gradual reduction in the level of force exerted by the prestressing tendons over time. These losses can significantly impact the structural behavior of concrete elements, such as beams and slabs, and can lead to excessive deflections.

Predicting prestress losses is essential for designing prestressed concrete girders. Prestressed concrete girder bridges require accurate camber and prestress loss predictions. Excessive camber reduces serviceability and constructability. Predicting prestress loss accurately can reduce prestressing reinforcement and improve girder behavior prediction. Eccentric prestress moment causes camber or upward deflection. Creep, shrinkage, concrete elastic modulus, tendon profile, superimposed dead loads, and service loads affect camber and prestress loss (Tadros, 2003).

Several prestress losses models, including the AASHTO 2020 LRFD approximate method, the AASHTO 2020 LRFD Refined method, the PCI Design Handbook method, a modified version of the PCI Design Handbook method, and the Jayaseelan Time-Step Method, were used to predict and compare prestress losses. On this bridge, the prestress loss results are compared to those obtained using vibrating wire gauges embedded in two girders. This research aims to investigate the effectiveness of mild steel as primary reinforcement and fully tensioned top strands in controlling prestress losses and camber. The camber of a prestressed concrete bridge is created by the initial tensioning of the prestressing tendons during construction. The tension in the tendons causes the concrete to arch upward, resulting in a positive camber. However, over time, the tension in the tendons may decrease, causing the concrete to deflect and reducing the camber of the bridge. This phenomenon is known as prestress loss and can significantly impact the structural behavior of the bridge. The purpose of this research was also to assess the effectiveness of the inclusion of mild steel and fully top strands in reducing and mitigating camber. Although vibrating wire gauges are typically applied in the monitoring of prestress losses; however, it is possible to employ these gauges in the

estimation of camber deformation. In spite of the fact that these gauges are utilized rather regularly, there has been, to the best of our knowledge, no research has suggested this. Therefore, one of the objectives of this research is to use the strain data of the gauges to calculate camber and compare them with physical measurements.

Furthermore, the State Highway 4 bridge was a candidate for moving and static load testing. Performing load tests on bridges is a critical step in assessing the live load distribution factors, which are crucial for ensuring the safety and efficiency of the bridge. The study assessed the accuracy of distribution factor (DF) approaches and determined if overestimating DFs for external girders leads to incorrect quantities of prestressing reinforcement. Excessive reinforcing can lead to an increase in camber and prestress losses, as well as have a negative effect on end region cracking and the constructability of the bridge. A comparison was made between the research findings and the analytical methodologies prescribed by AASHTO codes. In addition, a finite element model was developed to duplicate the load test and evaluate the effectiveness of the parapets and diaphragms in distributing the live load.

Last but not least, the Oklahoma Department of Transportation (ODOT) was tasked to re-evaluate the load ratings for all bridges affected by new emergency vehicle loading. To accomplish this goal, ODOT has reached out to Oklahoma State University for assistance in rating the steel girder bridges that would be affected. FHWA has stated that all bridges on the Interstates System and within reasonable access to the interstate systems must be rated for the new Emergency Vehicle by December 31, 2019 (Hartmann, 2016). The main purpose is to apply shear and moment loads per the FAST Act EV3 loading to the existing 40 ft. span bridge structures in the Bert Engineering Cooper Laboratory. Using

additional instrumentations to determine whether the LFR and the LRFR provide reasonable assurance of capacity for both shear and moment considering the larger of the axle loads.

The following describe the research methodology, and provide an overview of this dissertation:

II. **Chapter II:** This chapter include a comprehensive literature review of the following:

- Overview of load rating
- Prestress Losses and Camber
    - Self-Consolidating concrete.
- Live load distribution factors.
- Dynamic load allowance
- Fixing America Surface Transportation Act

III. **Chapter III:** This chapter contains a comprehensive discussion on instrumentation and the structural monitoring program. This chapter describes in full the instruments and the Data Acquisition system that were used for this research.

IV. **Chapter IV:** This chapter focuses on evaluating prestress losses evaluation models to measured losses. This chapter highlights the effectiveness of implementing fully tensioned top strands and mild steel in losses.

V. **Chapter V:** This chapter focuses on evaluating camber measurements. This chapter highlights the effectiveness of implementing fully tensioned top strands and mild steel in losses.

VI. **Chapter VI:** This chapter focuses on evaluating bridge behavior when subjected to service loads.

VII. **Chapter VII:** This chapter focuses on evaluation of the effects of new emergency vehicles on the load rating of steel girder bridges in Oklahoma.

CHAPTER II

2. REVIEW OF LITERATURE

This section provides a detailed literature review for this study. This section contains six main parts that are relevant to the research program. Which are:

1. Overview of Load Rating and Condition Assessment
2. Structural Health Monitoring
3. Prestress losses and Camber
    a. Self-Consolidating Concrete
4. Live Load Distribution Factors
5. Fixing America Surface Transportation Act

2.1. Overview of Load Rating and Condition Assessment:

In the United States, the condition assessment of bridges mainly depends on visual inspections required by the Departments of Transportation. It has been determined that the most significant technical obstacle to efficient infrastructure management is this subjective and potentially inaccurate methods for assessing the current condition (Aktan et al., 1998). For instance, the condition of bridges is typically expressed in terms of subjective indices, which are solely based on visual inspections of the structure. Therefore, it is challenging to accurately evaluate the conditions of the structure based on data from the visual inspection, even when specialists carry out this inspection (Aktan et al., 1998).

Analytical models and field testing are the two methods that have traditionally been provided by bridge evaluation standards (AASHTO, 2018) as approaches to load rating. Analytical models are derived from simplified assumptions, and as a result, they may not accurately reflect the realistic behavior of a bridge given its current physical conditions (Goulet et al., 2014).

A load rating is the strength evaluation procedure used to estimate the allowable in-service load that a bridge structure can withstand without taking damage and the maximum load that the structure can carry without collapsing or failing. This is accomplished by comparing the allowable in-service load to the maximum load the structure can carry without collapsing or failing (Hernandez Ramos, 2018).

Field tests have, for the most part, demonstrated that reserves of strength capacity beyond current ratings, despite the age and visual condition assessments. There is a wide variety of potential explanations for the difference, one of which is that it is caused by several in-

situ parameters that were not considered during the design or evaluation of the structural strength of the bridge. Because it provides an in-service and as-built characterization of the bridge's performance, load testing is an effective method used to evaluate bridges' structural performance (Hernandez Ramos, 2018).

Another method that can be implemented to evaluate bridge conditions is Structural Health Monitoring (SHM) or structural monitoring (SM). Within the scope of asset management, structural health monitoring of bridges is an essential tool that has seen a rise in popularity over the past decade. SHM assists engineers in locating damage to bridge structures, which may be either material or geometrical. SHM provides tools that can swiftly pinpoint defects and damage in bridge components. This can lead to designs that are safer and more reliable. Technological advancements in sensor technology, data acquisition technology, and networking technology have made these advancements possible. Recent technological advances have made it possible to use more complex and more accurate systems to evaluate the performance of bridges that already exist and bridges that have recently been constructed (Farrar & Worden, 2007).

2.2. Structural Health Monitoring:

It is anticipated that the rapid development of SHM technology will promote a condition-based maintenance philosophy that will be more cost-effective than the time-based philosophy that is used at present. This shift will occur in place of the time-based philosophy that is used at present (Farrar & Worden, 2007).

Vibration-based structural health monitoring has been investigated intensively. However, it is difficult to detect damage to a structure due to the incompleteness of the monitoring information, and the fact that damage at specific locations may not change the vibration

modes or frequency of the whole structure. The assessment of the condition and performance of a structure can be improved if more variables such as displacement, strains, temperatures, etc. are monitored (Bao & Li, 2021).

2.3. Prestress Losses and Camber:

The use of prestressed concrete in construction depends on applying compressive stresses to concrete elements. The purpose of compressive stress is to lower the maximum tensile stresses in the concrete, thereby preventing cracking from occurring. The element receives the pre-compression stress (prestress) through the use of tendons that are either stressed prior to the placement of the concrete (known as pretensioning) or after the concrete has been allowed to harden (known as post-tensioning). The level of prestress will change over time due to volume changes in concrete (like creep and shrinkage) and external events that affect the member (such as deck placement). Any reduction in the amount of pretension is referred to as pretension loss, while any increase in pretension is referred to as stress gain. Elongation of the strand is what causes stress gains. Elongation of the strand is typically the result of a positive moment being placed on the beam due to either an external load or the differential shrinkage of the deck; numerous sources provide additional information regarding this phenomenon.

With the increased use of prestressed concrete bridge girders in the United States, efficient and effective design of prestressed concrete beams is essential for providing quality infrastructure to the current highway system. Effective design of prestressed concrete girders requires accurate prediction of prestress losses. It is desired to make accurate predictions of camber and prestress losses in the design of prestressed concrete girder bridges. Controlling camber is essential, as excessive camber can limit serviceability and constructability and affect ride quality. Accurately predicting prestress loss can contribute to the need for less prestressing reinforcement and being able to predict the behavior of a prestressed girder more accurately. Upward deflection, or

camber, is caused by eccentric prestress forces, otherwise known as prestress moment. Camber and prestress loss are affected by several factors, such as creep, shrinkage, elastic modulus of the concrete, tendon profile, superimposed dead loads, and service loads (Tadros, 2003).

Loss of prestress can be defined as the strain-related decrease in the strand stress, which can either be permanent or temporary and is primarily caused by creep, shrinkage, and elastic strains. This type of loss can occur in a prestressing system. The investigation of prestress losses calls for careful consideration of the phenomena mentioned above, all of which must be framed within the context of the sectional behavior of a girder element, which will serve as the primary focal point of this section. The pretensioned concrete elements will serve as the focal point of this investigation; however, many of the hypotheses presented here are applicable to concrete elements in general (Méndez, 2014).

Numerous studies have demonstrated that the currently available models have a tendency to over-predict the long-term time dependent losses and, as a result, the camber and deflection in prestress beams:

Zia, P., Preston, H. K., Scott, N. L., Workman, E. B., (1979). Estimating prestress losses. ***Concrete International*****,** ***1*****(6), 32-38.**

In the article published in 1979 by Zia et al., the authors presented a new method for predicting the loss of prestress in PC beams. This method considered the effects of several factors, including relaxation, creep, and shrinkage. The method involved statistical analysis estimating the amount of prestress losses over time. The first step is to calculate the elastic shortening loss. After that, the method considers the effects of relaxation and creep on the prestress as a function of time are both required steps in this process. This method also considers the effect of shrinkage, which, as time passes, can lead to an even further reduction in the amount of prestress. This method offers a methodical strategy for predicting the loss of prestress, which can be helpful for engineers and designers when making decisions regarding the design and maintenance of prestressed concrete structures.

Tadros, Al-Omashi, Seguirant and Gallat: NCHRP Report 496, (2003)

Tadros et al. (2003) researched high strength pretensioned concrete bridge girder prestress losses to develop design guidelines. Due to limitations in current loss estimation methods, NCHRP report 496 developed new prestress loss guidelines and formulas. Experimental and theoretical programs comprised this research. Seven full-scale bridges from Nebraska, New Hampshire, Texas, and Washington were tested to determine how material properties and other factors affect prestress losses in pretensioned concrete bridge girders.

In addition to this investigation, concrete creep, shrinkage, and modulus of elasticity were examined. The research shows that the AASHTO-LRFD and ACI Committee 363 equations underestimate high-strength concrete's Modulus of Elasticity because they don't account for coarse aggregate properties. AASHTO-LRFD specifications did not account for high-strength concrete and the interaction between the precast pretensioned concrete girder and the precast or cast-in-place concrete deck.

Time-Step, Refined, and Lump-Sum Methods were examined, and their drawbacks discussed. Also, concrete creep and shrinkage factors were thoroughly studied. The age-adjusted effective modulus was used to estimate prestress losses. Both methods correlated better with experimental test results than AASHTO-LRFD. Numerical examples showed the loss prediction methods' applicability.

The experimental program tested and measured bridge girder material properties. Material testing was done in labs and on-site. Concrete strength, modulus of elasticity, creep, and shrinkage were measured using similar concrete specimen cylinders. Based on

test results, concrete modulus of elasticity, creep, and shrinkage formulas were developed. ASTM C469-94 determined concrete's modulus of elasticity. ACI 318, ACI 363, and AASHTO specifications did not account for aggregate type's effect on concrete's modulus of elasticity. The test results suggested a formula with two factors, K1 and K2, where K1 was the difference between the national and local average. K2 indicated the desired calculation upper-bound or lower-bound value. This formula can account for local materials and high-strength concrete. Creep and shrinkage specimens were observed similarly. Demountable Mechanical Gauges (DEMEC) measured strains in specimens with a V/S ratio of 1.0 at 30% to 40% ambient relative humidity. The AASHTO-LRFD and ACI 209 creep and shrinkage ratio was much lower than desired. The creep and shrinkage formulas included relative humidity, volume to surface ratio, loading age, concrete strength, and time-development correction factors. Long-term prestress loss estimation was also approximated.

The second part of the experimental program tested seven full-scale bridge girders from four states that represented a variety of geographic conditions and construction practices. Vibrating wire gauges measured concrete strains and temperatures to derive prestress losses. Total prestress losses averaged 37.3 ksi. Comparing predicted prestress losses with measured prestress losses verified the proposed detail method. The proposed modulus of elasticity formula outperformed the AASHTO-LRFD and ACI 363 formulas. The proposed shrinkage formula averaged 105% of measured values, compared to 174% for AASHTO-LRFD and 155% for ACI209. The creep formula averaged 98% of experimental values versus 161% for AASHTO-LRFD and 179% for ACI-209. The NCHRP 496 method performed better than the above methods because it compared

results on bridges with accurately measured material properties. The other methods used design formulas. Experimental results confirmed Hou et al. (2001) and Mokhtarzadeh and Gross (1996) findings that creep coefficient differences significantly affect long-term prestress loss estimation. The study found that the proposed prestress loss estimation methods correlated well with the tests.

Jayaseelan, H., & Russell, B. W. (2019). Reducing Cambers and Prestress Losses by Including Fully Tensioned Top Prestressing Strands and Mild Reinforcing Steel. In *PCI Journal* (Vol. 64).

The group came up with a model for the loss of prestressing known as the Jayaseelan Time-step method. This model is based on the AASHTO Refined method and breaks down the change in concrete strength and modulus over time by using the ACI 209R equation (2-1).

$$(f'_c)_t = \frac{t}{\alpha+\beta t}(f'_c)_{28} \text{ (ACI 209R 2-1)} \qquad \textbf{Eq. 2.1}$$

This method is developed analytically. There is no experimental data that support this methodology. One of the objectives of this research is to provide data that can be used to evaluate this model.

2.3.1. Self-Consolidating Concrete:

In recent years, the use of self-consolidating concrete (SCC) has increased significantly. Self-consolidating concrete is employed to produce durable concrete independent of heavy construction activities. Okamura proposed the economic benefits from this type of concrete in 1986 (Okamura & Ouchi, 1998). The use of SCC has increased rapidly in North America, particularly in the precast industry, where it has been employed extensively in the United States since the early 2000s. Most of this concrete is used to manufacture precast elements for bridges and parking garages (ACI Committee 237, 2007).

The essential components of SCC's mix composition are the same as traditional concrete. However, SCC concrete is made from smaller aggregates and smaller quantities of coarse aggregate (in a given concrete mixture). To achieve the desired fresh concrete properties, SCC requires a higher proportion of fine components like sand and cement, and now limestone fines, and the inclusion of specialty chemical admixtures (Holschemacher and Klug, 2002). Since the paste volume of SCC is usually greater than that of conventional concrete, Bonen and Shah suggest that the shrinkage of SCC is greater than that of conventional concrete. Similar conclusions can be drawn regarding creep because SCC includes a minimum amount of aggregate in the concrete mix. However, the research on the effects of creep in SCC is limited (Bonen & Shah, 2005).

The modulus of elasticity of self-consolidating concrete is lower than that of regular concrete of similar compressive strength since the elastic modulus of standard aggregate is higher than that of the paste, and the absolute volume of the paste is greater in SCC (Garcia Theran, 2009). According to (ACI Committee 237, 2007), SCC's modulus of

elasticity is about 10 to 15 percent lower than that of conventional concrete with a similar compressive strength because of the necessary adjustment of mixture proportions to form SCC. However, there is yet to be a consensus that the modulus of elasticity of SCC is lower than traditional concrete. Some researchers have reported that the AASHTO LRFD and PCI equations overestimate the compressive modulus of elasticity of the self-consolidating concrete. The researchers have also reported that the prestress losses are higher than predicted by the current models (Meyers et al., 2012).

2.3.2. Creep and Shrinkage-Consolidating Concrete (SCC):

Creep is the continued deformation of a material under sustained load. In concrete structures, creep refers to the concrete's gradual deformation as a result of a sustained load over time. Shrinkage of concrete refers to the change of volume in concrete elements over time. These changes of volumes are due to the water loss from mixture (Lin & Burns, 1981).

Several factors, including the magnitude of the applied load and the length of time it was applied, can affect the degree to which concrete creeps. The ratio of the creep strain that occurs over time divided by the initial elastic strain is what is referred to as the creep coefficient. This ratio typically represents creep. Concrete shrinkage can be broken down into two categories: autogenous shrinkage, which happens directly from the initial hydration reaction, and drying shrinkage. Although the effect of autogenous shrinkage on most typical concrete mixtures is negligible, it may have a greater impact on concrete mixtures that contain a high proportion of paste, such as SCC. Capillary forces are responsible for drying shrinkage, brought on by the loss of capillary and adsorbed water from the cement paste to the surrounding environment as the paste dries. Capillary forces resulting from the loss of capillary and adsorbed water from the cement paste to the environment during drying cause drying shrinkage (Videla et al., 2008).

Several variables influence creep and shrinkage, including aggregate content and stiffness, water-cement ratio (w/c), cement content, compressive strength, volume-to-surface area ratio (V/S), temperature, relative humidity, curing time, and age at loading (Hansen et al., 1966; Troxell et al., 1958; Videla et al., 2008).

The aggregate volume and the aggregate's inherent stiffness play a significant role in the provision of restraint against shrinkage and stiffness to resist creep (Pickett, 1956).

Furthermore, in most cases, a higher compressive strength will result in a smaller magnitude of creep (Lopez et al., 2004).

Numerous researchers have investigated creep and shrinkage models for both high strength SCCs and regular SCCs and compared the results of their findings. According to Bonen and Shah (2005), the amount that SCC shrinks is significantly higher than that of conventional concrete. Because of the reduced amount of aggregate that is used in the production of SCC, one can reach the same kinds of conclusions regarding creep. However, there hasn't been a lot of research done on the effects of creep in SCC (Bonen & Shah, 2005). However, none of the creep and shrinkage models are able to account for the wide variety of SCC mixes that are utilized in the industry at the present time (Alghazali & Myers, 2020).

Wendling et al. (2018) have examined two different concrete mixtures. Standard and Lightweight SCCs for shrinkage and creep. Wendling et al. (2018) discovered that the AASHTO method tended to overestimate shrinkage for both concrete mixtures, particularly at younger ages, and that no method accurately represented the lower shrinkage rate of LWSCC. Due to its greater elastic deformation, the LWSCC exhibited a lower one-year creep coefficient (2.0) than the SCC (2.9) for specimens loaded at one day. This difference was significantly smaller for specimens loaded at 28 days with, LWSCC having a creep coefficient of 0.90 and SCC having a creep coefficient of 0.80. The measured prestress losses were greater than those predicted using unmodified Zia et

al. and AASHTO LRFD methods. The results presented by the authors indicated that modifications may be required for SCC and LWSCC relating to creep coefficient and base shrinkage; however, the limited number of tests performed does not provide sufficient information to guide any such modifications, and additional research is required to identify these values for a variety of aggregates and conditions.

2.3.3. Measuring prestress losses from vibrating wire gauges:

Several structural health monitoring (SHM) approaches to prestress loss monitoring exist. SHM is the continuous monitoring of structural parameters to derive information regarding the performance of a structure. Several parameters have been linked to the magnitude of prestress losses, such as the natural frequencies of the structure (Saiidi et al., 1994), the magnetic permeability of the prestressing strands (Liu et al., 2014), and the stress wave velocity in acoustoelastic methods (Chaki & Bourse, 2009).

However, as detailed in a report on estimating prestress losses by the joint ACI-ASCE Committee 423, most successful field applications and large-scale laboratory experiments for monitoring prestress losses are based on strain measurements using strain sensors installed on the prestressing strands or other no-prestressed reinforcement embedded in the concrete. This is because strain measurements provide a more accurate representation of the amount of stress applied to the concrete (Joint ACI-ASCE Committee 423, 2016).

Because of this restriction, the methods can only be applied to newly constructed structures because instrumentation can only be added during the building process of new structures. The maturity of strain sensing technologies, which allows for accurate and stable long-term measurements, is one of the advantages of strain monitoring. Another advantage is the sensitivity and direct relationship to prestress losses, both of which are achieved without the need for calibration for each structure. The sole purpose of looking into other solutions for monitoring prestress loss was to find a way around the requirement that a structure is continuously monitored from the moment it is constructed onward. However, the growing need and use of SHM and the benefits of instrumentation during construction outweigh the inconvenience of continuous monitoring in terms of

early damage detection. This is the case even though continuous monitoring is required (Abdel-Jaber & Glisic, 2018).

A significant number of studies have been carried out. Using strain gauges, Almohammedi et al. (2021) instrumented girders to conduct tests on the concrete materials. They found that the elastic shortening loss could be underpredicted by as much as 10% or overpredicted by 26% when using the AASHTO 2017 LRFD Refined method. According to the group's findings, this loss method also resulted in an average overestimation of long-term prestress losses. The group found that the minimum compressive strength of concrete specified in the design was significantly underestimated, leading to an inaccurate prediction of the elastic modulus of the concrete. This was the cause of the inaccurate prediction of the prestress loss.

Hale & Russell (2006) looked into the allowable compressive stress limit at release in precast, pretensioned concrete girders. In addition, the effects of prestress loss were investigated, and various loss prediction methods were compared with measured losses. The objective of this research was to investigate the effects of increasing the allowable compressive stress at release from $0.60 f'ci$ to $0.70 f'ci$, as well as to compare the measured prestress losses to the following loss prediction models:

1. The 2004 American Association of Highway Transportation Officials load-resistant factor design (AASHTO LRFD) Bridge Design Specifications (Refined method),
2. The PCI Design Handbook method described by (Zia, 1979),
3. The method proposed in the National Cooperative Highway Research Program (NCHRP) Report 496 (detailed method).

For this project, four girders were fabricated. The four concrete girders were identical in terms of geometry, and they were all made with one of two concrete mixtures that were virtually identical to one another. A concrete mixture that included an admixture for entrapping air was used to construct two girders. In order to compensate for the volumetric difference in the mixture, the remaining two girders were cast with a concrete mixture that did not contain any admixture for air-entraining, and the sand content of the mixture was adjusted accordingly. The strand patterns in each girder were the same, and there were ten strands embedded in the concrete. For certain girders to meet a specified effective prestress after elastic shortening loss, the strands in those girders had to be deboned.

Prestressing was released for two girders when they reached a target strength of $0.60\ f'ci.$ The remaining two girders were released when they reached a target strength of $0.75\ f'ci$. No adverse effects were observed on the girders when the compressive strength limit provided by AASHTO was exceeded. Strains were measured and recorded using detachable mechanical strain (DEMEC) gauge targets attached to the concrete's surface at midspan near the bottom and top flange. The change in strain was found for both the top and bottom of the girders and was considered linear along the beam's depth. The change in stress could be measured by multiplying the elastic modulus of prestressing strands at the center of gravity of the prestressing strands.

Comparing the measured prestress loss to the three loss prediction methods found that the 2004 AASHTO LRFD Refined method and PCI Design Handbook method overestimated prestress loss, while the NCHRP Report 496 was found to be more accurate and slightly underestimated prestress loss. The AASHTO refined equations, on average,

overestimated prestress loss by 18%. The PCI Design Handbook method, on average, overestimated prestress loss by 13%. The NCHRP Report 496 method, on average, underestimated prestress loss by 6%.

The group concluded that the air that was entrained in the concrete did not have a significant impact on the loss of prestress. When it came to predicting prestress loss, the AASHTO Refined method was the one that was the least accurate. The method described in detail in NCHRP Report 496 was the method that produced the most reliable results. All loss prediction methods predicted losses that were within 10% of the actually measured losses when the release stress was 0.82 f'ci, and it was discovered that the amount of prestress loss increased with higher release stresses.

2.3.4. Jayaseelan Time-Step Method:

Using the ACI 209R Eq. (2-1), Jayaseelan & Russell (2019) developed a prestress loss model called the Jayaseelan Time-step method. This model is based on the AASHTO Refined method and breaks down the change in concrete strength and modulus over time. The group investigated the effects of fully tensioned top strands and included mild steel reinforcement near the center of gravity of prestressing strands.

Five designs were investigated: one being a base case with no top strands and mild steel included two designs that included either two or four fully tensioned top strands and two designs that included mild steel reinforcing using either four no. Seven bars or five no. 9 bars. The research group compared the losses found using the method from the PCI Design Handbook, the method from the 2014 AASHTO LRFD Approximate and Refined, and the method from the Jayaseelan Time-step. The Jayaseelan Time-Step method was also used to make predictions regarding camber by computing the curvature. Calculations of strain were performed at each time increment (daily), and camber calculations were performed at each time increment. To calculate camber, the curvatures at both the ends and the midspan were utilized. In the computations of strain, the effects of gravity have already been incorporated. In addition to this, the variations in the properties of the material over time were taken into consideration. Following the placement of the slab, the camber that developed as a result of the additional creep strain was factored into the final deflection.

Both short-term and long-term camber can be reduced by 16% and 45%, respectively, when four fully tensioned top strands are included in the design. The utilization of top strands was also responsible for an 8% decrease in long-term losses. Additionally, it was

discovered that the use of reinforcing made of mild steel reduced camber by 12% in the short term and 24% in the long term. Reinforcing made of mild steel placed near the center of gravity of prestressed steel has been shown to reduce long-term losses by an additional 5%. The combination of fully tensioned top strands and mild steel reinforcement was shown to reduce cambers by 31% and 72%, respectively, over the short and long term.

The main concern about the findings of this research is mainly that the work performed relied on analytical data. The researchers have not employed experimental data to evaluate and validate their findings. **This research aims to collect experimental data that can be used to evaluate this method and evaluate the findings.**

2.3.5. Previous research on Camber measurements:

The long-term deflection and camber of eight pretensioned AASHTO Type IV girders were studied by Kelly et al. (1987). The deflection was measured by employing a reference piano wire pretensioned with a system that maintained a constant force. The results from these measured deflections were evaluated and analyzed compared to an updated version of the PCI multiplier method. The concept that time-dependent properties like concrete modulus, creep, shrinkage, and steel relaxation can have an effect on camber and prestress loss is brought up for discussion by the group. Additionally, the effects of having a composite deck are discussed. Adding a concrete deck increases the system's stiffness, which in turn slows the rate at which the camber grows. Additionally, the added dead load causes the strands below the center of gravity to regain their tensile stresses.

Camber was measured by the team, beginning with the detensioning of the prestressing strands, continuing through before and after deck casting, and continuing up to one year after the deck was put into service. The research team discovered that camber varied from -0.75 to 2 inches while in service but can be anywhere from 2 to 6 inches when they are first erected. The group discovered, through the use of AASHTO and PCI methods, that the camber was overpredicted by 0.64 inches and 0.15 inches, respectively, before and after deck casting. The discrepancy between the measured camber and the camber that was estimated is that the design strength at deck casting was specified as 6660 psi, but the measured concrete strength was 11,000 psi.

2.3.6. Parameters that can affect camber and prestress losses:

Storm et al. (2013) investigated the factors in the construction of precast, prestressed girders that affect camber. Compressive strength, elastic modulus, void deformation in box beams and cored slabs, debonding, and transfer length are the primary factors contributing to the camber that were investigated. Secondary factors were also discussed by the author, including temperature change of the strands as a result of sun exposure, cement hydration, and heat curing prior to the transfer of prestressing force, the production schedule for the girders, and the curing procedure. The researchers found that, on average, the measured concrete strength at transfer was 1.24 times that of the specified strength at transfer. On average, the 28-day compressive strength of concrete was measured at 1.45 times that of the specified 28-day strength. The investigation into elastic modulus found that, on average, the measured elastic modulus was 0.85 times that of the predicted modulus.

2.4. Live Load Distribution Factors:

A common method of understanding a bridge behavior is through load testing. This can be combined with visual inspection, structural health monitoring, non-destructive testing, and finite element-based structural modeling to evaluate bridge performance, strength, and serviceability. The distribution factor of the bridge girders is one important finding that may be made during load testing. The distribution factor (DF) for girders has traditionally been established using conservative methods. This frequently results in overestimating the load on exterior girders, which causes the girders to utilize more reinforcing. In addition to raising the cost of the bridge girders and potentially increasing camber and prestress losses, more reinforcement, specifically prestressing steel, might be detrimental to the bridge's durability.

2.4.1. Parameter influencing live load distribution:

Numerous studies on the distribution of loads on various types of vehicles have been conducted for several decades. As the outcomes of these studies have been reported, the empirical equations that are provided in the Standard Specifications have frequently been changed in order to reflect the findings of this research to achieve more precision in their results. However, this resulted in inconsistencies in the way distribution factors are calculated (Michaelson, 2010). Sanders (1984) provided the following concise summary of these conflicts and shortcomings: The majority of those distribution factors were established by taking into consideration only a select few parameters, which are as follows:

- Most Distribution Factors were developed by considering a limited set of variables such as:
    - Floor Type
    - Girder Spacing
    - Beam Type.
- The format of these distribution factors varies even within bridges of similar construction
    - Steel Girder Bridges
    - Precast Beams
    - Composite Box Girders.

Michaelson (2010) has investigated multiple parameters that can affect the distribution factors as follow:

- Girder spacing/number of girders

- Span length
- Girder stiffness
- Slab thickness
- Number of loaded lanes
- Deck overhang
- Skew
- Load configuration
- Boundary conditions
- Diaphragm
- Secondary stiffening elements

One of the objectives of this research program is to investigate the effectiveness of the following parameters on live load distribution factors:

1. **Diaphragm**
2. **Secondary stiffening elements**

Diaphragms:

Tarhini & Frederick, (1992) have researched, to a limited extent, the effect of diaphragms on live load distribution. Various configurations of the most prevalent channel diaphragm cross-bracing did not affect wheel load distribution, as determined by their analytical investigations. According to field experiments conducted by Kim & Nowak (1997), widely separated diaphragms result in more consistent girder distribution factors between girders, while there is no information about a correlation between increasing or reducing distribution and cross-frame distance.

Barr et al. (2001) used finite element analysis to determine prestressed concrete girder bridge distribution factors. The group conducted a static load test to validate their results and used the model to investigate the effects of lifts, intermediate diaphragms, end diaphragms, and load types. Comparisons were made between results and AASHTO methods for determining distribution factors. During load testing, the group discovered that FEA could predict the midspan moment within 6% of the measured moment. In addition, it was determined that AASHTO methods were typically conservative by between 6% and 28% when compared to the finite element results. The FEA results also revealed that intermediate diaphragms had little impact on load distribution, whereas end diaphragms and lifts significantly decreased distribution factors in the bridge girders.

Lin & VanHorn (1968) Investigated the influence of diaphragms on the load distribution of prestressed concrete girder bridges. Using strain gauges, the crew conducted load tests on a bridge and assessed strain. Strain gauge data was utilized to calculate deflection and internal moments. Comparing observed and projected distribution factors, the panel

concluded that diaphragms had a minimal impact on load distribution by up to 3% and advised that they are unnecessary in design.

Secondary Stiffening Elements:

The influence of secondary stiffening components (such as sidewalks, parapets, and railings) on live load distribution has also been investigated. However, these efforts have yielded generally inconclusive outcomes. Using the finite element computer, Mabsout et al. (1997) investigated the impacts of sidewalks and railings placed on one or both sides of a bridge. According to these investigations, adding these individuals did not result in a discernible pattern of bridge behavior.

On the other hand, a different research report conducted in 1997 by Mabsout et al. reveals a more significant association between the existence of walkways and railings and girder distribution characteristics. Comparisons were made between the results obtained from various combinations of sidewalk and/or railing on one or both sides of the bridge and distribution factors acquired from the most recent LFD and LRFD Specifications. In conclusion, the researchers found that the current LRFD girder distribution factors are 9 to 30 percentage points higher than those obtained in the finite element studies. This discrepancy depends on the combination of added stiffening elements and the location of those elements (sidewalk and/or railing, one or both sides of the bridge).

While secondary stiffening elements (such as guard rails and parapets) affect live load distribution, Nutt et al. (1988) note that including these members in design may be conservative. For instance, if the bridge was widened after its initial construction, the curbs and parapets would be removed. Therefore, the improved distribution provided by these elements would be lost, and girders designed to take advantage of this behavior could become overstressed.

Conner & Huo (2006) have developed finite element models to investigate the impact of parapets and aspect ratio on the distribution factors for live loads. The research group created finite element models with varying skew angles, overhang lengths, and width-to-length ratios (aspect ratios). The researchers maintained consistent girder spacing throughout the experiment and added new girders as the model's breadth rose. The team discovered that distribution factors of outside girders increased as the deck overhang increased. The distribution factors of the external girder grew at a greater rate as the overhang increased than they did in the model with the parapets included, indicating that the parapet becomes more effective at distributing load as the overhang increases. The study discovered that parapets could significantly reduce distribution factors in exterior girders by up to 36% and interior girders by up to 13%. The group also discovered that the AASHTO lever rule overestimated the distribution factors of external girders by an average of 21% due to the method's failure to account for the effects of parapets in the analysis.

Boundary Conditions:

Nutt et al. (1988) also investigated the difference in distribution factors between simple-span and two-span continuous bridges with the same other parameters. The analyzed two-span bridges had two equal-length spans (where the length of each span was equal to the equivalent simply supported bridge), five girders, and were not skewed. The results demonstrated that the distribution factors for the two-span bridges were 1 to 11% greater than those for the corresponding simple-span bridges. By analyzing the average increase in distribution factor between two-span continuous and simply supported bridges, Nutt et al. (1988) suggested that a constant correction factor of 1.04 be applied to distribution factors obtained for shear and a distribution factor of 1.10 be used for all bending moments.

Skew:

Nutt et al. (1988) observed that skew affected the distribution of live load. In particular, increasing skew tends to reduce the wheel load distribution for a moment and increase the shear distributed to the bridge's acute corner. In addition, they determined that this is a nonlinear effect and stated that its magnitude would increase as skew increases. As a result of their sensitivity analyses, two correction factors for skewed bridges (to be applied to the distribution factors obtained for a non-skewed bridge with identical geometry) were developed; one suggested correction factor is to be applied to the distribution factor for moment, and the other is to be applied to the distribution factor for shear in the bridge's obtuse corner. These correction factors depend on girder spacing, span length, slab thickness, transformed girder moment of inertia, transformed girder area, girder eccentricity, and skew angle.

2.4.2. Design code:

Live Load Distribution Factors for Interior Girders:

The AASHTO LRFD methodology (AASHTO 2020) was used to compute the interior and exterior girder distribution factors for single and multiple loaded lanes. The load distribution factors for an interior girder with two or more (multiple) design lanes loaded was estimated using the following expression (AASHTO 2020 4.6.2.2.2b):

For one lane loaded:

$$DF_i^s = 0.06 + \left(\frac{S}{14}\right)^{0.4}\left(\frac{S}{L}\right)^{0.3}\left(\frac{K_g}{12.0Lt_s^3}\right)^{0.1} \quad \textbf{Eq. 2.2}$$

For two or more lanes loaded:

$$DF_i^m = 0.075 + \left(\frac{S}{9.5}\right)^{0.6}\left(\frac{S}{L}\right)^{0.2}\left(\frac{K_g}{12.0Lt_s^3}\right)^{0.1} \quad \textbf{Eq. 2.3}$$

Where:

L: span length (in.)

S: girder spacing (in.)

t_s: deck thickness (in.)

K_g: Longitudinal stifness parameter can be computed as follow (AASHTOO 2020 4.6.2.2.1-1)

$$K_g = n\left(I + Ae_g{}^2\right) \quad \textbf{Eq. 2.4}$$

Where:

$$n = \frac{E_B}{E_D}$$ **Eq. 2.5**

A: Noncomposite area of the girder

e_g: Distance between the centers of gravity of the basic beam and deck

I: Non composite area of the girder

Live Load Distribution Factors for Exterior Girder:

The live load distribution factors for exterior girders were estimated as specified in the AASHTO LRFD 2020 edition as shown in **Error! Reference source not found.**

Table 2.1: Table provided by AASHTO for determining distribution factors.

Table 4.6.2.2.2d-1—Live Load Distribution Factor for Moment in Exterior Longitudinal Beams

Type of Superstructure	Applicable Cross-Section from Table 4.6.2.2.1-1	One Design Lane Loaded	Two or More Design Lanes Loaded	Range of Applicability
Wood Deck on Wood or Steel Beams	a, 1	Lever Rule	Lever Rule	N/A
Concrete Deck on Wood Beams	1	Lever Rule	Lever Rule	N/A
Concrete Deck or Filled Grid, Partially Filled Grid, or Unfilled Grid Deck Composite with Reinforced Concrete Slab on Steel or Concrete Beams; Concrete T-Beams, T- and Double T-Sections	a, e, k and also i, j if sufficiently connected to act as a unit	Lever Rule	$g = e\,g_{interior}$ $e = 0.77 + \frac{d_e}{9.1}$	$-1.0 \le d_e \le 5.5$
			use lesser of the values obtained from the equation above with $N_b = 3$ or the lever rule	$N_b = 3$

The exterior girder's load distribution factor for two or more design lanes loaded was computed with the following expressions:

$$DF_e{}^m = e(DFi^m) \qquad \textbf{Eq. 2.6}$$

$$e = 0.77 + \frac{d_e}{9.1} \qquad \textbf{Eq. 2.7}$$

Where:

d_e: the horizontal distance from exterior girder's centroid to barrier of the edge in (in.)

Lever Rule Method:

The lever rule is found in chapter 4 of the 2020 edition of AASHTO LRFD. Provisions on computing distribution factors with the lever rule can be found in section 4.6.2.2.1. This method assumes a hinge on top of the girders in a span. Truck loading is placed on the span and reactions of the girders are calculated, deriving the distribution factor.

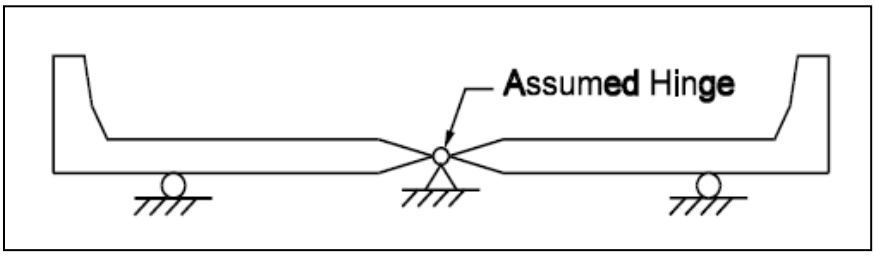

Figure 2.1: Lever rule example from section C4.6.2.2.1-1 of 2020 AASHTO LRFD.

2.5. Fixing America Surface Transportation Act (FAST Act):

The Federal Highway Administration (FHWA) has established new weight restrictions for vehicles to consider growing emergency vehicle sizes. The FHWA has specifically described a new emergency vehicle that bridges must be rated with in a letter referencing the transportation law known as the FAST Act that was passed at the end of 2015. An emergency vehicle, according to the memo, "is designed to be utilized under emergency conditions to carry persons and equipment to help the mitigation of other dangerous situations and the suppression of fires." The ability of these vehicles to successfully navigate roads can swiftly become a matter of life and death due to their significance in emergency scenarios. The FAST legislation intends to improve the effectiveness of emergency vehicle travel and shorten overall response times with the amendments made to weight restrictions.

The FAST act made revisions to the regulations on the weight of emergency vehicles. The modifications are meant to account for the load impacts of all common emergency vehicles. When these vehicles cross bridges, the FHWA cautions that they "may cause larger load impacts relative to AASHTO authorized loads" (Hartmann, 2016). The FHWA "found that, for load rating, two emergency vehicle configurations provide load effects in typical bridges that encapsulate the effects arising from the family of typical emergency vehicles" to mimic these load effects (Hartmann, 2016). The EV3 designation refers to these wrapped vehicle designs (Stansfield, 2018).

The restrictions on vehicle weight limits that were previously in place for all bridges are listed in **Error! Reference source not found.** below. The new restrictions placed on

automobiles due to the FAST legislation are shown in **Error! Reference source not found.** below.

Table 2.2: Vehicle Weight Limitations Prior to FAST Act

Vehicle Weight Limitations Prior to FAST Act	
Restriction	Weight Limit (kips)
Gross Vehicle Weight	80
Single Drive Axle	20
Tandem Axle	34

Table 2.3: FAST Act Vehicle Weight Limitations

FAST Vehicle Weight Limitations	
Restriction	Weight Limit (kips)
Gross Vehicle Weight	86
Single Drive Axle	34
Tandem Axle	62

In accordance with the FHWA directive, the AASHTO LRFR approach is required to be utilized in the rating process for all bridges. When determining the rating of a structure, the LRFR approach employs the HL-93 loading condition just like the LRFD method does. According to the FHWA document, the only modification made to the standard LRFR approach is the addition of the new EV3 vehicles. This is the only adjustment that is done. Only in cases where the bridge structure is "on the Interstate System (or) within reasonable access to the Interstate System" are these configurations eligible for load rating consideration (Hartmann, 2016). The memorandum provides additional clarification regarding the meaning of "reasonable access" by stating that it must be "at least one road mile from access to and from the National Network of roadways" (Hartmann, 2016).

When making any changes to the legal loads, careful thought needs to be given to the implications of those changes. This is because additional loading has the potential to have a detrimental effect on the lifespan of bridges and other transportation constructions. According to the FHWA, the purpose of adding the new emergency vehicles is to "accelerate the dispatch and safe movement of firefighters and fire trucks by eliminating the existing permitting and routing process." This will "accelerate" the sending out firefighters and moving fire trucks. It can also result in cost savings, particularly when emergency vehicles need to go through numerous jurisdictions (Office of Bridges and Structures, 2018). The Federal Highway Administration (FHWA) believes that the potential for emergency vehicles to be dispatched with improved efficiency is of more significance than the potential for additional weight constraints to have a detrimental impact on the ratings of bridge structures (Stansfield, 2018).

Based on the LRFD bridge standard and the LRFR approach, the following **Error! Reference source not found.** provides a summary of the live load factors that are necessary for the various loading configurations that have been described in this study.

Table 2.4: Load rating factors for HL-93 and for EV-3

	Live Load Factors Used for The Analysis	
Loading Configuration	Inventory/Operating	Live Load Factors
HL93	Inventory	1.75
	Operating	1.35
EV3	N. A	1.30

Oklahoma Department of Transportation was tasked to re-evaluate the load rating for all bridges affected by the new emergency vehicle loading. Federal Highway Administration stated that “bridges on the Interstate System and within reasonable access to the Interstate System (Hartmann, 2016). Therefore, the interstate bridges within the state of Oklahoma must be rated for the new emergency vehicle EV3. The FAST act bill is meant to simplify the permitting process for emergency vehicles by including a new provision.

CHAPTER III

3. IMPLEMENTATION OF STRUCTURAL MONITORING AND INSTRUMENTATION FOR STEEL AND CONCRETE BRIDGES

3.1. Introduction

Structural Monitoring systems were installed on two bridges in Oklahoma. One SM system was installed on SH 11 over the Chikaskia River in Kay Co. near Blackwell. The SH 11 Bridge was rehabilitated by casting new concrete decks atop existing steel plate girders. The SM system was actively taking measurements before construction began and continued through construction which occurred mostly in 2020 and 2021. The SM system remains active, and data are being recorded in present time. The system allows real time measurements 24 hours per day, seven days per week, and every day of the years (24/7/365). The system stores data while not actively acquired – and data is transmitted via cell-phone technology. The cost of the data line is about $400 per yar.

Two SM systems were installed on SH 4 Bridge over the North Canadian River in Candian Co., Oklahoma. This bridge has 15 spans, each nominally 100 ft. in length and built with concrete decks atop new precast/pretensioned concrete bridge (PC) beams. Each span is supported by four (4) Type IV girders, so there are 60 Type IV girders in the bridge.

Two of the PC beams were instrumented and connected to data acquisition systems. So each of the beam beams carries a self-contained SM system. All systems are powered by batteries that are in turn powered and charged by solar panels. The technology is relatively inexpensive – but the selection of instrumentation and the rapidity of measurement affect the power requirements of the system. All three of these systems have performed reliably and without fail. The solar- powered battery systems have never failed to deliver power needed for the constant, 24/7/365 monitoring of the systems except for the theft of a solar panel and battery that occurred at SH 11. Since that theft, we have obscured the solar panel and the system remains in-place, and measures and transmits data undeterred.

The structural monitoring program implemented in this research integrates sensors derived from a variety of different technologies into a single database system and has a friendly user interface system. The structural monitoring system employed for this research is similar to the one that was implemented by Jayaseelan to monitor a full-scale prototype bridge. (Jayaseelan, 2019)

Jayaseelan (2019) presented the performance of various instrumentation installed on the full-size laboratory prototype bridge. She also discussed the advantages of each type of sensor used. Furthermore, the researcher planned and implemented the structural health monitoring program for the SH 11 Bridge. This research is built from the Structural Monitoring research conducted by Jayaseelan. Through the experience gained from the installation and monitoring of the laboratory prototype bridge, a structural monitoring system was set up and installed for a field bridge.

For this research, two bridges were candidates for a structural health monitoring program. First, a newly rehabilitated steel girder bridge is located in Blackwell, Oklahoma, on State Highway 11 over the Chikaskia River. Also, a prestressed concrete girder bridge located on State Highway 4 over the Canadian county river, Oklahoma, in the United States was instrumented.

The sensors that were selected to perform these measurements include:), Thermocouples, Vibrating Wire Strain Gauges (VWSG), Linear Variable Differential Transducers (LVDT), and Accelerometers. The instrumentation system used in this research was designed and programmed to monitor both early age and long-term and the dynamic performance of the bridges.

This chapter reviews the performance of various instrumentation installed on field bridges. The signal output from the sensors was monitored continuously since the time of installation, and their performance in monitoring short-term and long-term responses was recorded and evaluated. A detailed description of the scope, installation, and performance of each sensor used in this research is discussed.

3.2. Data Acquisition System Implemented for Long and Short Term

Campbell Scientific Technology data loggers and equipment was employed for the data acquisition system for this research. The requirements for instrumentation include temperature measurements from thermocouples, strain measurements from Electrical Resistance and Vibrating Wire Strain gages, and deflections. The data acquisition system layout is shown in Figure 3.1 The data logger, modem, and multiplexers are mounted inside a weatherproof enclosure box.

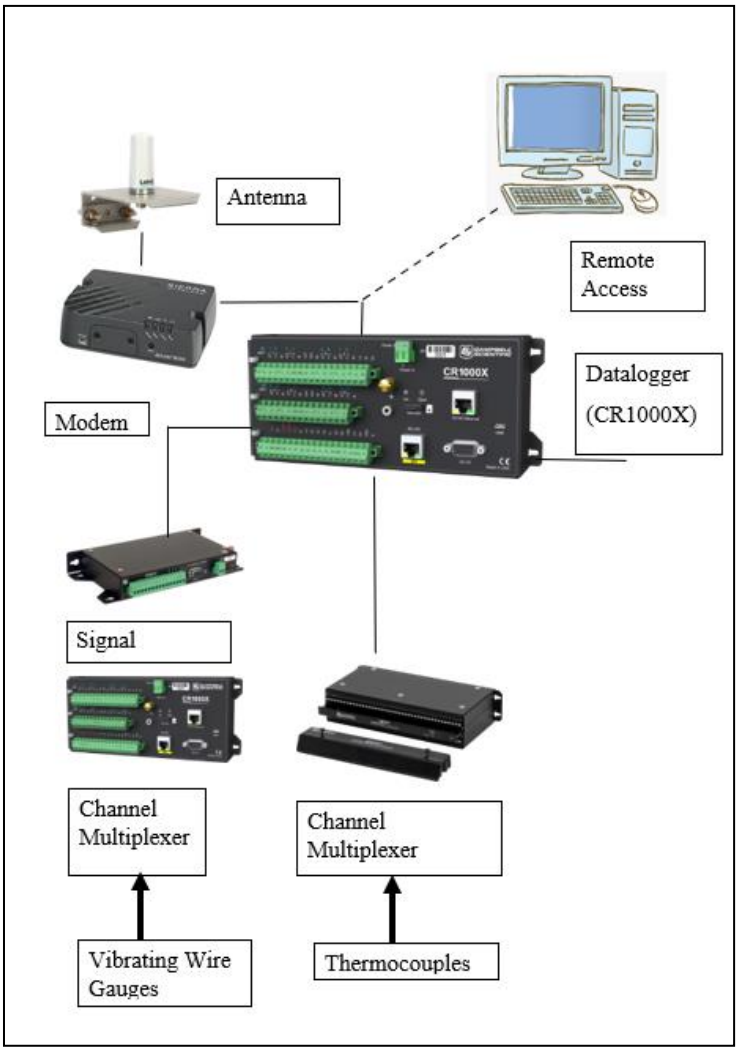

Figure 3.1: Schematic of Instrument and Data Acquisition Systems.

3.2.1. Interface Systems and Communication and Power Supply.

CR1000X:

The CR1000X is a popular data logger in the market. The CR1000X provides measurements and control for a wide variety of applications. This Datalogger is a low-power device (under 12V). The benefits of using this data logger are:

- Operates under extreme weather conditions (-40°F to 158°F).
- Includes microSD card drives for extended memory
- It has a friendly user interface and is easy to program.
- The resolution of the measurements is high (24-bit)
- It can connect directly to a computer with a USB port
- It can be programmed to access it remotely.
- Its maximum scan rate is 1k Hz.

GRANITE VOLT 116 16- or 32-Channel 5V Analog Input Module

VOLT 116 is a 24-bit analog input module. Using these modules in a data logger system can greatly expand the number of analog channels available. The VOLT 108 has a total of four differential channels, whereas the VOLT 116 has a total of sixteen differential channels.
In order to deliver excellent analog readings, the VOLT 116 comes equipped with both a low-noise analog front-end and a 24-bit analog-to-digital converter. In addition to that, it is capable of performing average period measurements and incorporates current in addition to voltage in its excitation channels.24-bit ADC and low-noise inputs for increased measurement quality

- Distributed data acquisition
- Channel count expansion via the CPI bus on Campbell Scientific data loggers
- Easier to program than traditional multiplexers
- Programmable noise rejection
- CANbus 2.0 A/B output available with the Extended Duty (-XD) version

- USB 2.0 interface for PC-based operation with Campbell Scientific Surveyor software

The Granite VOLT 116 was employed for the static and moving load testing.

3.2.2. Channel Relay Multiplexer AM16/32:

The AM16/32 multiplexer is a device from Campbell Scientific. This device provides the datalogger with more channels for sensors. The benefit of employing this device is:

- Increase the number of sensors that the data logger can measure.
- Support many types of sensors.

3.2.3. Channel Solid State Multiplexer AM25T

The AM25T is another device from Campbell Scientific Technology. This device increases the number of thermocouples that the datalogger can support. This device is also compatible with the CR1000X datalogger. The benefits of using the AM25T are:

- Increases the number of thermocouples a data logger can measure (up to 25 thermocouples)
- Uses a metallic, internal ground plane to reduce thermal gradients, which ensures more accurate measurements

3.2.4. Vibrating Wire Analyzer Module (AVW200):

This module is also from Campbell Scientific Technology and can measure vibrating wire strain gauges. This module uses vibrating wire spectral technology that overserves the incoming sensor signal. Then, the module performs a spectral analysis (transforming the time series into individual sinusoidal components in the frequency spectrum) and determines the sensor frequency by identifying the largest signal in the acceptable range while filtering out environmental and electrical noise. The benefits of employing this module are:

- Provides better measurements by significantly reducing incorrect readings caused by noise sources

- Interfaces two vibrating-wire sensors; more sensors may be connected if an AM16/32B multiplexer is used
- High resolution—less than 0.001 Hz (industry standard is 0.1 Hz)
- Interfaces both temperature and frequency measurements from vibrating-wire sensors
- Low current drain
- Self-checking diagnostics give continual feedback on sensor condition

Instrumentation and data acquisition systems allowed continuous monitoring of data from the time of P.C. beam fabrication through handling and storage, including transportation and erection, and continuously through the construction of the entire bridge and service life.

3.1. Instrumentation Implemented in this Research

3.2.5. Vibrating Wire Strain Gages:

GEOKON 4000 & GEOKON 4200:

The vibrating wire strain gauges of the Model 4000 variety are primarily designed to measure strain on structural steel members. Attachment to steel surfaces can be achieved by arc welding the mounting blocks to the surface. The vibrating wire principle is utilized in the measurement of strain. A section of wire made of steel is stretched taut between two mounting blocks that have been welded to the steel surface, which is the subject of the investigation. Because of the surface's deformations, the two mounting blocks will shift in relation to one another, resulting in a different tension on the steel wire.

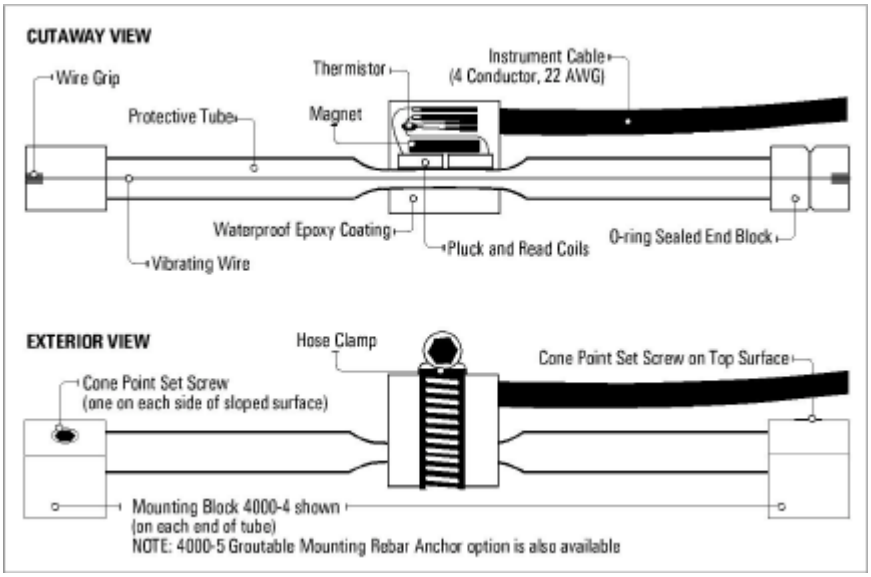

Figure 3.2: Vibrating Wire Strain Gauge (GEOKON)

The vibrating wire strain gauges of the Model 4200 variety are primarily made to be directly embedded in concrete for optimal performance. It is possible to accomplish this by either grouting the gauge into boreholes in the concrete or by attaching the gauge to rebar or tensioning cables and then casting the gauge into a concrete element cast into the structure. Another option is to cast the gauge directly into the structure.

As the steel surrounding the sensor contracts or expands, the tension in the wire is changed by the movement of flanges relative to one another. This causes changes in the resonant frequency of the vibrating wire. The vibrating wire is excited with a range of frequencies by plucking it with an electromagnetic coil. The electromagnetic coil detects the resonant frequency of the vibrating wire. The detected frequencies are converted to a DC voltage and recorded by the datalogger as strain values. Each vibrating wire strain gauge is equipped with a thermistor that measures the temperature (20°C to +80°C) in the surrounding concrete at the gauge level. (Jayaseelan, 2019)

GEOKON Manual has prescribed how to calculate the change in strains. The apparent strain can be calculated as follow:

$$\mu\varepsilon apparent = (R_1 - R_0)B \qquad \textbf{Eq. 3.1}$$

Where:

R_0: Initial Reading

R_1: Current Output reading taking at a specific time.

In addition to the strain measurements, the vibrating wire gauges can also measure temperatures. These temperature differences also affect the functioning of the gauge. The increase in concrete temperatures causes the vibrating wire inside the gage to elongate, and as a result, it becomes slack, which indicates what would appear to be compressive strains in the concrete. Additionally, the coefficient of concrete expansion is not the same as that of steel. The application of a temperature correction brings this to its correct state. As a result, the following formula can be used to calculate the load-related strain in concrete that is produced by both external loads and temperature effects after temperature adjustment:

$$\mu\varepsilon apparent = (R_1 - R_0)B + (T_1 - T_0)((C_1 - C_2) \qquad \textbf{Eq. 3.2}$$

Where:

R_0: Initial Reading

R_1: Current Output reading taking at a specific time.

C_1: Coefficient of expansion of steel, taken as 12.2 microstrains/ºC

C_2: Coefficient of expansion of concrete, taken as 10 microstrains/ºC

Figure 3.3: Geokon model 4000 VWSGs welded and glued to the steel beam of the prototype bridge

The Geokon 4000 VWSG series are commonly designed to be arc or spot welded to the structural steel. In order to reduce stress concentration on the plate girders, this research employed a typical alternative connection method, including adhesives such as superglue or epoxy. Based on a laboratory study conducted by certain researchers (James & Yarnold, 2017), selected adhesives were identified and utilized for simple installation and quick setting times when bonding steel plate girders on the job site. Using a combination of Loctite superglue and Loctite 5-minute Epoxy, the Geokon 4000 VWSGs have been attached to the steel girders. On the laboratory prototype bridge, laboratory tests were conducted to evaluate the performance of the welded and glued VWSGs. By welding the end mounting blocks and attaching the VWSG to the blocks, one gauge was affixed close to the bottom flange of the steel girder. The second gauge was put on the beam's opposite face by gluing the end mounting blocks to the beam's face and clamping the VWSG. For durability, a epoxy bead was put along the sides and back of each end mounting

block. Figure 3.3 depicts images of welded and bonded Geokon 4000 VWSGs to the webs of the steel girder.

In order to evaluate the performance of the prototype bridge and compare the strains in the welded and bonded strain gauges, loading tests were conducted on the bridge after the strain gauges had been mounted for about twenty-four hours. On the bridge prototype, an asymmetrical load test was carried out. The strains were recorded and monitored with the assistance of a CR1000X Campbell Scientific datalogger and an AVW200 and AM16/32 interface system. The strains with the time recorded from both VWSGs are plotted in Figure 3.4. The strains measured by the welded VWSGs and the bonded VWSGs correlate quite well with one another, as is demonstrated quite plainly by the graph. It should also be pointed out that once the load was removed after the loading cycle, the stresses in both directions went back to being equal to zero.

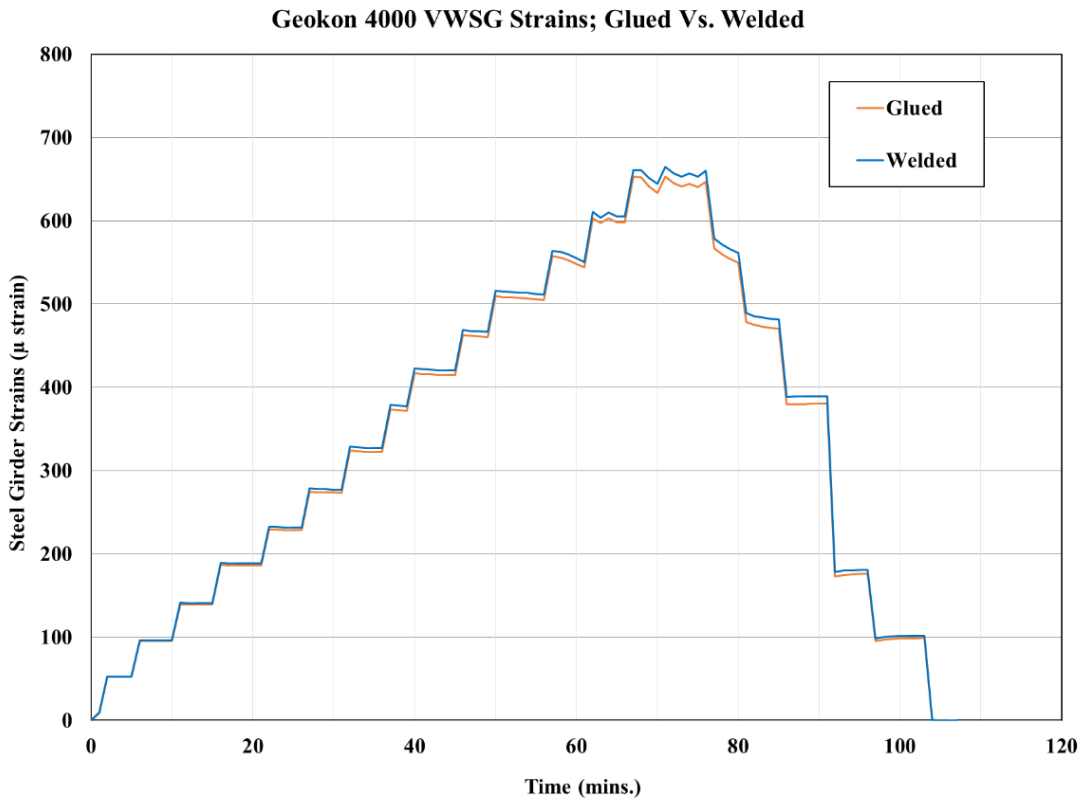

Figure 3.4: Performance of Glued vs. Welded Geokon 4000 VWSGs

3.2.6. Thermocouple

A thermocouple is a sensor that can measure temperature. It is made up of two distinct kinds of alloys, each connected to the other on one end. A voltage is produced at the junction of the two metals whenever either one is heated or cooled. This voltage can be correlated back to the temperature. The thermocouple is a type of temperature sensor widely employed in various temperature-measuring procedures due to its ease of use, durability, and low cost.

Type T is a very stable thermocouple and is often used in extremely low-temperature applications such as cryogenics or ultra-low freezers. It is found in other laboratory environments as well. The type T has excellent repeatability that rages from –380F to 392F.

3.2.7. Linear Variable Displacement Transducer

This type of electrical transducer is used for measuring linear displacement. It converts a position or linear displacement from a mechanical reference to a proportional electrical signal. The LVDT operation solely relies on electromagnetic coupling and does not require electrical contact between the moving part and the coil assembly.

3.2.8. Micro Electromechanical System Accelerometer:

The term "microelectromechanical system" (often abbreviated as "MEMS") refers to any sensor that was created through the application of microelectronic manufacturing techniques. Microscopic mechanical sensing structures can often be created using these methods, and silicon is the material of choice. MEMS sensors can monitor physical properties such as acceleration when combined with microelectronic circuits. MEMS sensors can measure frequencies as low as 0 Hz (static or DC acceleration).

3.3. Monitoring on Bridges:

Instrumentation and Data Acquisition systems for this project were built initially in the Bert Cooper Engineering Laboratory at Oklahoma State University. The Instruments that are implemented are vibrating wire gauges and thermocouples. The Instruments are monitored using data logger equipment that has been successfully used on other projects. This research made extensive use of several different forms of data collection technology. Both bridges were a candidate for static and moving load test programs.

3.1.1. State Highway 11 Steel Girder Bridge in Blackwell, Oklahoma United States:

The bridge is located in Blackwell, Oklahoma, on State Highway 11 over the Chikaskia River. The bridge featured a 30-degree skew, which had to be considered. The two-lane bridge consisted of a 6-in. concrete deck supported on six 54-in. deep by 3/8-in. Thick plate girders. This bridge was scheduled to be rehabilitated with a new bridge deck installed upon the existing bridge girders, so it offered a prime opportunity to study the long-term strains in the concrete and girders while subjected to traffic loading.

Altogether, 40 electronic sensors were installed to measure and monitor concrete strains and temperatures. Instrumentation was installed prior to concrete casting. The instrumentation included the following:

- Thermocouples measure the concrete's temperature and the bridge's ambient temperature.
- Vibrating wire gages that are embedded within the concrete deck.
- Vibrating wire gages that are attached to the steel girder bridge.

All the sensors were wired into a data acquisition box. The data acquisition is made of a datalogger and multiplexers. The data logger was programmed to record and store sensor data continuously every 2 min.

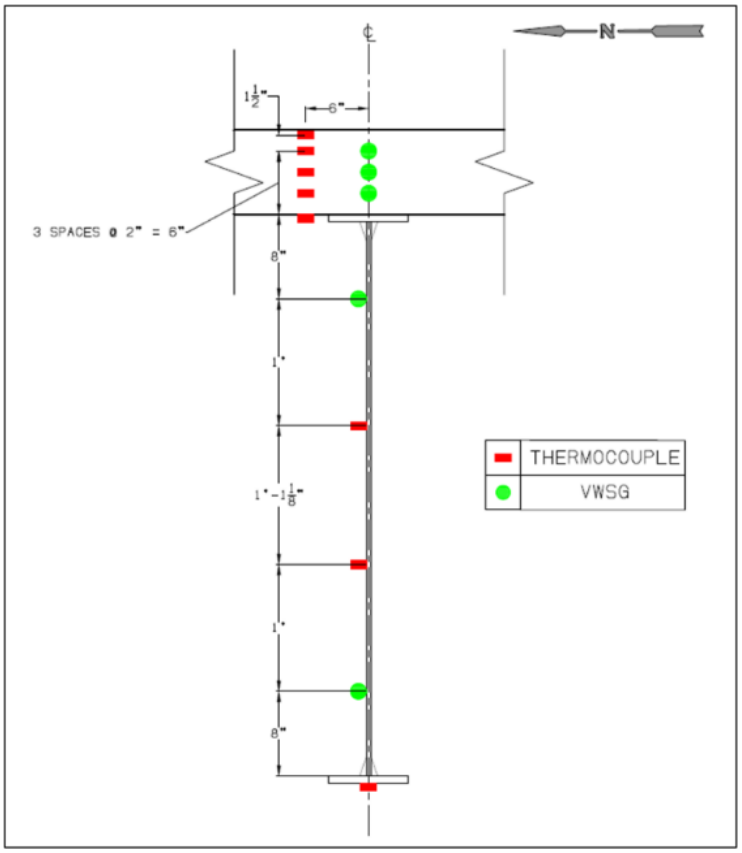

Figure 3.5: Sensor Locations in Composite Cross Section for Steel Composite Girder Bridge - SH 11 over the Chikaskia River in Kay Co., Oklahoma, USA

The instrumentation system was programmed to monitor the field bridge's early age and long-term performance. Figure 3.6 shows the instrumentation setup for the field bridge. The CR1000X datalogger was used for the field bridge monitoring. The sensors were programmed to collect data every 2 min interval.

A rechargeable battery pack, BP24, with 12 Vdc and 24 Ah of capacity, was used to supply power to the datalogger, interface systems, and remote cell modem simultaneously. Due to the isolated position of the potential bridge site and the lack of accessibility to an AC power supply, photovoltaic solar panels were used. Due to the high-power demands of this study, a solar panel with a capacity of 20 watts designated as SP20 was utilized. It can quickly and simply connect to the Campbell Scientific datalogger and the BP24 battery base to facilitate the recharging of the battery to provide a constant and uninterrupted power supply. Using a local network and a remote

mobile modem made it possible to continuously monitor the bridge. The internet access for the Campbell Scientific dataloggers and the interfaces was provided by the RV50, which is an industrial 4G LTE cellular gateway. It is compatible with a sim card from the Verizon network and a data plan that has been pre-loaded onto the device.

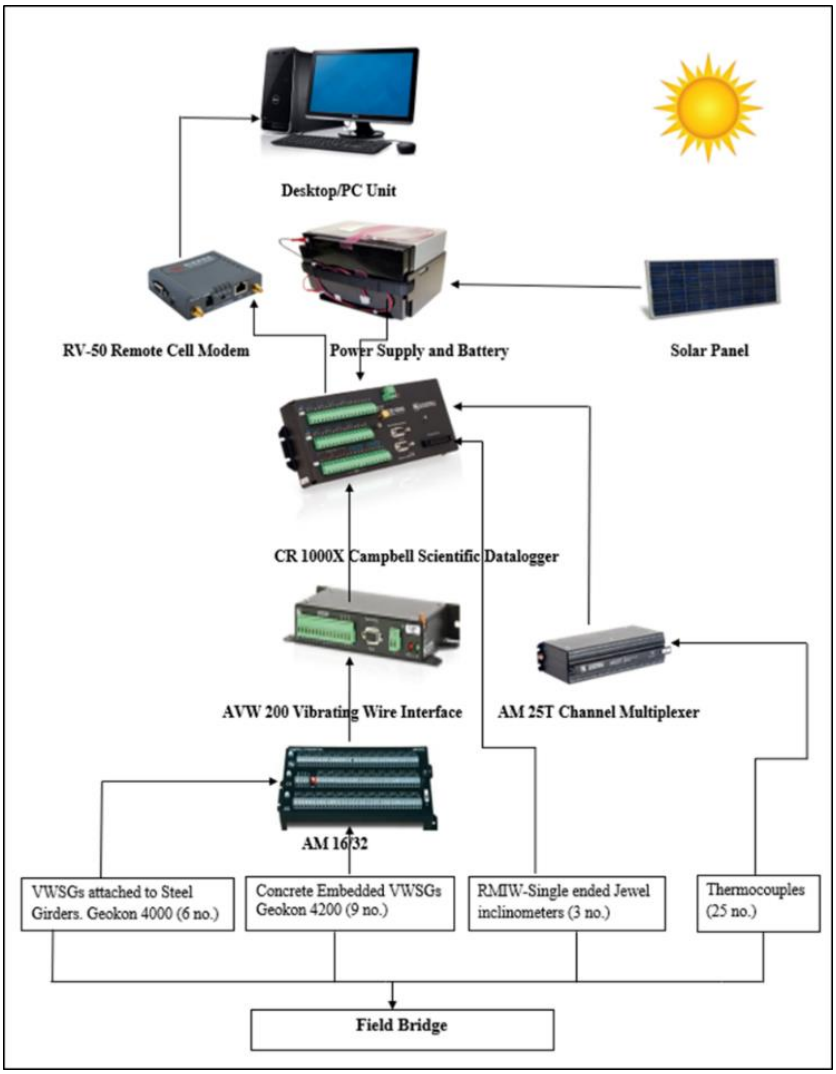

Figure 3.6. Schematic for Instrumentation and Data Acquisition for Structural Monitoring SH 11 Bridge over the Chikaskia River in Kay Co., Oklahoma, USA.

Static & Moving Load Test Program for SH11 Bridge:

Static load tests were performed on the exterior span by placing loaded trucks on the bridge spans in specific arrangements and a specific manner and by measuring beam deflections at midspan. Moving load tests were also performed using the same trucks for the static tests.

Two highway maintenance trucks were loaded with gravel and used to perform the load testing. The two trucks had different gross vehicle weights (GVW), and the individual axle weights were not provided. Truck 1 had a GVW of 50,460 lbs. Truck 2 had a GVW of 50,620 lbs. A total of two trucks were used during load testing. Both trucks were identical in geometry. Each truck had three axles, 1 in the front and two paired in the rear. The front tires had a six ft. center-to-center wheel spacing. The center-to-center axle spacing from the front to the first rear axle was 14 ft. The distance from the first rear axle to the second rear axle was 4.5 ft. The Instrumentation for the load test consisted of the following:

- Six LVDTs were placed at the midspan of each girder to measure deflection (a total of 6 LVDTs per span).
- One triaxial accelerometer was placed on the southernmost girder bottom flange to measure acceleration at midspan.
- One triaxial accelerometer was placed on the Southernmost interior girder (adjacent to the exterior girder) bottom flange to measure acceleration at midspan.
- One triaxial accelerometer was placed on the southern interior girder (the girder closer to the middle of the cross-section of the deck) bottom flange to measure acceleration at midspan.

The sample rate for accelerometers and LVDTs was set to 125 Hz. Figure 3.7 shows the Plan View of the Chikaskia River Bridge, East Span. The figure also shows the location of instrumentation for load testing. Thermocouples and Vibrating Wire Gages (VWG) are already installed and are part of the Structural Health Monitoring system that has been in place since

2020. New instrumentations for load testing are LVDTs to measure vertical displacement and accelerometers, which are equipped to measure accelerations over time on three axes. Figure 3.8 depicts the cross-section at the midspan of the SH 11 Bridge. The LVDTs will be placed at midspan beneath each girder. Accelerometers will be placed on the external girder to the South and the two adjacent interior girders.

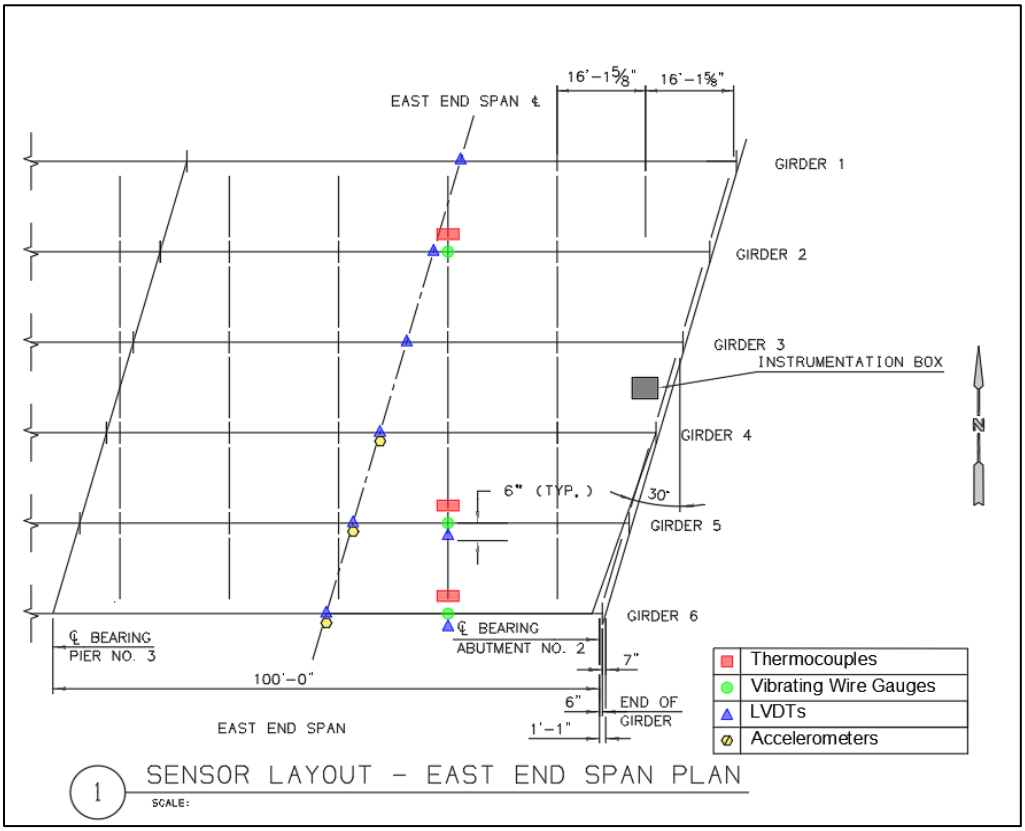

Figure 3.7: Instrument locations for load testing.

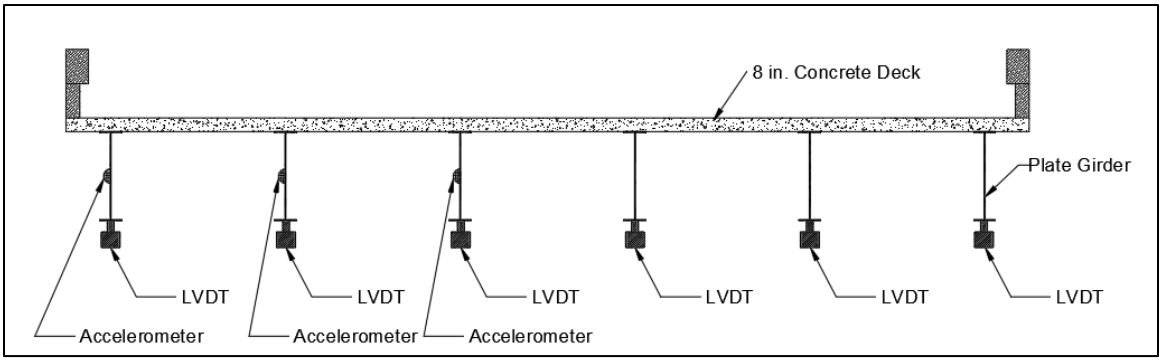

Figure 3.8:Cross Section of the SH 11 Bridge at midspan with view looking west. LVDT's are placed under each girder for load testing. Girders are labeled "Girder 1" through "Girder 6" from North to South, so "Girder 1" is located on the right in the figure.

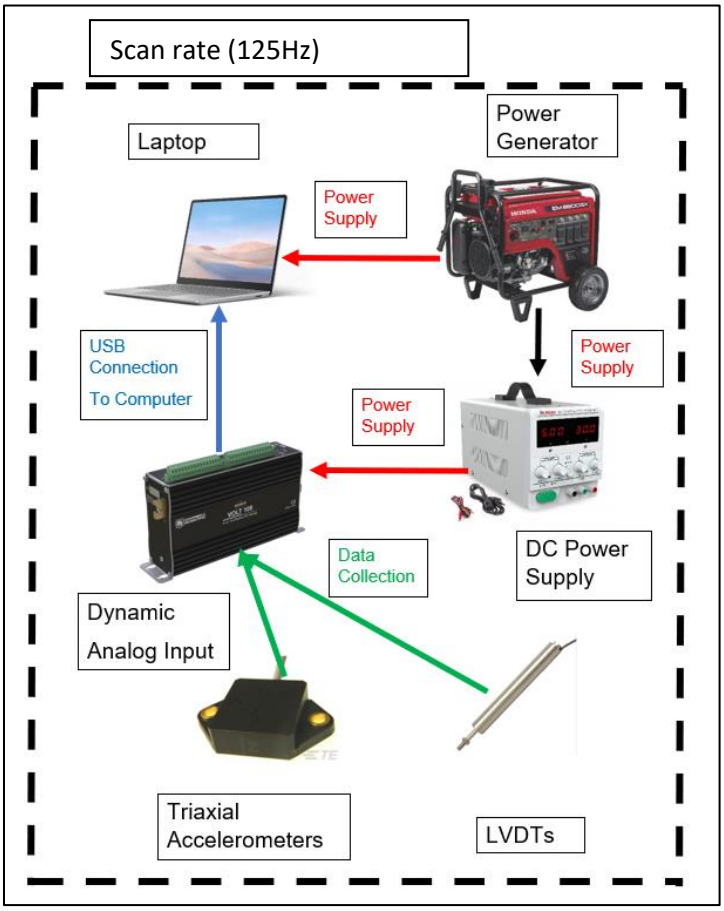

Figure 3.9: SH11 monitoring and instrumentation schematic plan for load testing.

3.1.2. State Highway 4 Concrete Girder Bridge in Yukon, Oklahoma United States:

The bridge is on State Highway 4 over the Canadian county river, Oklahoma, in the United States and was selected for a structural health monitoring program. This bridge features 15 different spans. The span length is about 98.0 ft., eight in. from center to center (c/c). The concrete deck thickness is designed to be 8.0 in. the spans are 42.0 ft. 2.0 in. out-to-out dimensions supported by four type IV girders with 4.0 ft. 1.0 in. center to out dimensions. Figure 3.10 shows the fully constructed bridge.

Figure 3.10: Photograph of the SH 4 Bridge over N. Canadian R., Canadian Co., OK.

Altogether, 58 electronic sensors were installed to measure and monitor concrete strains and temperatures. Instrumentation was installed prior to concrete casting. The instrumentation included the following:

- Thermocouples measure the concrete's temperature and the bridge's ambient temperature.
- Vibrating wire gages that are embedded within the concrete girder.

- Triaxial Accelerometers that measure bridge accelerations.

All the sensors were wired into a data acquisition box. The data acquisition is made of a datalogger and multiplexers. The data logger was programmed to record and store sensor data continuously every 2 min.

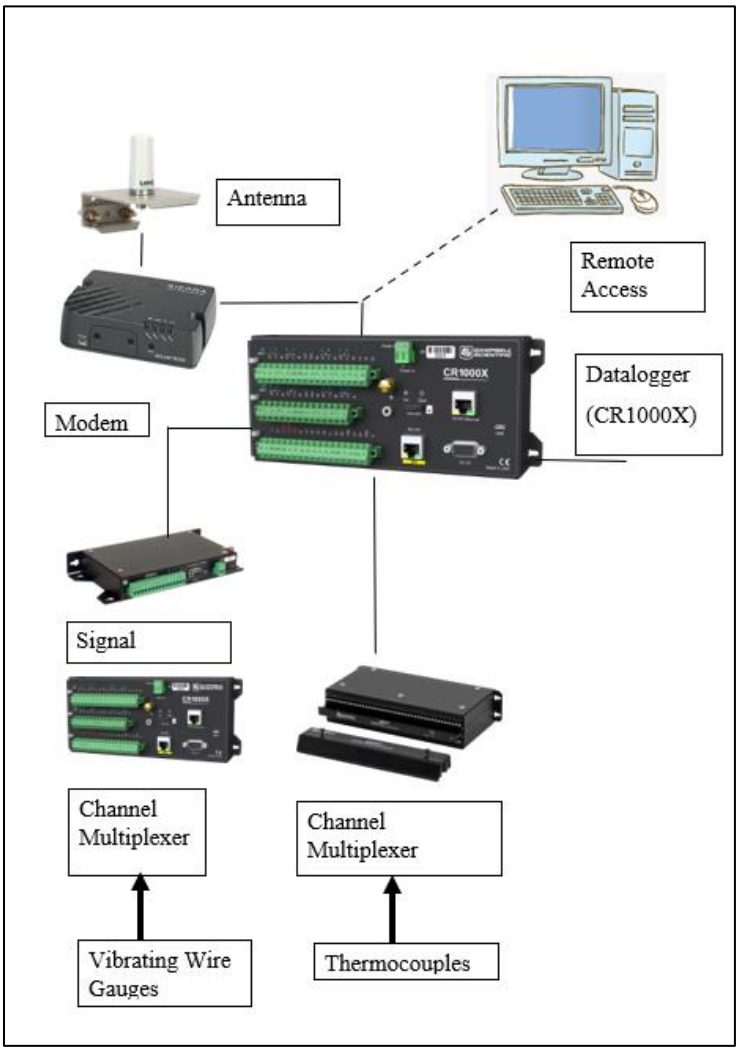

Figure 3.11: Schematic for Instrumentation and Data Acquisition for Structural Monitoring SH 4 Bridge over the North Canadian River in Canadian Co., Oklahoma, USA

The beams Mark 27, Span 9, and Mark 42, Span 14, were selected and instrumented for the structural monitoring program for this study. According to the bridge plan, both beams will be exterior girders on the West side of their respective spans. Beam Mark 27 serves as the

westernmost external girder for Span 9, while Beam Mark 42 serves the same function for Span 14.

Using vibrating wire gauges and thermocouples, strain and temperature data were measured. Instruments were installed at:

- Four in. from the end region of the beams.
- 16.0 in. from the end region of the beams.
- 32.0 in. from the end region of the beams.
- At the midspan of the beams.

Figure 3.12 illustrates the mounted sensors' location along the girder cross-section. Instrumentation and data capture technologies enabled continuous monitoring of data throughout the fabrication, handling, storage, transit, erection, and service life of the bridge. Current measurements are still being recorded. This program's data is used to quantify concrete strain, which can be used to calculate prestress losses and midspan.

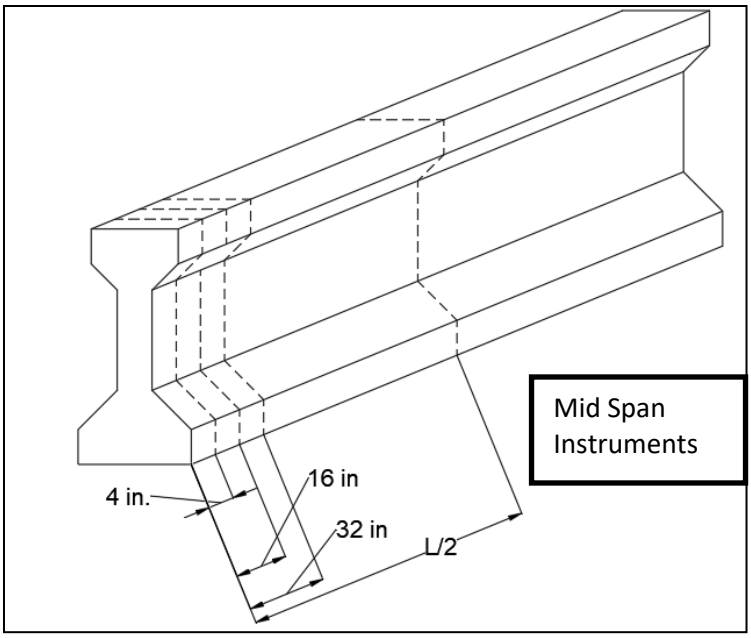

Figure 3.12: Sensor locations at each length increment of the girders.

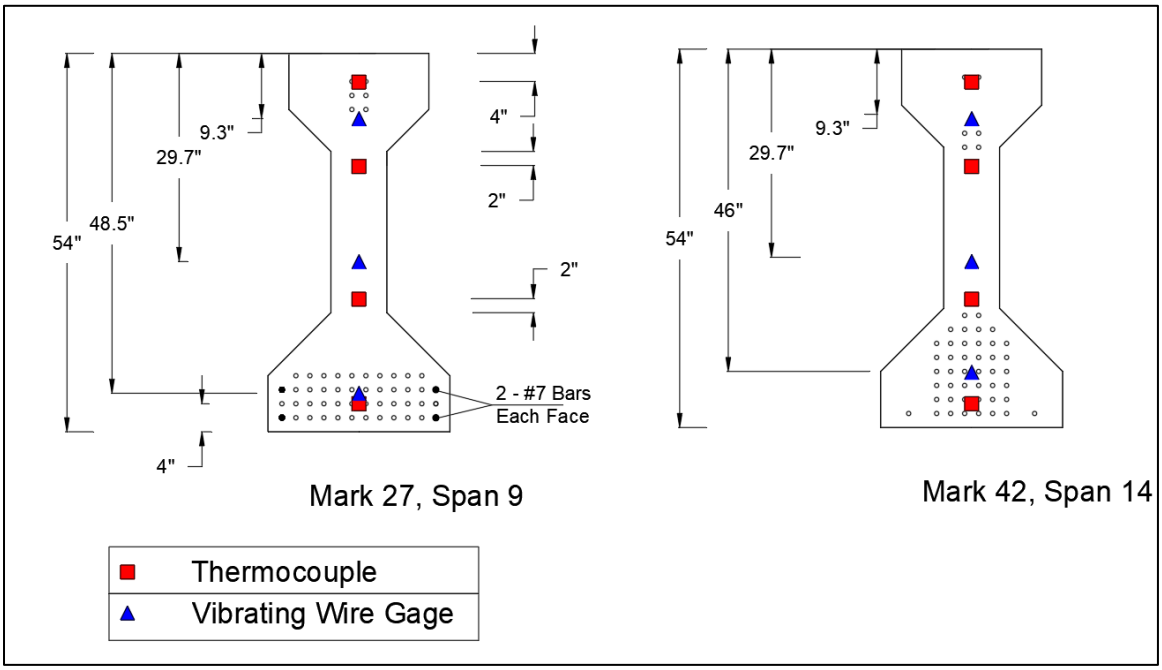

Figure 3.13: Sensor locations shown in girder cross-section.

Figure 3.14: North end reinforcement and instrumentation, Beam Mark 27, Span 9.

Figure 3.15: North end reinforcement and instrumentation, Beam Mark 27, Span 9.

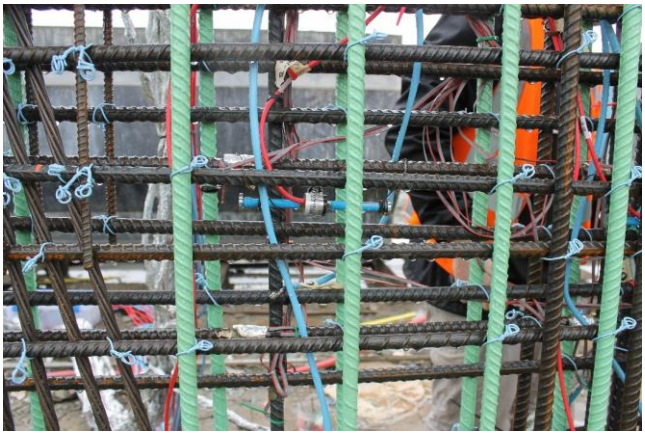

Figure 3.16: Vibrating Wire Gauge (blue) is located in the foreground at approximately C.G.S.

Figure 3.17: Instrumentation at midspan, Mark 27, Span 9. Four #7 reinforcing bars are placed in the corners of the bottom flange.

The instrumentation for girder Mark 27 Span 9 was installed on April 21 and 22, 2020. The beam was cast on April 23, 2020, and on April 24, 2020, it was de-tensioned. The procedure was repeated for the Mark 42 and Span 14 beam. The installation of instruments occurred on April 26 and 27, 2020. The beam was cast on April 28 and detention the following day, on April 29. The structural monitoring system recorded and stored concrete strain and temperature data during the concrete casting, curing, form removal, detensioning, transit, hauling, and deck cast phases.

The schematic Figure 3.18 shows the basic outline of each span, with four (4) Type IV girders supporting a two-lane traffic deck that is 40 ft. clear in width. Instrumentation is located at both midspan and end regions of the westernmost girders in Span 9 Mark 27 and 14 Mark 42. The data logger for each of these two beams is located at approximately the quarter point, toward the Northern end, and on the western side of the girders. Solar panels are mounted directly onto the pier north of each span. As noted, the power systems have operated without interruptions since the beams were fabricated.

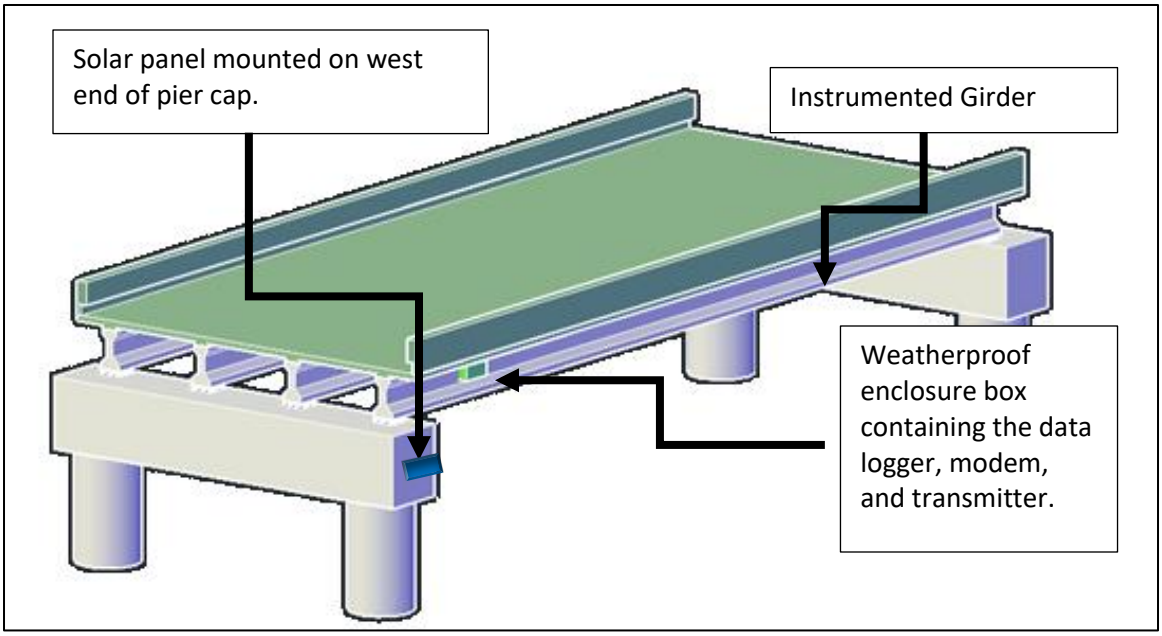

Figure 3.18: Schematic of S.H. 4 Bridge Span over the N. Canadian River in Canadian Co., OK. Nominal span = 100 ft. with an 8 in. thick deck slab supported by four Type IV girders. The clear roadway width = 40'-0.

The data logger for each of these two beams is located at approximately the quarter point, toward the Northern end, and on the western side of the girders. Solar panels are mounted directly onto the pier north of each span. As noted, the power systems have operated without interruptions since the beams were fabricated.

Static & Moving Load Test Program for SH 4 Bridge:

Static load tests were performed on Span 9 and Span 14 by placing loaded trucks on the bridge spans in specific arrangements and a specific manner and by measuring beam deflections at midspan. Moving load tests were also performed using the same trucks for the static tests.

Instrumentation for the load test consisted of the following:

- One LVDT was placed at the midspan of each girder to measure deflection (a total of 4 LVDTs per span).
- One triaxial accelerometer was placed on the Westernmost exterior girder bottom flange to measure acceleration at each span.

- One triaxial accelerometer was placed on the Westernmost interior girder bottom flange to measure the acceleration of each span.
- One triaxial accelerometer was placed on the bottom side of the deck at the span's midspan and mid-length between the exterior and interior girders.

The sample rate for accelerometers and LVDTs were set to 200 Hz. Details and photographs of the instrumentation plan are shown in the following figures:

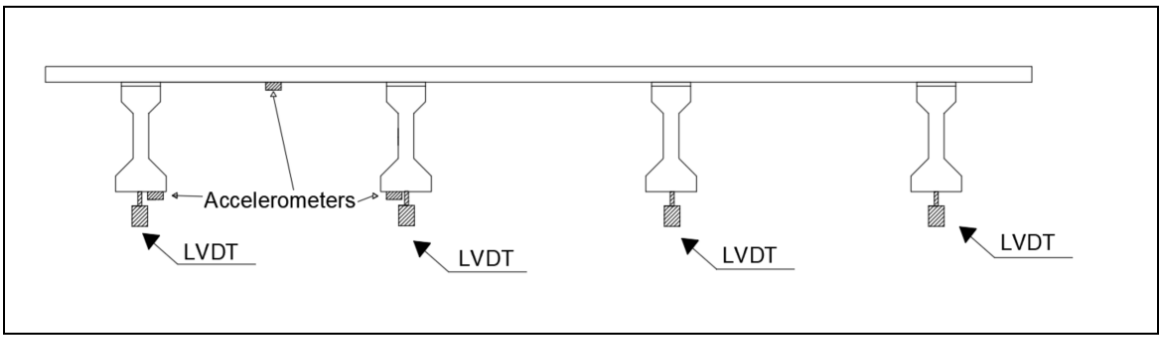

Figure 3.19: LVDT and accelerometer locations.

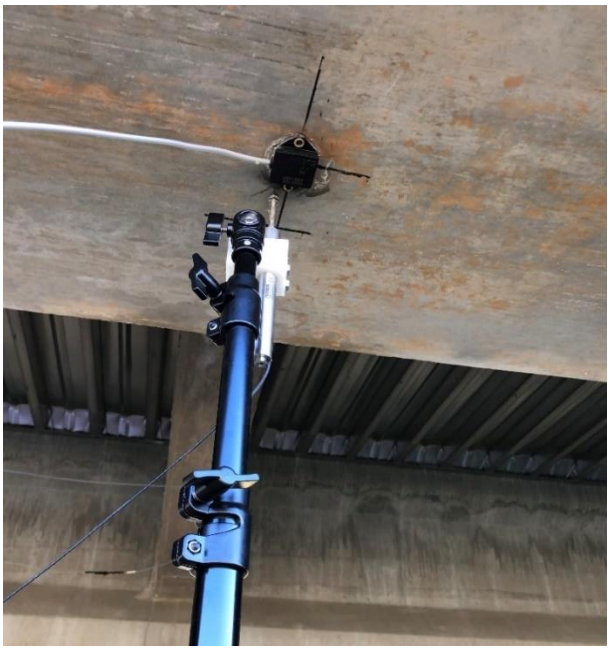

Figure 3.20: Instruments at midspan for SH 4 load test. Viewed are an LVDT and accelerometer.

Figure 3.21: Testing setup for SH 4 load test.

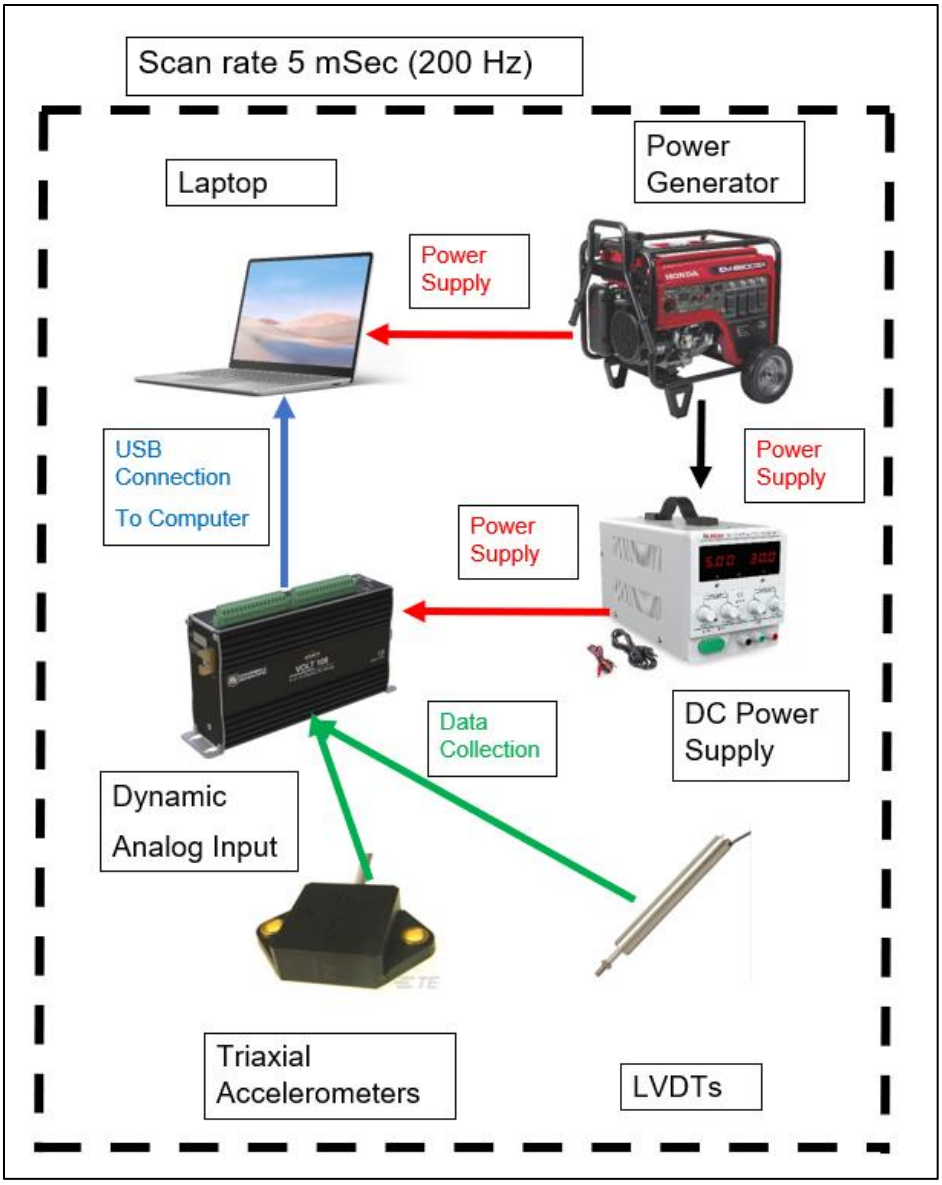

Figure 3.22: SH 4 monitoring and instrumentation schematic plan for load testing.

3.2. Results

3.2.1. Short Term Structural Monitoring Bridge

The data acquisition system continually collects data in real-time 24/7/365 and has been collecting data without interruption since installation. The measured data is downloaded and stored daily. The sensors measure concrete strains and temperatures within several points of each girder.

State Highway 4 Bridge:

Temperature Monitoring:

Both Girders (Mark 27 and Mark 42) were cast in the late morning. The heat from the hydration of cement begins immediately upon water being combined with the cement. Even though the appropriately called “dormant period,” when sulfate ions impede the acceleration of hydration, heat from hydration is building. Figure 3.23 captures the full heating and cooling cycle during concrete hydration, along with measured concrete temperatures for Mark 27.

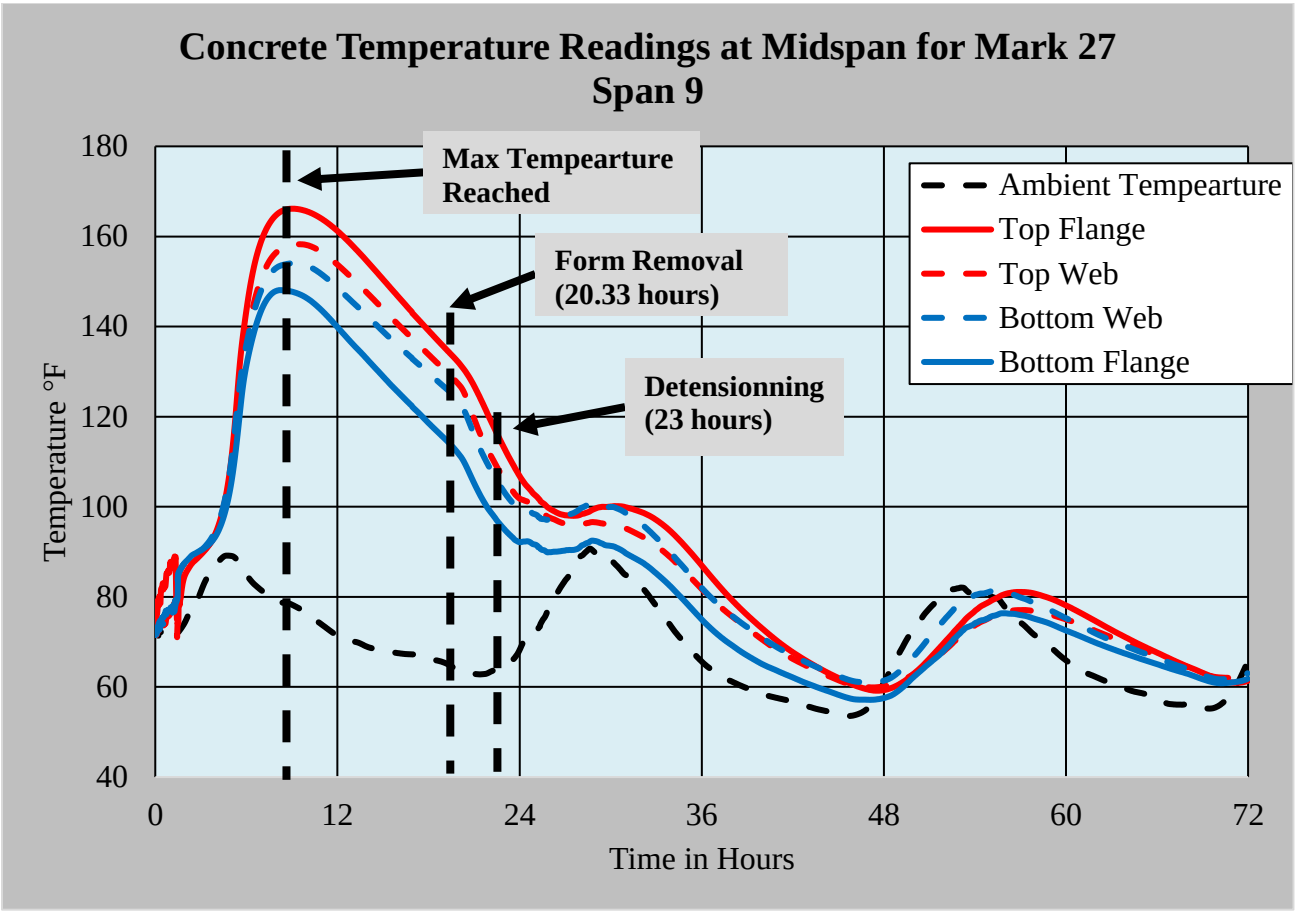

Figure 3.23: Girder Mark 27, Span 9. Recorded temperatures at midspan during the first 72 hours of the PC Beam life. Time of casting is 1.0 hr.

Concrete and Steel Strain Monitoring

Figure 3.24 charts the concrete strains measured by vibrating wire gages installed in Beam Mark 42 Span 14 at Midspan during the first 72 hours of the beam's life, respectively. Strains show positive strains (lengthening strains) as concrete temperatures increase. Cooling does not alter the measured strains greatly, which indicates that a combination of reinforcement and the formwork restrained the concrete. However, significant changes in concrete strains are noted with the de-tensioning of the prestressing force. With detensioning, the prestressing forces impose net compressive strains into the concrete. Additionally, because the prestress force is eccentrically located (the C.G.S. is below the C.G.C.), the compressive strains following de-tensioning are larger in the bottom flange. The figure shows concrete strains at the bottom flange, located at the approximate location of the C.G.S., concrete strains at the centroid of the Type IV girder, or the C.G.C., and strains near the top flange.

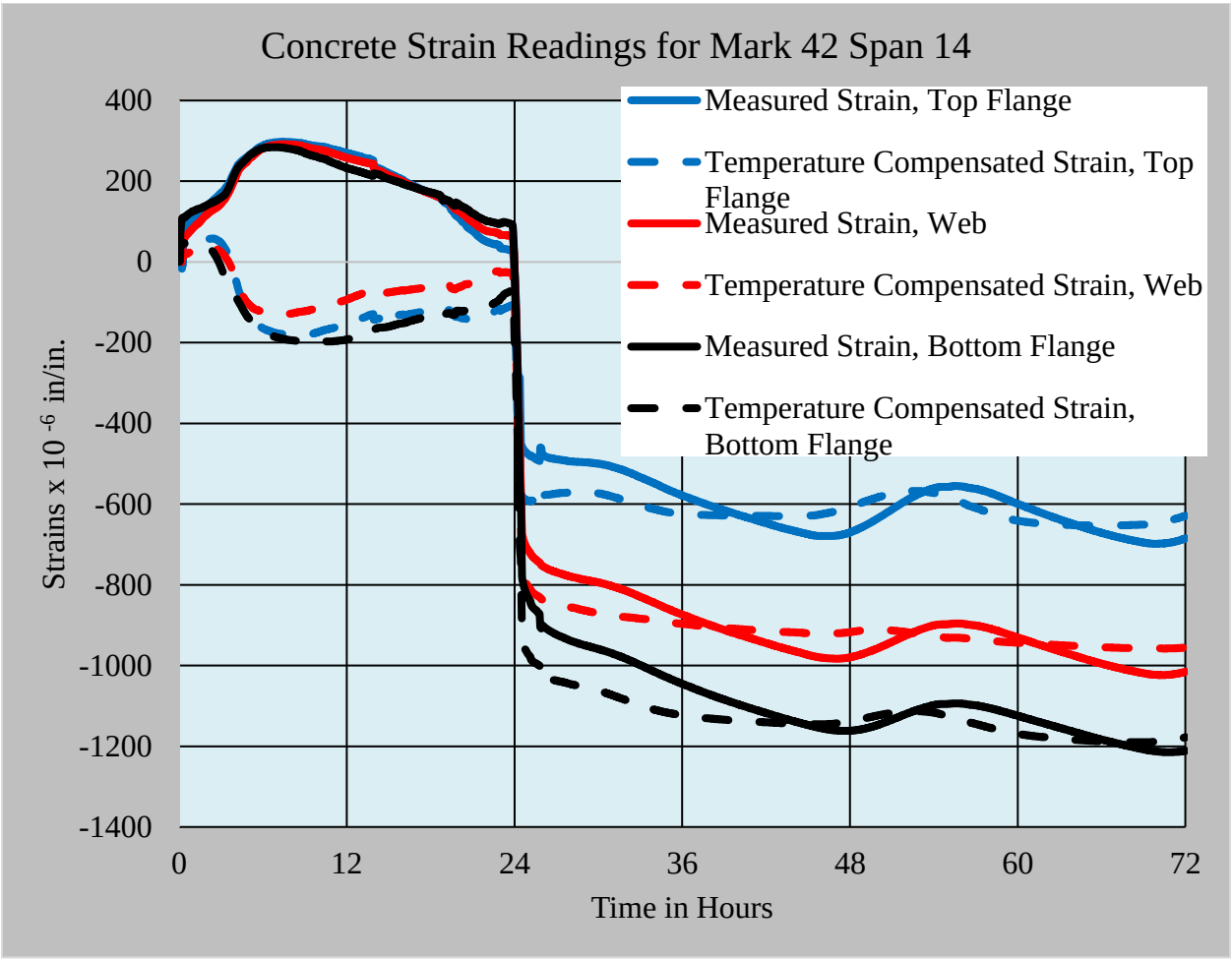

Figure 3.24: Girder Mark 42, Span 14. Recorded strains at midspan during the first 72 hours of the PC Beam life.

3.2.1. Long Term Structural Monitoring

The purpose of long-term monitoring is to understand the structural behavior response of bridges due to traffic loads and environmental loads such as temperature loads and wind loads.

Temperature Monitoring:

State Highway 4 Bridge:

Figure 3.25 charts the temperature fluctuations in PC Beam Mark 27 from its "birth" in April 2020 until Day 900, which corresponds to October 10th, 2022.

In this chart, the seasonal fluctuations in temperature are readily apparent. Day 80 corresponds roughly to the 3rd week in July 2020, and daily high temperatures exceeding 100°F are not uncommon, with nightly lows of approximately 75°F to 80°F. These patterns are repeated through the summer months of 2021, where the middle of July would be approximately Day 450.

In February 2021, Oklahoma experienced extremely low temperatures, and the systems recorded a low temperature of -9.8°F on Day 301 for PC Beam Mark 27 and Day 295 for PC Beam Mark 42 (February 18, 2021). It is interesting to note that temperatures in excess of 70°F were recorded within seven days after these extraordinarily low temperatures were recorded. It is remarkable that our temperatures can swing and change dramatically in a short time. Further, it is remarkable that we can capture these temperature swings in real time and download the data via widely available and relatively simple technologies. We should point out that our current methods of construction using spans that are essentially simply supported (both ends of the PC Bridge Beams supported by flexible neoprene pads) allow the system to "move" with the temperature variations. Assuredly, if our bridges were continuous, we would see large secondary effects, including relatively large secondary loadings from these temperature swings.

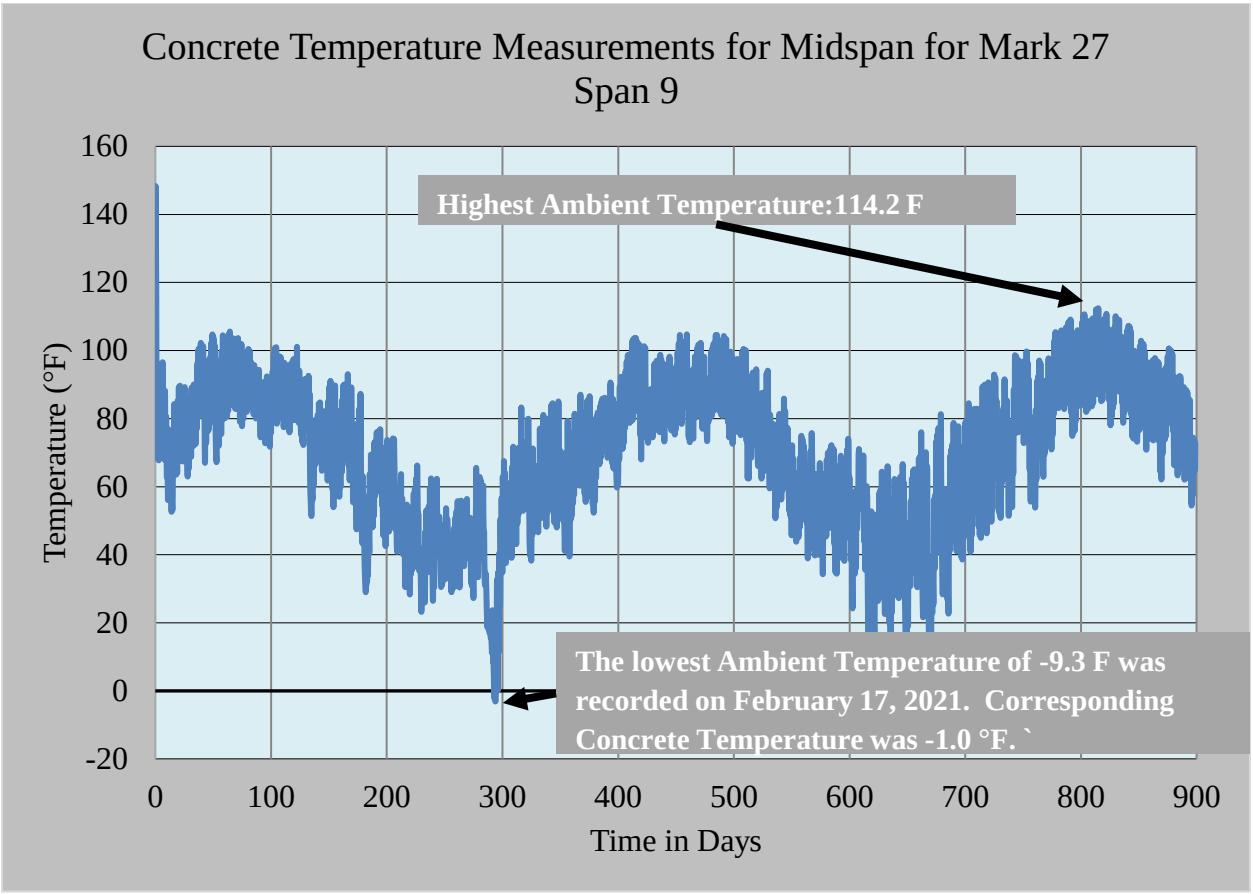

Figure 3.25: Measured bottom flange concrete temperature at midspan for Mark 27, Span 9 for SH 4 bridge. (t = 0; represents 23 Apr 2020)

State Highway 11 Bridge:

Our systems continually collect data in real-time 24/7/365 and have collected data since each deck was cast on March 9th of, 2020 (North side) and July 22nd, 2020 (South Side). We directly measure temperature within several points of each girder from these data. February 2021 in Oklahoma saw extreme temperature fluctuations. A crucial part of implementing structural health monitoring is to monitor Temperatures and Concrete strains. The data from Figure 3.26 shows concrete, steel, and ambient temperatures during the month of February 2021.

As shown, the SH 11 Bridge experienced more than 80 F temperature fluctuation during the month. The high temperature of 78 F occurred on February 23, just seven days after the concrete's low temperature of -4 F on the morning of February 16. Ambient temperatures reached a low of about -9 F.

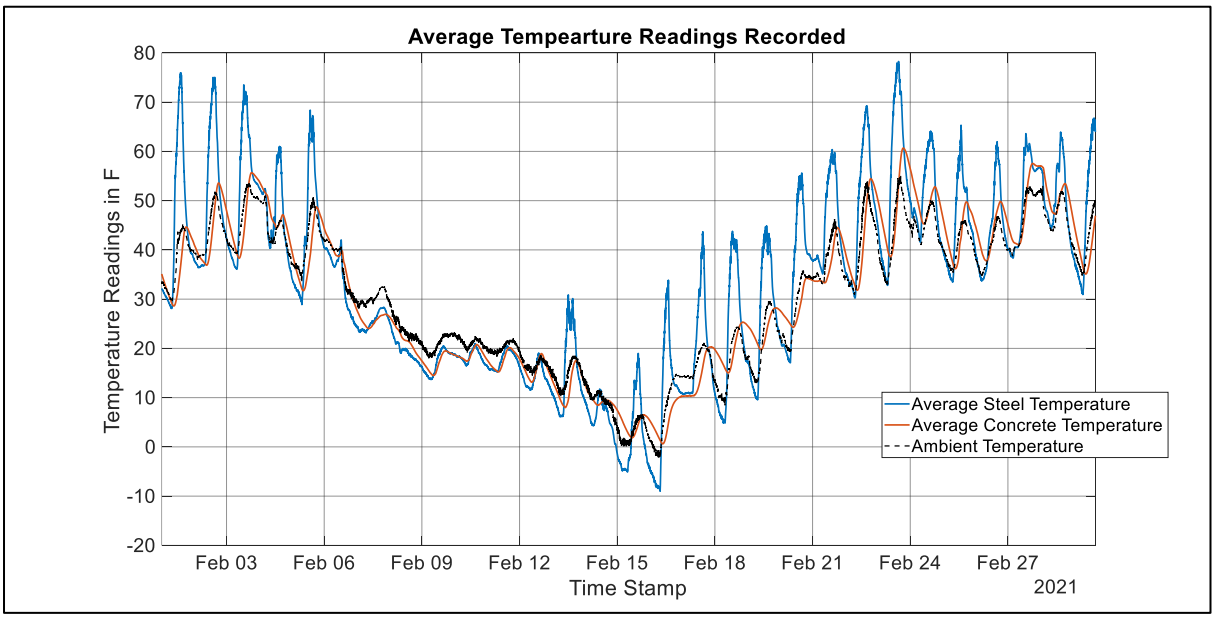

Figure 3.26: Steel and Concrete and Ambient Temperature Record for February 2021, SH 11 Bridge, Blackwell Co., OK

Concrete and Steel Strain Monitoring:

State Highway 4 Bridge:

Figure 3.27 charts the strain measurements at midspan for PC Beam Mark 42 (Span 14). In this chart, the concrete strains at midspan are charted over the entire life of the PC Beams, with continuous data collected from the time before the concrete cast, through concrete casting, concrete hydration, curing, de-tensioning of the prestressing strands, handling, and storage, transportation, erection, and the through bridge construction. Please note that the data shows many interesting things.

- The initial strain near the top fiber is -500 microstrains; the initial strain near the bottom fiber is -1000 microstrains. These initial strains represent the beam mechanics and the strain conditions after the initial prestress losses due to the concrete's elastic shortening (ES). The higher compressive strains at the bottom flange, as compared to those at the top flange, indicate that the beam is cambering upward.

- In the first 30 days from initial beam fabrication, all concrete strains increase considerably toward additional compression (shortening) strains. These strains are those associated with prestress losses, including both creep and shrinkage. Within approximately three weeks (21 days), the compressive strains have increased by more than 30 percent.
- Girders were transported and erected in May 2020. The handling and transportation of the two girders caused a change in the pattern of steadily increasing compressive strains
- From approximately 21 days until the time of deck slab casting, compressive strains continue to increase but at a slower rate.

- As the concrete deck was cast, and the dead load of fresh concrete was resisted by the pre-tensioned bridge girder, we see a further increase in compression near the top fiber, balanced by a decrease in compression near the bottom fiber.
- The "closing' of variation in the measured strains from top to bottom indicate that the dead loads are effectively "balanced." We note that LOAD BALANCING is a common design practice in posttensioned concrete, but not prevalent (and rarely mentioned) in pre-tensioned concrete. But the load balancing can still be employed to ensure effective design. The effects of this "load balancing" can be seen in both Figures as the concrete strains "come together" (and the differences in strains from top to bottom are decreased) on the day that the deck slabs are cast.

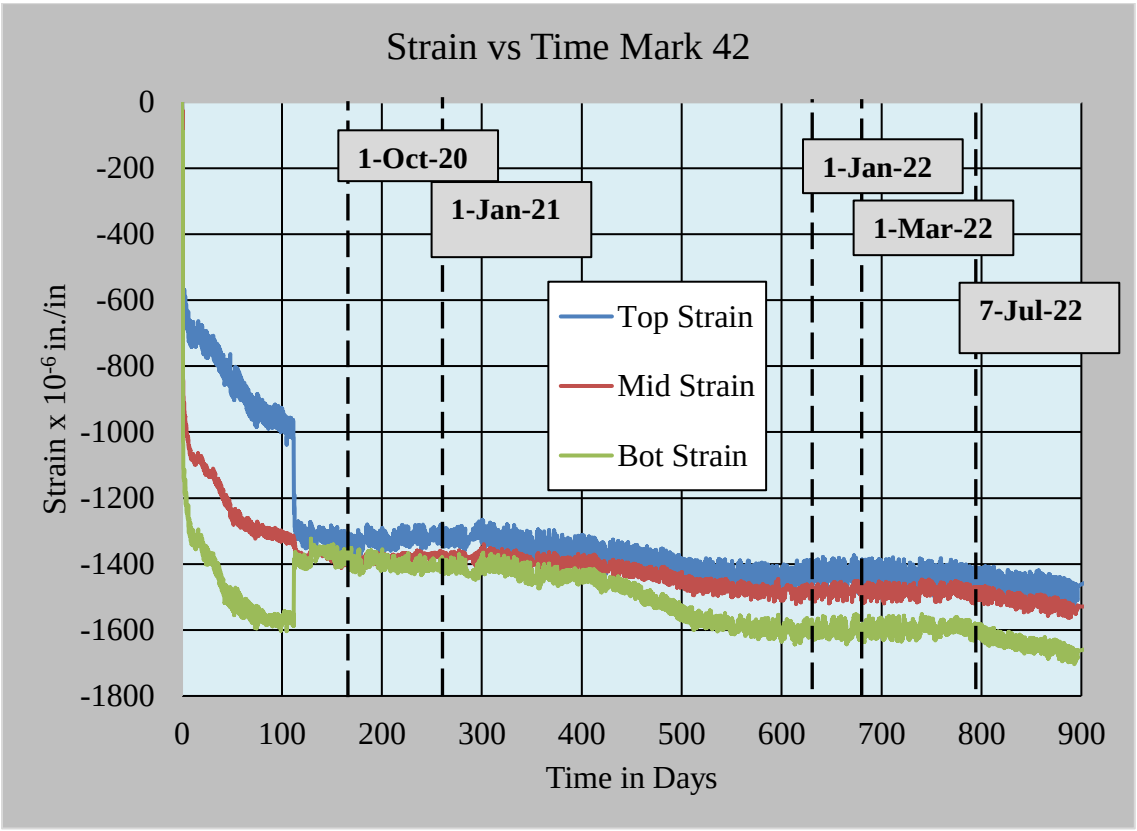

Figure 3.27: Measured compensated concrete strain for temperature at midspan for Mark 42, Span 14. (t = 0; represents 27 Apr 2020)

State Highway 11 Bridge:

Figure 3.28 charts the strain reading Steel and Concrete Strains for Girder 2. Figure 3.29 charts the strain reading Steel and Concrete Strains for Girder 5. Figure 3.30 charts the strain reading Steel and Concrete Strains for Girder 6. Between June to July 2020, the solar panels that were recharging the battery were stolen. Therefore, the research team had to replace the solar panels in July 2022. Also, the sensor that was attached to the top web in girder 2 was damaged, and we did not have the resources to replace it.

One can see in the data that the temperature fluctuation that occurs daily and through the weather cycles indicates that concrete and steel are expanding (increasing positive strains) when the temperatures become warmer. From a monitoring point of view, several things are:

- Daily temperature fluctuations are typically varying +/- 20 to 30 F in a single day. These appear to directly result in +/- 130 microstrains within the concrete material.
- Note that the measured strain is consistent with the change in temperature multiplied by the approximate coefficient of thermal expansion, $\alpha \approx 6.5 \times 10\text{-}6$ in/in/°F. So, a 20 F change in temperature would produce strains approx. +/-130 με. These values are consistent with measured data.

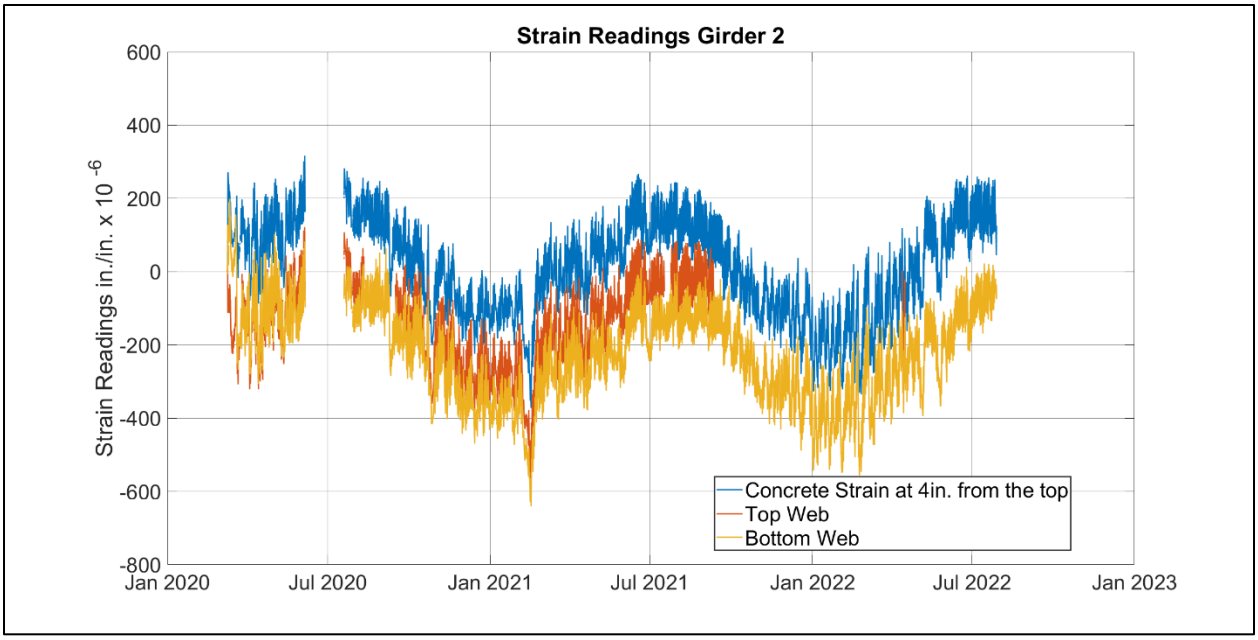

Figure 3.28: Measured concrete and steel strain for Girder 2, SH 11 Bridge, Blackwell Co., OK

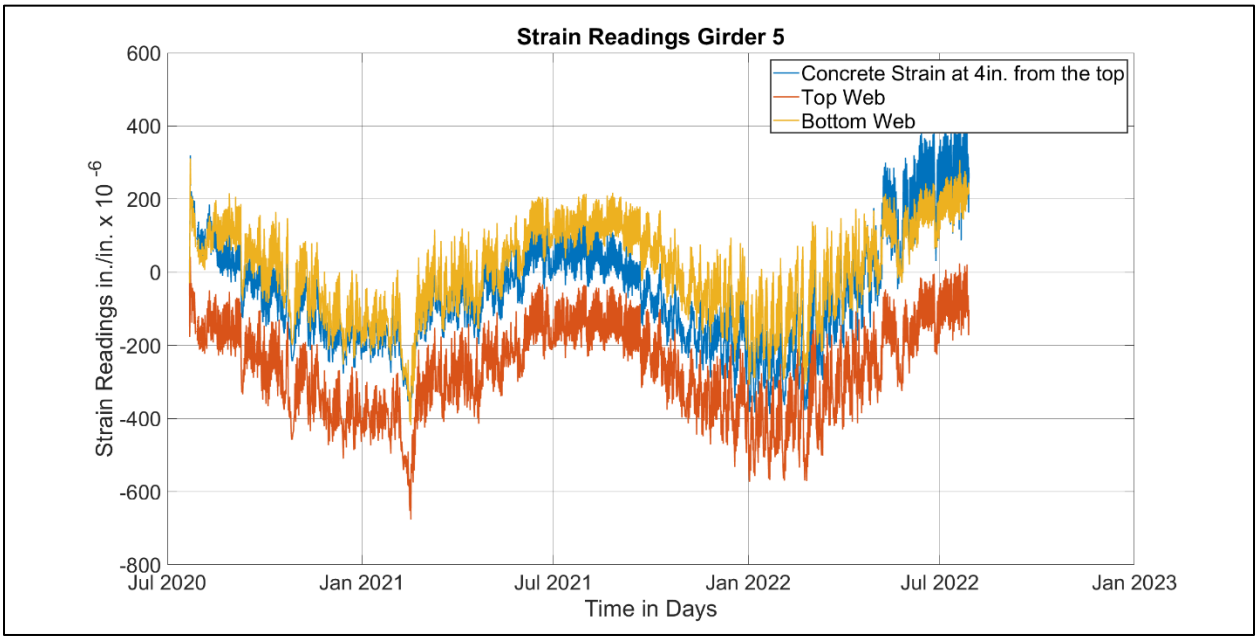

Figure 3.29: Measured concrete and steel strain for Girder 5, SH 11 Bridge, Blackwell Co., OK (t = 0; represents 22 July 2020)

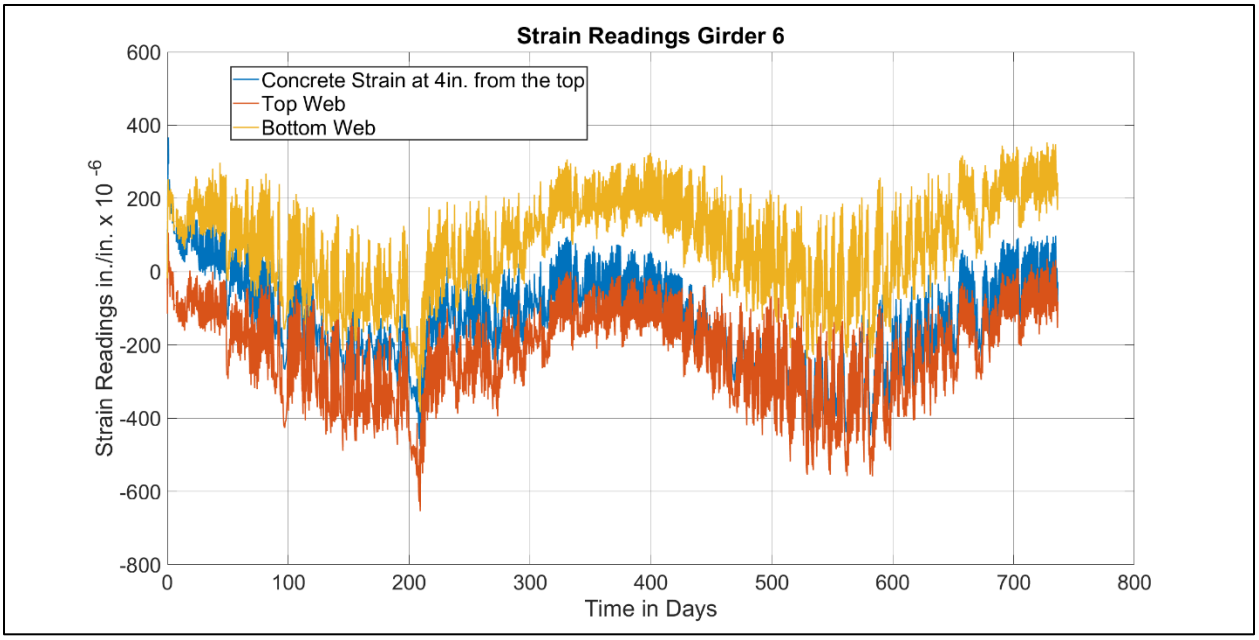

Figure 3.30: Measured concrete and steel strain for Girder 6, SH 11 Bridge, Blackwell Co., OK. (t = 0; represents 22 July 2020)

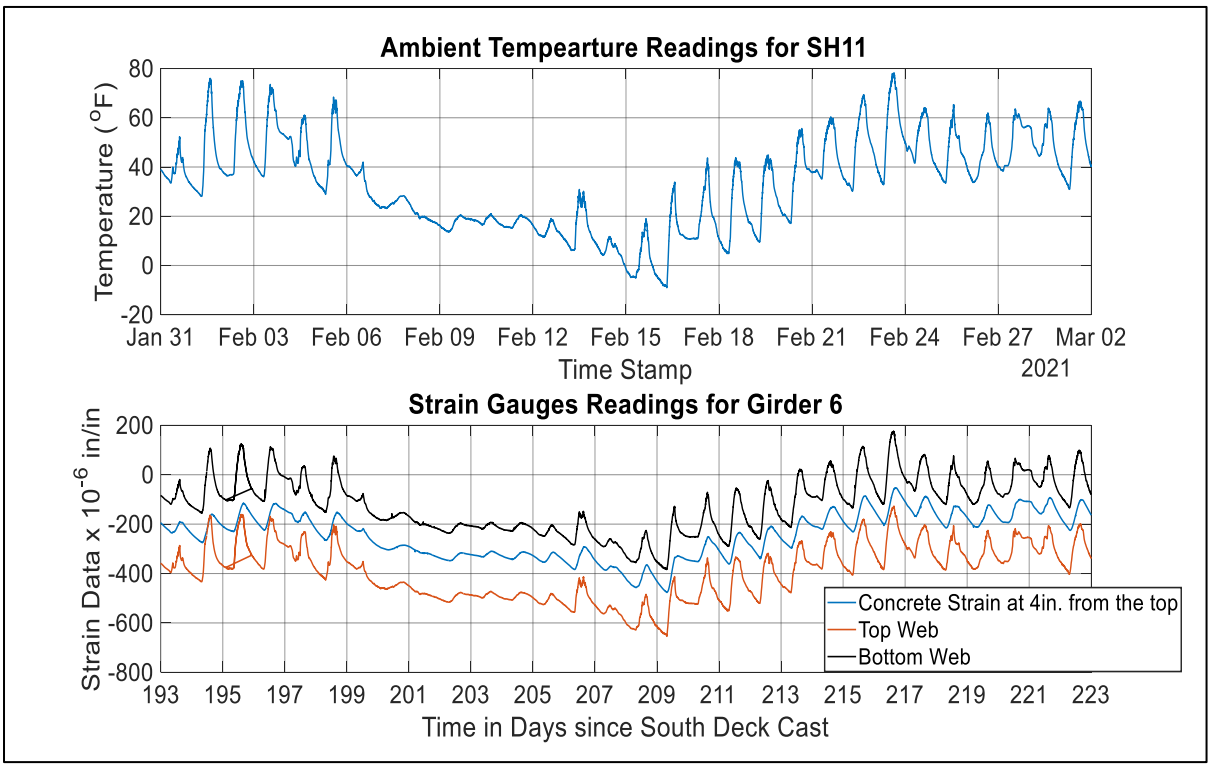

Figure 3.31: Steel and Concrete Strains Due to Extreme Weather Changes. Note that @ time = 193 days is compatible with January 31st, 2021. Note that the time = 0 is equivalent to July 22nd, 2020 (Concrete deck cast of the south side of the bridge)

Figure 3.31 shows the concrete strain data from SH 11 Bridge girder 5 in February 2021. The ambient temperature is also shown in the figure for the purposes of direct comparison. One can see in the data that the temperature fluctuation that occurs daily, and also through the weather cycles indicate that concrete and steel are shortening (increasing negative strains) when the temperatures become colder. From a monitoring point of view, there are several things that are important to point out:

- Daily temperature fluctuations typically vary +/- 20 to 30 F in a single day. These appear to directly result in +/- 130 microstrains within the concrete.
- Note that the measured strain is consistent with the change in temperature multiplied by the approximate coefficient of thermal expansion, $\alpha \approx 6.5$ x 10-6 in/in/°F. So, a 20 F change in temperature would produce strains approx. +/-130 με. These values are consistent with measured data.

Note that the daily change in strains reflects throughout the depth of the cross-section. So, if the bridge experiences daily fluctuations of 150 microstrains, that represents a length change for the bridge girder of approximately 0.18 in. per span. There may be some independent data on girder movement, but this daily change in length is not widely reported. Support conditions (neoprene bearing pads and other supporting hardware) must accommodate the daily change in length.

3.2.2. Static and Moving Load Test Monitoring:

The Moving Load Testing aims to measure the displacements and accelerations at midspan under each of the four girders with known loads at different speeds. The variations in dynamic loading will produce a difference in measured displacements, strains, and stresses. The system should be able to capture this information. The system also allows to physically measure the natural frequencies of the first modes of vibrations. The results of the displacement and acceleration can be used to derive the natural frequencies of the bridge and the other dynamic properties. The following sections show the dynamic response of Span 9, followed by the Dynamic Response of Span 14 for Truck Configuration 2. In these moving load tests, Truck 1 travels southbound within the traffic lane at or near the prescribed velocities.

The following sections show the dynamic response of Span 9, followed by the Dynamic Response of Span 14 for Truck Configuration 2. In these moving load tests, Truck 1 travels southbound within the traffic lane at or near the prescribed velocities. Figure 3.32 shows the vertical deflections of the four girders in Span 9, and vertical accelerations for the two westernmost girders in Span 9. From the figure, one can see that deflection response of each of the four girders in Span 9. The maximum response occurs in the Interior West girder. Figure 3.33 shows the vertical deflections for the four girders in Span 14, and the vertical accelerations of the two westernmost girders in Span 14. The maximum deflection, including dynamic effects is ***0.1484 in.*** for Span 9 and ***0.1286 in.*** for Span 14. Maximum VERTICAL acceleration is ***0.0899 g*** for Span 9 and ***0.1165 g*** in Span 14.

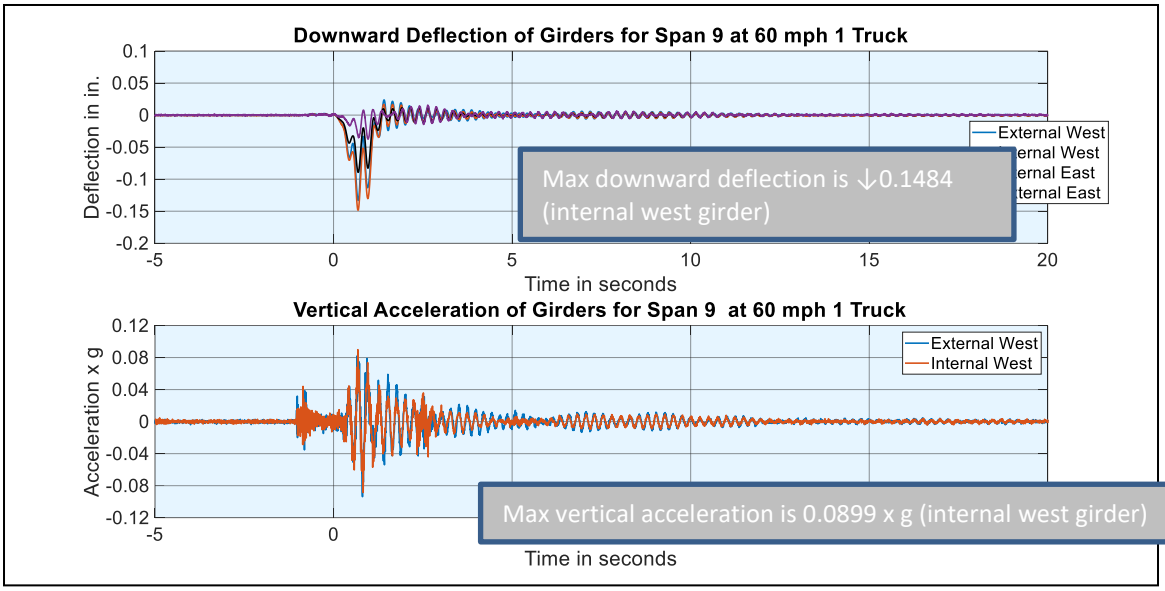

Figure 3.32: Midspan Acceleration and Deflection Records for Span 9 when Truck 1 was traveling 60 mph.

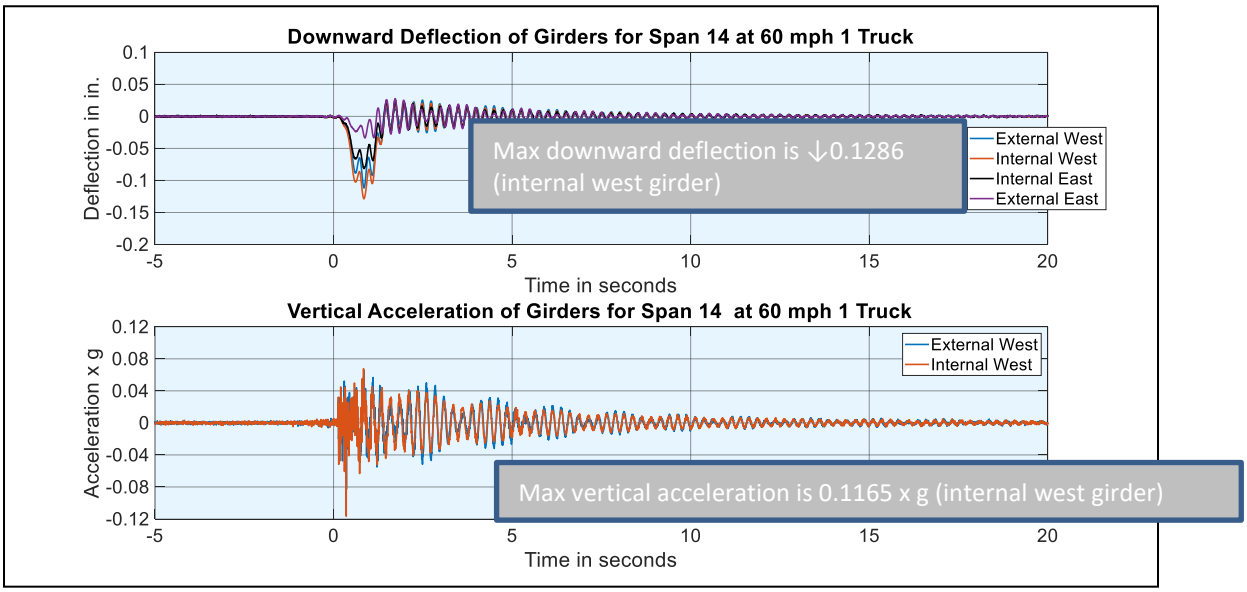

Figure 3.33: Midspan Acceleration and Deflection Records for Span 14 when Truck 1 was traveling 60 mph.

3.3. Summary & Conclusions

Bridge instrumentation and monitoring are valuable to accurately evaluate structural conditions and performance. This research's structural monitoring program integrates sensors from several technologies into a seamless system using a single database and user interface. The instrumentation system was programmed to monitor the prototype bridge's performance over the short and long term. This Structural Monitoring Program can be used to monitor other bridges.

1. Instrumentation can be employed to acquire concrete temperatures and concrete and steel strains during P.C. Bridge Beam Fabrication, and these data are useful for structural collecting data in both the short-term period (during fabrication, storage, handling, transportation, erection, and bridge construction) and the long-term (post-construction and in-service conditions)
2. The implementation of the data acquisition system was successful in acquiring the strain and temperature data in real-time and for use in analyses of overall bridge beam behavior, including evaluations of design methods, design choices, and construction processes,
3. Temperature fluctuations during fabrication (heat of hydration and steam curing followed by form removal) create significant concrete strains at early ages during fabrication.
4. The selection of instruments and sensors for structural monitoring of bridges should consider the possible damage that can be caused to gages during construction and also consider the potential for harsh and adverse environmental conditions (rat bites, theft solar panels, etc.).
5. The dataloggers and interface systems employed in this research have shown that they can provide reliable data collection and monitoring systems for both short-term and long-term monitoring of bridges.
6. Vibrating Wire Strain Gages can also be installed on steel girders to record and monitor static and dynamic strains in bridge structures.

7. Thermocouple sensors provide accurate temperature measurements for long-term monitoring.
8. LVDT sensors provide direct and precise measurements of linear displacement. LVDT's were seamlessly integrated into the SM systems during short termload testing. However, Installing the LVDTs for field bridges requires mounting camera tripods. The LVDTs were employed for the short term (During Load Test). The LVDTs are expensive.
9. Accelerometers deliver precise acceleration readings throughout the load testing and during long-term monitoring. The accelerometers assist in measuring the bridge's dynamic behavior while receiving traffic loading. The dynamic properties of the bridge can be used to provide an overall picture of the current condition. On the other hand, the sample frequency rate of the accelerometers is significantly higher. As a result, it is recommended that S.D. cards be utilized so that the data collecting system's storage capacity can be increased. We note that accelerometers provided accurate recording of the passage of individual vehicles – both trucks and lighter personal vehicles like cars.
10. A photovoltaic solar panel was used in the field bridge monitoring to provide a continuous and uninterrupted power supply for the instrumentation systems.

CHAPTER IV

4. EVALUATION OF PRESTRESS LOSS PREDICTION MODELS THROUGH REAL-TIME MEASUREMENTS OF PRESTRESS LOSSES

This chapter investigates prestress losses and cambers of precast, prestressed concrete bridge beams (PC Beams) fabricated and built for the State Highway 4 (SH 4) Bridge over the North Canadian River in Canadian County, OK. The bridge consists of 15 spans; each span is nominally 100 ft. in length. As part of our research project, each span featured unique reinforcement details in end regions and midspans. Additionally, a structural monitoring program measured strains and temperatures within hardened concrete on two of the 60 PC beams. The data for prestress losses were compared to several prediction models, including the AASHTO Refined Method and the Jayaseelan Time Step Method (2019). The purpose of this research was to compare different prestressing strand layouts, and the inclusion of mild steel reinforcement in the bottom to determine the effects on prestress losses.

4.1. Introduction

This paper describes the SH4 bridge project's background information, the structural monitoring program, and prestress loss estimates. The paper's principal purpose is to examine the impacts of mild steel reinforcement and alternative prestressing strand patterns and their effects on camber and prestresses losses. The primary objective of this research is to experimentally examine the effects of the inclusion of mild reinforcing steel in the bottom flange of PC girder and the alternative prestressing pattern on prestressing losses of pretensioned bridge girders. The study also different methods for computing prestress losses on three different PC beam designs, including based on the PCI Handbook method, methods from the AASHTO LRFD Bridge Design Specifications (2020), and the Jayaseelan Time Step Method (2019). A strain gauge-based structural monitoring program was implemented to measure strains and temperatures within hardened concrete in two precast, prestressed concrete bridge beams.

Jayaseelan and Russell (2019) investigated the inclusion of fully tensioned top strands and the effects on prestress losses and cambers.

Within the same article, the authors also examined the effect of placing mild-steel reinforcement near the center of gravity of prestressing strands at the midspan of prestressed concrete bridge beams.

In their research, five (5) designs were analyzed:

1. A base case with no top strands
2. Two cases with mild steel that included two or four fully tensioned top strands
3. Two cases with variations in mild steel reinforcement using either four #7 or five #9 bars

The authors developed a prestress loss model known as the Jayaseelan Time-step method that breaks down the change in concrete strength and modulus over time using the ACI 209R Eq. (2-1).

$$(f'_c)_t = \frac{t}{\alpha+\beta t}(f'_c)_{28} \text{ (ACI 209R 2-1)} \qquad \textbf{Eq. 4.1}$$

The research compared the prestress losses using methods found in the PCI Design Handbook, the 2014 AASHTO LRFD Approximate and Refined methods, and the Jayaseelan Time-step method. Beam cambers were also computed using the Jayaseelan Time-Step method. However, the authors' work was analytical and experimental data was not evaluated.

In recent years, the use of self-consolidating concrete (SCC) has increased significantly. SCC (or variations based on SCC principles) is widely used in the present-day fabrication of prestressed concrete bridge beams. SCC has been shown to produce durable concrete with hardened concrete properties sufficient for use in heavy construction activities. Okamura first proposed this type of concrete in 1986. (Okamura & Ouchi, 1998). Since then, the use of SCC has increased rapidly in North America, particularly in the precast industry, where it has been employed extensively in the United States since 2000. SCC is widely used to manufacture precast elements for bridges (ACI Committee 237, 2007).

There are several advantages of using Self-consolidating concrete (SCC). SCCs improve workability because it is fluid enough to flow into forms and around reinforcement without vibration. Self-consolidating concrete minimizes labor and equipment expenses because it does not require vibration and operators, hence reducing labor costs significantly (Rasekh et al., 2020). SCC has compressive strengths comparable to normal concrete. SCC, a high-performance concrete, has low segregation and great flowability, making it more uniform and consistent (Aggarwal & Aggarwal, 2020).

The essential components of SCC's mix composition are the same as traditional concrete. However, SCC concrete usually consists of smaller aggregate particles and smaller quantities of coarse aggregate (for a given concrete mixture). To achieve the desired fresh concrete properties, SCC requires a higher proportion of smaller particle sizes from constituent materials – principally the coarse aggregate - and the inclusion of chemical admixtures (Holschemacher & Klug, 2002). Because of these changes, the paste volume of SCC is greater than that of conventional concrete.

The modulus of elasticity of self-consolidating concrete is generally lower than that of conventional concrete with similar compressive strength. This is because the elastic modulus of aggregates is usually higher than that of the paste, and the absolute volume of the paste is greater in SCC (Garcia Theran, 2009). According to (ACI Committee 237, 2007), SCC's modulus of elasticity is about 10 to 15 percent lower than that of conventional concrete with a similar compressive strength because of the necessary adjustment of mixture proportions to form SCC. Some researchers have reported that the prestress losses are higher than predicted by the current models (Meyers et al., 2012). Underpredicting the young modulus of concrete for SCCs can lead to underpredicting the elastic shortening and creep of concrete because these parameters are related to the young modulus of concrete.

Many researchers have investigated and compared creep and shrinkage models for high-strength SCC and conventional SCCs. Bonen and Shah (2005) suggest that the shrinkage of SCC is greater than that of conventional concrete. Similar conclusions can be drawn regarding creep because SCC includes a smaller amount of aggregate in the concrete mix. However, the research on the effects of creep in SCC is limited (Bonen & Shah, 2005).

However, none of the creep and shrinkage models can include a broad range of SCC mixes that are applied in the market today (Alghazali & Myers, 2020)

Several structural health monitoring (SHM) approaches to prestress loss monitoring exist. SHM is the continuous monitoring of structural parameters to derive information regarding the performance of a structure. Several parameters have been linked to the magnitude of prestress losses, such as the natural frequencies of the structure (Saiidi et al., 1994), the magnetic permeability of the prestressing strands (Liu et al., 2014), and the stress wave velocity in acoustoelastic methods (Chaki & Bourse, 2009).

Baran et al. (2010) have conducted a comparison study on different methods for experimentally determining losses in pre tensioned concrete girders. The authors have concluded that the most

effective ways of determining to prestress losses in prestressed concrete beams are by using vibrating wire gages embedded in the concrete or attaching a strain gauge to an exposed strand. Furthermore, as detailed in a report on estimating prestress losses by the joint ACI-ASCE Committee 423, most successful field applications and large-scale laboratory experiments for monitoring prestress losses are based on strain measurements using strain sensors installed on the prestressing strands or other no-prestressed reinforcement embedded in the concrete. This is because strain measurements provide a more accurate representation of the amount of stress applied to the concrete (Joint ACI-ASCE Committee 423, 2016).

4.2. Methodology

This research was performed on precast, prestressed concrete bridge beams made for and included in the construction of the State Highway 4 Bridge over the North Canadian River near Yukon, Oklahoma. The bridge features fifteen 100 ft. (nominal) spans supported by Type IV girders. Designs called for four girders per span spaced at 11.3 ft c/c with an 8.0 in. composite concrete deck. A photograph of the bridge structure is shown in Figure 4.1. The cross-section of the concrete bridge girders with the deck is shown in Figure 4.2.

Figure 4.1: Photograph of the SH 4 Bridge over N. Canadian R., Canadian Co., OK.

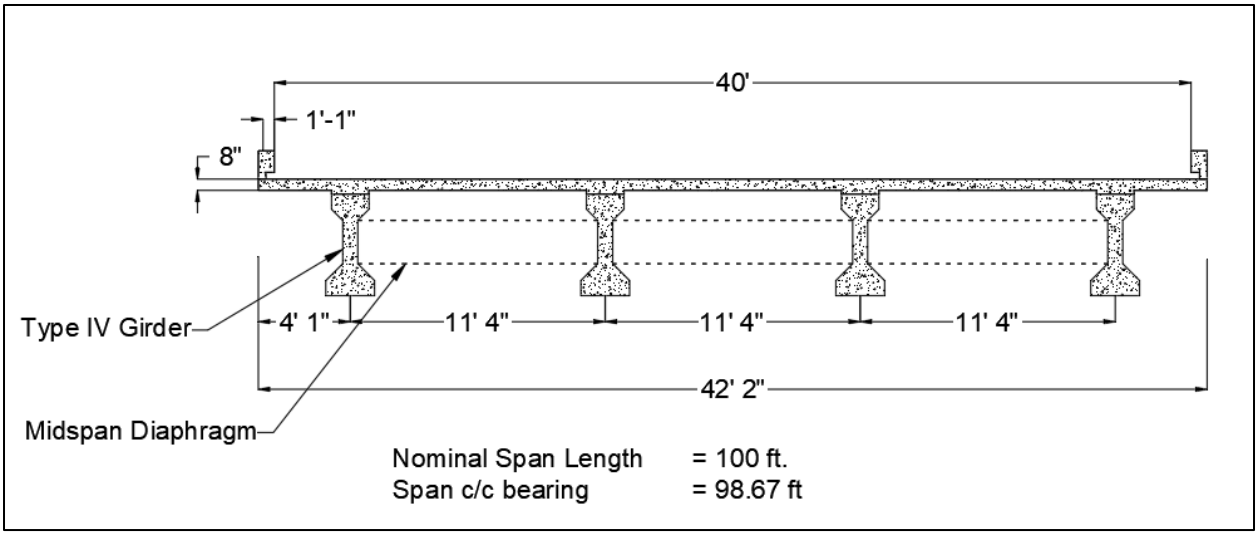

Figure 4.2: Cross-section of the bridge

The bridge was designed and built, each span of the 15 spans containing different reinforcing details. Variations in mild reinforcement and prestressing strand patterns were made for each span. Variations included variations in end zone reinforcement, but these variations do not impact this research. Considering variations at midspan, which affect the prestress losses at midspan, and the predominate effects on beam camber, each of the fifteen (15) span used one of four reinforcement details. In this paper, three different longitudinal patterns are considered. Figure 4.3 displays the strand pattern and reinforcement layout for each beam under consideration:

1. Base Detail (which was not built but is considered for comparison purposes)
2. Detail B (which conforms to strand pattern layout typical for Oklahoma bridges but includes four (4) #7 Bars in the bottom flange of the beams, and
3. Detail C (an "alternate" strand layout that decreases the prestressed eccentricity compared to Detail B. Detail C contained no mild horizontal steel).

The primary design configuration of bridge girders built in Oklahoma includes fully tensioned top strands in combination with bottom prestressing strands. Fully tensioned top-strand patterns and their variants have been used in Oklahoma since 1997 (Russell, 2018). Since then, more than 800

precast, prestressed concrete bridges have been built and entered service in our highway infrastructure.

“Alternate” strand pattern refers to the detail where the prestressing strands have less eccentricity. Detail C does not include horizontal mild steel reinforcement.

Two of the 60 prestressed concrete bridge girders required for the SH 4 bridge were instrumented with vibrating wire strain gages, traditional bonded foil strain gages, and thermocouples. The two girders with instrumentation are these:

- Beam Mark 27, the westernmost girder of the four girders in Span 9. These beams match the design of Design Detail B.
- Beam Mark 42, the westernmost girder of the four girders in Span 14. These beams match the design of Design Detail B.

Beam Mark 27 and Beam Mark 42 were instrumented with embedded thermocouples and vibrating wire gauges (VWGs) to monitor the changes in concrete temperature and strains. Instrumentation at midspan ensured that the strains, curvatures, and concrete temperatures would be acquired.

The instrumentation and data acquisition system were built to enable continuous monitoring of data throughout the fabrication, handling, storage, transit, erection, and service life of the bridge. Mark 27 of span 9 utilized the strand pattern of Detail B, and girder Mark 42 of Span 14 featured the Detail C alternative strand pattern.

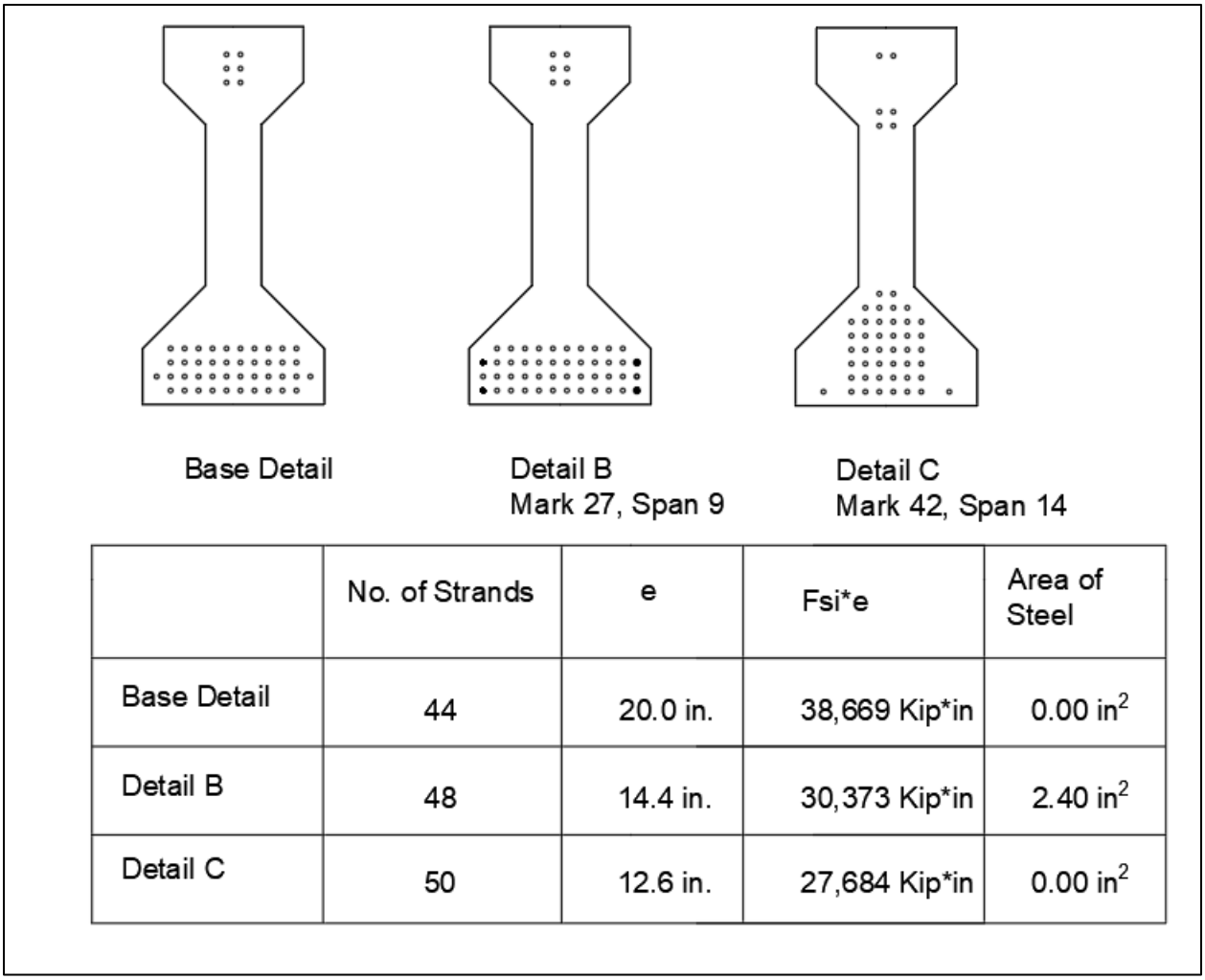

	No. of Strands	e	Fsi*e	Area of Steel
Base Detail	44	20.0 in.	38,669 Kip*in	0.00 in^2
Detail B	48	14.4 in.	30,373 Kip*in	2.40 in^2
Detail C	50	12.6 in.	27,684 Kip*in	0.00 in^2

Figure 4.3: Detailing of longitudinal reinforcement layouts

4.2.1. Material Properties

The concrete mix design of the prestressed girders conformed to the Class P specifications, and the mix design for the concrete deck conformed to the Class AA specifications of the Oklahoma Department of Transportation Standard Specifications for Highway Construction. Table 4.1 displays the concrete mix design specifications for the girder and the deck. The girders were cast at Coreslab Structures, Inc. in Oklahoma City, Oklahoma. The four prestressed beams of Span 9 and Span 14 were cast in the same prestressing bed on April 23 and April 27, 2020. Fresh and hardened concrete properties were collected, measured, and reported in Table 4.2.

Table 4.1: Class AA and Class P ODOT mix proportions

Class AA and Class P ODOT mix Proportions		
	ODOT Requirements for Class P Concrete (Girders)	ODOT Requirements for Class AA Concrete (Deck Placement)
Minimum Cement Content (PCY)	564	564
Total Air Content (%)	5±1.5	6.5±1.5
Water to Cementitious Materials Ratio (w/cm)	0.25-0.44	0.25-0.44
Slump (in.)	3±1	2±1
Minimum Compressive Strength at Prestress Release (psi)	7500	n.a.
Minimum Compressive Strength at 28 days (psi)	10,000	4,000
Note: Class P concrete is used for prestressed concrete bridge girders		

Table 4.2: Fresh concrete properties and hardened concrete properties for Beam Mark 27, Span 9 and Mark 42, Span 14

Fresh concrete properties and hardened concrete properties				
	Beam Mark 27, Span 9		Beam Mark 42, Span 14	
Spread (ASTM C1611) (in):	20.6		21	
Air Content (ASTM C231) (%):	5		3.6	
Air Temperature (°F):	70		74	
Unit Weight (ASTM C138) (lb/ft3):	134.6		143.4	
3 days Concrete Compressive Strength (ASTM C39) (ksi):	Mean	8.76	Mean	8.66
	STD	0.25	STD	0.43
3 days Concrete Elastic Compressive Modulus (ASTM C469) (ksi):	Mean	4093	Mean	4571
	STD	699	STD	"-"
28 days Concrete Compressive Strength (ASTM C39) (ksi):	Mean	10.81	Mean	10.49
	STD	0.04	STD	0.57
28 days Concrete Elastic Compressive Modulus (ASTM C469) (ksi):	Mean	4137	Mean	4848
	STD	607	STD	247

Table 4.3: Significant dates PC beam fabrication, handling, transportation and erection, and SH 4 Bridge construction.

Significant dates PC beam fabrication, handling, transportation and erection, and SH 4 Bridge construction.				
	Beam Mark 27, Span 9		Beam Mark 42, Span 14	
	Dates	Time in Days	Dates	Time in Days
Girder Casting	April 23, 2020	0	April 28, 2020	0
Detensioning	April 24,2020	1	April 29, 2020	1
Placement of girders	May 26, 2020	33	June 1, 2020	34
Deck Placement	August 14, 2020	113	August 18, 2020	112
Time Scope of Study	September 5, 2022	900	September 10, 2022	900

4.3. Results

4.3.1. Measured Concrete Temperatures and Strains at Early Ages:

Concrete temperature and strains were measured using thermocouples and vibrating wire strain gauges (VWSG) embedded at the midspan of Mark 27 and Mark 42 beams, respectively. Figure 4.4 and Figure 4.5 show the recorded concrete temperatures at midspan for the first 72 hours after the fabrication of girders. The graphs show that the heat from the hydration of cement results in an increase in temperature to about 167 ˚F at a time approximately 9 hours after casting. Also, the top flange of the beams is roughly 22 ˚F warmer than the bottom flange. The graphs also show that the temperature decreases over the next 48 hours until the temperature of the concrete approaches the ambient temperature.

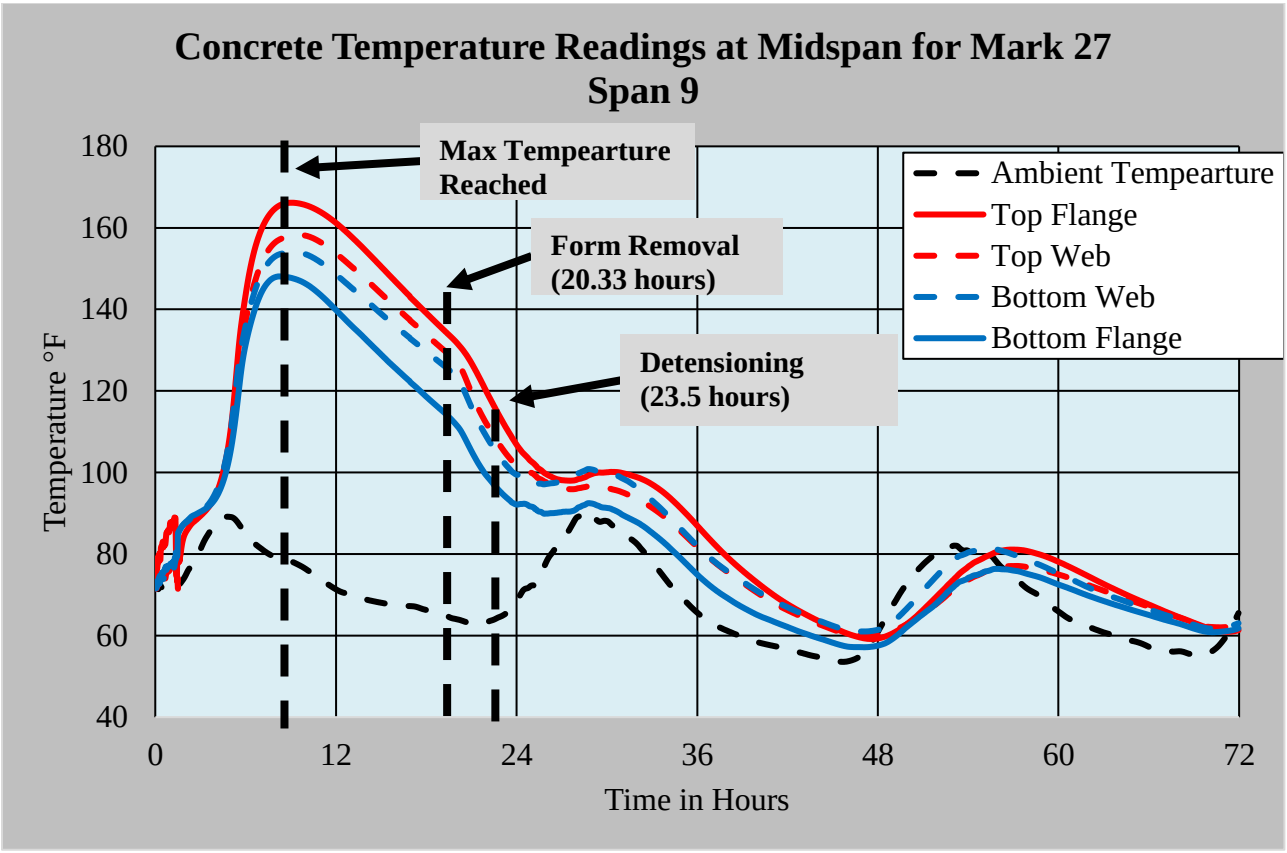

Figure 4.4: Girder Mark 27, Span 9. Recorded temperatures at midspan during the first 72 hours of the PC Beam life. Time of casting is 1.0 hr.

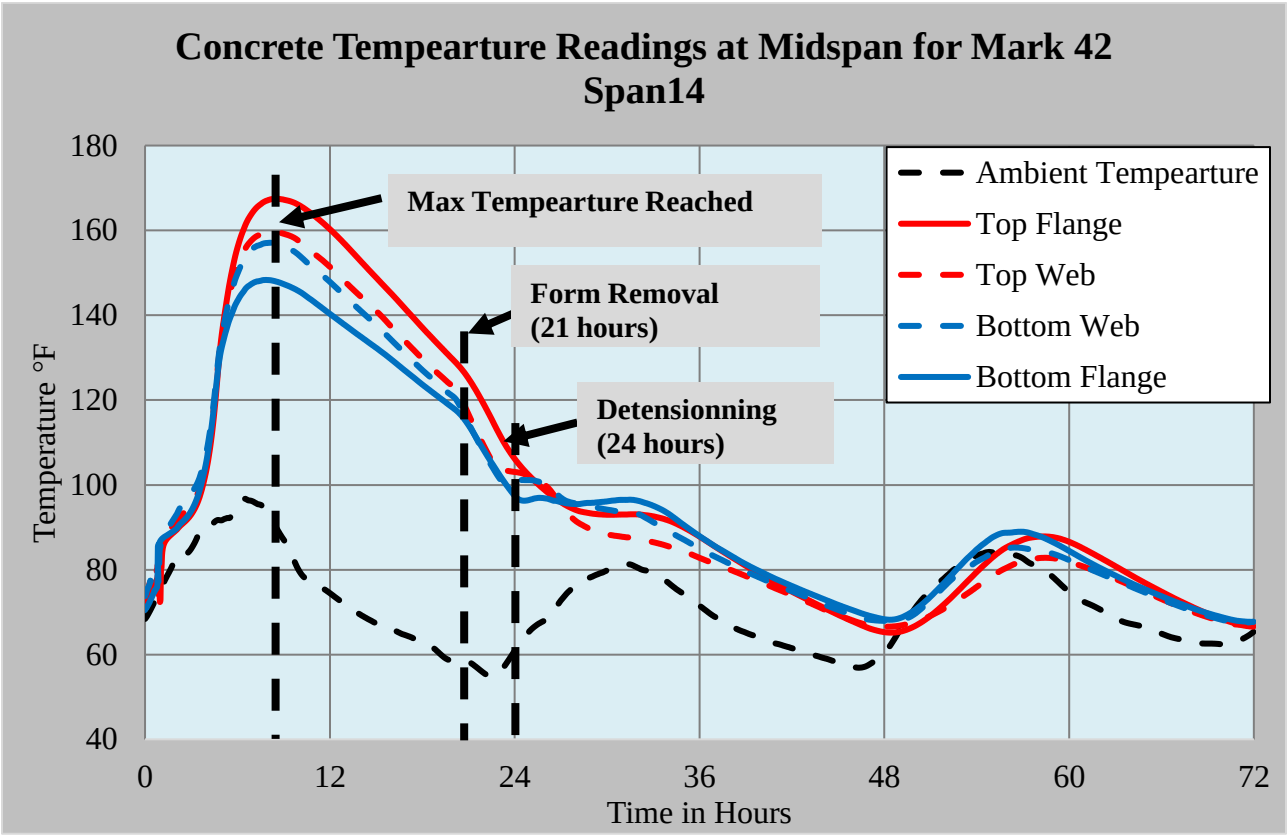

Figure 4.5: Girder Mark 42, Span 14. Recorded temperatures at midspan during the first 72 hours of the PC Beam life. Time of casting is 1.33 hr.

Figure 4.6 shows the recorded concrete strains at midspan for the first 72 hours for Beam Mark 27. The data that are shown are collected from VWSG's located in the at a location 9.3 in. from the top of the beam (top flange), at a location 29.3 from the top of the beam (web), and at a location 48.5 from the top of the beam (in the bottom flange near the cgs). The figure charts both the "actual" strains vs. the "temperature compensated" strains. The Actual Strain or Measured Strain refers to the actual measured change of length for the vibrating wire gauge. These changes of length cane induced by temperatures, and loads. The Temperature Compensated Strains refers to the change of length of the vibrating wire gauge, without including the changes that occurred due to temperature.

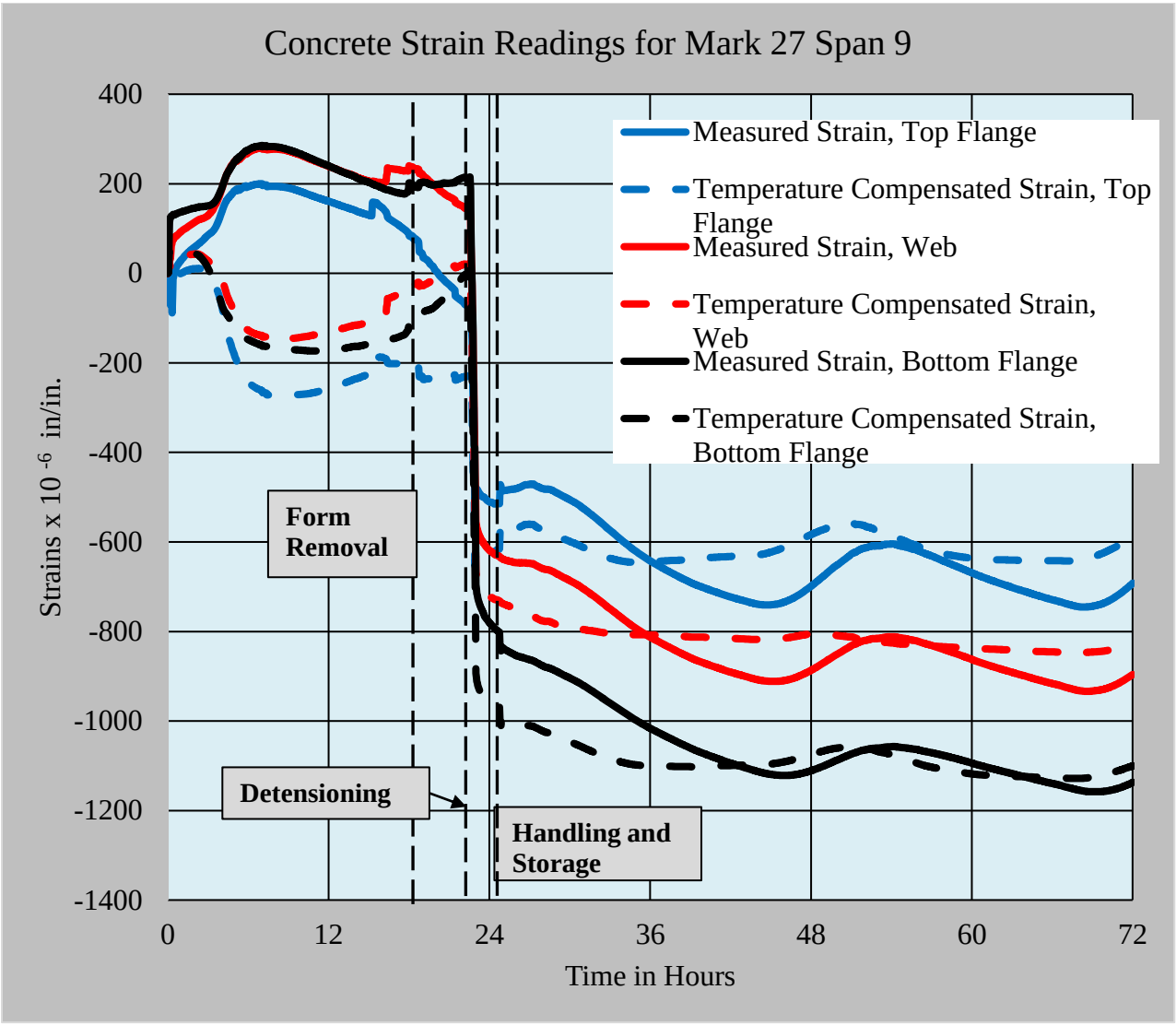

Figure 4.6: Measured strains in concrete at midspan during the first 72 hours for Mark 27, Span 9.

Figure 4.7 shows recorded concrete strains at midspan of Beam Mark 42 in the first 72 hours. The data that are shown are collected from VWSG's located in the at a location 9.3 in. from the top of the beam (top flange), at a location 29.3 from the top of the beam (web), and at a location 46 in. from the top of the beam (in the bottom flange near the cgs). The figure charts both the "actual" strains vs. the "temperature compensated" strains. The measured strains did not significantly change after the concrete had cooled because the concrete was held in place by the reinforcement and formwork.

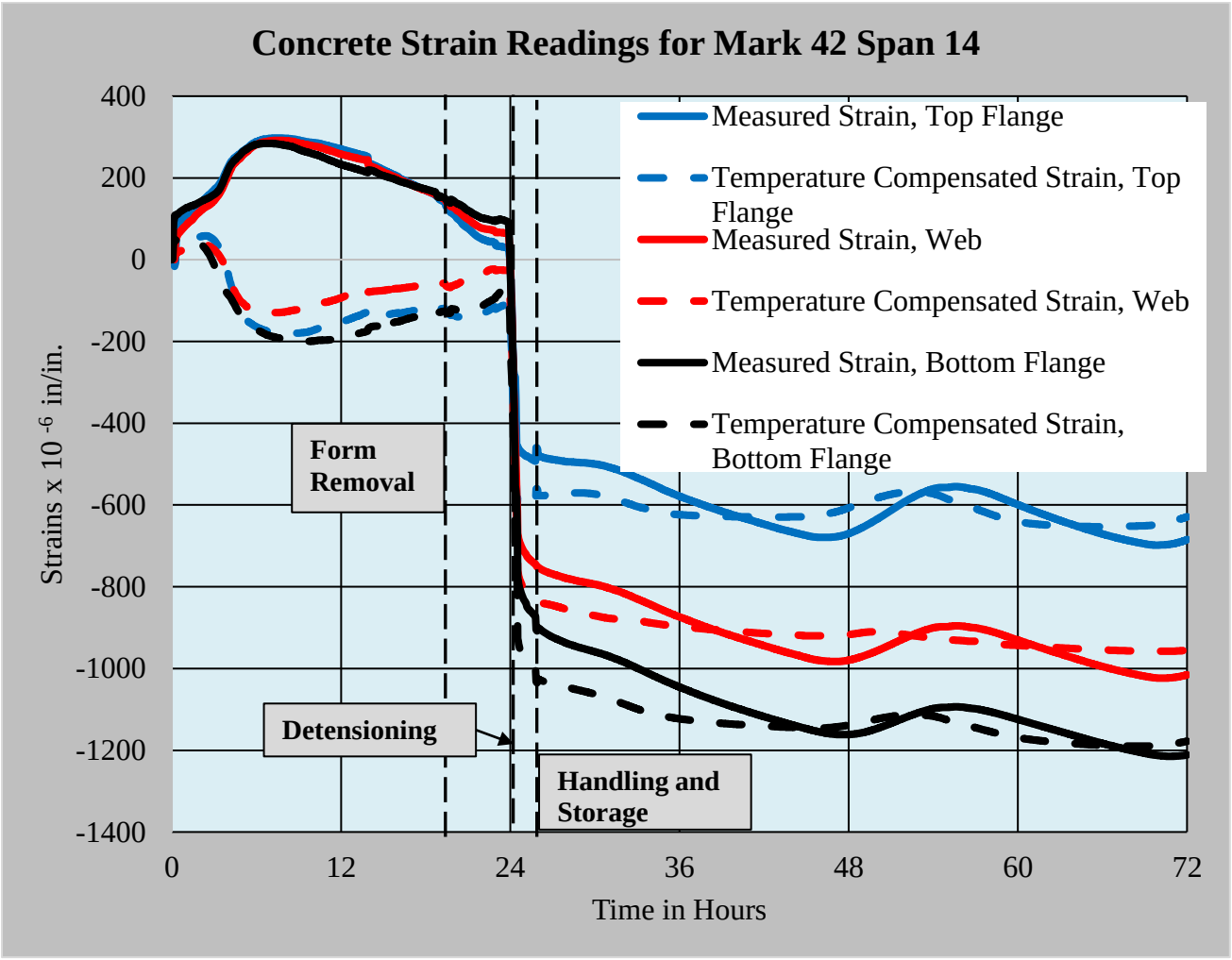

Figure 4.7: Measured strains in concrete at midspan during the first 72 hours for Mark 42 Span 14.

Detensioning the prestressing strands, on the other hand, results in observable and significant changes in the concrete strains. The prestressing forces caused the concrete to go into net compressive strains. Notably, the eccentricity of the prestressing force further caused higher compressive strains in the bottom flange. The figures show that the concrete strains close to the top flange experienced significantly less compression than those close to the bottom flange throughout the early stages of the bridge fabrication before the slab cast. The increase in concrete compressive strains at an early age was prominent since the concrete at a younger age is more prone to creep and shrinkage. The creep and shrinkage rate slows as the concrete ages, and this occurs concurrently with an increase in the amplitude of compressive forces. z

After the girders were removed from prestressing bed, the strains have decreased in the top and increased in the bottom as shown Figure 4.8. A possible explanation of this change is an existence of a small frictional force of a long prestressing bed acting on the concrete, reducing elastic shortening of the concrete. If friction reduces the ability for the concrete to shorten under transfer, then elastic shortening may not fully occur until the frictional restraint is remove (Cook et al, 2005).

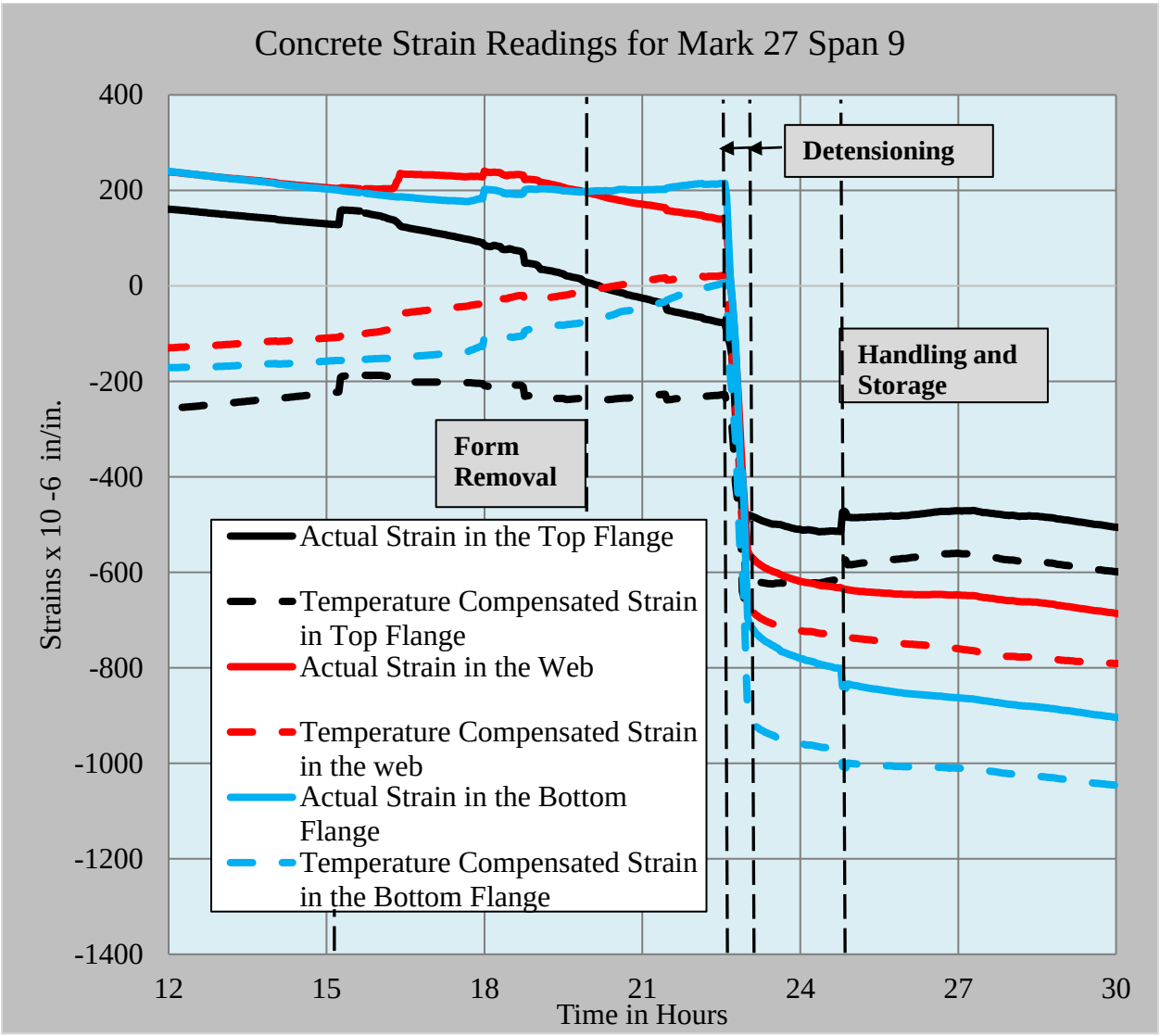

Figure 4.8: Measured strains in concrete at midspan during detensioning and storage for Mark 27, Span 9.

4.3.2. Long Term Measured Concrete Strains:

Figure 4.9 charts the strain measurements at midspan for PC Beam Mark 27, Span 9. Figure 4.10 charts the strain measurements at midspan for PC Beam Mark 42, Span 14. In these two charts the concrete strains at midspan are charted over the entire life of the PC Beams, with continuous data collected from the time before the concrete cast, through concrete casting, concrete hydration, curing, de-tensioning of the prestressing strands, handling and storage, transportation, erection and the through bridge construction.

- Initial strain near the top fiber is -500 microstrains; initial strain near the bottom fiber is -1000 microstrains. These initial strains represent the beam mechanics and the strain conditions after the initial prestress losses due to the elastic shortening (ES) of the concrete. The higher compressive strains at the bottom flange, as compared to those at the top flange, indicate that the beam is cambering upward.
- In the first 30 days from initial beam fabrication, all concrete strains increase considerably toward additional compression (shortening) strains. These strains are those associated with prestress losses including both creep and shrinkage. Within approximately three weeks (21 days), the compressive strains have increased by more than 30 percent.
- Girders were transported and erected during May of 2020. The handling and transportation of the two girders caused a change in the pattern of steadily increasing compressive strains
- From approximately 21 days and until the time of deck slab casting, compressive strains continue to increase but at a slower rate.
- As the concrete deck was cast, and the dead load of fresh concrete was resisted by the pre-tensioned bridge girder, we see a further increase in compression near the top fiber, balanced by a decrease in compression near the bottom fiber.

- The “closing’ of variation in the measured strains from top to bottom indicate that the dead loads are effectively “balanced.” We note that LOAD BALANCING is a common design practice in posttensioned concrete, but not prevalent (and rarely mentioned) in pre-tensioned concrete. But the load balancing can still be employed as a technique to ensure effective design. The effects of this “load balancing” can be seen in both Figures as the concrete strains “come together” (and the differences in strains from top to bottom are decreased) on the day that the deck slabs are cast.

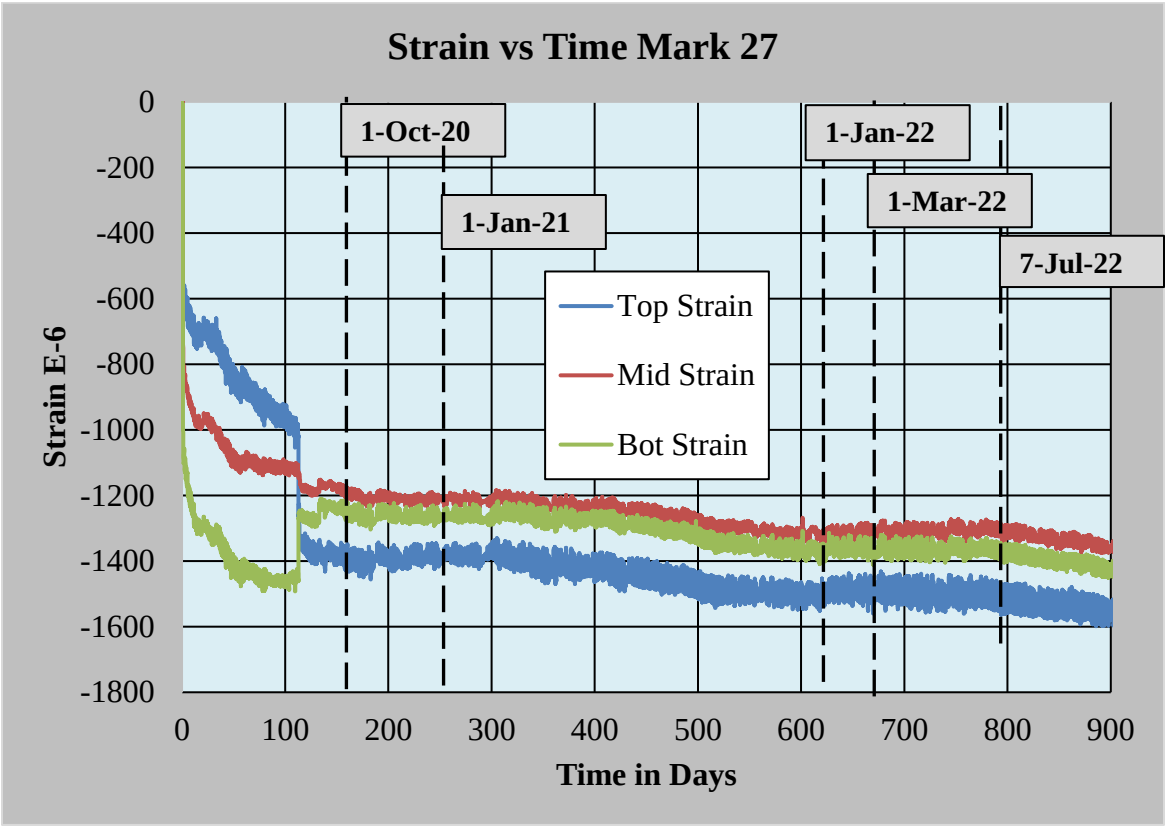

Figure 4.9: Measured compensated concrete strain for temperature at midspan for Mark 27, Span 9. (t = 0; represents 23 Apr 2020)

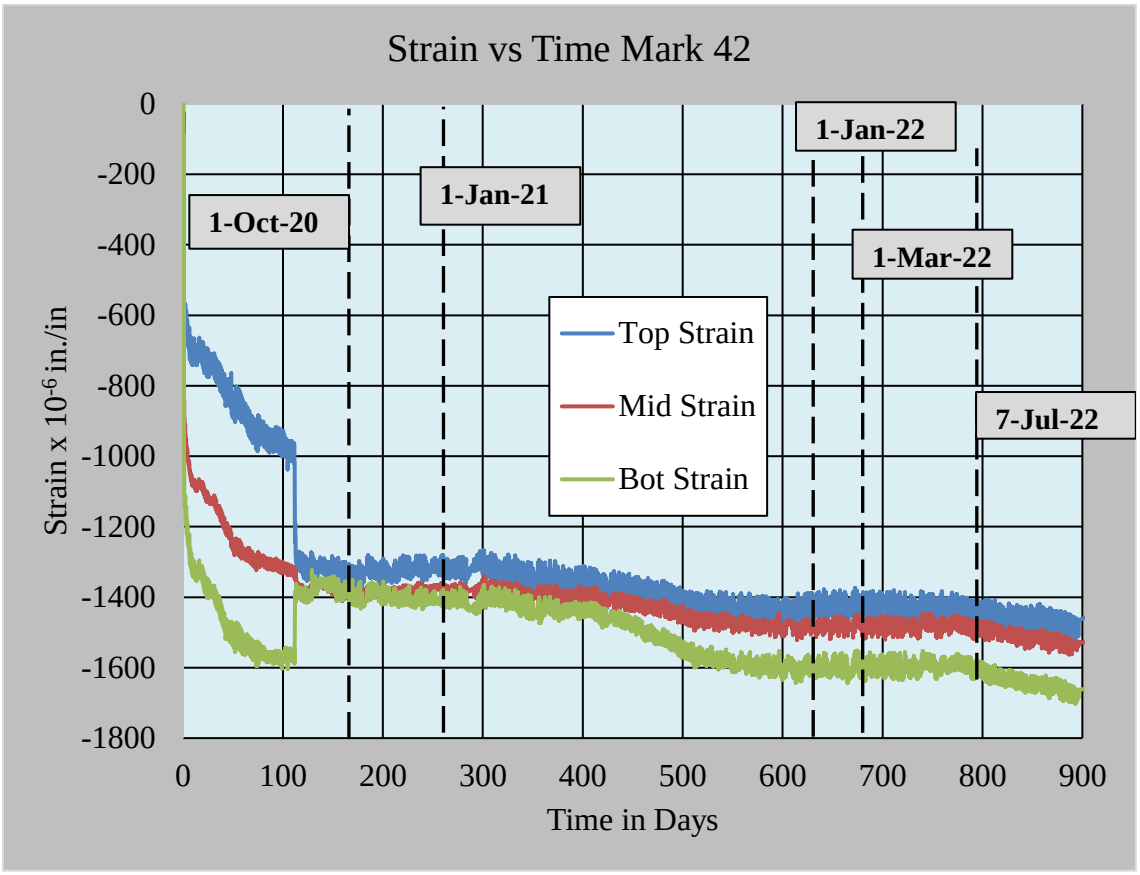

Figure 4.10: Measured compensated concrete strain for temperature at midspan for Mark 42, Span 14. (t = 0; represents 27 Apr 2020)

4.3.3. Measured Prestress Losses

The prestress losses in the bridge girders were computed from the measured concrete temperatures and strains. The total prestress losses for the girders were computed by multiplying the interpolated strain readings calculated at the center of gravity of the prestressing steel by its modulus of elasticity. The modulus of elasticity of prestressing steel was defined as 28500 ksi. Figure 4.11 and **Error! Reference source not found.** show the interpolated prestress losses at midspan for the girders Mark 27 of span 9 and Mark 42 of span 14, respectively. The figure shows that the prestress losses in Mark 27 beam were approximately 40 ksi before the deck cast. After the deck cast, the additional tension from the slab self-weight caused the losses to decrease to about 35 ksi. Over time the losses further increased to about 40 ksi. The prestress loss trend for Mark 42 girder followed the same profile as the Mark 27 girder with slighter lower values.

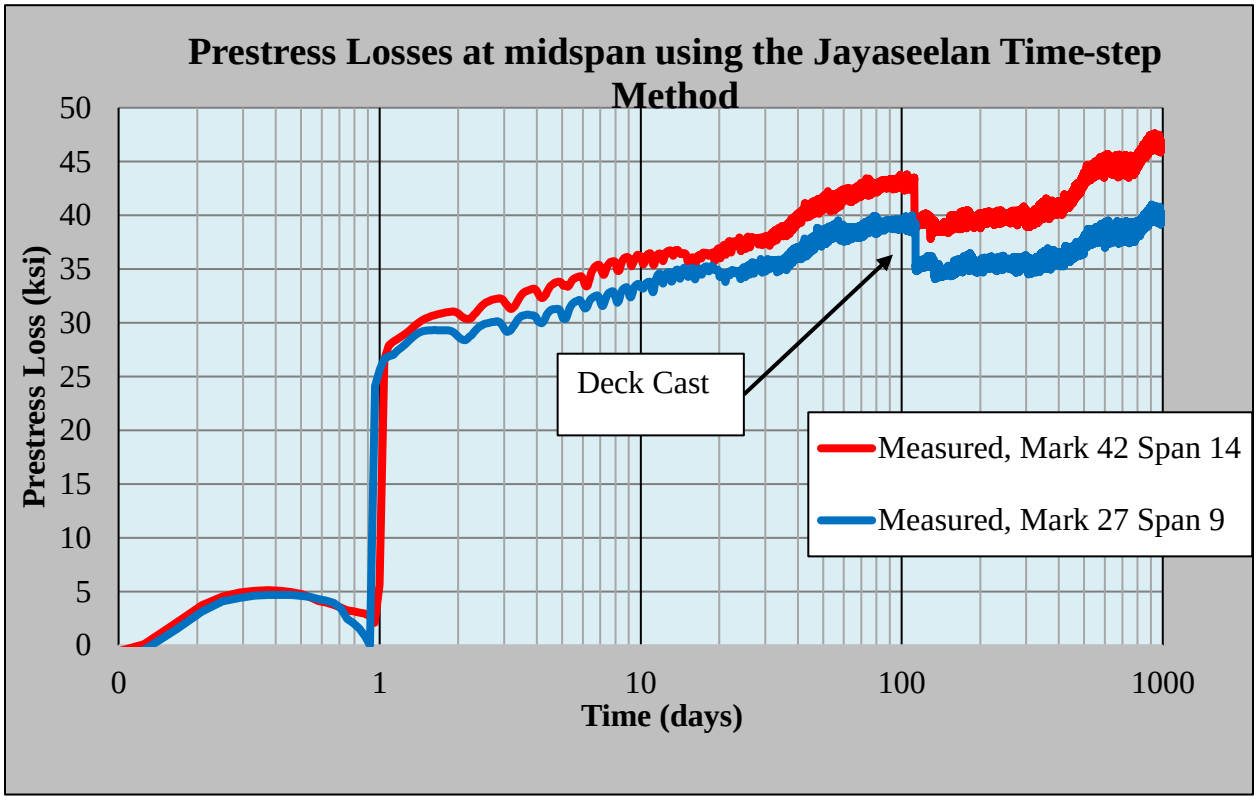

Figure 4.11: Direct measurements of prestress losses from strain gauge data at midspan for Mark 27 Span 9 and for Mark 42 Span 14

Table 4.4: Measured Prestress losses for Mark 27, Span 9

Prestress Losses for Mark 27, Span 9		
Dates	**Time in Days**	**Prestress Losses in ksi**
4/23/20 10:00 AM	**0 Day Start of the recordings**	**0.0**
4/25/2020	**1 Day Before Release**	**-0.3**
4/25/2020	**1 Day At Release**	**23.8**
4/25/2020	**2 Day**	**28.7**
4/26/2020	**3 Days**	**29.5**
4/30/2020	**7 Days**	**31.8**
5/7/2020	**14 Days**	**34.3**
5/21/2020	**28 Days**	**35.1**
5/26/2020	**33 Days Transportation and Erection**	**35.4**
8/14/2020	**113 Days After Casting**	**38.4**
8/14/2020	**113 Days After Casting**	**34.5**
10/1/2021	**526 Days**	**37.3**
1/1/2022	**618 Days**	**38.3**
3/1/2022	**677 Days**	**37.5**
7/1/2022	**799 Days**	**37.9**
10/10/2022	**900 Days**	**39.4**

Table 4.5: Measured Prestress losses for Mark 42, Span 14

Prestress Losses for Mark 42, Span 14		
Dates	**Time in Days**	**Prestress Losses in ksi**
4/23/2020	**0 Day Start of the recordings**	0.0
4/29/2020	**1 Day Before Release**	1.7
5/1/2020	**1 Day At Release**	25.2
5/1/2020	**2 Day**	29.2
5/2/2020	**3 Days**	30.3
5/6/2020	**7 Days**	33.4
5/13/2020	**14 Days**	35.0
5/27/2020	**28 Days**	36.1
6/1/2020	**34 Days Transportation and Erection**	36.9
8/18/2020	**112 Days After Casting**	41.8
8/18/2020	**112 Days After Casting**	37.8
10/1/2021	**521 Days**	42.1
1/1/2022	**613 Days**	43.2
3/1/2022	**672 Days**	42.4
7/1/2022	**794 Days**	43.0
10/15/2022	**900 Days**	44.3

4.3.4. Estimated Prestress Losses

This paper computed the prestress losses at the girder midspan using different models. The following methods were used to estimate the prestress losses:

- AASHTO 2020 LRFD Specification, Approximate method (AASHTO, 2020) The results are reported in Table 4.6

- AASHTO 2020 LRFD Specification, Refined method (AASHTO, 2020). The results are reported in Table 4.7
- PCI Design Handbook method. The results are reported in Table 4.8
- Modified Version of the PCI Design Handbook method (using transformed cross-section properties). The results are reported in Table 4.9
- Jayaseelan Time-Step Method (Jayaseelan & Russell, 2019). The results are reported in Table 4.10.

AASHTO Approximate Losses

The prestress losses computed using the AASHTO 2020 LRFD approximate method combined the long-term losses from concrete creep, shrinkage, and relaxation of prestressing strands. This method utilizes the gross section characteristics; therefore, the inclusion of mild reinforcing steel was not directly accounted for in the prestress loss calculations.

Table 4.6: Approximate loss estimates for time-dependent losses according to the AASHTO 2020 LRFD Design Specifications.

Prestress Losses Results Using AASHTO Approximate Method			
Reinforcement Detail	**ES, (ksi)**	**Δf_{pLT} (ksi)**	**Total, ksi**
Base	25.0	26.4	51.3
B	20.5	27.8	48.3
C	19.6	28.6	48.2
Note: ES = prestress loss due to elastic shortening; Δf_{pLT} = long term losses (CR +SH +RE); 1 ksi = 6.895 MPa. E_{ci}/E_c s: Calculated using (AASHTO 5.4.2.4-1)			

AASHTO Refined Method Losses:

The AASHTO 2020 LRFD refined method utilized the transformed cross-section properties to estimate the prestress losses. This procedure uses time-dependent analysis by calculating the creep coefficient of concrete and shrinkage strain of concrete for both the girder and concrete deck at varying time intervals. The prestress losses were calculated before deck cast at 110 days and 900 days at midspan.

For the AASHTO Methods, the initial or design modulus of elasticity of concrete, E_{ci}, or E_c was estimated using the equation given in *American Association of State Highway and Transportation Officials LRFD Bridge Design Specifications*

$$E_c = 120000 K_1 w_c^2 f'^{0.33}_c \quad \text{(AASHTO Eq.5.4.2.4-1)} \qquad \textbf{Eq. 4.2}$$

Where,

w = unit weight of concrete in kcf.

K_1: a correction factor for the source of aggregate to be taken as 1.0

Table 4.7: Refined estimates of time-dependent prestress losses at midspan calculated using transformed section properties according to the 2020 AASHTO LRFD Bridge Design Specifications.

Prestress Losses Results Using AASHTO Refined Method							
Reinforcement Detail	**Concrete age, days**	**ES, ksi**	**CR, ksi**	**SH, ksi**	**RE, ksi**	**SH of Deck, ksi**	**Losses at midspan, ksi**
Base	110	23.2	17.4	5.7	1.1	0	47.4
	115	23.2	14.4	5.8	1.1	-0.2	47.4
	900	23.2	18.1	7.1	2.2	-0.9	49.7
B	110	18.1	14.2	5.9	1.3	0	39.5
	115	18.1	14.0	6.1	1.3	-0.1	39.3
	900	18.1	14.4	7.4	2.6	-0.8	41.6
C	110	17.9	14.2	6	1.3	0	39.4
	115	17.9	13.8	6.1	1.3	-0.1	38.6
	900	17.9	14.7	7.5	2.6	-0.6	42.1

Note: CR = prestress loss due to creep; ES = prestress loss due to elastic shortening; RE = prestress loss due to relaxation; SH = prestress loss due to shrinkage. 1 ksi = 6.895 MPa.
f_{ci}= 7 ksi
f_{c28} = 10 ksi
E_{ci}/E_c s: Calculated using (AASHTO 5.4.2.4-1)

PCI Methods:

Although more sophisticated methods for predicting losses exist, the PCI design handbook method developed by Zia et al. (Zia, 1979) remains a vital tool for evaluating prestress losses for precast, prestressed concrete structural elements. This method estimates prestress losses using gross section characteristics that exclude the effects of mild reinforcement. The equations of the PCI design handbook method were modified to predict losses. This modified PCI design method

utilized the same equations as the traditional PCI design handbook method but was slightly modified to accommodate the transformed cross-section properties. For the PCI Methods, the initial or design modulus of elasticity of concrete, E_{ci}, or E_c was estimated using the equation given by ACI 3163R. The equation is given as follows:

$$E_c = 40000\sqrt{f'_c} + 1 \times 10^6 psi \text{ (ACI 363R10 Eq.6-1)} \quad \textbf{Eq. 4.3}$$

Table 4.8: Approximate loss estimates using gross section properties according to PCI Design Handbook 6th Edition.

Prestress losses at midspan calculated using gross section properties with the PCI Design Handbook method						
Reinforcement Detail	**Concrete age, days**	**ES, ksi**	**CR, ksi**	**SH, ksi**	**RE, ksi**	**Losses at midspan, ksi**
Base	110	26.5	38.8	5.9	2.2	73.4
	900	26.5	19.4	5.9	2.9	54.7
B	110	21.7	33	5.9	2.6	63.2
	900	21.7	19	5.9	3.1	49.7
C	110	20.9	31.9	5.9	2.7	61.4
	900	20.9	19.7	5.9	3.1	49.6

Note: CR = prestress loss due to creep; ES = prestress loss due to elastic shortening; RE = prestress loss due to relaxation; SH = prestress loss due to shrinkage. 1 ksi = 6.895 MPa.
f_{ci}= 7 ksi
f_{c28} = 10 ksi
E_{ci}/E_c s: Calculated using (ACI 363R10 Eq.6-1)

Table 4.9: Approximate loss estimates using transformed section properties according to PCI Design Handbook 6th Edition

Prestress losses at midspan calculated using transformed section properties with the PCI Design Handbook method						
Reinforcement Detail	**Concrete age, days**	**ES, ksi**	**CR, ksi**	**SH, ksi**	**RE, ksi**	**Losses at midspan, ksi**
Base	110	25.6	37.8	5.9	2.2	71.5
	900	25.6	20.6	5.9	2.9	55.0
B	110	20.9	31.9	5.9	2.7	61.4
	900	20.9	19.7	5.9	3.1	49.6
C	110	20.8	31.9	5.9	2.7	61.3
	900	20.8	20.7	5.9	3.1	50.5

Note: CR = prestress loss due to creep; ES = prestress loss due to elastic shortening; RE = prestress loss due to relaxation; SH = prestress loss due to shrinkage. 1 ksi = 6.895 MPa.
f_{ci}= 7 ksi
f_{c28} = 10 ksi
E_{ci}/E_c s: Calculated using (ACI 363R10 Eq.6-1)

Jayaseelan Time Step Method:

Jayaseelan and Russell (2019) proposed time-step methods for estimating day-to-day losses. This method evaluates the strength and modulus of concrete as a function of time, calculated daily. This method also utilizes transformed cross-section properties of the girder. Creep and shrinkage strains were analyzed independently and estimated as comparable to the AASHTO LRFD Refined approach. The actual concrete age during transfer was assumed to be one day, and the time of deck cast was 110 days. Prestress losses at midspan were computed daily up to 900 days. For the Jayaseelan Time-Step Method, the initial or design modulus of elasticity of concrete, E_{ci}, or E_c was estimated using the equation given in Building Code Requirements for Structural Concrete (ACI 38-14) and Commentary ACI318R-14) Section 19.2.2.1a. ACI 3163R. The equation is given as follows:

$$E_c = 33w^{1.5}\left(f'_c\right)^{0.5} \quad \text{(ACI 318-14 Eq.19.2.2.1. a)} \qquad \textbf{Eq. 4.4}$$

Where,

w = unit weight of concrete in lb/ft3

Table 4.10: Prestress losses at midspan calculated with the Jayaseelan Time-step method

Prestress losses at midspan calculated with the Jayaseelan time-step method						
Reinforcement Detail	**Concrete age, days**	**ES, ksi**	**CR, ksi**	**SH, ksi**	**RE, ksi**	**Losses at midspan, ksi**
Base	110	24.0	13.6	5.3	1.0	43.9
	115	24.0	8.70	5.2	1.1	39.1
	900	24.0	10.5	6.5	1.6	42.6
B	110	19.7	11.1	5.3	1.3	37.3
	115	19.7	6.9	5.2	1.3	33.1
	900	19.7	8.2	6.3	1.7	35.9
C	110	19.5	11.1	5.4	1.2	37.2
	115	19.5	6.7	5.4	1.4	32.9
	900	19.5	8.0	6.5	1.7	35.7

Note: CR = prestress loss due to creep; ES = prestress loss due to elastic shortening; RE = prestress loss due to relaxation; SH = prestress loss due to shrinkage. 1 ksi = 6.895 MPa.
f_{ci}= 7 ksi
f_{c28} = 10 ksi
E_{ci}/E_c s: Calculated using (ACI 318-14 19.2.2.1.a)

4.4. Elastic Shortening Discussion

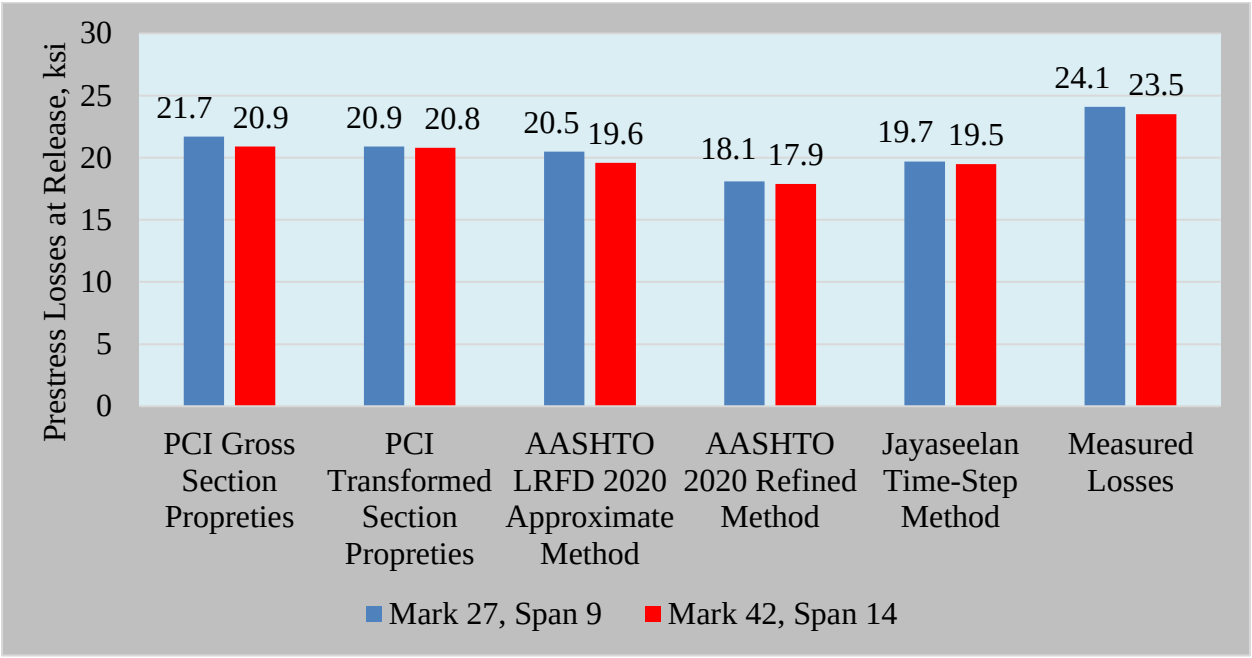

Figure 4.12: Comparison of measured and predicted concrete modulus at detensioning.

Figure 4.12 compares the measured elastic shortening vs. the predicted elastic shortening using different design equations. The results from the PCI Gross Section Properties method underpredicted the elastic shortening loss by 2.4 ksi for Mark 27, Span 9, and by 2.6 ksi for Mark 42, Span 14. The results from PCI Transformed Section Properties method underpredicted the elastic shortening loss by 3.2 ksi for Mark 27, Span 9, and by 2.7 ksi for Mark 42, Span 14. The results from the AASHTO Approximate method underpredicted the elastic shortening loss by 3.6 ksi for Mark 27, Span 9, and by 3.9 ksi for Mark 42, Span 14. The results from AASHTO Refined method underpredicted the elastic shortening loss by 6.0 ksi for Mark 27, Span 9, and by 5.6 ksi for Mark 42, Span 14. The results from Jayaseelan Time-Step Method underpredicted the elastic shortening loss by 4.4 ksi for Mark 27, Span 9, and 4.0 ksi for Mark 42, Span 14.

The overprediction of concrete modulus can be observed in early strain readings. Strain data at detensioning gives a direct measurement of elastic shortening loss. This can be found by finding a

change in strain between the start and end of detensioning. The change in strain measured by the VBWs can be interpolated to the center of gravity of prestressing steel and multiplied by the elastic modulus of the prestressing steel to find elastic shortening loss. The measured elastic shortening loss can then be input into equations for predicting elastic shortening and an estimate of true concrete modulus at detensioning can be calculated algebraically.

$$ES = \frac{E_p}{E_c} f_{cgp} \qquad \textbf{Eq. 4.5}$$

Where:

ES = Elastic shortening loss.

E_p = Modulus of prestressing steel, taken as 28,500 ksi.

E_c = Modulus of concrete at detensioning.

f_{cgp} = Sum of concrete stresses at the center of gravity of prestressing strands due to prestressing force at transfer and the self-weight of the member, calculated to be 3.25 ksi for Mark 27 Span 9, and 3.22 ksi for Mark 42 Span 14.

The equation can be rearranged to compute concrete modulus at detensioning:

$$E_c = \frac{E_p}{ES} f_{cgp} \qquad \textbf{Eq. 4.6}$$

Using the measured elastic shortening loss from strain readings in this equation, true concrete modulus at detensioning can be found. Results are tabulated in Table 4.10. The data show that the AASHTO 5.4.2.4-1 and the ACI 318 14 19.2.2.1a equations overpredict the modulus at transfer

by up to 30%. The ACI 363R-23 5-1 equation overpredicts the elastic shortening by up to 13%. The AASHTO 5.4.24-1 and ACI 318 14 19.2.2.1a equations were developed for conventional concrete. Self-consolidating concrete tends to have a lower elastic modulus compared to conventional concrete. ACI 363R-23 5-1 equation was developed for higher concrete strength. The Jayaseelan Time-Step Method overpredicted concrete modulus at transfer by up to 21%, and underpredict the elastic shortening by 4.4 ksi for Mark 27 Span 9, and by 4.0 ksi for Mark 42 Span 14. The results show that concrete modulus is significantly and consistently overpredicted at early ages, meaning that elastic shortening loss is underpredicted in design.

Table 4.11: Comparison of the Derived Modulus from the Measured Elastic Shortening vs Different design Equations.

Elastic Modulus of the Concrete at Release in ksi	
	Modulus of Elasticity in ksi
AASHTO Eq 5.4.2.4-1	5132
ACI 363R-10 Eq 6-1	4347
ACI 318-14 19.2.2.1a	5072
Derived from ES of Mark 27 Span 9	**3846**
Derived from ES of Mark 42 Span 14	**3914**
Note: Ec = Concrete modulus at detensioning ES = Measured Elastic Shortening Loss Ep = 28500 ksi fci = 7 ksi fcgp = 3.25 ksi (Mark 27) and fcgp =3.23 ksi (Mark 42)	

4.5. Comparison of Measured vs. Estimated Prestress losses

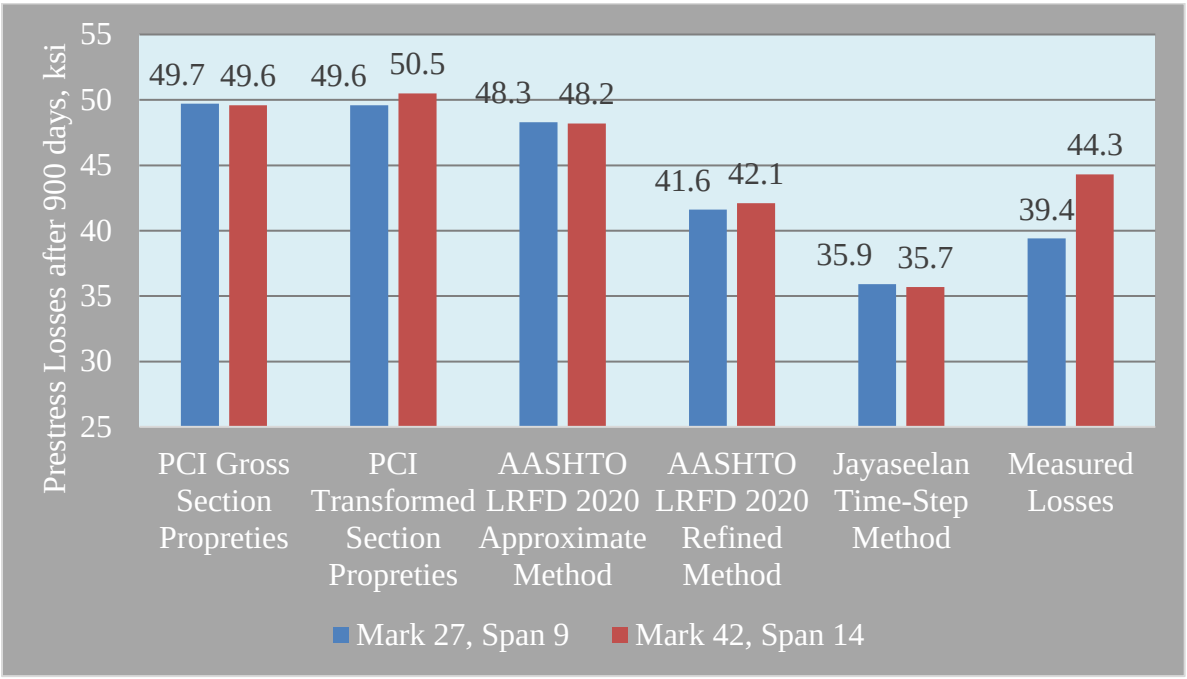

Figure 4.13: Predicted and measured losses at 900 days.

Figure 4.13 compares the 900 days of prestress losses that were estimated using the various prediction models and the measured losses for the girders Mark 27 and 42, respectively. It is important to note here that the AASHTO Approximate method cannot predict losses before the deck cast. The AASHTO Refined method overpredicted the losses in Mark 27 girder by 2.2 ksi and underpredicted the losses in Mark 42 beam by 2.2 ksi than the measured losses.

PCI Design guide method that utilized the gross section properties of the girders overestimated the losses in beam Mark 27 by 7.7 ksi and overestimated losses in beam Mark 42 by 5.3 ksi. On the other hand, the modified PCI design manual that utilized the transformed section overpredicted losses for both Mark 27 and Mark 42 girders by 10.3 ksi and 6.2 ksi, respectively. The Jayaseelan time-step method underestimated the prestress losses in Mark 29 by 3.5 ksi and it underestimated losses for Mark 42 by 8.6 ksi.

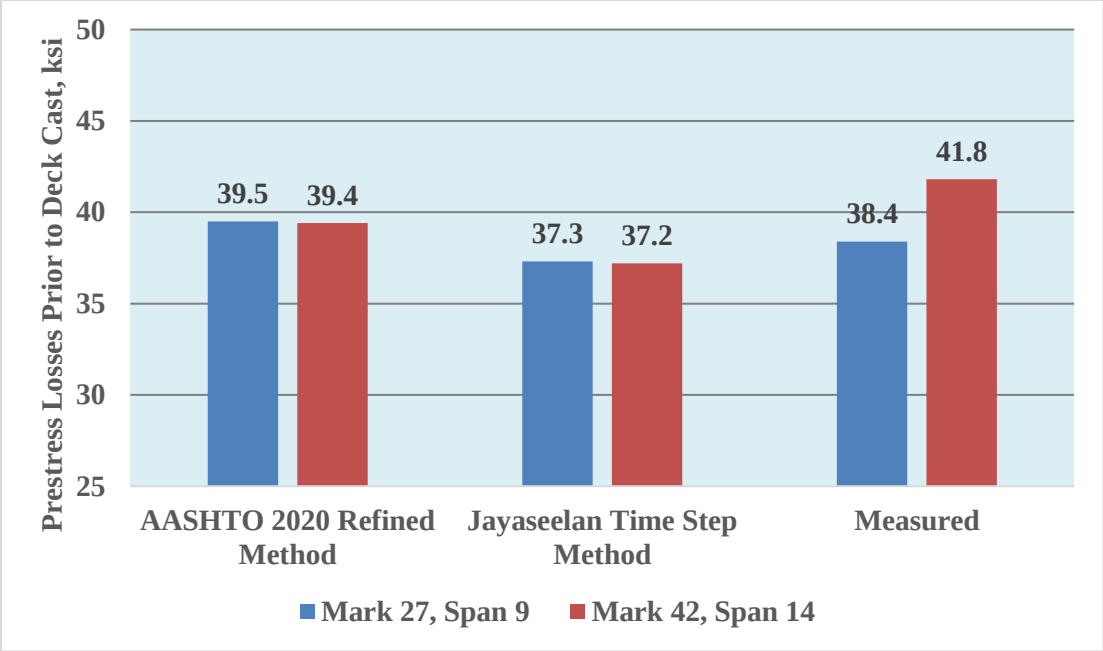

Figure 4.14:Predicted and measured losses prior to deck cast

Figure 4.14 compares prestress losses prior to deck cast that were estimated using the various prediction models and the measured losses for the girders Mark 27 and 42, respectively. It is important to note here that the AASHTO Approximate method cannot predict losses before the deck cast. The AASHTO Refined method overpredicted the losses in Mark 27 girder by 1.1 ksi and underpredicted the losses in Mark 42 girder by 2.4 ksi than the measured losses.

The Jayaseelan time-step method underestimated the prestress losses in Mark 27 by 1.1 ksi and it underestimated losses for Mark 42 by 4.6 ksi.

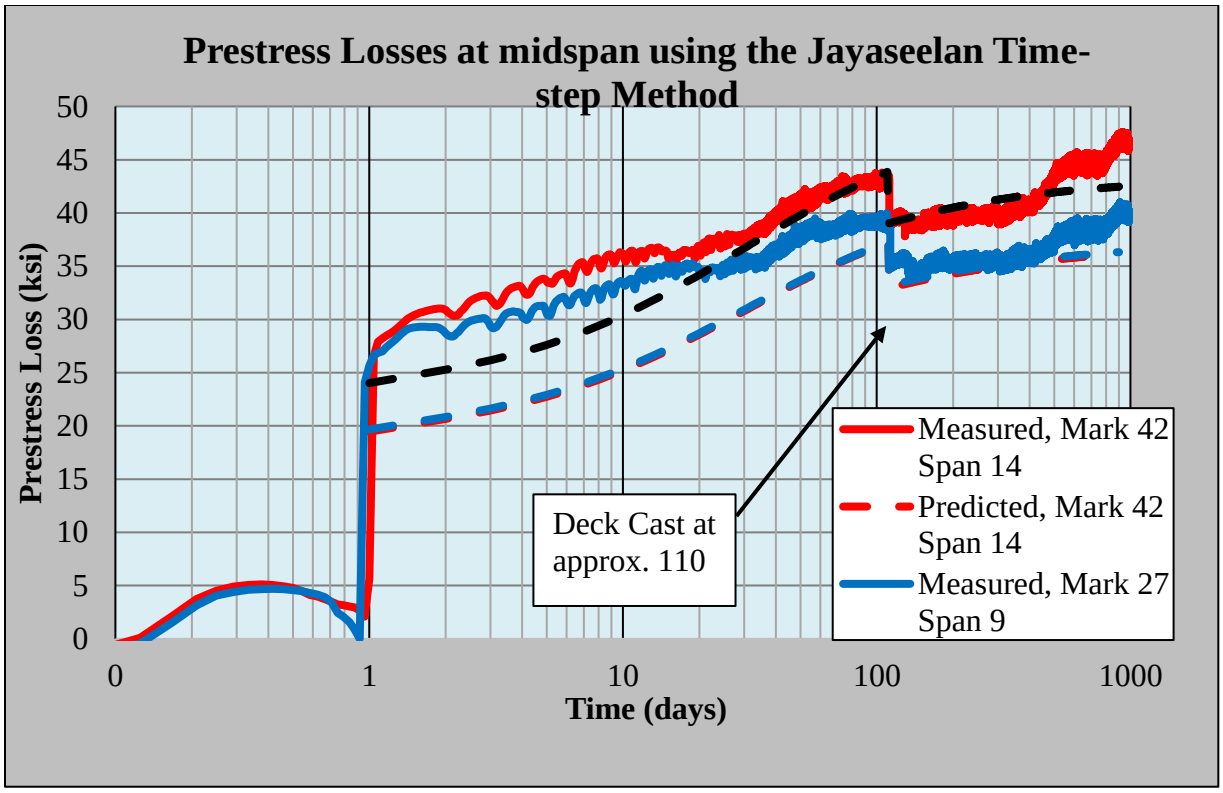

Figure 4.15: Estimated prestress losses using the Jayaseelan Time-step method and the measured losses.

Figure 4.15 graphs the measured and computed day-to-day losses using the Jayaseelan time-step method for the girders Mark 27 of Span 9 and Mark 42 of Span 14. The Jayaseelan time-step method was utilized to determine to prestress losses in both the girders immediately after release at 24 hours, during storage, at girder installation on the bridge site, just prior to deck casting, right after deck casting, and after 900 days (approximately 800 days of life in-service). The trend of the loss prediction curve graphed using the Jayaseelan time-step method closely follows the measured losses for both the girders Mark 27 & 42.

According to Table 4.12, the prestress losses estimated using different methods are significantly different. The AASHTO LRFD Refined method is based on the experiment of normal strength concrete, and in this study, the predicted values of prestress losses using the AASHTO LRFD Refined method are 2.4% larger than Mark 27 Span 9, and 8.7% lower than the measured.

Table 4.12: Summary of prestress losses

Total Prestress losses at midspan						
Reinforcement Detail	**Concrete age, days**	**AASHTO 2020 Approximate method, ksi**	**AASHTO 2020 Refined, ksi**	**PCI, ksi**	**Modified PCI, ksi**	**Jayaseelan Time-Step Method, ksi**
Base	110	-	47.4	-	-	43.9
	900	51.3	49.7	55	55	42.6
A	110	-	42.1			40.2
	900	50.5	44.3	52.9	53.6	38.5
B	110	-	39.5	-	-	37.3
	900	48.3	41.6	49.7	49.6	35.9
C	110	-	39.4	-	-	37.2
	900	48.2	42.1	49.6	50.5	35.7
D	110	-	38.7	-	-	36.4
	900	48.2	40.8	49.6	49.5	34.7
Note: 1 ksi = 6.895 MPa.						

4.6. Comparison of Measured Losses and Jayaseelan Time-Step Method with corrected Modulus of Elasticity:

The overprediction of the elastic Modulus led them to underestimate the losses. One of the aims of this study is to evaluate the Jayaseelan Time-Step Method. Therefore, the Jayaseelan Time-Step method was calculated again with the corrected Modulus for both Girders.

The initial modulus (at release) of elasticity of concrete, E_{ci}, was set to 3846 ksi for Mark 27, Span 9, and 3914 ksi for Mark 42, Span 14. Unfortunately, we don't have much test data for the modulus of elasticity of the beams. Therefore, when the concrete was aging, the modulus of elasticity of concrete E_c was estimated using the ACI 363R-10 Eq 6-1.

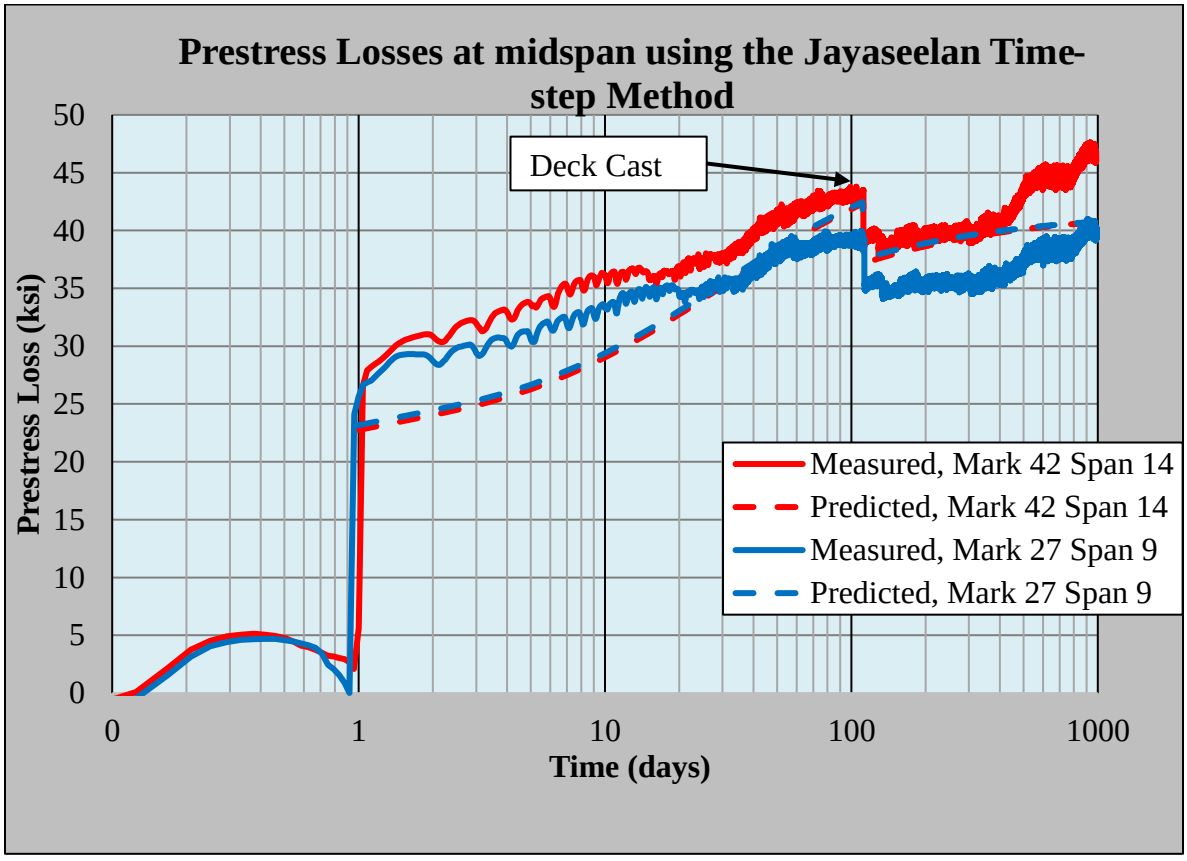

Figure 4.16: Estimated prestress losses using the Jayaseelan Time-step method using the corrected modulus of elasticity of concrete and the measured losses.

Figure 4.16 graphs the measured and computed day-to-day losses using the Jayaseelan Time-Step method for the girders Mark 27 of Span 9 and Mark 42 of Span 14, using the corrected modulus. The Jayaseelan time-step method was utilized to determine to prestress losses in both the girders immediately after release at 24 hours, during storage, at girder installation on the bridge site, just before deck casting, right after deck casting, and after 900 days (approximately 800 days of life in-service). The trend of the loss prediction curve graphed using the Jayaseelan time-step method closely follows the measured losses for both the girders Mark 27 & 42.

5 ksi approximately underestimated the time-dependent losses at early ages (first 10 days) for Mark 27 Span 9 and 7 ksi for Mark 42 Span 14. When the beams were transported to the construction site, both received construction loads that are not accounted for in this model.

After the deck cast, the Jayaseelan Time-Step Method underestimated the losses for Mark 27 Span 9 by 5 ksi until 400 days. However, at 900 days, the measured losses matched the predicted losses for Mark 27 Span 9.

After the deck cast, the Jayaseelan Time-Step Method accurately predicted the losses for Mark 42 Span 14 until 400 days. However, at 900 days, the measured losses were underestimated by approximately 5 ksi, about 3.2% of the total effective prestressing force.

4.7. Conclusions

- Comparing strain data to AASHTO refined, AASHTO Refined overpredicted losses at 110 days for Span 9 by 1.3% and underpredicted losses at 110 days for Span 14 by 8.7%. For losses at 900 days, AASHTO Refined overpredicted losses by 1.5% for Span 9 and underpredicted losses for Span 14 by 9.5%.
- Comparing strain data to AASHTO Approximate, the AASHTO Approximate method overpredicted losses at 900 days in Span 9 by 19% and overpredicted losses in Span 14 by 4.6%.
- Comparing strain data to the PCI Design Handbook method, the PCI Design handbook method overpredicted losses at 110 days in Span 9 by 47% and overpredicted losses in Span 14 by 35%. PCI overpredicted losses at 900 days in Span 9 by 22.4% and overpredicted Span 14 by 19%.
- Comparing strain data to the Modified PCI method, overpredicted losses at 110 days in Span 9 by 45% and overpredicted losses in Span 14 by 35%. This method also overpredicted losses at 900 days in Span 9 by 22.2% and overpredicted losses in Span 14 by 9.5%.
- Comparing strain data to Jayaseelan time step, overpredicted losses at 110 days in Span 9 by 4.5% and underpredicted losses in Span 14 by 11.6%. Jayaseelan time-step underpredicted losses at 900 days in Span 9 by 0.3% and underpredicted losses in Span 14 by 22.6%.
- The comparison of prestress loss prediction methods to losses derived from strain measurements shows that the AASHTO Refined method provides the best reference to accurately predicting prestress losses for prestress girder bridges.

- Analysis between predicted and measured elastic shortening loss shows that current equations significantly overpredict early-age concrete elastic modulus by up to 30%, leading to an underprediction of elastic shortening loss.
- Analysis between predicted losses using a more accurate young modulus using the Jayaseelan time step method and the measured losses shows that the Jayaseelan Time-Step Method can be reliable if we use the correct modulus.

4.8. Recommendations

- The camber of a PC bridge girder is directly tied to the parameter that is best described as the “PRESTRESSED MOMENT” which is the total prestressing force times its eccentricity, i.e., Fp*ep. Therefore, the use of fully tensioned top prestressing strands reduces prestress losses by reducing the eccentricity of the prestressing force. Additionally, other prestressing patterns that raise the center of gravity of the prestressing force (cgs) work in the same manner to reduce prestress losses.
- AASHTO Refined is a reliable method for estimating the prestress loss. However, this model is very complicated, and it can be inaccurate to varying degrees. The results of this research suggest that a simpler equation that provides similar accuracy should be developed to estimate prestress losses.
- The Jayaseelan Time-Step Method is a decent method that helps estimate losses. However, the under-prediction of the elastic shortening at early ages, resulted in underpredicting the losses at early ages.
- The elastic modulus for self-consolidating concrete is usually lower compared to conventional concrete. Overestimating the modulus of elasticity of concrete leads to underestimating the elastic shortening losses at early age.
    - A new equation that provides best accuracy for estimating elastic modulus for self-consolidating concrete should be developed, to better estimate losses.
- The experimental data has shown that the losses can be reduced by including top prestressing strands and incorporating mild steel in the bottom flange of the concrete girder bridge.
    - Prestress girder bridge should include mild steel and top strands to minimize prestress losses.

CHAPTER V

5. INCLUSION OF MILD REINFORCEMENT TO REDUCE AND CONTROL EXCESSIVE CAMBERS

Camber of the Prestressed Concrete bridge beams (PC Beams) of the SH 4 Bridge over the North Canadian River in Canadian County, Oklahoma, is investigated in this study. The bridge has 15 spans. Each span is 100 ft. long. Each span was also designed and built with unique reinforcement details. An instrument-based structural monitoring program was implemented to measure strains and temperatures within hardened concrete. Materials testing was also performed. Camber measurements were taken at several intervals during the fabrication of the PC Beams and during the construction of the SH 4 Bridge and continuing through service. The purpose was to compare how different strand layouts and the inclusion of mild steel reinforcement in the bottom flanges of the girders affected long-term cambers. Furthermore, vibrating wire gauges strain data was used to estimate camber and was compared to the physical measurements.

It is important to accurately predict prestress losses and cambers for prestressed concrete girder bridges. Overestimating prestress losses leads to an increase of number of prestressing strands for any particular girder design the increase of number of prestressing strands in a beam can adversely, affects the bridge serviceability, and durability of the bridge overall.

The over estimation of the prestress losses also results in high cambers in prestressed concrete girder bridges and differential of cambers in consecutive and identical girders. On the other hand, underestimating prestress losses can lead to higher service load tensile stresses in concrete, cracking, and perhaps decreased durability of the pretensioned girder bridge.

Jayaseelan et. Russell (2019) examined the effects on prestress losses and cambers from including:

a) fully tensioned top strands
b) horizontal mild steel reinforcement near the center of gravity of prestressing strands.

For SH 4 bridge in Canadian Co., OK, five different pretensioned girder reinforcement designs were built with variations over the 15 spans. Figure 5.1 shows the five different cross sections and includes the computed eccentricities for the various strand patterns, computes the "prestress moment, $\boldsymbol{M_{pi}}$" which is defined as $\boldsymbol{F_{si} \cdot e}$, and where is defined as the prestressing force prior to strand detensioning, and the includes the area of horizontal mild steel, $\boldsymbol{A_s}$ contained in the bottom flanges. Note that the "alternative" strand design used in Design Details C and D has less eccentricity than Design Details A and B, and therefore smaller Prestressed Moment, $\boldsymbol{M_{pi}}$.

Jayaseelan and Russell (2019) estimated prestress losses for similar Type IV girder designs. In their publication, they compared the estimates of prestress losses made from (1) the PCI Design Handbook method, (2) the PCI Design Handbook method with transformed cross section properties, (3) the 2014 AASHTO LRFD Approximate and (4) Refined methods, and (5) the Jayaseelan Time-step method. Cambers were also predicted using computed curvature with the Jayaseelan Time-Step method. The work performed by Jayaseelan, and Russell concluded that the inclusion of the fully top strands plus the inclusion of mild steel reinforcement reduced cambers by as much as 72%.

However, their work was analytical. In other words, Jayaseelan did not possess experimental data suitable for comparison to their behavioral and computation models. The purpose of this research is to collect experimental camber data to evaluate the findings of the Jayaseelan and Russell analyses. The purpose of this research is also to use the Vibrating wire gauges data to derive the curvature, then use beam mechanics to estimate the girder deflection. This deflection will be compared to the field measurements data.

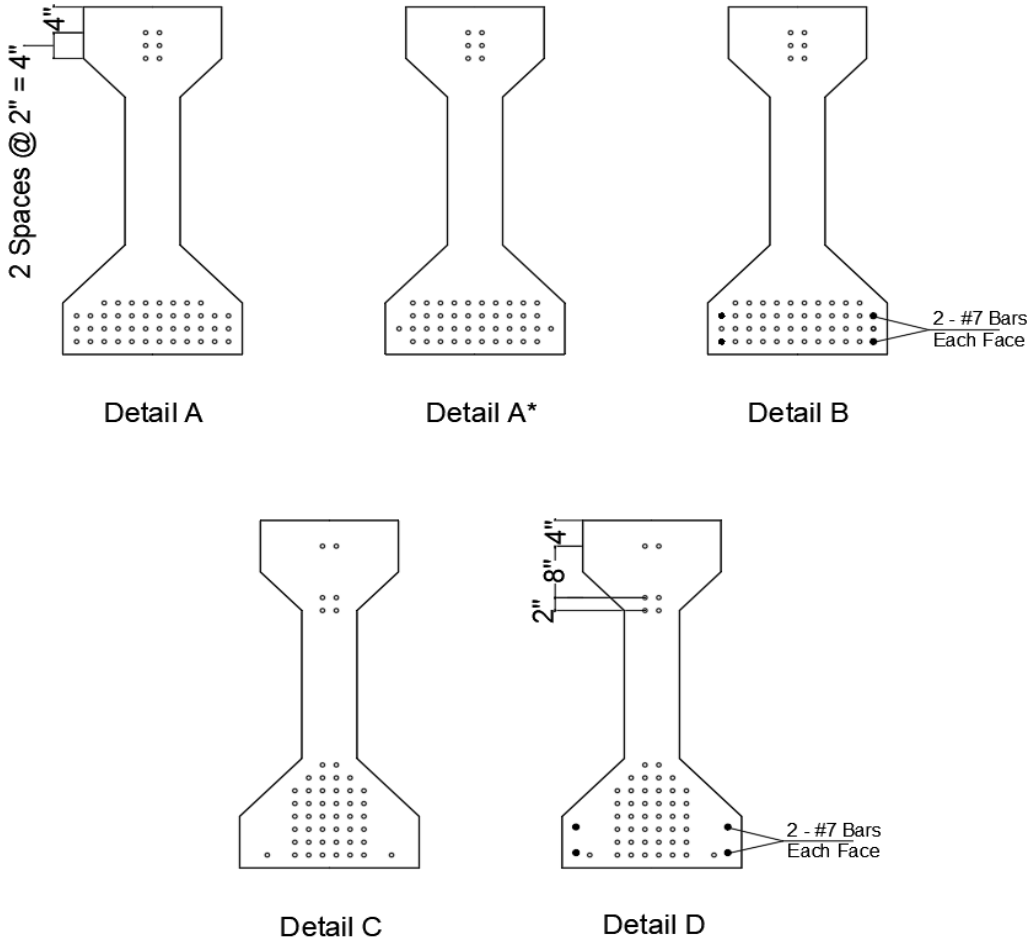

	No. of Strands	e	Fsi*e	Area of Steel
Detail A	50	14.8 in.	32517 kip*in	0.00 in^2
Detail A*	48	14.4 in.	30373 Kip*in	0.00 in^2
Detail B	48	14.4 in.	30373 Kip*in	2.40 in^2
Detail C	50	12.6 in.	27684 Kip*in	0.00 in^2
Detail D	50	12.6 in.	27684 Kip*in	2.40 in^2

Figure 5.1: Detailing of longitudinal reinforcement layout

5.1. Camber Measurements

Camber was measured using an engineering level and a Philadelphia rod, or a graduated tape measure. Elevation measurements were made most commonly at the bottom of the girder. The same methodology was used throughout to ensure consistency of measurement from beam fabrication, transportation, erection, and through bridge construction. Elevation measurements were made at varying stages over the bridge's construction.

Table 5.1 reports the dates when girder cambers were measured. Note that cambers were measured on all 15 spans on each date except for June 11, 2020. At that time, spans 14 and 15 had not yet been erected and the girders for these spans were not yet set on the bearings.

Table 5.1: Dates for Camber Measurements

				Deck Placement			
Beam Mark 27, Span 9 (Det. B)	11-Jun-20	18-Jun-20	29-Jul-20	14-Aug-20	20-Oct-20	26-Oct-21	7-Apr-22
Days since Casting	49	56	97	113	180	551	714
Beam Mark 42, Span 14 (Det. C)	11-Jun-20	18-Jun-20	29-Jul-20	18-Aug-20	20-Oct-20	26-Oct-21	7-Apr-22
Days since Casting	-	51	92	112	175	546	709

Camber was measured from the elevation surveys taken at the bottom of each girder for each individual bridge beam; average cambers was calculated for each span. Average camber measurements by span and date are reported in Table 5.2. Elevations for each girder were measured at both ends and midspan. The average elevation of each end was found and compared to the elevation at midspan to find camber. All camber measurements were taken from under the bridge, except for measurements taken on July 29, 2020, in which cambers were measured from on top of the bridge days before deck casting. Since elevations could not be taken at the center of bearing of the girders, a correction factor of 1.0638 was applied to account for the measurements being taken approximately 18 in. distant from center of bearing.

Camber measurements continued after the placement and hardening of the composite deck slabs. The purpose of the camber measurements after the completion of bridge construction is to continue to glean information regarding the long-term effects of the variations in primary reinforcement details.

5.1.1. Methodology

5.1.2. Results

Tabulated data points for camber measurements are displayed in Table 5.2. The camber data that are reported are the average of the camber measurements taken from the four girders in each span. Span 8 is spanned the main river channel, so it was inaccessible from underneath the bridge. Measurements for Span 8 were taken only on July 29, 2020.

Table 5.2: Average Camber Measurements of Each Span Over Time

Average Camber Measurements of Each Span Over Time							
	Longitudinal Reinforcement	Cambers Measured June 11, 2020	Cambers Measured June 18, 2020	Cambers Measured July 29, 2020	Cambers Measured October 1, 2020	Cambers Measured October 27, 2021	Cambers Measured April 7, 2022
	Case	Camber (in)	Camber (in)	Camber (in)	Camber (in)	Camber (in)	Camber (in)
Span 1	**Case C**	2.55	2.72	2.54	1.31	0.76	0.47
Span 2	**Case C**	2.69	2.76	2.64	0.66	0.62	0.78
Span 3	**Case A**	3.55	3.5	3.66	1.77	1.79	1.85
Span 4	**Case A**	4.21	4.19	4.13	2.1	2.19	2.27
Span 5	**Case C**	3.18	3.42	3.12	0.93	1.02	1.1
Span 6	**Case D**	2.77	2.87	2.77	0.66	0.65	0.66
Span 7	**Case D**	2.82	2.77	2.78	0.79	0.86	0.87
Span 8	**Case B**	(a)	(a)	2.69	(a)	(a)	(a)
Span 9	**Case B**	3.29	3.25	3.36	1.19	1.1	1.23
Span 10	**Case A***	3.46	3.23	3.42	1.28	1.38	1.47
Span 11	**Case C**	3.21	3.06	3.18	0.98	1.23	1.11
Span 12	**Case A**	4.11	4.02	3.95	2.01	2.15	2.19
Span 13	**Case A**	4.14	3.94	4.05	2.15	2.19	2.26
Span 14	**Case C**	(b)	2.85	2.93	0.75	0.91	0.98
Span 15	**Case C**	(b)	3.02	3.27	1	1.11	0.98
Average Camber	**All Cases**	3.33	3.26	3.23	1.25	1.28	1.30

Note:
1: Reported cambers are the average of all four girders in a span.
2: Camber measurements were taken from the bottom of the bridge except for measurements taken on July 29, 2020, in which cambers were measured from the top of the bridge.
3: Camber measurements taken from the bottom of the bridge are multiplied by a correction factor of 1.06 to account for the direct center of bearing not being accessible.
4: Span 8 is inaccessible from under the bridge. Readings were only taken on July 29, 2020, from the top of the bridge prior to deck casting.
5: Girders for spans 14 & 15 had not been placed at the time of measurements on June 11, 2020.

Error! Reference source not found. reports the camber data as averages for the five different Primary Reinforcement Details. The largest cambers are measured from beams reinforced with Detail A. Detail A had the highest prestressed moment, as shown in Figure 3, and no mild

horizontal reinforcement. Detail A* had the second highest measured cambers. It has a smaller prestressed moment than Detail A but had no mild horizontal reinforcement. Detail B matched the prestressing strand pattern of Detail A, but it contains horizontal mild reinforcement. Its measured cambers are less than that of Detail A. Details C and D had the smallest prestressed moment – which results directly from the lowest amount of prestressing eccentricity. Beams made with Details C and D exhibited the lowest measured cambers, and, of the two, Beams made with Detail D containing horizontal reinforcement had less camber than Beams made with Detail C that had no horizontal reinforcement. So, these results directly indicate the following findings:

1. Reduced eccentricity results in reducing camber of prestressed concrete beams, and
2. The inclusion of horizontal mild steel reduces the camber measured in prestressed concrete bridge girders.

These results are consistent with the analytical findings of Jayaseelan and Russell

Table 5.3: Cambers measured on SH 14 Bridge. All Spans.

Primary Reinforcement Detail at Midspan	No. of Spans	Mpi (k-in.)	As (in.^{2})	Cambers Measured June 11, 2020	Cambers Measured June 18, 2020	Cambers Measured July 29, 2020	Cambers Measured October 1, 2020	Cambers Measured October 27, 2021	Cambers Measured April 7, 2022
				Camber (in)	Camber (in)	Camber (in)	Camber (in)	Camber (in)	Camber (in)
				49	**56**	**97**	**180**	**551**	**714**
Detail A	**4**	**32,520**	**0.00**	4.00	3.91	3.95	2.01	2.08	2.14
Detail A*	**1**	**30,370**	**0.00**	3.46	3.23	3.42	1.28	1.38	1.47
Detail B	**1**	**30,370**	**2.40**	3.29	3.25	3.03	1.19	1.10	1.23
Detail C	**6**	**27,680**	**0.00**	2.91	2.97	2.95	0.94	0.94	0.90
Detail D	**2**	**27,680**	**2.40**	2.80	2.82	2.78	0.73	0.76	0.77
All Details				3.27	3.26	3.25	1.26	1.28	1.30

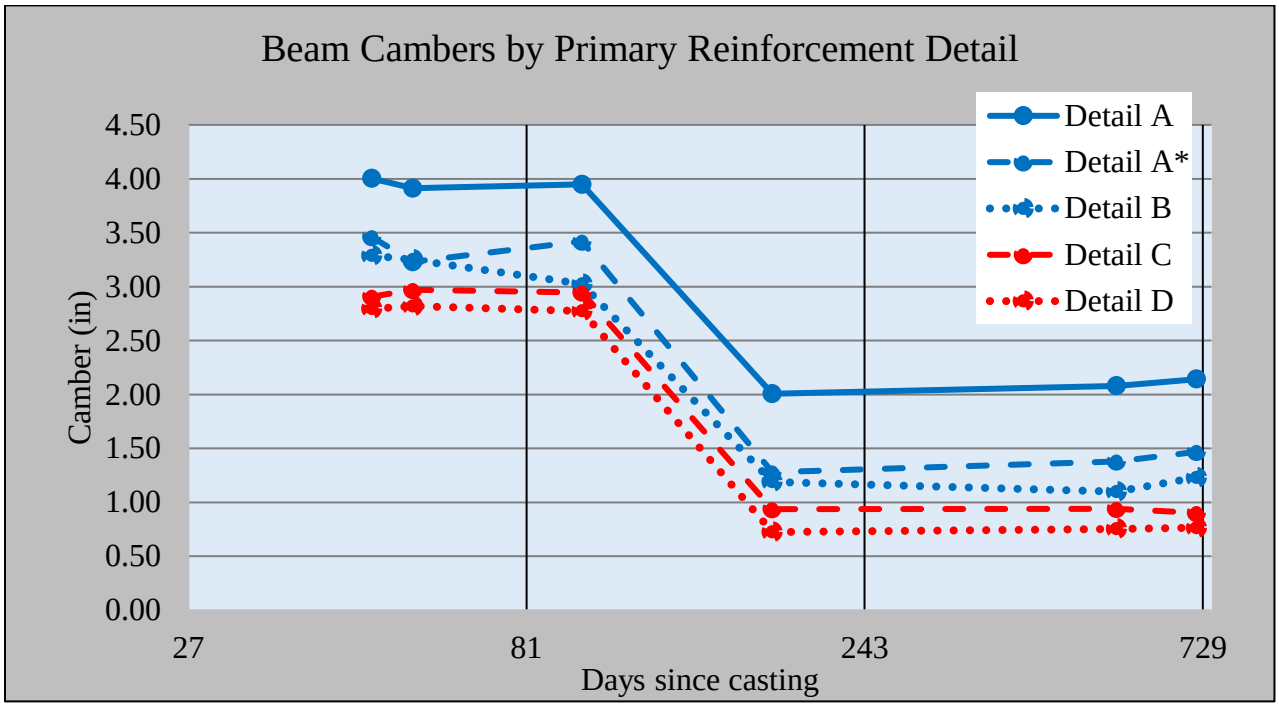

Figure 5.2: Average measured camber by reinforcement layouts. Note that girders were transported to the site approximately 35 days after detensioning.

Figure 5.2 displays data that is reported in **Error! Reference source not found.** and plots the average measured camber for each reinforcement layout at varying dates. The first camber measurements were made soon after the girders were transported and erected at the bridge site. Cambers were not measured using the same methodology while stored in the precast plant. While the precast plant QA/QC personnel measure cambers at the precast plant, the reliability of these measurements are not verified. Note that the figure shows graphically the ranking of Primary Reinforcement Details. The beam cross sections where the prestressing strand arrangement makes a smaller prestressed moment experiences smaller cambers than others. Similarly, when the primary reinforcement design includes mild reinforcement, camber is reduced when compared to cross sections that do not contain horizontal mild steel.

5.1.3. Discussion

Measurements taken before deck casting show that girders that features the Detail D design experienced the least amount of camber. This shows that combining the use of a distributed strand pattern and mild steel likely improved constructability of the deck in these spans, as haunch and deck thickness was likely more consistent along the length of these spans due to them being more level during deck construction. Deck casting occurred for all spans in August of 2020. Measurements taken afterward in October show an average decrease in camber of 2.02 in. (range of 1.23 in. to 2.27 in.). Comparing the decrease in camber immediately after deck casting, on average, girders falling under Details: A, A*, B, C, and D reinforcement layouts experienced a downward deflection of 1.94 in., 2.14 in., 1.84 in., 2.17 in., and 2.05 in, respectively. The data shows that the deflection caused by the dead load of the deck immediately after casting was not significantly different between the reinforcement layouts.

Table 5.4 displays the difference in cambers between traditional strand patterns with no mild steel reinforcement (Detail A) to each of the other longitudinal reinforcement variations. Long-term camber was reduced by 0.67 in (31%) when the number of prestressing strands were reduced by 2 (Detail A*). Including mild steel in the bottom flange (Detail B) the long-term camber was reduced by 0.91 in (43%) was used. Using a distributed strand pattern (Detail C) reduced long-term camber by 1.15 in. (54%). Combining the use of a distributed strand pattern and mild steel reinforcement (Detail D) reduced long term camber by 1.38 in. (64%).

Table 5.5 displays the difference in cambers between traditional strand patterns with no mild steel reinforcement (Detail A*). Long-term camber was reduced by 0.24 in (16%) when the flange contained mild steel reinforcement in the bottom flange. Using a distributed strand pattern (Detail C) reduced long-term camber by 0.48 in. (33%). Combining the use of a distributed strand pattern

and mild steel reinforcement (Detail D) reduced long term camber by 0.71 in. (48%). Estimation of Camber.

The data shows that girders containing distributed strand patterns (Detail C & D) experienced the least amount of camber during all stages of bridge construction and service. Detail D girders experienced significantly less camber prior to deck casting when compared to Detail C girders, but no appreciable difference between both Details was observed after the bridge had been in service for over a year.

Table 5.4: Effects of distributed strand patterns and mild steel on camber (Measured Camber)

Effects of distributed strand patterns and mild steel on camber.									
		Change in Camber (in) From Case A				% Percent Change			
Date	Days After Girder Placement	Traditional w/o Mild Steel	Traditional w/ Mild Steel	Distributed w/o Mild Steel	Distributed , w/ mild steel	Traditional w/o Mild Steel	Traditional w/ Mild Steel	Distributed w/o Mild Steel	Distributed , w/ mild steel
		Case A*	Case B	Case C	Case D	Case A*	Case B	Case C	Case D
11-Jun-20	1	-0.54	-0.71	-1.10	-1.21	-0.14	-0.18	-0.27	-30%
18-Jun-20	7	-0.68	-0.66	-0.89	-1.09	-0.17	-0.17	-0.23	-28%
29-Jul-20	48	-0.53	-0.92	-0.92	-1.17	-0.13	-0.23	-0.23	-30%
1-Oct-20	112	-0.73	-0.82	-1.14	-1.28	-0.36	-0.41	-0.57	-64%
26-Oct-21	502	-0.70	-0.98	-1.10	-1.33	-0.34	-0.47	-0.53	-64%
7-Apr-22	665	-0.67	-0.91	-1.15	-1.38	**-0.31**	**-0.43**	**-0.54**	**-64%**
Note: 1: Negative values indicate the camber was reduced when corresponding reinforcement layout was used. 2: Percent Change = (Case "X" - Case A)/Case A * 100%									

Table 5.5: Effects of distributed strand patterns and mild steel on camber

Effects of distributed strand patterns and mild steel on camber.							
		Change in Camber from Case A*			% Percent Change		
Date	Days After Girder Placement	Traditional w/ Mild Steel	Distributed w/o Mild Steel	Distributed, w/ Mild steel	Traditional w/ Mild Steel	Distributed w/o Mild Steel	Distributed, w/ Mild steel
		Case B	Case C	Case D	Case B	Case C	Case D
11-Jun-20	1	-0.17	-0.55	-0.67	-0.05	-0.16	-0.19
18-Jun-20	7	0.02	-0.21	-0.41	0.01	-0.06	-0.13
29-Jul-20	48	-0.40	-0.39	-0.65	-0.12	-0.11	-0.19
1-Oct-20	112	-0.09	-0.42	-0.56	-0.07	-0.33	-0.43
26-Oct-21	502	-0.28	-0.40	-0.63	-0.20	-0.29	-0.45
7-Apr-22	665	-0.24	-0.48	-0.71	-0.16	-0.33	-0.48

Note:
1: Negative values indicate the camber was reduced when corresponding reinforcement layout was used.
2: Percent Change = (Case "X" - Case A)/Case A * 100%

5.2. Camber Prediction Using the Jayaseelan Time-Step Method using the Design Modulus.

The Jayaseelan time-step method computed beam camber directly from cross section concrete strain curvatures. Strain and camber were calculated daily. Camber calculations used end and midspan curvatures. Strain computations include gravity. The concrete strain computations considered material property changes over time. The final deflection included creep strain camber after slab placement.

The Modulus of Elasticity that was used in these equations, was the one recommended by Jayaseelan and Russell (2019).

$$E_c = 33w^{1.5}\left(f'_c\right)^{0.5} \quad \text{(ACI 318-14 Eq.19.2.2.1. a)} \qquad \textbf{Eq. 5.1}$$

5.2.1. Results:

The tabulated camber results obtained through the application of the Jayaseelan time-step method are presented in Table 5.6. The results of these measurements are presented in the form of a graphical representation in Figure 5.3. Cambers were predicted beginning with the first date on which physical measurements were obtained, which was June 11th, 2020.

Table 5.6: Estimated Camber using the Jayaseelan Time-Step Method using the ACI Modulus equation.

Jayaseelan Time-Step Method						
Date	Days after Detensioning	Predicted Camber (in)				
		Detail A	Detail A*	Detail B	Detail C	Detail D
11-Jun-20	40	3.5	3.27	3.14	2.92	2.78
18-Jun-20	47	3.53	3.3	3.17	2.95	2.8
29-Jul-20	88	3.63	3.4	3.26	3.04	2.88
1-Oct-20	152	1.78	1.53	1.38	1.12	0.96
26-Oct-21	542	1.75	1.49	1.33	1.08	0.90
7-Apr-22	705	1.75	1.49	1.33	1.07	0.89

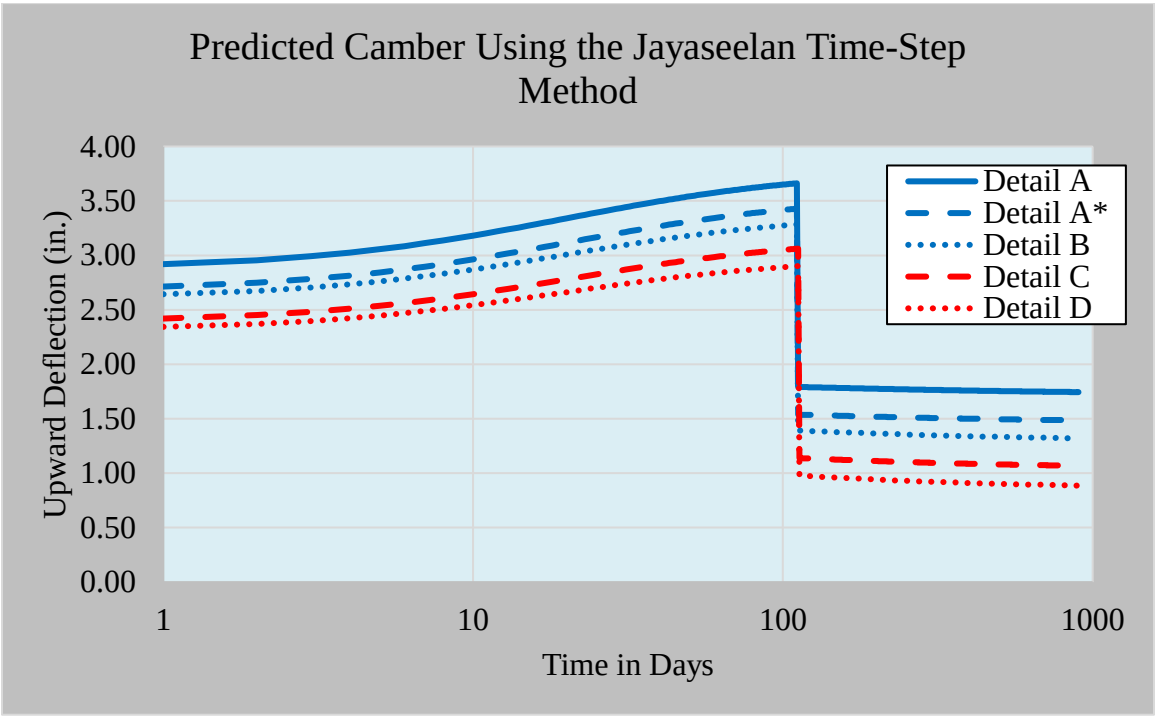

Figure 5.3: Predicted camber using the Jayaseelan time step method using the design modulus.

5.2.2. Discussion:

Table 5.7: Effects of distributed strand patterns and mild steel on camber (Using the Jayaseelan Time Step Method with the design Modulus of elasticity)/

Effects of distributed strand patterns and mild steel on camber.									
Change in Camber (in) From Case A						% Percent Change			
Date	Days after Detensioning	Traditional w/o Mild Steel	Traditional w/ Mild Steel	Distributed w/o Mild Steel	Distributed, w/ mild steel	Traditional w/o Mild Steel	Traditional w/ Mild Steel	Distributed w/o Mild Steel	Distributed, w/ mild steel
		Case A*	Case B	Case C	Case D	Case A*	Case B	Case C	Case D
11-Jun-20	40	-0.23	-0.36	-0.58	-0.72	-7%	-10%	-17%	-21%
18-Jun-20	47	-0.23	-0.36	-0.58	-0.73	-7%	-10%	-16%	-21%
29-Jul-20	88	-0.23	-0.37	-0.59	-0.75	-6%	-10%	-16%	-21%
1-Oct-20	152	-0.25	-0.40	-0.66	-0.82	-14%	-22%	-37%	-46%
26-Oct-21	542	-0.26	-0.42	-0.67	-0.85	-15%	-24%	-38%	-49%
7-Apr-22	705	-0.26	-0.42	-0.68	-0.86	-15%	-24%	-39%	-49%

Note:

1: Negative values indicate the camber was reduced when corresponding reinforcement layout was used.

2: Percent Change = (Case "X" - Case A)/Case A * 100%

Table 5.7 displays the difference in cambers between traditional strand patterns with no mild steel reinforcement (Detail A) to each of the other longitudinal reinforcement variations. Long-term camber was reduced by 0.26 in when the number of prestressing strands were reduced by 2 (Detail A*). Including mild steel in the bottom flange (Detail B) the long-term camber was reduced by 0.42 in was used. Using a distributed strand pattern (Detail C) reduced long-term camber by 0.68 in. Combining the use of a distributed strand pattern and mild steel reinforcement (Detail D) reduced long term camber by 0.86 in.

5.3. Camber Prediction Using the Jayaseelan Time-Step Method using the Modified Modulus.

In the previous chapter, we discovered that the elastic modulus for Mark 27 Span 9 and Mark 42 Span 14 was overestimated. Using the following equation, we have performed the calculations for the Jayaseelan Time-Step method.

$$E_c = 40000\sqrt{f'_c} + 1 \times 10^6 psi \text{ (ACI 363R10 Eq.6-1)} \qquad \textbf{Eq. 5.2}$$

In this equation, however, we have used the measured modulus at release rather than the predicted modulus.

5.3.1. Results:

The tabulated camber results obtained through the application of the Jayaseelan time-step method with the modified modulus are presented in Table 5.6. The results of these measurements are presented in the form of a graphical representation in Figure 5.3.

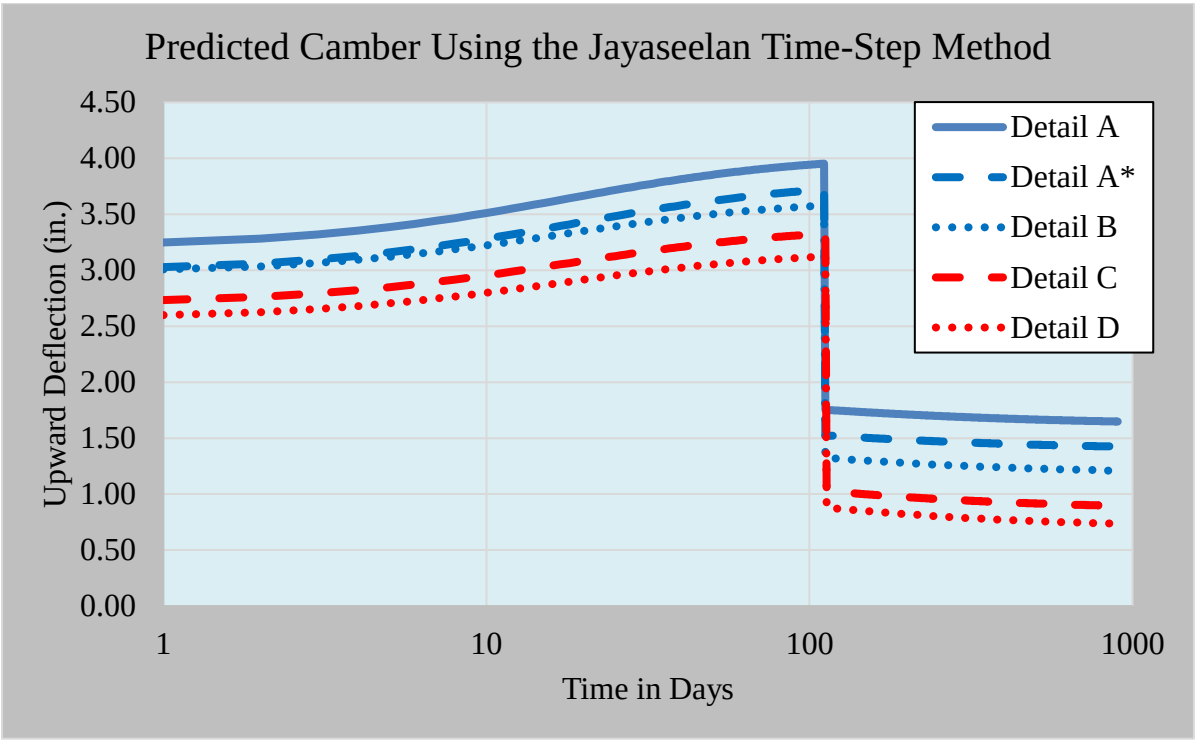

Figure 5.4: Predicted camber using the Jayaseelan time step method using the modified modulus of elasticity.

Table 5.8: Estimated Camber using the Jayaseelan Time-Step Method using the modified modulus elasticity.

Jayaseelan Time-Step Method						
Date	**Days after Detensioning**	**Predicted Camber (in)**				
		Detail A	**Detail A***	**Detail B**	**Detail C**	**Detail D**
11-Jun-20	**40**	3.81	3.58	3.47	3.21	3.02
18-Jun-20	**47**	3.84	3.61	3.49	3.23	3.04
29-Jul-20	**88**	3.93	3.70	3.56	3.31	3.11
1-Oct-20	**152**	1.73	1.50	1.30	1.00	0.85
26-Oct-21	**542**	1.65	1.43	1.21	0.90	0.74
7-Apr-22	**705**	1.66	1.43	1.22	0.90	0.74

Note:

The Elastic Modulus at Release of the girders was set to 4000 ksi for Detail A, Detail A* and Detail D.

The Elastic Modulus at Release of the girders was set to 3846 ksi for Detail B and 3914 ksi for Detail C.

At each time increment Eq 5.2 was used to predict the elastic modulus of the girders.

5.3.2. Discussion:

Table 5.9: Effects of distributed strand patterns and mild steel on camber (Using the Jayaseelan Time Step Method with Modified Modulus of Elasticity of the Girders).

Effects of distributed strand patterns and mild steel on camber.									
Change in Camber (in) From Case A						% Percent Change			
Date	Days after Detensioning	Traditional w/o Mild Steel	Traditional w/ Mild Steel	Distributed w/o Mild Steel	Distributed, w/ mild steel	Traditional w/o Mild Steel	Traditional w/ Mild Steel	Distributed w/o Mild Steel	Distributed, w/ mild steel
		Case A*	Case B	Case C	Case D	Case A*	Case B	Case C	Case D
11-Jun-20	40	-0.23	-0.34	-0.61	-0.79	-6%	-9%	-16%	-21%
18-Jun-20	47	-0.23	-0.35	-0.61	-0.80	-6%	-9%	-16%	-21%
29-Jul-20	88	-0.23	-0.37	-0.62	-0.82	-6%	-9%	-16%	-21%
1-Oct-20	152	-0.23	-0.43	-0.73	-0.88	-13%	-25%	-42%	-51%
26-Oct-21	542	-0.22	-0.44	-0.75	-0.91	-14%	-27%	-45%	-55%
7-Apr-22	705	-0.22	-0.44	-0.75	-0.91	-14%	-27%	-45%	-55%

Note:

1: Negative values indicate the camber was reduced when corresponding reinforcement layout was used.

2: Percent Change = (Case "X" - Case A)/Case A * 100%

Table 5.7 displays the difference in cambers between traditional strand patterns with no mild steel reinforcement (Detail A) to each of the other longitudinal reinforcement variations. Long-term camber was reduced by 0.22 in when the number of prestressing strands were reduced by 2 (Detail A*). Including mild steel in the bottom flange (Detail B) the long-term camber was reduced by 0.44 in was used. Using a distributed strand pattern (Detail C) reduced long-term camber by 0.75 in. Combining the use of a distributed strand pattern and mild steel reinforcement (Detail D) reduced long term camber by 0.91 in.

5.4. Comparison of Measured Camber and Predicted Camber vs Derived Camber using Measured Curvatures.

5.4.1. Methodology:

Vibrating Wire Strain Gages (VWSG) were installed at midspan into two of the 60 pretensioned concrete beams that were made part of the SH 4 bridge. These two beams were Beam Mark 27, located in Span 9, and Beam Mark 42, located in Span 14. These two beams contained reinforcement details that match the PC beams for that span. So, Beam Mark 27 was designed with Detail B and Beam Mark 42 was designed with Detail C. Beam Mark 27 contained a higher prestressed moment but included mild steel whereas Beam Mark 42 contained the smaller prestressed moment but did not include mild steel. The VWSG's were located in positions within the midspan of the beams to measure strains through the depth of the cross section and are useful to measure the curvature of the cross section. For the camber calculation, the strain readings were reset approximately 23 hours since beam fabrication.

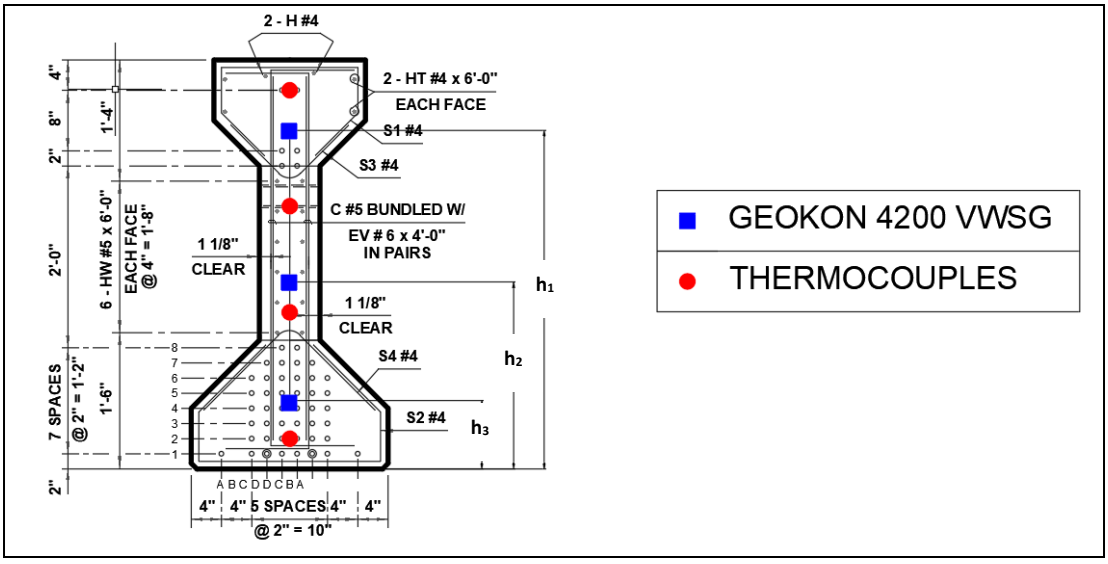

Figure 5.5: Location of the Strain Gauges across the cross section in a PC Beam

Table 5.10: Location of the vibrating wire gauges at midspan for both Mark 27, Span 9 and Mark 42, Span 14

Location of the Vibrating Wire Gauges from Bottom Flange.		
	Mark 27, Span 9	Mark 42, Span 14
h_1	44.7 in.	44.7 in.
h_2	24.7 in.	24.7 in.
h_3	05.5 in.	08.0 in.
Note: The total height of the girder is 54 in. h_1: location of the vibrating wire gauge in the top flange from bottom flange. h_2: location of the vibrating wire gauge in the web. (Near the CGC). h_3: location of the vibrating wire gauge in the bottom flange. (Near the CGS).		

The curvature was determined using all three stain gauges for each beam in the analysis. The initial calculation for the curvature was done between the top gauge and the bottom gauge. A measurement between the top gauge and the center gauge was used to determine the second curvature. Calculations were done with the center and bottom gage to determine the third curvature. After that, the curvature utilized in the camber calculation was the average of the previous three curvatures. However, the curvature that runs from the top to the bottom was given double the weight in this average.

Camber calculations used measured midspan curvatures. The strain measurements include gravity. Before the deck cast, the measured curvature was assumed to be uniform across all the beam lengths. Therefore, the calculation of camber before the deck cast was conducted as follows:

$$\Delta\,(t) = \emptyset_1(t)\frac{L^2}{8} \qquad \textbf{Eq. 5.3}$$

Where:

$\Delta\,(t)$: Calculated Camber from curvature measurements.

$\emptyset_1(t)$: Measured curvature at time t.

L: Span Length. (98.67 ft.)

After the deck cast, the girder will receive a dead load. Therefore, the calculation of camber will become as follow:

$$\Delta\,(t) = [\emptyset_1(t) + \emptyset_{DC}]\frac{L^2}{8} - \frac{5}{48}L^2\emptyset_{DC} \qquad \textbf{Eq. 5.4}$$

Where:

$\Delta\,(t)$: Calculated Camber from curvature measurements.

$\emptyset_1(t)$: Measured curvature at time t.

$\emptyset_{DC}$: Measured change of curvature due to the deck cast. (11.7 x10^{-6} rad/in for Mark 27 Span 9, and 9.25 x 10^{-6} rad/in. for Mark 42 Span 14).

L: Span Length. (98.67 ft.)

5.4.2. Results and Discussion:

Table 5.11 reports the strains measured at top, middle and bottom of the midspan for these two beams. Also reported in Table 4 is the resulting calculation for beam curvature at midspan. The curvature can then be used to compute the beam camber. In this manner, the research shows that the Structural Monitoring system can be used to directly measure camber through the early life of the Prestressed concrete bridge beam. So, Table 5.11 reports the measured strains, the curvature computed from the measured strains and finally, the beam camber that is computed directly from beam curvature.

Table 5.11: Calculation of Camber using Vibrating Wire Gauge Data

	Beam Casting	Prestressed Release	Hauling & Erection				Deck Placement			
Beam Mark 27, Span 9 (Det. B)	23-Apr-20	24-Apr-20	26-May-20	11-Jun-20	18-Jun-20	29-Jul-20	14-Aug-20	20-Oct-20	26-Oct-21	7-Apr-22
Days since Casting	0	1	33	49	56	97	113	180	551	714
Top Strain x 10^{-6}	0	-416	-758	-809	-770	-935	-1189	-1508	-1520	-1610
Middle Strain x 10^{-6}	0	-712	-1222	-1253	-1193	-1280	-1133	-1498	-1511	-1606
Bottom Strain x 10^{-6}	0	-920	-1591	-1629	-1572	-1653	-1701	-1592	-1600	-1361
Average Curvature	*	-12.8 E-06	-21.2 E-06	-20.9 E-06	-20.4 E-06	-18.3 E-06	-05.7 E-06	-02.2 E-06	-02.1 E-06	-02.3 E-06
Computed Camber	*	2.25	3.72	3.66	3.58	3.21	1.35	0.72	0.71	0.75
Beam Mark 42, Span 14 (Det. C)	28-Apr-20	29-Apr-20	1-Jun-20	11-Jun-20	18-Jun-20	29-Jul-20	18-Aug-20	20-Oct-20	26-Oct-21	7-Apr-22
Days since Casting	0	1	34	44	51	92	112	175	546	709
Top Strain x 10^{-6}	0	-512	-820	-876	-871	-1010	-1252	-1415	-1542	-1633
Middle Strain x 10^{-6}	0	-783	-1245	-1310	-1284	-1398	-1394	-1592	-1484	-1705
Bottom Strain x 10^{-6}	0	-932	-1522	-1599	-1571	-1668	-1466	-1624	-1585	-1849
Average Curvature (rad/in.)	*	-11.3 E-06	-19.0 E -6	-19.6 E-06	-19.3 E-06	-17.8 E-06	-05.8 E-06	-03.0 E-06	-05.6E-06	-6.0 E-06
Computed Camber (in.)	*	1.99	3.33	3.43	3.39	3.13	1.28	0.8	1.25	1.32

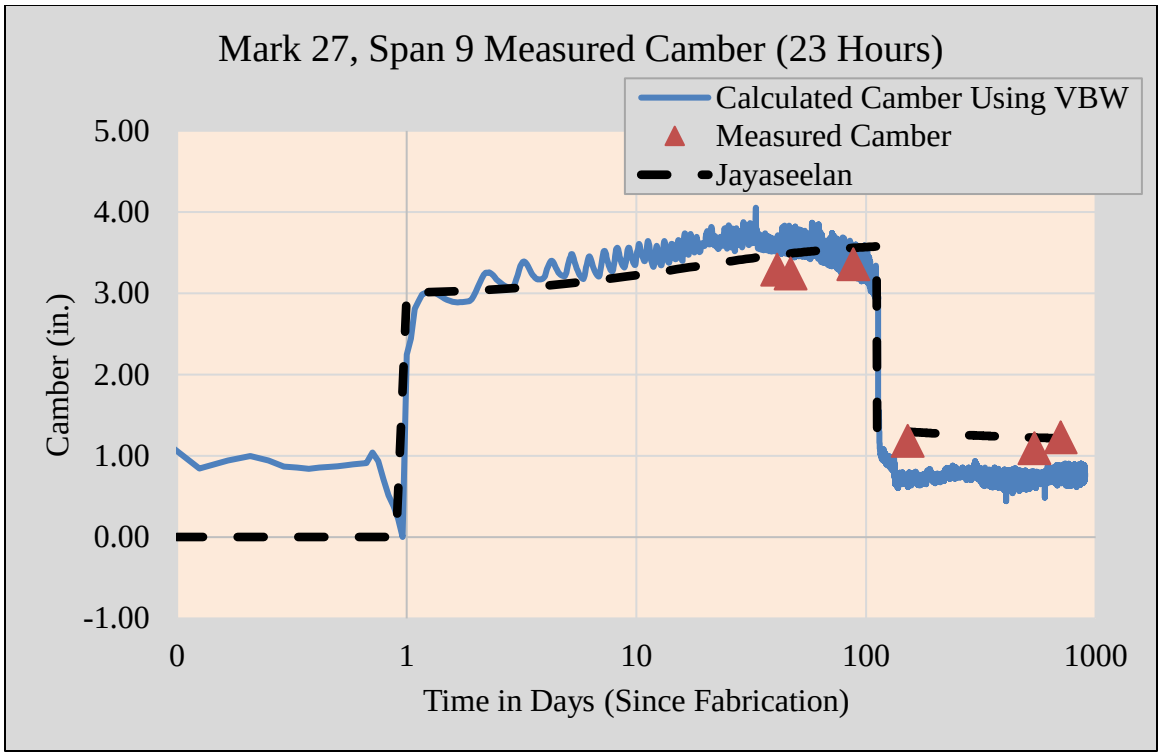

Figure 5.6: Mark 27, Span 9 measured derived camber from strain and measured camber on site.

Figure 5.6 charts the measured camber, the calculated camber derived from the vibrating wire gauges, and the curvature predicted using the Jayaseelan Time-Step Method for Mark 27, Span 9. This chart demonstrates that the camber can be accurately predicted using the Jayaseelan Time-Step Method using the modified modulus of elasticity. Furthermore, the measured camber using the vibrating wire gauges accurately calculates the camber before the deck cast. However, the calculated camber using vibrating wire gages under-estimated camber after the deck cast. This is probably because the top flange has overseen more compression due to cracks at the midspan.

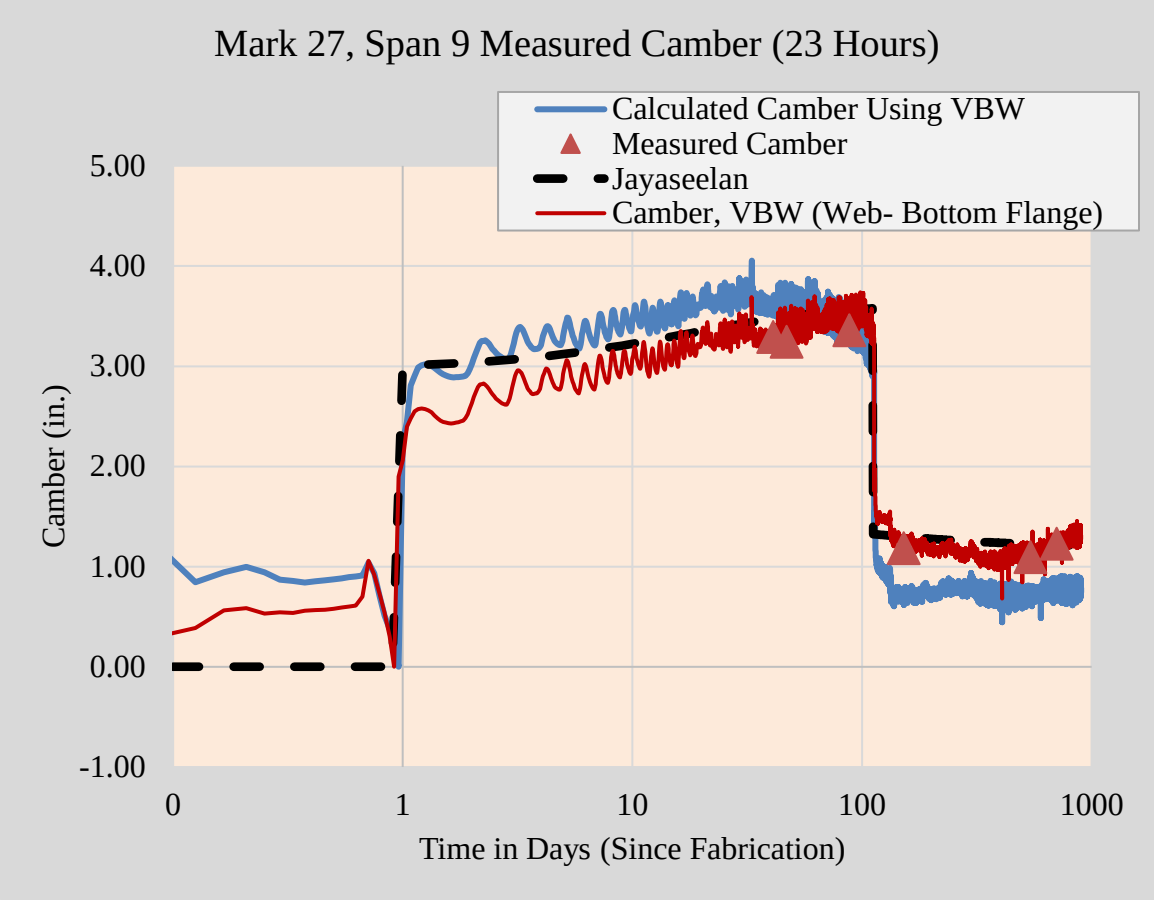

Figure 5.7: Mark 27, Span 9 measured derived camber from strain and measured camber on site.

Figure 5.7 charts the measured camber, the calculated camber derived from the vibrating wire gauges, and the curvature predicted using the Jayaseelan Time-Step Method for Mark 27, Span 9. The figure also charts the camber using the curvature calculated between the center and bottom gauge. This method shows that the camber calculated with the web and bottom gauge curvature follows better than the measured camber during construction and deck cast. This can be explained due to some residual stress in the top flange that occurred during beam fabrication and existence of some cracks in the cross section. However, this is beyond the scope of this research.

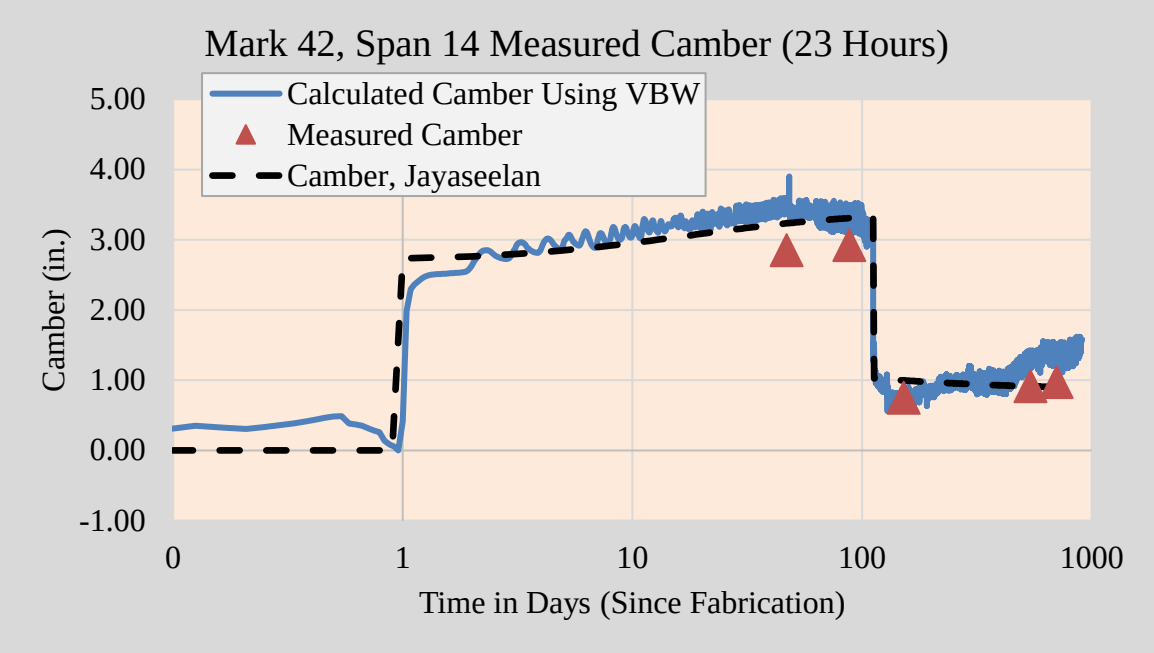

Figure 5.8: Mark 42, Span 14 measured derived camber from strain and measured camber on site.

Figure 5.8 charts the measured camber, the calculated camber derived from the vibrating wire gauges, and the curvature predicted using the Jayaseelan Time-Step Method for Mark 42, Span 14. This chart demonstrates that the camber can be accurately predicted using the Jayaseelan Time-Step Method using the modified modulus of elasticity. Furthermore, the measured camber using the vibrating wire gauges accurately calculates the camber before the deck cast.

The findings from this indicate that the strain readings provide a measurement of camber that is in a range of hundred percent accurate; however, they can be an extremely helpful instrument for estimating the camber that will be present in bridges over the long term.

5.5. Conclusions

1. By reducing the number of prestressing strands from 50 (Case A) to 48 strands (Case A*), the long-term camber was reduced by 0.67 in. (31%).
2. The inclusion of mild steel reinforcement in the bottom flange (Case B) reduced the long-term camber by around 0.24 in. (16%), compared to Case A*.
3. The distributed strand pattern (Case C) significantly reduced the long-term camber by approximately 0.48 in. (33%) from the Case A*.
4. By combining mild steel reinforcement in the bottom flange and employing a distributed strand pattern (Case D), the long-term camber was reduced by approximately 0.71 in. (48%) compared to Case A.
5. The inclusion of mild steel reinforcement in the bottom flange (Case B) reduced the long-term camber by around 0.76 in. (38%), compared to Case A.
6. The distributed strand pattern (Case C) significantly reduced the long-term camber by approximately 1.1 in. (54%) from the Case A.
7. By combining mild steel reinforcement in the bottom flange and employing a distributed strand pattern (Case D), the long-term camber was reduced by approximately 1.2 in. (62%) compared to Case A.
8. The inclusion of mild steel reinforcement in the bottom flange (Case D) reduced the long-term camber by around 0.278 in. (27%), compared to Case C.
9. The inclusion of mild steel only, reduced long term camber by a maximum of 27%.
10. Using distributed strand pattern reduced long term camber by a maximum of 54%.
11. By combining mild steel reinforcement in the bottom flange and employing a distributed strand pattern reduced long term camber by 62%.

- The systems enable the direct computation of P.C. Bridge Beam cambers during fabrication, storage, transportation, erection, bridge construction, and throughout life in-service; these computations are roughly correlated with direct physical measurements of

camber This can be a valuable tool in assessing performance of a bridge and should be utilized in future structural monitoring programs.

- From this, it is suggested to implement mild steel reinforcing into the bottom flanges of prestressed concrete girders or/and use a distributed strand pattern in the design of pretensioned girder bridges. Using this recommendation will significantly decrease camber without significantly increasing fabrication cost or time.

5.6. Recommendations

- Implementing mild steel reinforcing into the bottom flanges of prestressed concrete girders or using a distributed strand pattern in the design of pretensioned girder bridges is recommended. This will significantly decrease camber and slightly decrease prestress losses without significantly increasing fabrication cost or time. Combining both mild reinforcing and a distributed strand pattern further reduced camber and is recommended if viable.
    - Including 2.4 in^2 of mild reinforcement can significantly reduce camber by up to 38%.
    - Limiting prestress moment by using a distributed strand pattern can limit camber by up to 54%.
    - Combining both mild reinforcement and distributed strand patterns can limit camber by up to 62%.

- The systems enable the direct computation of PC Bridge Beam cambers during fabrication, storage, transportation, erection, bridge construction and throughout life in-service. The derived Camber correlates with the field measured Camber before deck cast for both girders. (Mark 27, Span 9 and Mark 42, Span 14). However, after the deck cast, the derived camber from strain data was off by 0.41 in. from the physical measured data.
    - More prestressed girder should be instrumented.

CHAPTER VI

6. EVALUATION OF MEASURED DISTRIBUTION FACTORS THROUGH LOAD TESTING & EVALUATION OF THE EFFECTIVENESS OF THE SECONDARY STIFFENING ELEMENTS IN DFs

The State Highway 4 Bridge across the North Canadian River was subjected to static load testing and moving load testing to determine the live load distribution factors of the girders and the bridge's dynamic features. The study assessed the accuracy of distribution factor (DF) approaches and determined if overestimating DFs for external girders leads to incorrect quantities of prestressing reinforcement. Excessive reinforcing can lead to an increase in camber and prestress losses, as well as have a negative effect on end region cracking and the constructability of the bridge. A comparison was made between the research findings and the analytical methodologies prescribed by AASHTO codes.

The State High 4 over the Canadian river was instrumented with accelerometers and LVDTs at strategic locations. For different dynamic tests, the spans' responses were measured with accelerometers and LVDT. The purpose was to measure the bridge's dynamic properties. In addition, a finite element model was developed in order to duplicate the load test and evaluate the effectiveness of the parapets and diaphragms in dispersing live load.

6.1 Introduction

It is of the utmost necessity to accurately evaluate how bridges behave when subjected to heavy traffic loads. At the same time, it is a well-known fact that there are gaps in determining the traffic loads that a bridge must be able to handle during its anticipated lifetime.

Bridge live load is considered one of the most questionable simplifications. The overestimation of the loads on prestress girders can lead to excessive reinforcement. As a consequence, the excessive reinforcements can cause an increase in camber and prestress losses and negatively affect end region cracking and the constructability of the bridge. This will affect the durability of the bridge in general.

Therefore, accurately predicting the live loads for design and evaluation is very helpful for designing reliable and durable bridge structures. This study investigates two usually overestimated parameters, the distribution load factors for bridges and the dynamic load allowance.

Despite their age and current state, existing bridges have considerable strength reserves, according to the majority of field tests. Diverse parameters may account for these variances, which may be attributable to field parameters that are not considered during the design or evaluation of a bridge's strength.

Field load measurements reveal that, in many instances, the recorded live load stresses are significantly less than those predicted by analytical approaches, particularly for prestressed concrete bridges (Cai & Shahawy, 2003). In addition, test results suggest that measured load distribution factors are typically smaller than those predicted by design codes.

Live Load, and Distribution Load Factors, are simplified design methods. The purpose of the use of DFs is to simplify the calculation for engineers. The current design methods were developed for bridges with varying span lengths, girder spacing, and stiffness.

This research aims to investigate the effectiveness of the inclusion of secondary stiffening elements and the diaphragm on live load distribution for external girders. Additionally, this research aims to obtain the dynamic load allowance of the bridge for both spans by analytical and experimental methods and compare and evaluate the different design methods; however, this is beyond the scope of this research.

6.2 Load Test Program

The work performed was on the bridge located on State Highway 4 over the North Canadian River near Yukon, Oklahoma. The bridge has 15 100-foot spans. Each span is 99.67 feet long and 42.2 wide. Corselab in Oklahoma City precast all Type IV Prestressed girders. 8-inch concrete deck. On Span 9 and 14, static load tests were conducted by placing loaded trucks on the spans in certain arrangements and specific ways, measuring beam deflections at midspan, and recording strains during the load testing. The same vehicles used for the static load tests were also used for the moving load tests.

The load testing was carried out using two highway maintenance vehicles loaded with gravel. Figure 6.10, Figure 6.11, and Figure 6.11 show photographs of the trucks. Figure 6.1 depicts a schematic of axle spacings. The gravity vehicle weight (GVW) of the two trucks differed, and the individual axle weights were not specified. Truck 1 had a GVW of 45,000 lb. whereas Truck 2 had a GVW of 50,000 lb. During the load tests, just two trucks were used. The geometry of both vehicles was identical. Each vehicle had three axles, one in the front and two in the back. The wheel distance between the front tires was 6 feet. The separation from the front axle to the first rear axle was 14 feet. The distance between the first and second rear axles was 4.5 ft. Due to the lack of truck axle weights, we presumed that 20% of the truckload was applied to the front axle of the trucks, with the remaining 80% shared evenly between the two rear axles, as shown in Table 6.1.

Table 6.1: Assumed Truck Axle Weights

Presumed Truck Axle Weights		
	Truck 1	**Truck 2**
Total Weight (kip)	**45.0**	**50.3**
Front Axle weight (kip)	**9.0**	**10.1**
1st Rear Axle Weight (kip)	**18.0**	**20.1**
2nd Rear Axle Weight (kip)	**18.0**	**20.1**

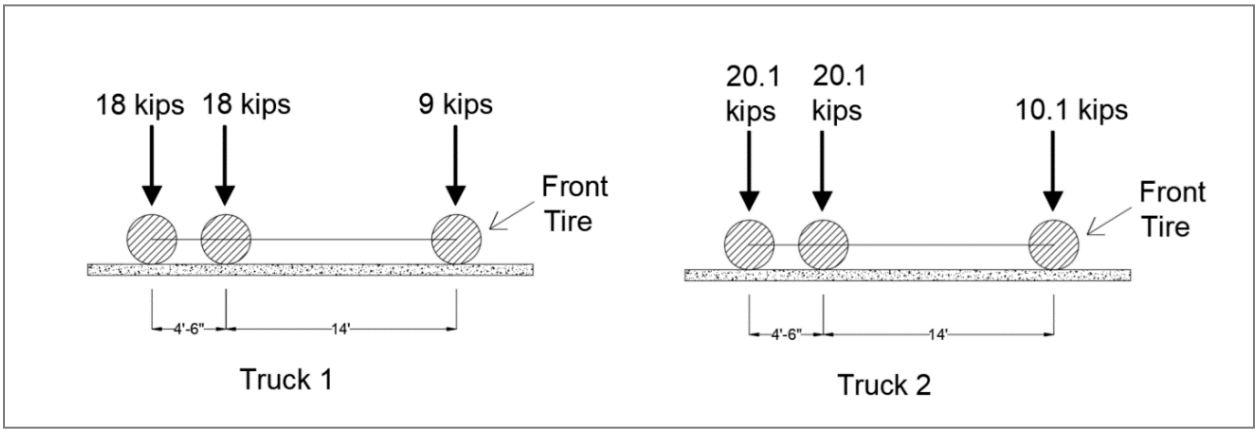

Figure 6.1: Assumed axle weights of each truck.

Instrumentation for the load test consisted of:

- One (1) LVDT placed at the midspan of each girder to measure deflection (total of 4 LVDTs per span).
- One (1) triaxial accelerometer placed on the Westernmost exterior girder bottom flange to measure acceleration at each span.
- One (1) triaxial accelerometer placed on the Westernmost interior girder bottom flange to measure acceleration of each span.
- One (1) triaxial accelerometer was placed on the bottom side of the deck at the span's midspan and mid-length between the exterior and interior girders.

The sample rate for accelerometers and LVDTs was set to 200 Hz. Details and photographs of the instrumentation plan are shown in Figure 6.2, Figure 6.3, Figure 6.4, and Figure 6.5

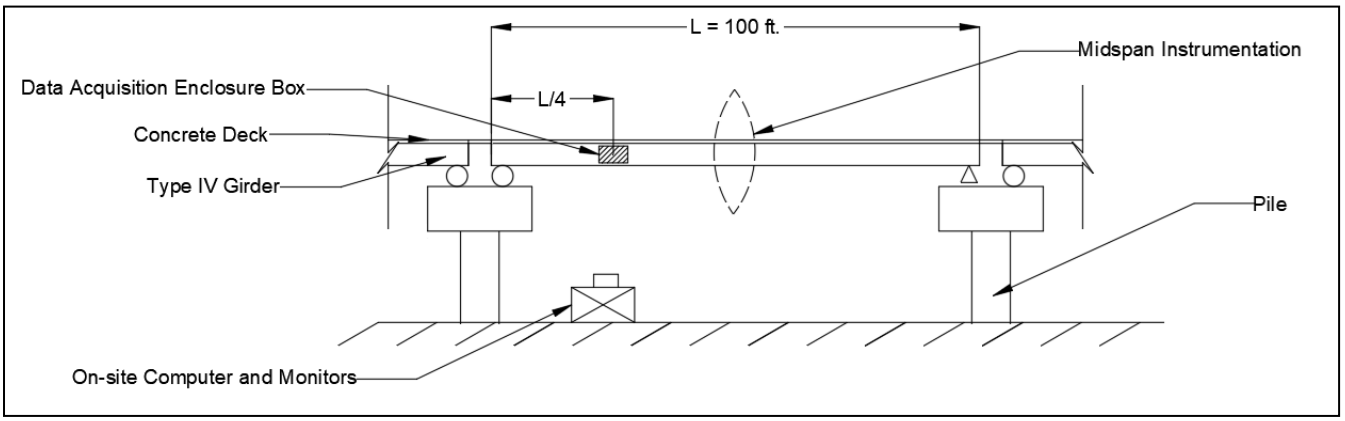

Figure 6.2: Instrumentation location for load testing plan.

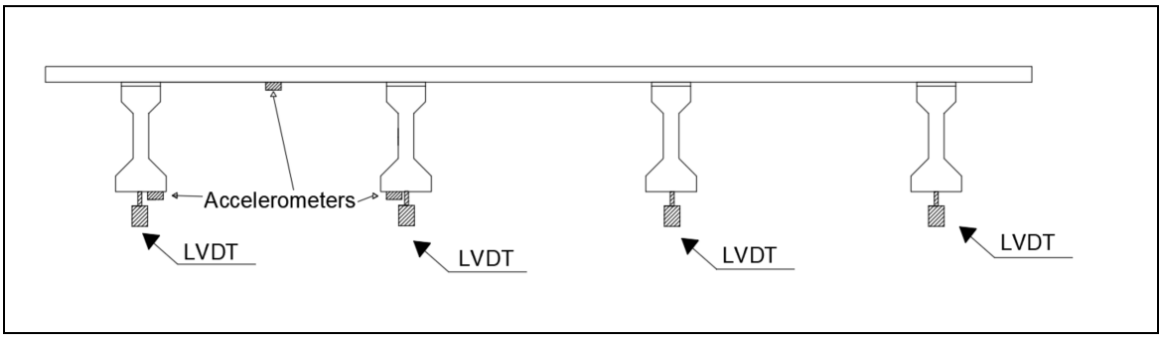

Figure 6.3: LVDT and accelerometer locations.

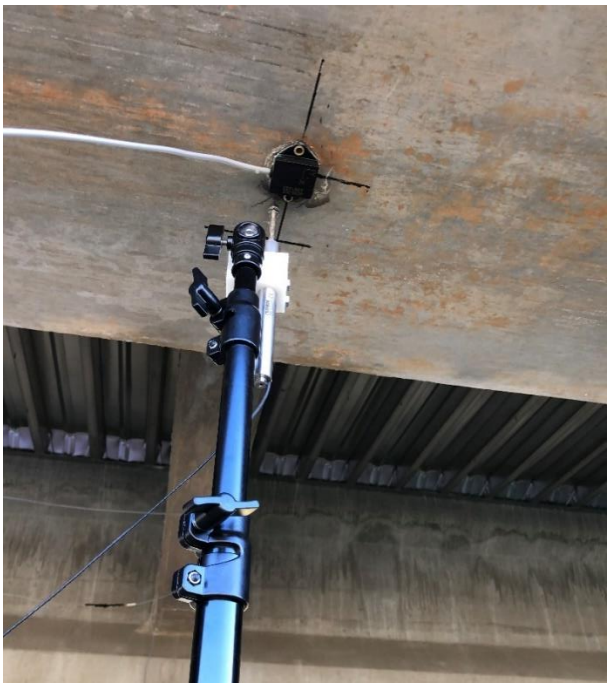

Figure 6.4: Instruments at midspan for SH 4 load test. Viewed are an LVDT and accelerometer.

Figure 6.5: Testing setup for SH 4 load test.

6.2.1 Static Load Test

The static load testing plan for Span 9 and 14 consisted of two identical scenarios. In the first scenario, which was referred to as Configuration 1, one truck was positioned on the westernmost part of the span at an offset distance of 2 ft from the tire closest to the parapet's edge. In the second scenario, which is referred to as Configuration 3, a second truck is positioned on the western part of the span, ten feet away from the parapet. In this case, the initial truck is still in the same location. The relevance of Configuration 3, which mimics the lever rules technique of computing the distribution factor for bridge girders, lies in the fact that it is the only configuration that does so. Figure 6.6 and Figure 6.8 provide more information regarding the positioning of the trucks in both circumstances. For each scenario, the front tires of the rear axle were positioned along the length of each span at increments of 16 feet and 8 inches. There was a total of five tests performed for each configuration. Figure 6.7 and Figure 6.9, respectively, present further information regarding the positioning of the trucks in the Configuration 1 and Configuration 3 layouts. In order to give the necessary amount of time for the instrumentation to take measurements, the trucks were required to remain parked for three minutes at each increment.

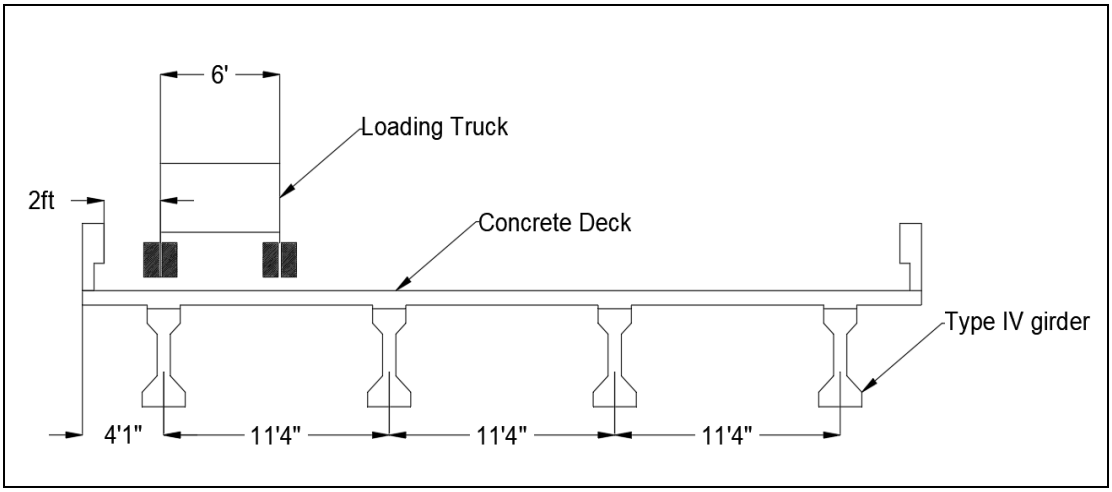

Figure 6.6: Truck Configuration 1 view looking North.

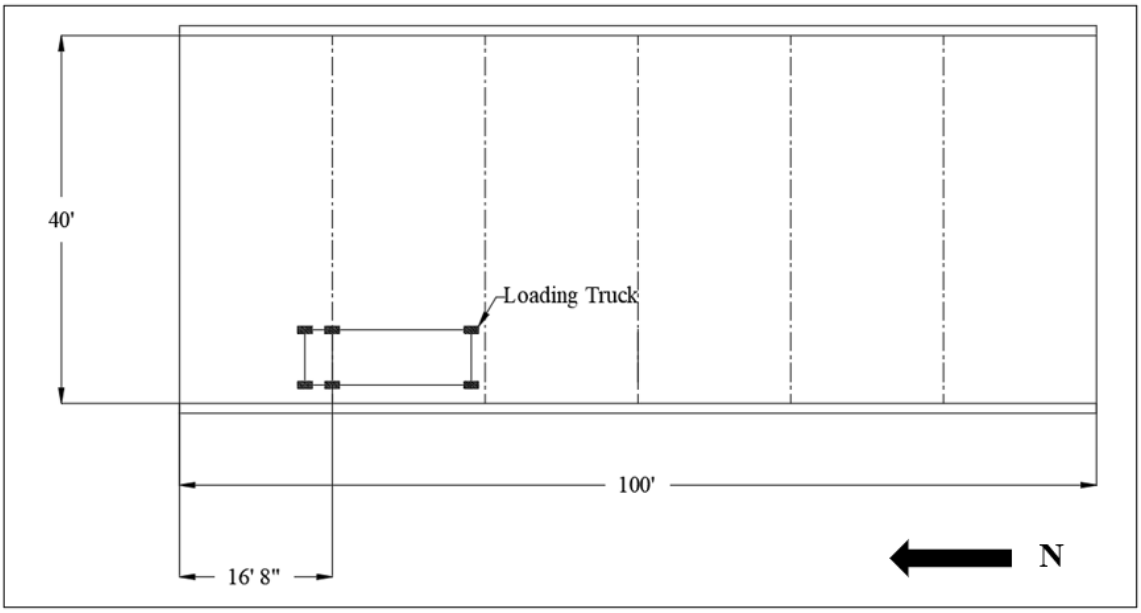

Figure 6.7: Truck Configuration 1 plan view.

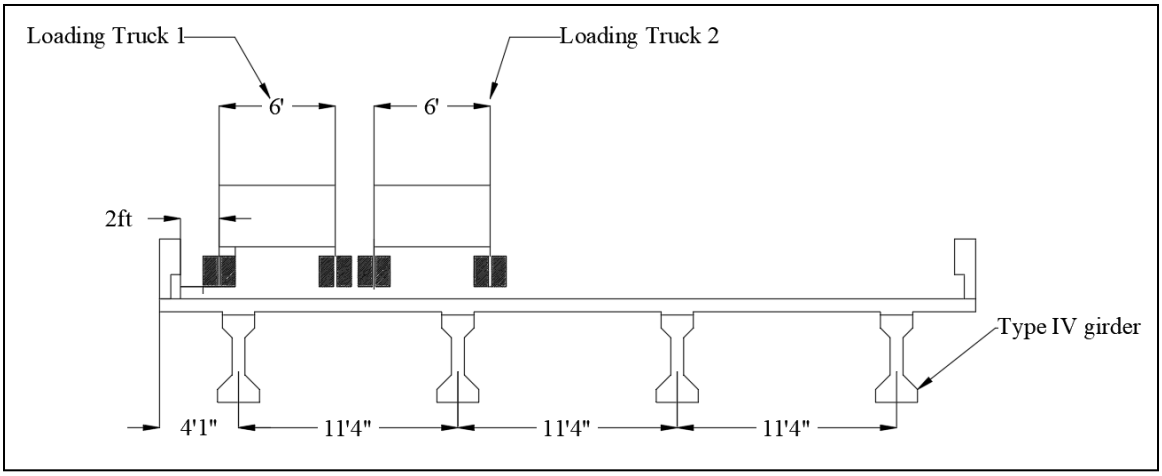

Figure 6.8: Truck Configuration 3 view looking North.

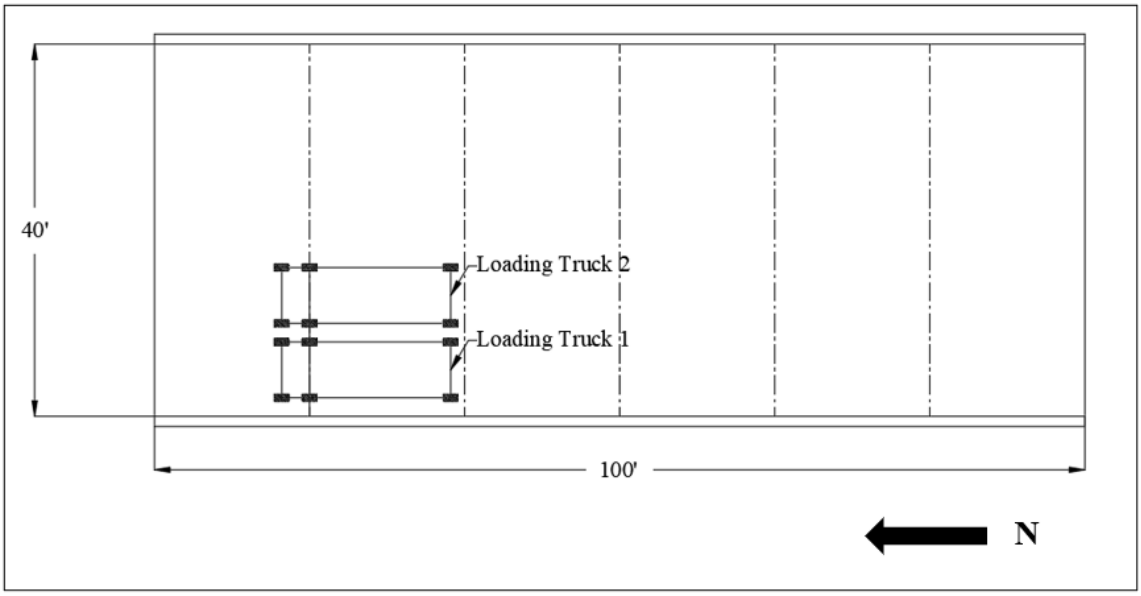

Figure 6.9: Truck Configuration 3 plan view.

Figure 6.10: Truck Configuration 1 for static load testing.

Figure 6.11: Truck Configuration 3 for static load testing.

Deflections measurements were used to determine distribution factors for the girders of the spans This is shown in the following equation, modified from Eq. 6.1 (Dong et al., 2020).

$$DF = \frac{\Delta_{girder}}{\sum \Delta_{girders}} * N_L \qquad \textbf{Eq. 6.1}$$

The results of the tests were compared to AASHTO prescribed methods, specifically the lever rule and rigid method.

6.2.2 Moving Load Test

Speeds varying from 15 to 60 mph were used during the moving load test. For each test, the truck speed was increased at a rate of 15 mph until the maximum speed of 60 mph was reached. The experimental data were recorded with VOLT 116 at a sampling rate of 200 Hz. The truck was traveling from the north to the south on the westernmost driving lane.

6.3 Results

6.3.1 Static Load Testing

Figure 6.12, Figure 6.13, Figure 6.14, and Figure 6.15 illustrate the raw deflection data gathered from LVDTs during the static load testing. These figures can be found below. During the testing performed on Span 14, Configuration 1, an error occurred in which one of the truck rear tire placements at 33.3 feet was skipped by accident. This should be taken into consideration. After some time had passed, the test was repeated, but the results from that station are not included in Figure 6.15

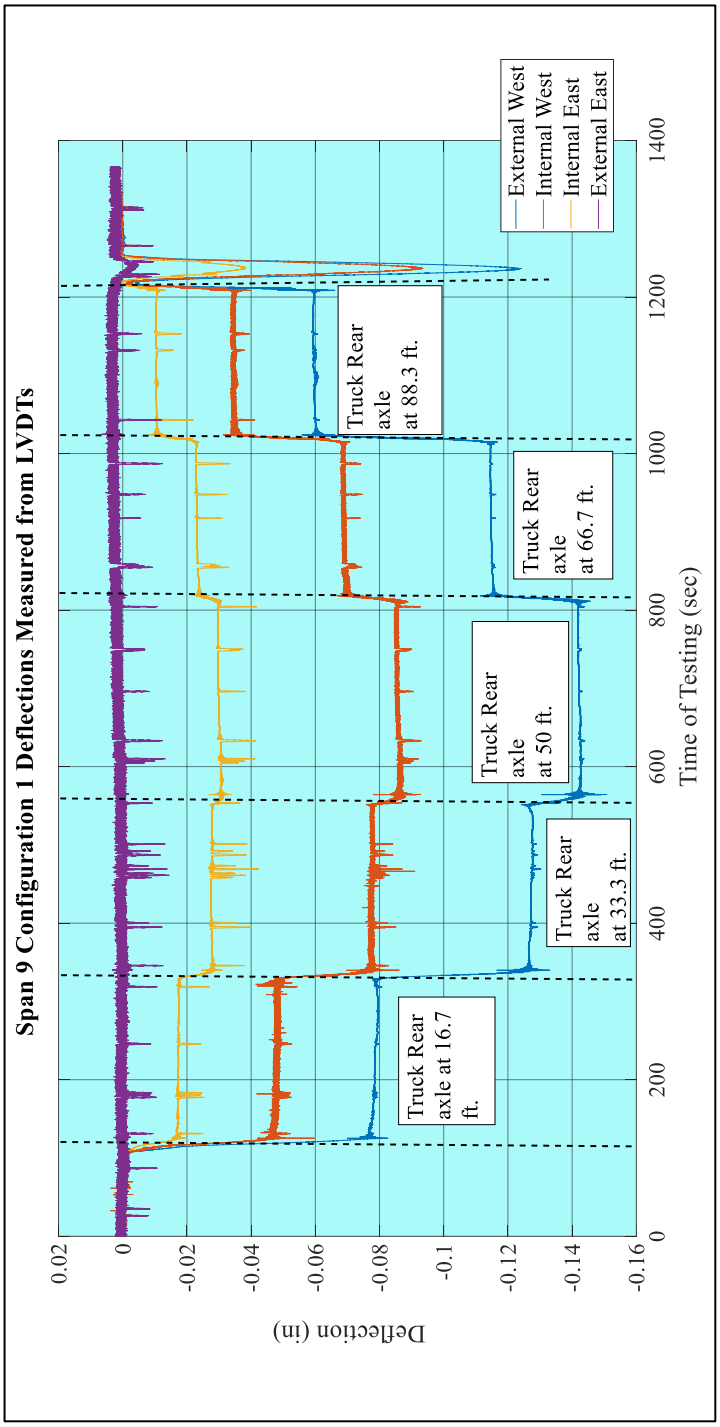

Figure 6.12: Span 9 Configuration 1 measured Midspan deflections.

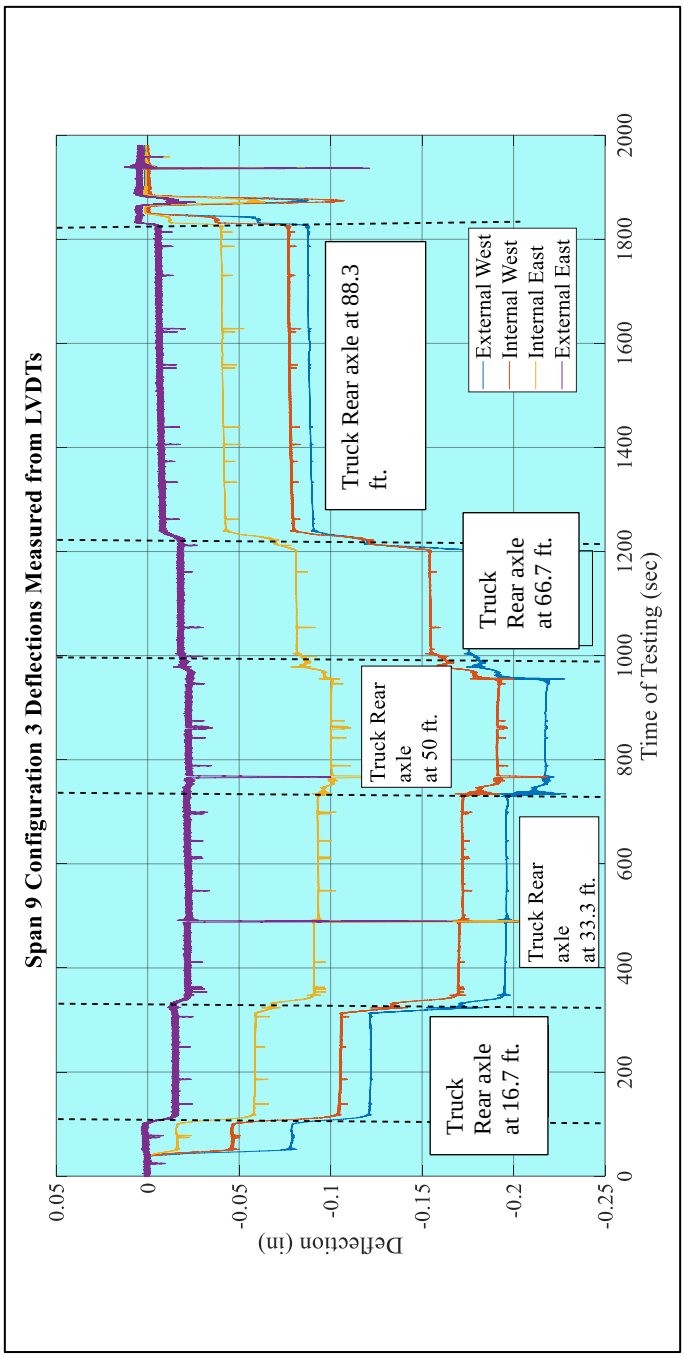

Figure 6.13: Span 9 Configuration 3 measured midspan deflections.

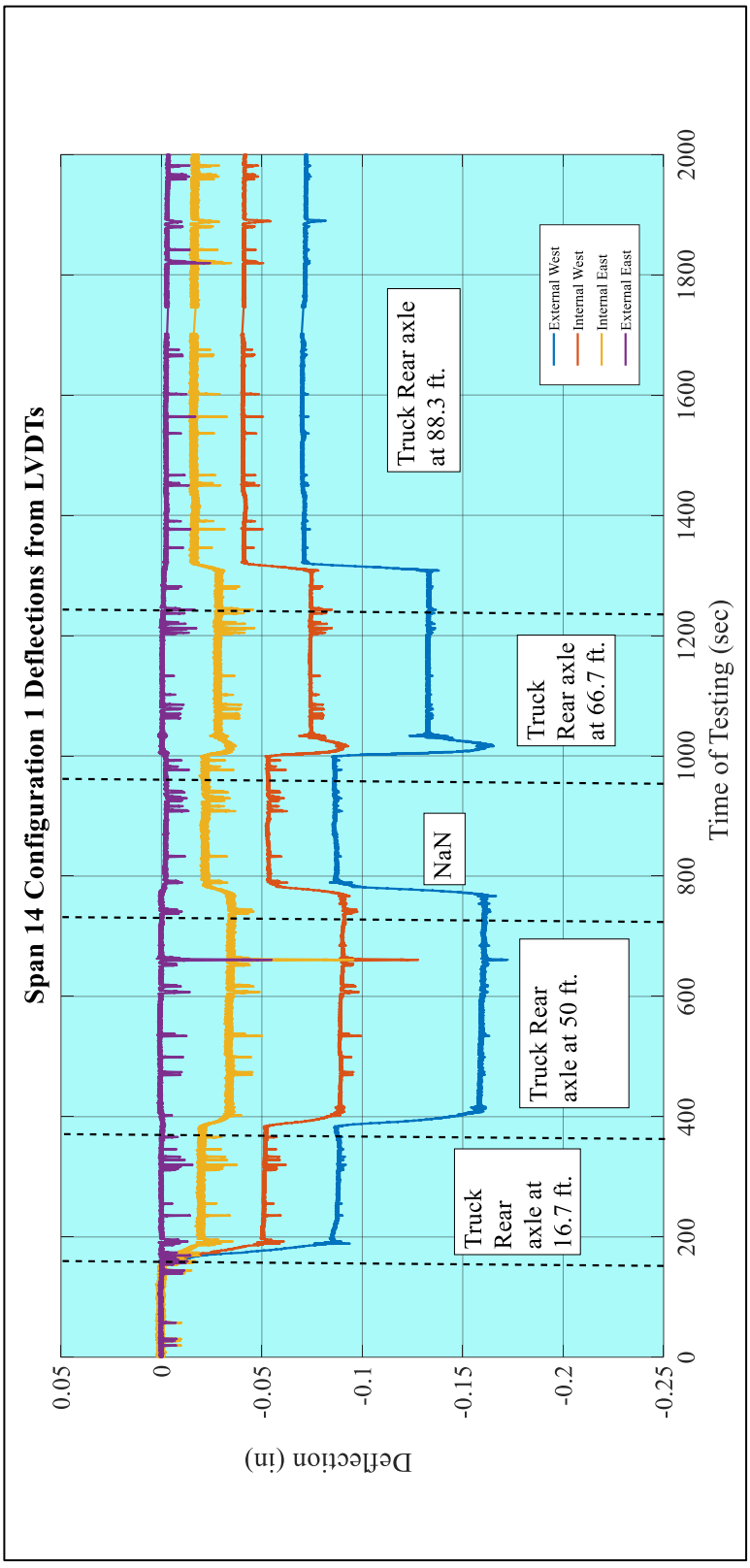

Figure 6.14: Span 14 Configuration 1 measured midspan deflections.

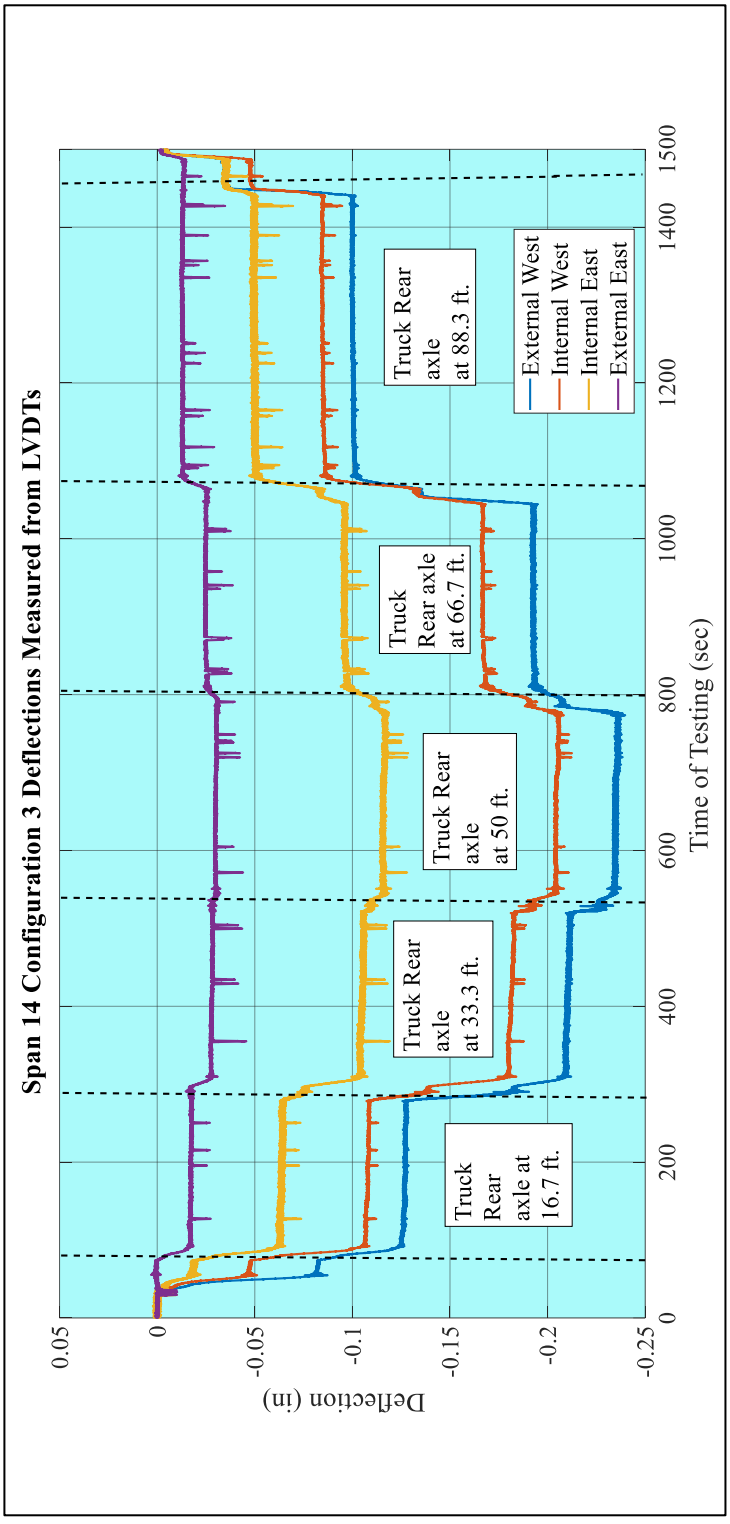

Figure 6.15: Span 14 Configuration 3 measured midspan deflections.

The deflections and distribution factors from the static load tests are reported in the tables and graphs below. Deflection values were obtained from LVDTs used during the tests, and distribution factors were computed using the relative deflections at each station. For ease of comparison, the distribution factors calculated using the lever rule, rigid method, and FEA are listed at the bottom of the tables.

Table 6.2: Span 9 Configuration 1 tabulated results.

Span 9 (Configuration 1 (Truck 1)) Deflections (in) and Distribution Factors (DF)								
	Deflections (in.)				Distribution Factors			
Girders	**External West**	**Internal West**	**Internal East**	**External East**	**External West**	**Internal West**	**Internal East**	**External East**
Truck location	1	2	3	4	1	2	3	4
16.7	-0.079	-0.048	-0.018	0.000	0.546	0.333	0.122	-0.001
33.3	-0.127	-0.078	-0.028	0.000	0.544	0.333	0.121	0.001
50	-0.142	-0.086	-0.030	0.001	0.553	0.334	0.118	-0.004
66.7	-0.115	-0.069	-0.023	0.002	0.560	0.337	0.115	-0.011
83.3	-0.060	-0.035	-0.011	0.003	0.585	0.340	0.105	-0.029
Note: 1: All DFs displayed at the bottom of the table are calculated at midspan. 2: Multi presence factors are excluded from results.			**Measured at Midspan**		**0.55**	**0.33**	**0.12**	**0.00**
			Rigid Method		**0.65**	**0.38**	**0.12**	**-0.15**
			Lever Rule		**0.82**	**0.18**	**0.00**	**0.00**

Table 6.3: Span 9 Configuration 3 tabulated results.

Span 9 Configuration 3 (Truck 1 + Truck 2) Deflections (in) and Distribution Factors (DF)								
	Deflections (in.)				Distribution Factors			
Girders	**External West**	**Internal West**	**Internal East**	**External East**	**External West**	**Internal West**	**Internal East**	**External East**
Truck location	1	2	3	4	1	2	3	4
16.7	-0.122	-0.105	-0.059	-0.015	0.808	0.700	0.390	0.102
33.3	-0.196	-0.172	-0.093	-0.023	0.810	0.710	0.386	0.094
50	-0.217	-0.191	-0.101	-0.023	0.818	0.720	0.378	0.086
66.7	-0.175	-0.154	-0.081	-0.018	0.816	0.720	0.380	0.084
83.3	-0.089	-0.078	-0.041	-0.007	0.826	-0.726	0.384	0.066
Note: 1: All DFs displayed at the bottom of the table are calculated at midspan. 2: Multi presence factors are excluded from results			**Measured at Midspan**		**0.82**	**0.72**	**0.38**	**0.09**
			Rigid Method		**1.03**	**0.68**	**0.30**	**-0.01**
			Lever Rule		**0.93**	**0.57**	**0.50**	**0.00**

Table 6.4: Span 14 Configuration 1 tabulated results.

Span 14 Configuration 1 (Truck 1) Deflections (in) and Distribution Factors (DF)								
	Deflections (in.)				Distribution Factors			
Girders	**External West**	**Internal West**	**Internal East**	**External East**	**External West**	**Internal West**	**Internal East**	**External East**
Truck location	1	2	3	4	1	2	3	4
16.7	-0.088	-0.052	-0.020	-0.001	0.548	0.322	0.127	0.003
33.3	-0.120	-0.070	-0.028	0.000	0.549	0.320	0.128	0.002
50	-0.160	-0.090	-0.035	0.000	0.560	0.316	0.122	0.001
66.7	-0.133	-0.075	-0.029	-0.001	0.558	0.314	0.122	0.006
83.3	-0.071	-0.041	-0.017	-0.003	0.539	0.314	0.127	0.020
Note: 1: All DFs displayed at the bottom of the table are calculated at midspan. 2: Multi presence factors are excluded from results.			**Measured at Midspan**		**0.56**	**0.32**	**0.12**	**0.00**
			Rigid Method		**0.65**	**0.38**	**0.12**	**-0.15**
			Lever Rule		**0.82**	**0.18**	**0.00**	**0.00**

Table 6.5: Span 14 Configuration 3 tabulated results.

Span 14 Configuration 3 (Truck 1 + Truck 2) Deflections (in) and Distribution Factors (DF)								
	Deflections (in.)				Distribution Factors			
Girders	**External West**	**Internal West**	**Internal East**	**External East**	**External West**	**Internal West**	**Internal East**	**External East**
Truck location	1	2	3	4	1	2	3	4
16.7	-0.127	-0.108	-0.064	-0.018	0.802	0.682	0.404	0.110
33.3	-0.210	-0.182	-0.105	-0.028	0.800	0.692	0.400	0.108
50	-0.235	-0.205	-0.116	-0.030	0.802	0.698	0.396	0.104
66.7	-0.193	-0.167	-0.096	-0.025	0.800	0.694	0.400	0.106
83.3	-0.100	-0.085	-0.050	-0.013	0.806	0.684	0.404	0.108
Note: 1: All DFs displayed at the bottom of the table are calculated at midspan. 2: Multi presence factors are excluded from results.			**Measured at Midspan**		**0.80**	**0.70**	**0.40**	**0.10**
			Rigid Method		**1.03**	**0.68**	**0.30**	**-0.01**
			Lever Rule		**0.93**	**0.57**	**0.50**	**0.00**

6.3.2 Moving Load Testing Results

The static deflection that was measured at midspan for the static tests of the Span 9 for Configurations 1 and 3 are shown in Table 6.2 &Table 6.3, consecutively. The results of the vertical displacement during the static tests of span 14 for Configuration 1 and Configuration 3 are shown in Table 6.4 and Table 6.5, consecutively.

The acceleration data was recorded when the truck was driven from north to south at different speeds.

Figure 6.16 presents the acceleration and the vertical displacement responses of the girders at midspan.

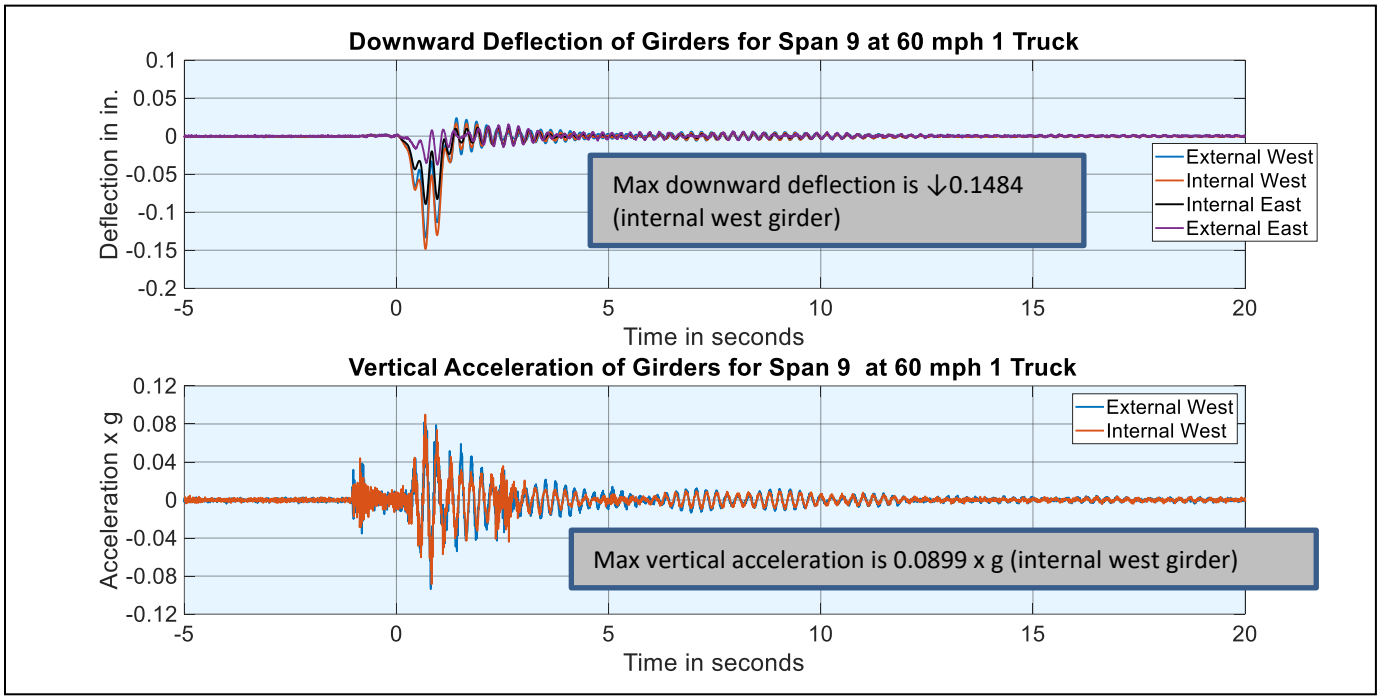

Figure 6.16: Midspan Acceleration and Deflection Records for Span 9 when Truck 1 was traveling 60 mph.

Figure 6.16 (a) presents acceleration response collected with the accelerometer at midspan (Span 9). This acceleration data was recorded when the truck was driven from north to south at 60 mph.

Figure 6.16 (b) presents the fundamental frequency estimated from Fast Fourier Transformation. (FFT) applied to the recorded acceleration Figure 6.16 (a).

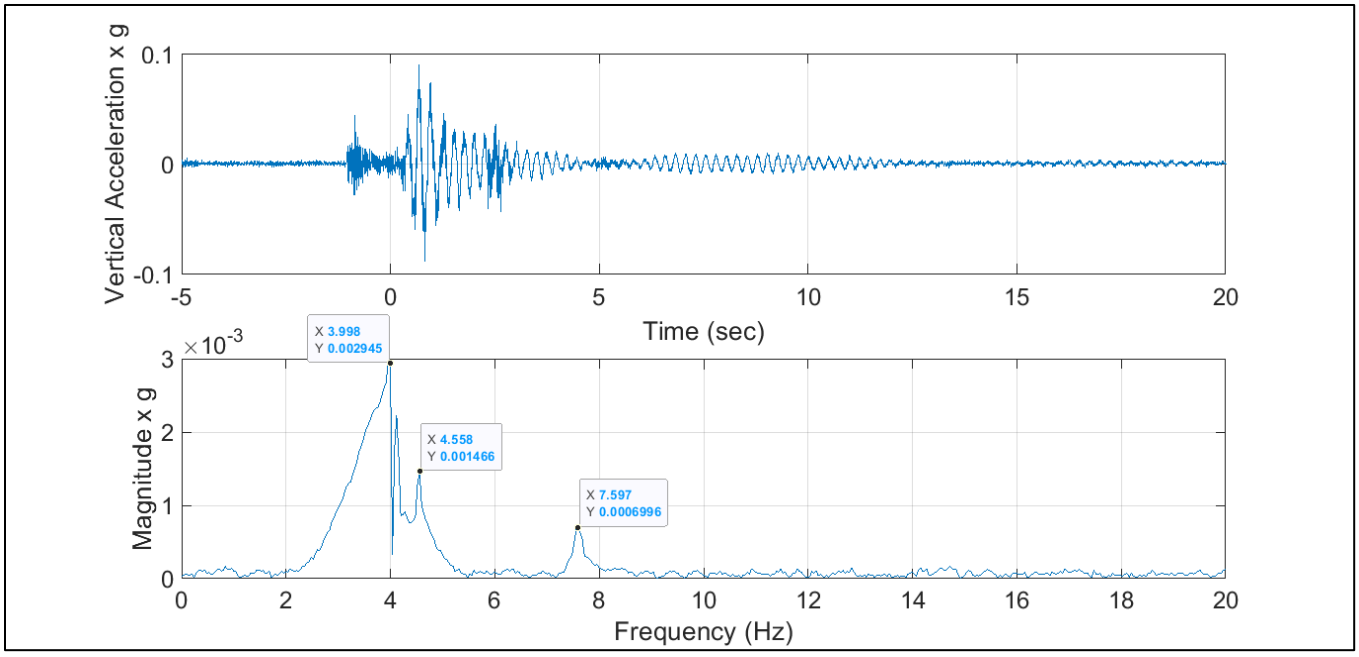

Figure 6.17: Dynamic response for Span 9 when the truck was traveling at 60 mph.
(a) Measured Acceleration for the interior west girder.
(b) Natural Frequency extracted through FFT

The fundamental frequency of the bridge Span 9 corresponded to a value of 3.998 Hz for Span 9.

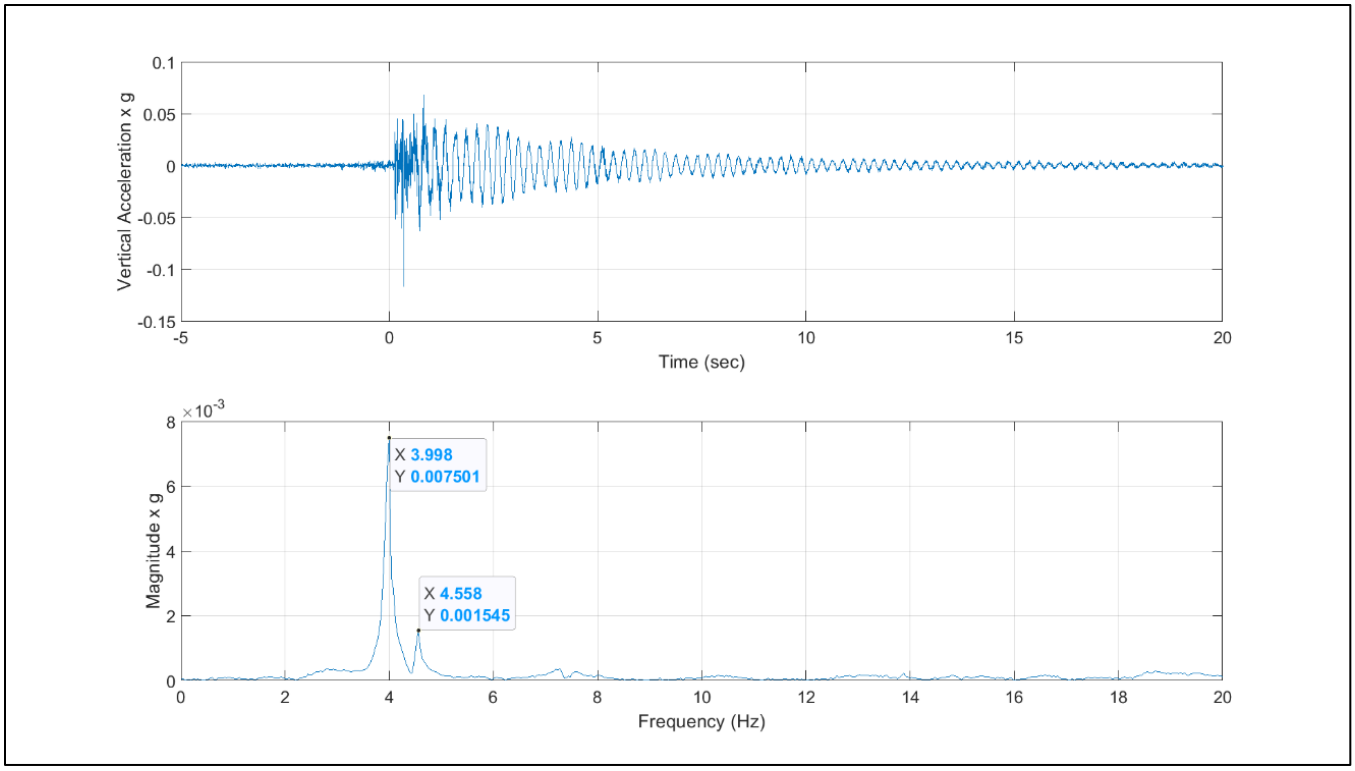

Figure 6.18: Dynamic response for Span 14 when the truck was traveling at 60 mph.
(a) Measured Acceleration for the interior west girder.
(b) Natural Frequency extracted through FFT

The fundamental frequency of the bridge Span 9 corresponded to a value of 3.998 Hz for Span 14.

6.4 Finite Element Modeling

Finite Element Analysis aims to simulate the behavior of the bridge during load testing; a three-dimensional finite element model was created. The model was created that represents Span 14. The girders, deck, diaphragms, and parapets were all represented as three-dimensional solids. The model includes all reinforcement in the deck, diaphragms, and girders. The prestressing strands and rebar were modeled as 2-dimensional wire elements to reduce computation time.

The modulus of elasticity for the girders was set to 5853 ksi. The modulus of elasticity for the deck, diaphragms, and parapets was set to 4684 ksi. The modulus of elasticity of the prestressing strands was set to 28500 ksi, and the modulus for reinforcing steel was set to 29000 ksi. The meshing was set to 5.5 in. for the deck and 6 in. for all other components, shown in Figure 6.19. The deck, parapets, and diaphragms were attached to the girders using a "Tie" constraint to simulate composite action between these components. Prestressing was applied to the model by imposing strain on the strands before the first step in the analysis. Since Abaqus cannot simulate the bridge's construction steps, the prestressing force in the model is not entirely accurate. To negate this inaccuracy, deflection and strain values were taken from the model with no truck loading applied and then compared to deflection and strain values taken after truck loading was applied to find deflection and strain caused by truck loading on the structure.

Bearing pads were set as 7 in. long and 26 in. wide. The center of each bearing pad was placed 7.5 inches away from the end face of each girder. Bearing pads were constrained to make the span act similar to a simply supported beam.

All static load tests were recreated in the finite element models. The models were run once without truck loading and once with truck loading. The deflection and change in strain caused by truck loading were found using superposition. Deflection and strain were found by subtracting the test results without truck loading from the test results that included truck loading. Distribution factors were computed similarly to

the static load test, where the deflection of one girder is divided by the sum of the deflections of all girders to get the distribution factor.

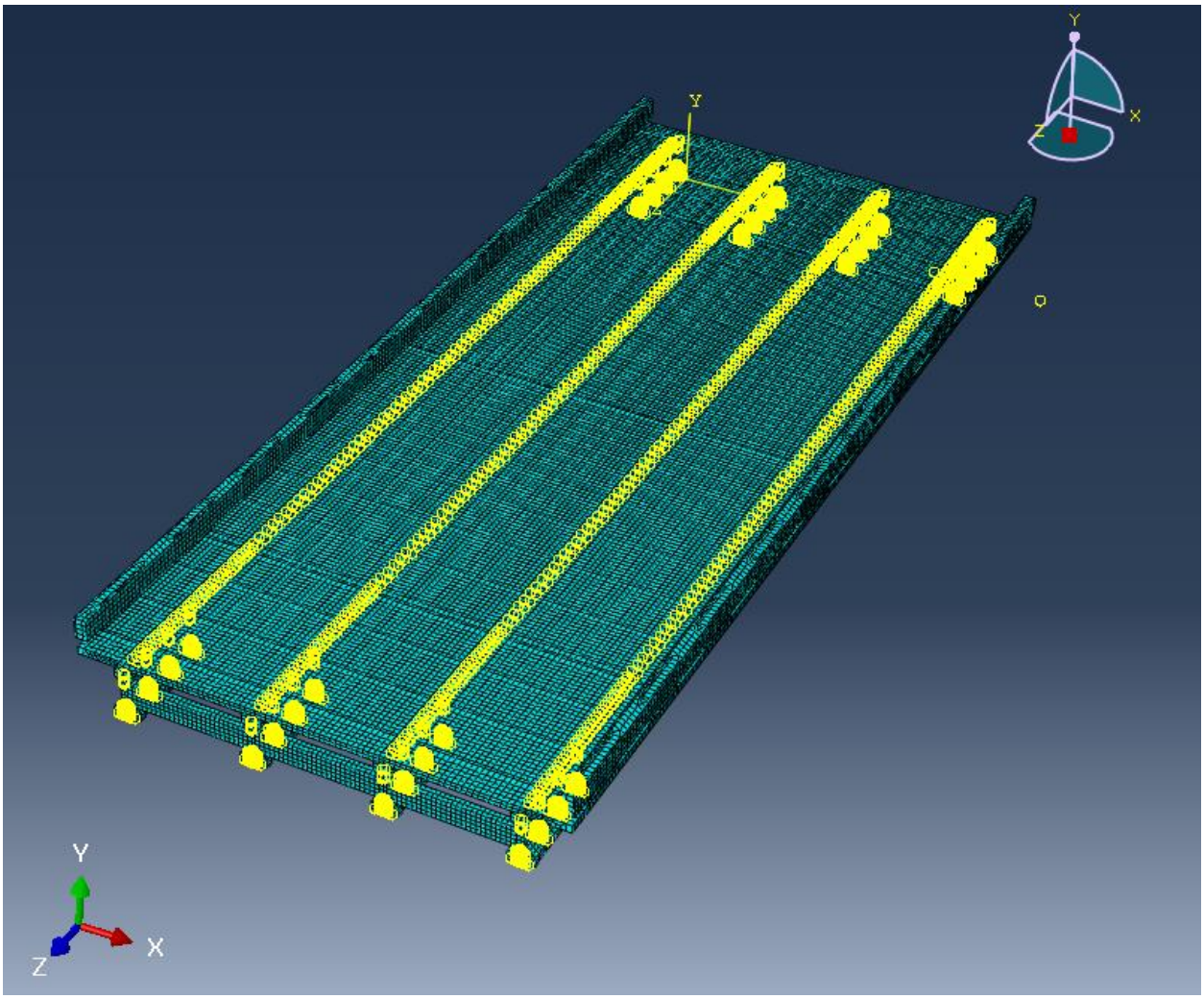

Figure 6.19: Photograph of the Abaqus model

6.4.1 Results of FEA Model:

The results of the FEA model are shown in the following tables:

Table 6.6: Span 14, Configuration 1 FEA results.

Span 14 (Configuration 1 (Truck 1)) Deflections (in) and Distribution Factors (DF) from Finite Element Analysis								
	Deflections (in.)				Distribution Factors			
Girders	External West	Internal West	Internal East	External East	External West	Internal West	Internal East	External East
Truck location	1	2	3	4	1	2	3	4
16.7	0.06	0.04	0.02	0.01	0.44	0.29	0.18	0.09
33.3	0.12	0.07	0.04	0.02	0.47	0.30	0.16	0.07
50	**0.14**	**0.09**	**0.05**	**0.02**	**0.49**	**0.30**	**0.15**	**0.06**
66.7	0.12	0.07	0.04	0.01	0.50	0.30	0.15	0.05
83.3	0.07	0.04	0.02	0.01	0.50	0.30	0.15	0.05

Table 6.7: Span 14, Configuration 3 FEA results.

Span 14 Configuration 3 (Truck 1 + Truck 2) Deflections (in) and Distribution Factors (DF) from Finite Element Analysis								
	Deflections (in.)				Distribution Factors			
Girders	External West	Internal West	Internal East	External East	External West	Internal West	Internal East	External East
Truck location	1	2	3	4	1	2	3	4
16.7	0.11	0.09	0.06	0.04	0.36	0.31	0.21	0.13
33.3	0.22	0.18	0.11	0.06	0.38	0.32	0.20	0.11
50	**0.27**	**0.22**	**0.13**	**0.06**	**0.40**	**0.32**	**0.19**	**0.09**
66.7	0.22	0.18	0.11	0.05	0.40	0.32	0.19	0.09
83.3	0.11	0.09	0.05	0.02	0.40	0.32	0.19	0.09

6.4.2 Validation of the FEA Model:

6.4.2.1 Validation of the FEA through Deflection:

Figure 6.20 displays deflections and distribution factors for the Westernmost girders of Span 14 at each truck station. It is observed that the deflections found with the finite element model are relatively consistent with deflection measured to the load test. FEA underpredicted deflections by as low as 0.018 in and as much as 0.033 in. The FEA model is consistent with deflection results for Span 14.

For the internal West girder, the DF of the midspan station from the load test was 0.32 and 0.70 for truck Configurations 1 and 3, respectively. FEA found a distribution factor of 0.30 and 0.64, which is a 6.5% and 9% percent difference for C1 and C3, respectively.

FEA found a distribution factor of 49.1% and 29.7% for Load Configuration 1 and Load Configuration 3, respectively. The FEA underpredicted the DFs by 2.3% for the internal west girder and 6.9% for the external girder for Load Configuration 1. The FEA underpredict the DF for the external west girder by 1%, and underpredict the DF for interior girder by 6%.

These results show that FEA can consistently and accurately measure the relative deflection of the girders, therefore measuring distribution factors accurately.

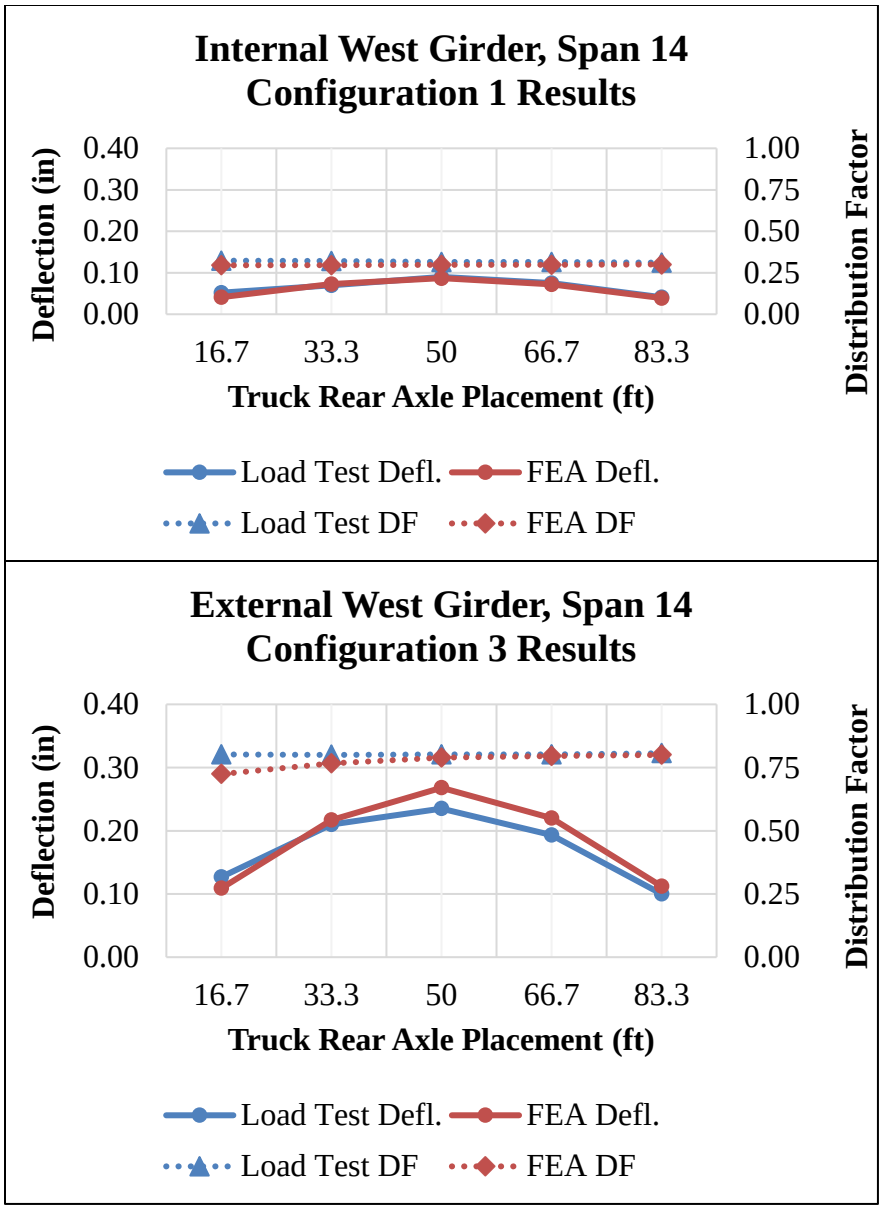
Internal West Girder, Span 14
Configuration 1 Results
Deflection (in)
0.40
0.30
0.20
0.10
0.00
1.00
0.75
0.50
0.25
0.00
Distribution Factor
16.7
33.3
50
66.7
83.3
Truck Rear Axle Placement (ft)
Load Test Defl.
FEA Defl.
Load Test DF
FEA DF
External West Girder, Span 14
Configuration 3 Results
Deflection (in)
0.40
0.30
0.20
0.10
0.00
1.00
0.75
0.50
0.25
0.00
Distribution Factor
16.7
33.3
50
66.7
83.3
Truck Rear Axle Placement (ft)
Load Test Defl.
FEA Defl.
Load Test DF
FEA DF

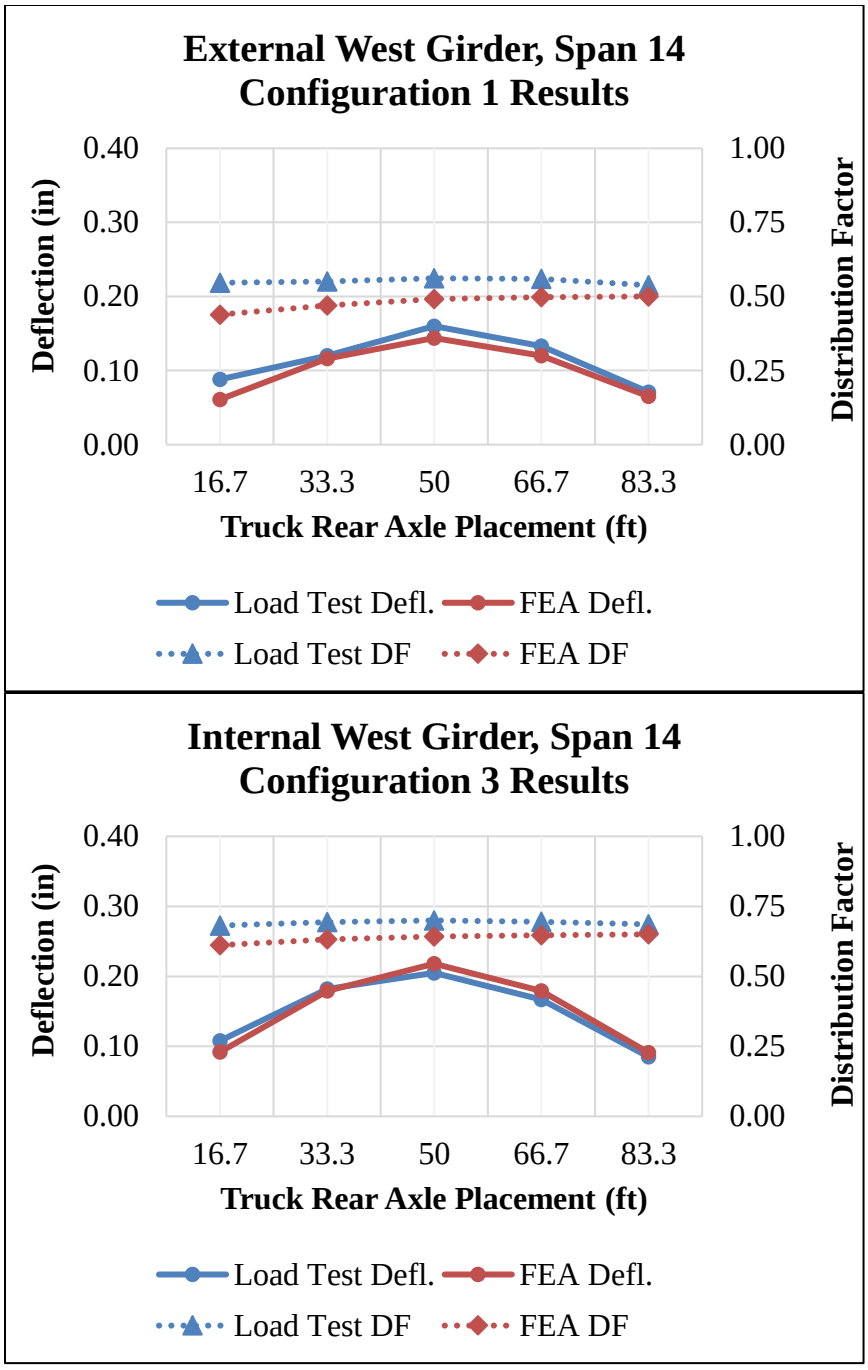

Figure 6.20 Span 14 Western Girders Load Test and FEA results.

6.4.2.2 Validation of the FEA through Strain Gauge Data

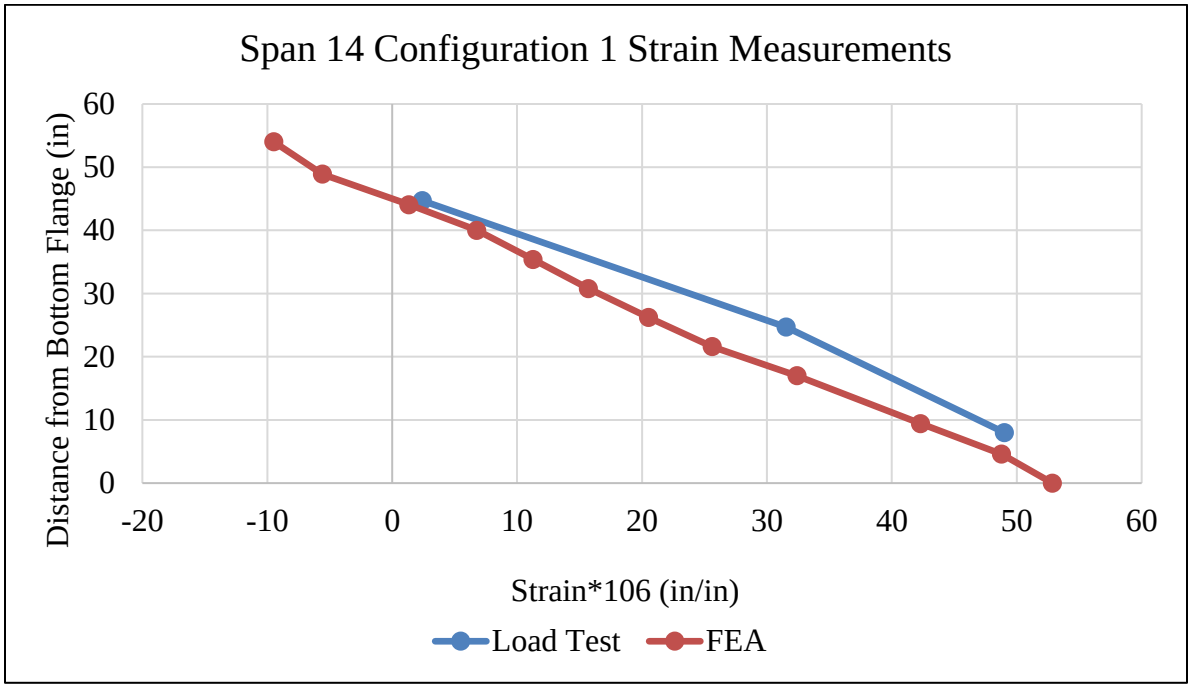

Figure 6.21: Midspan Strain measurements of external West girders from load tests and FEA for trucks placed at midspan for Configuration 1.

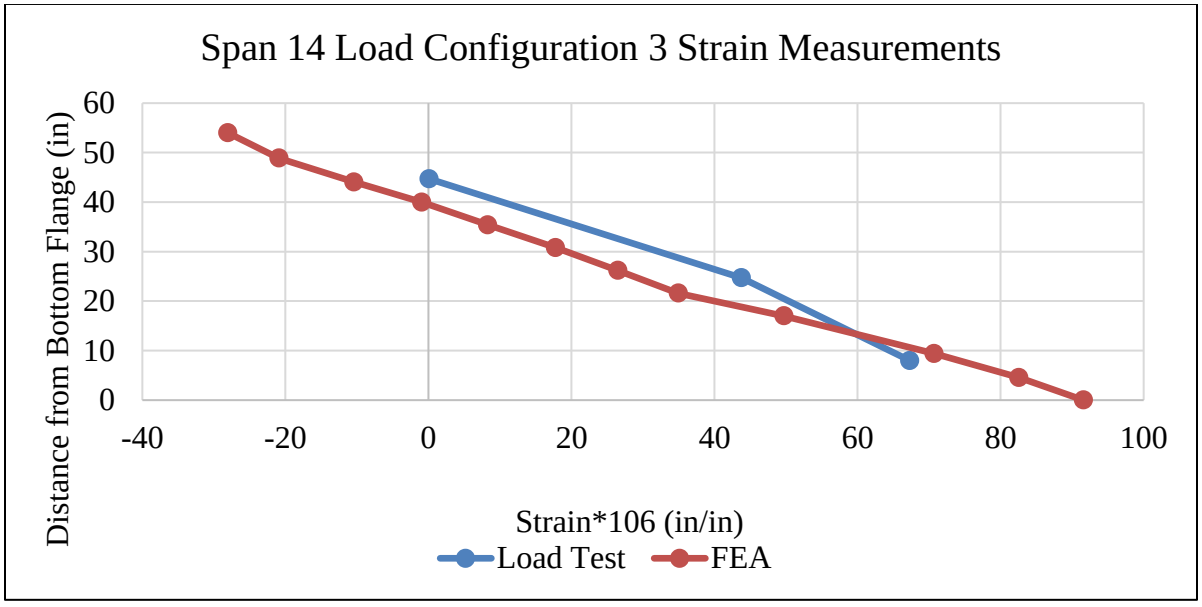

Figure 6.22: Midspan Strain measurements of external West girders from load tests and FEA for trucks placed at midspan for trucks placed at midspan for Configuration 1.

The measured strain of the Westernmost Girders from truck axles at the bridge's midspan from both instrumentation and the FEA model is shown Figure 6.21 and Figure 6.22. Vibrating wire gauges are only located in three locations along the depth of each girder. Strain measurements from the finite element model can be obtained for all nodes on the girder at midspan. Both sets of strain measurements are not perfectly linear along the depths of the beam. Interpolating the FEA results to the depth at which the vibrating wire gauges were placed shows a maximum underprediction of FEA results of 10 microstrains and a maximum overprediction of 6 microstrains between all tests.

6.4.2.3 Validation of the FEA through Modal Analysis

To estimate the dynamic properties of the bridge, the accelerations versus time histories collected by the accelerometers installed on the bridge were processed. One of the other objectives of the moving load testing is to use its results to update the FE model of the bridge as explained in previous report. These dynamic results can be tracked over time to determine any global changes. They were employed to validate or calibrate FEM of the bridge.

Figures 3,4 and 6 present the first mode shapes results from Abaqus. The experimental modal frequencies and the modal frequencies that were found for span 9 are displayed in the Table 6.8.

Table 6.8: Measured vs Calculated Mode Shapes.

Mode Shapes			
	Frequencies in (Hz)		
Recorded Modes	Span 9	Span 14	Finite Element Analysis
Mode 1	3.958	3.998	4.040
Mode 2	4.558	4.558	4.500
Mode 3	7.607	7.608	8.150

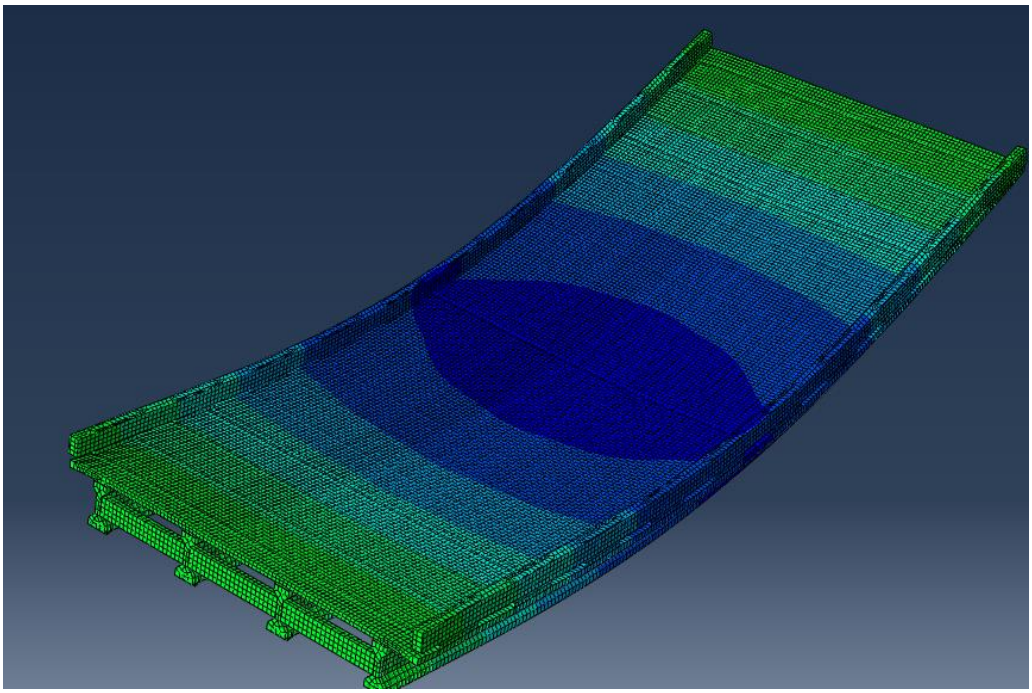

Figure 6.23: First Mode Shape, or the Fundamental Mode Shape of the dynamic response of SH 4 Bridge to moving loads, Spans 9 f_1 = 4.04 Hz

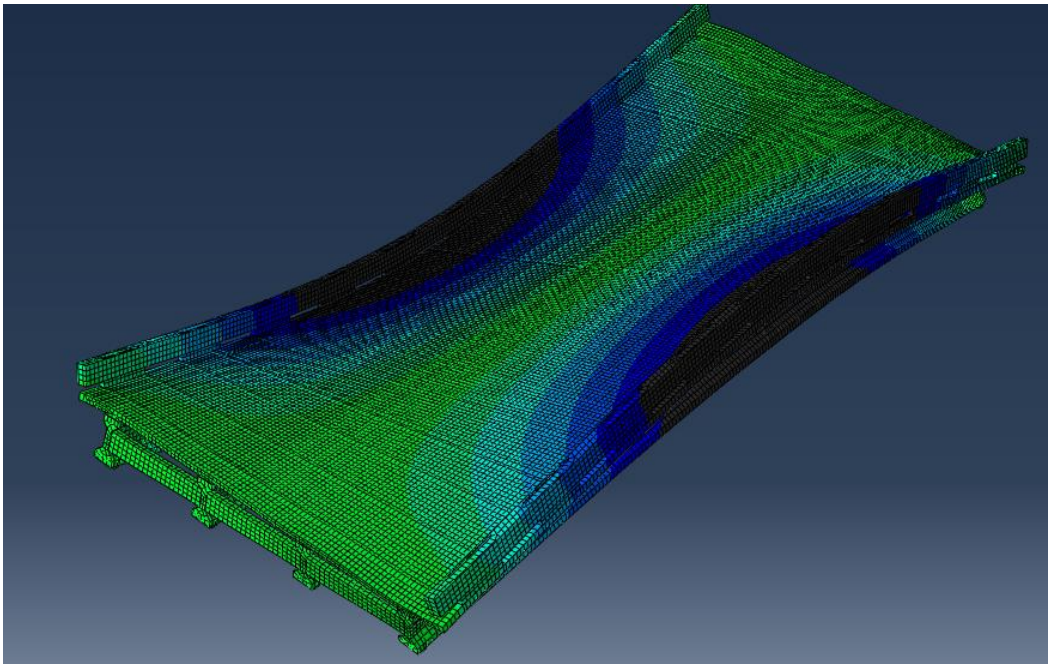

Figure 6.24: Second Mode Shape, Dynamic Response of SH 4 Bridge, Spans 9 and 14, f_2 = 4.50 Hz. This Mode is fundamentally flexural in nature for each individual girder but with torsion of the bridge deck and some torsion of the beams.

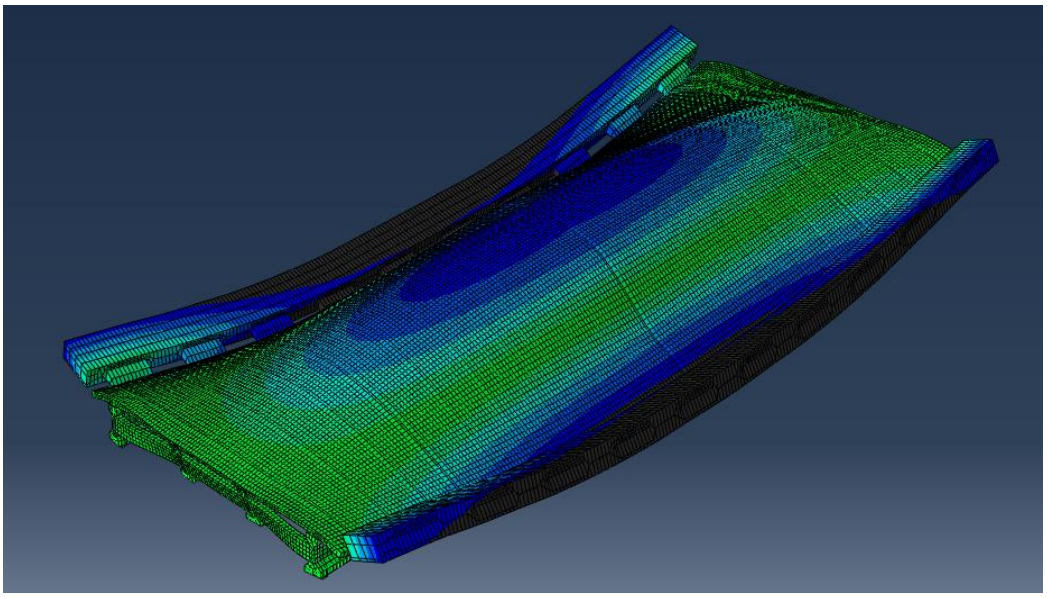

Figure 6.25: Third Mode Shape for Dynamic Response of SH 4 Bridge, Spans. f_3 = 8.15 Hz. The mode shape remains principally first mode flexural but with significantly more twisting required.

Compared with the updated FE model of the bridge, it was observed to be a difference only for the third mode. However, the modal participation mass ratio of this mode (3rd mode) was

obtained to be relatively lower, which means that the importance of this mode on a dynamic load can be neglected. Such data and dynamic response can be collected efficiently under operating traffic and evaluated to track any stiffness or boundary condition change.

The results of the FEA model matched closely the measured data (Displacements, Strains and Mode Shapes). The FEA model can accurately predict the bridge behavior.

6.5 Discussion

6.5.1 Comparison of AASHTO Methods and Load Test Results

Table 6.9 displays the calculated results of the varying AASHTO methods for exterior and interior girders in both single lane and two lane loaded scenarios. Results varied between all methods in all scenarios with the AASHTO LRFD table method consistently providing the most conservative results. Note that multiple presence factors were not considered in these computations except for in the AASHTO LRFD case for an exterior girder, single lane loaded scenario, in which the lever rule was used and multiplied by a factor of 1.2.

Table 6.9: Comparison of AASHTO methods for determining distribution factors of exterior and interior girders.

Girder Location	Number of Lanes Loaded	Lever Rule	Rigid Method	AASHTO LRFD	Measured Span 9	Measured Span 14
Ext	1	82%	65%	99%	55%	56%
Ext	2	93%	103%	89%	82%	80%
Int	1	18%	38%	55%	33%	32%
Int	2	57%	68%	81%	72%	70%

Note:
1. Lever rule and rigid method results do not include multiple presence factors in this analysis.
2. The AASHTO LRFD method requires use of the lever rule to calculate distribution factors of a single lane loaded exterior girder. A multiple presence factor of 1.2 was used in calculation for this case. All other cases in this method consider multiple presence in their equations.

Table 6.9 tabulates the calculated results of the varying AASHTO methods for exterior and interior girders in both single lane and two lane loaded scenarios. Results varied between all methods in all scenarios with the AASHTO LRFD table method consistently providing the most conservative results. Note that multiple presence factors were not considered in these computations except for in the AASHTO LRFD case for an exterior girder, single lane loaded scenario, in which the lever rule was used and multiplied by a factor of 1.2.

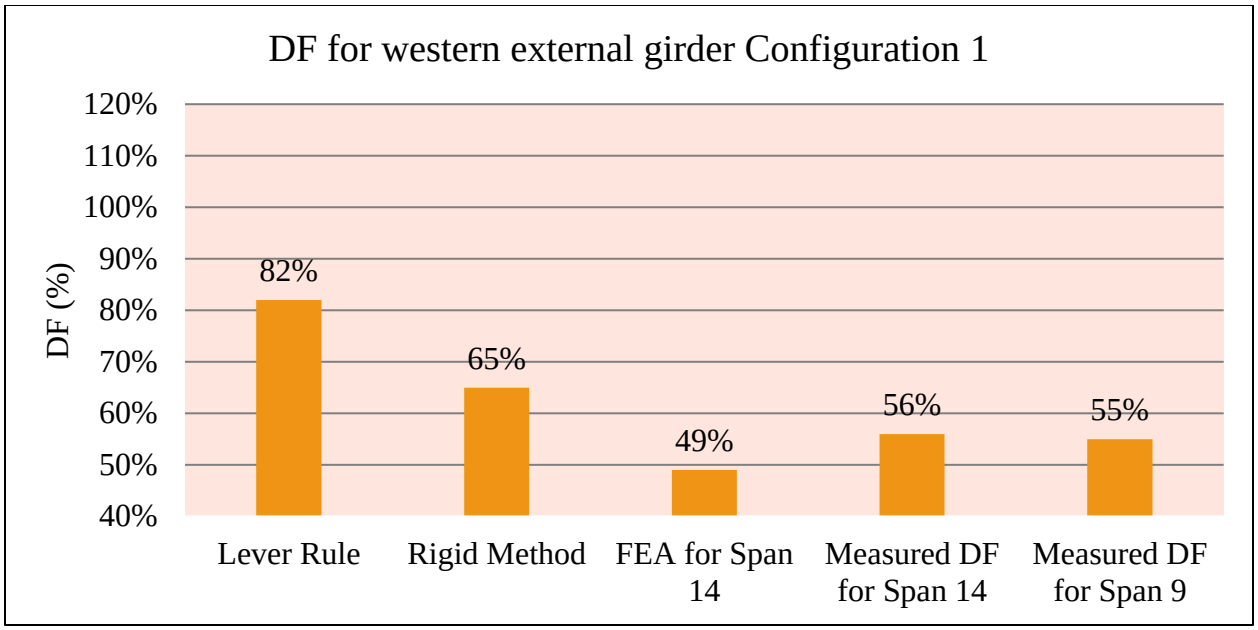

Figure 6.26: Truck Configuration 1 at midspan results for Span 14
The multiple presence factors is not included.

Figure 6.26 displays the midspan distribution factors from the load test, FEA, the lever rule, and the rigid method for Configuration 1. Comparing the load test results for Span 14, the lever rule overpredicts the distribution factor of the external West girder by about 26 % and underpredicts the distribution factor of the internal West girder by 14%. The rigid method overpredicts the distribution factor of the external West girder by about 14%. and overpredicts the distribution factor of the internal West girder by 19%.

The finite element analysis underpredicts the distribution factor of the external West girder by about 6% and underpredicts the distribution factor of the internal West girder by 2%.

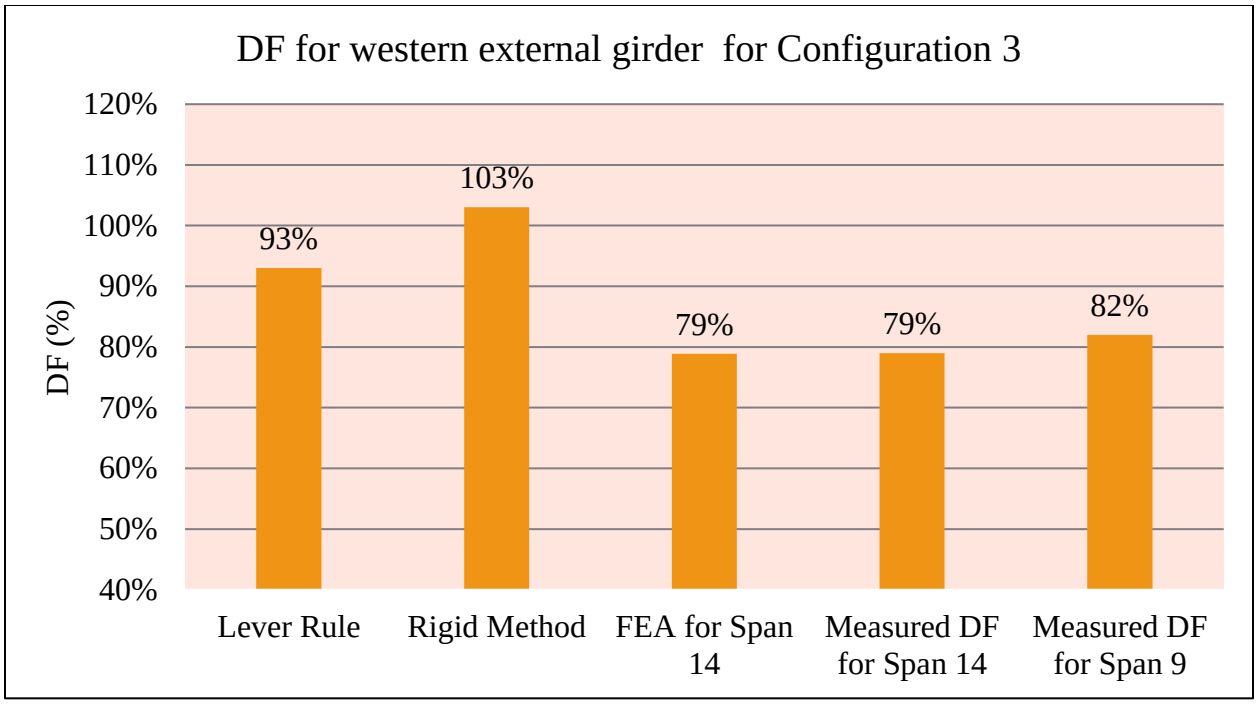

Figure 6.27: Truck Configuration 3 at midspan results for Span 14
The multiple presence factors is not included

Figure 6.27 displays midspan distribution factors for the external girder for Configuration 3 from the load test, FEA, the lever rule, and the rigid method.

Comparing the load test results for Span 14, the lever rule overpredicts the distribution factor of the external West girder by about 13%. The rigid method overpredicts the distribution factor of the external West girder by about 23. The finite element analysis underpredicts the distribution factor of the external West girder by about 1.3%.

From this analysis, it is shown that the lever rule and rigid method are conservative in the calculation of the distribution factor for external girders. In contrast, the finite element approach showed to accurately measure distribution factors. The overestimation of the distribution factors of the external girder likely means more reinforcement was used in this span then was necessary.

6.5.2 Effects of Parapets and Diaphragms

Table 6.10 and Table 6.11 tabulate results found using Finite Elements for Load Configuration 1 and Load Configuration 3. For these tests, results from the original model are compared to results in which the parapet, diaphragms, or both are taken off the model, and distribution factors are found.

FEA = Results using the original finite element model Results using the original finite element model, including parapets and diaphragms in the analysis.

FEA P0 = Results using a modified finite element model includes diaphragms, but parapets were taken out of the analysis.

FEA D0 = Results using a modified finite element model includes parapets, but diaphragms were taken out of the analysis.

FEA P0D0 = Results using a modified finite elements model, diaphragms and parapets were taken out of the analysis.

Table 6.10: Results of the Parametric Study for Load Configuration 1

Configuration 1 Distribution Factors at Midspan		
Girders	**External West**	**Internal West**
FEA (Model Contains Both Parapet and Diaphragm)	49.1%	29.7%
FEA (Without Parapet)	53.7%	30.6%
FEA (Without Diaphragm)	52.9%	29.1%
FEA (Without Diaphragm and Without Parapet)	57.7%	28.8%

Table 6.10 displays the distribution factors at midspan for Configuration 1 using finite element analysis in which secondary structural elements of the span were removed from the model.

Comparing the results of the original model of Span 14, removing the parapet increased the DF of the external West girder by 4.5 %. It increased the DF of the internal West girder by 0.9%. Removing the diaphragm increased the DF of the external West girder by 3.7 % and decreased the DF of the internal West girder by 0.6%. Removing both the parapet and diaphragm increased DF of the external West girder by 8.5% and decreased the DF of the internal West girder by -0.9%.

Table 6.11: Results of the Parametric Study for Load Configuration 3

Span 14, Configuration 3 Distribution Factors at Midspan		
Girders	**External West**	**Internal West**
FEA (Model Contains Both Parapet and Diaphragm)	78.9%	64.2%
FEA (Without Parapet)	89.7%	64.5%
FEA (Without Diaphragm)	78.5%	70.8%
FEA (Without Diaphragm and Without Parapet)	90.9%	68.1%

Table 6.11 tabulate the distribution factors at midspan for Configuration 3 using finite element analysis in which key span characteristics were removed from the model. Comparing the results of the original model of Span 14, removing the parapet increased the DF of the external West girder by 11.9% and increased the DF of the internal West girder by 0.3%.

Removing the diaphragm only and keeping the parapet decreased the DF of the external West girder by 0.5% and increased the DF of the internal West girder by 6.6%. Removing both the parapet and diaphragm increased DF of the external West girder by 11.9% and increased DF of the internal West girder by 3.9%. The results show that removing the parapets in analysis increases the distribution factor of the external girders while removing the diaphragms slightly increases the distribution factor of the internal girders. This work shows that including the parapets effectively distributes live load away from exterior girders and that diaphragms do not contribute significantly to load distribution.

6.6 Conclusions

Comparison Between Load Test Data for Span 14 and Span 9

- The distribution factors for each girder for different load testing configurations were close. Therefore, different reinforcement layouts and prestressing strands

Comparison Between Load Test Data and AASHTO Prescribed Methods:

- Lever Rule Method:
    - The lever rule method overestimates the live load distribution factor for external girders by up to 39%.
    - The lever rule method overestimates the live load distribution factor for internal girders by up to 25%.

AASHTO Specification prescribed methods significantly overestimate the distribution factors for bridge girders. The lever rule significantly overpredicts distribution factors of external girders by up to 39%, meaning a significant amount of unnecessary reinforcement is needed to meet design standards. The rigid method overpredicts distribution factors of external girders by up to 30%, meaning that significantly less reinforcement is needed to meet design standards than the lever rule.

Finite Element Modeling

- The distribution factors for bridge girders can be predicted with finite element analysis. However, the engineer should know that several parameters cannot be included in the models. The Finite element model underpredicts the live load distribution factor by 6% for the external girder and overestimates the DFs by 6% for the internal girder.

Inclusion of Secondary Stiffness Elements (Parapet) and Diaphragm in the DFs.

- The investigation of the effectiveness of the inclusion of the secondary stiffness elements and diaphragm using the Finite Element Models are:
    - When the model's parapets were removed, the distribution factors of the external girder went up by a maximum of 10.8%. In contrast, the distribution factors for internal girder went up by a maximum of 0.9%.
    - When the diaphragm was removed from the model, the load distribution factors for the external girder went up by a maximum of 3.7% and a maximum of 6.6% for internal girders.
    - When both diaphragms and parapets were removed from the model, the distribution factor of the external girder increased by a maximum of 11.9%.
    - **The results from the finite element analysis show that the parapets help distribute the loads around more than the diaphragms do by making the concrete deck more rigid.**
        - **No current method considers how parapets affect live load distribution, but several methods do consider how diaphragms affect it.**
        - **The diaphragm and parapet should be included in the DF calculation.**

To accurately evaluate the distribution factors of bridge girders, a more accurate method will need to be developed. There is a large margin of error associated with the lever rule. Because of this, it is strongly recommended to refrain from using it in almost all situations. The finite element method, explored in this work, is recommended for use in complex situations; nevertheless, the amount of time required to construct a model makes it inefficient for use in normal practice. It is recommended that the rigid technique be utilized whenever it is applicable because the AASHTO-prescribed method is the way with the highest level of accuracy.

6.6.1 Recommendations

- The AASHTO methods always overestimated DF's. The rigid method is preferred for analysis because the load test results closely match the rigid method's results. It is also suggested that when a single lane is full, multiple presence factors should not be used in the analysis.
- The result of the Parametric Study shows the effectiveness and contribution of the inclusion of the secondary stiffening elements (parapets) and Diaphragm to load distribution between exterior and interior girders. Therefore, the results of this research recommend that the contribution of the secondary stiffening elements and diaphragms (combined) should be considered for the estimation of Live Load Distribution for Bridge Evaluation (Only).

CHAPTER VII

7. EVALUATION OF THE EFFECTS OF NEW EMERGENCY VEHICLE LOADS ON THE LOAD RATING OF STEEL GIRDER IN OKLAHOMA BY PROOF LOAD TESTING THE PROTOTYPE BRIDGE

The FAST Act. (Fixing America's Transportation Act) made certain Emergency Vehicles (EV's) including fire trucks legal on the Interstate Highway System, which can generate large load effects for bridges when compared to other legal truck loads. Therefore, the EV Loadings now must be considered when load rating and posting bridges within the range of reasonable access to the Interstate Highway System. The State of Oklahoma and ODOT chose the EV-3 as a representative vehicle from this group of trucks. The EV-3 features two 31-kip axles spaced at 4' centers with a third axle spaced at 15 from the tandem with an axle weight of 24 kips. This gives the EV-3 a combined weight of 86 kips is significantly larger, and with smaller axle spacings than either the HS-20 truck (72 kips with 28 ft. total span) or the design tandem found in the current AASHTO LRFD Bridge Specifications. Testing was performed on a steel girder bridge with an 8 in. composite concrete deck. The test bridge was constructed at the Bert Cooper Engineering Laboratory at Oklahoma State University, and same span and cross-section properties as the SH 14 Bridge over Eagle Chief Creek in Woods Co., OK.

From the results of the testing program, we conclude that steel girder bridges in Oklahoma, of which more than 1600 exist on the State Highway System, can support the EV-3 loadings without concern for posting loads or limiting access for emergency vehicles. Moreover, the testing demonstrates that generally accepted engineering principles can be used to predict bridge response to the EV-3 loadings mandated by the FAST ACT. It should be noted, however, that each bridge should be investigated individually by a qualified engineer to make final determination whether an individual bridge should be posted to limit truck weights or access by EV's since each bridge has variations in design details, spans, and section properties.

7.1. Introduction:

The Highway transportation infrastructure within the United States (USA) is aging. Today in the United States there are more than 617,000 bridges. Of those bridges, 42% of the bridges are over 50 years old. Also, 46,154 or 7.5% of the nation's bridges are considered structural deficient by the National Bridge Inventory (ASCE, 2021).

Within the State of Oklahoma, approximately 43 percent of ODOT's 3727 bridges are listed as steel girders bridges. Many of these are originally constructed in the 1950s, 1960s, and 1970s with the build-out of the Interstate Highway System.

Figure 7.1 shows that the ODOT Bridge Inventory contains 1618 Steel Girder Bridges, and that construction of these bridges peaked during the 1960s. Figure 7.2 shows the estimated replacement cost of those same bridges (Russell et al, 2015).

With data show that with each passing year, the number of bridges that are over the age of 80 increases. In the year 2020, ODOT will have, within its inventory, nearly 1400 bridges that are

over the age of 80. Figure 7.3 shows the advancing age of the ODOT Bridge Inventory year by year.

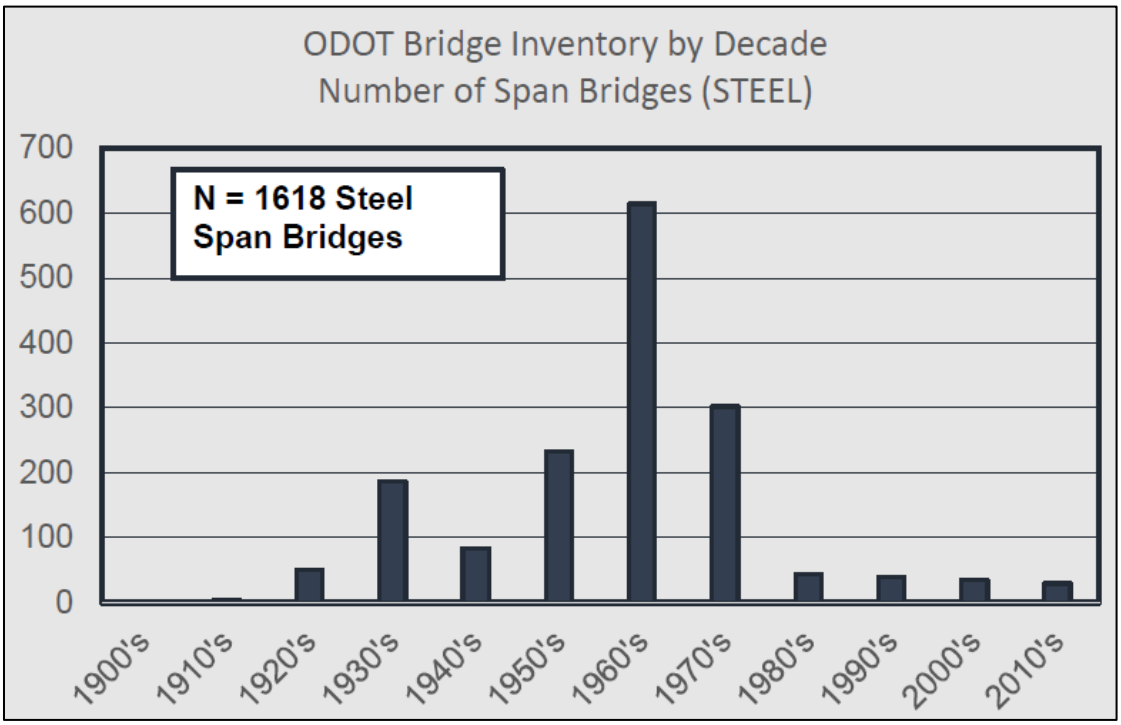

Figure 7.1: ODOT Steel Girder Bridge Inventory by Decade (Russell et al, 2015)

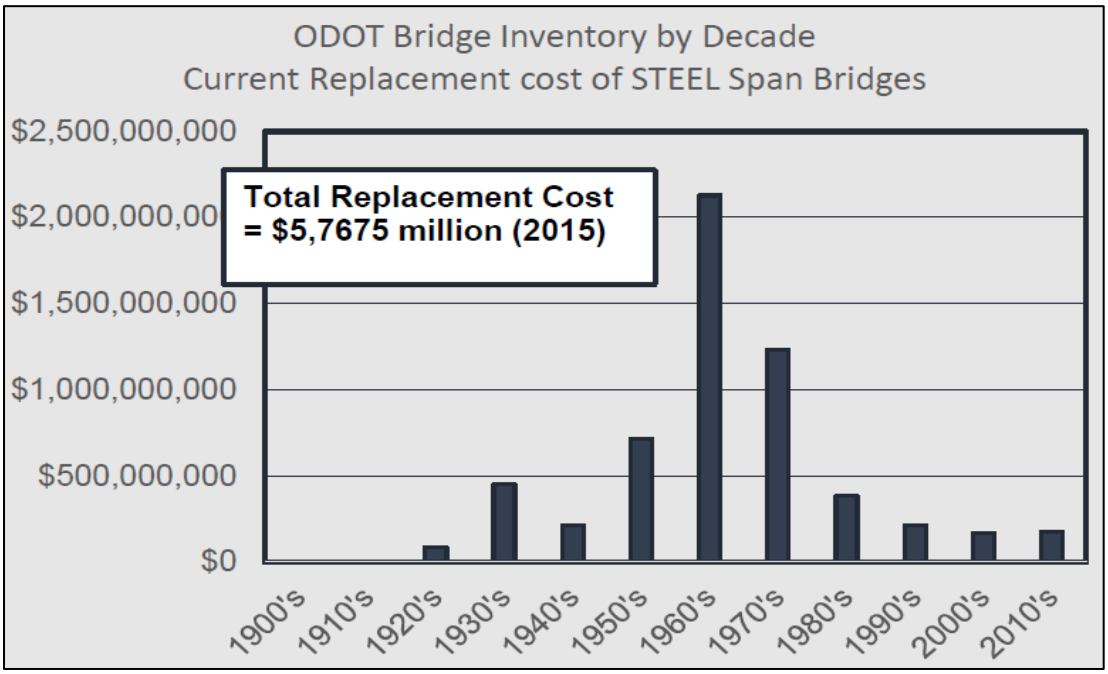

Figure 7.2: Total Replacement Cost of Steel Girder Bridges (Russell et al, 2015)

From a policy point of view, the ODOT manages a bridge inventory with an overall replacement cost of approximately $12 billion. This is the asset base for bridges constructed, owned, and maintained by the ODOT. Annually, the transportation budget is a fraction of that cost, so it is imperative that ODOT manages its resources to ensure the optimization of resources to benefit taxpayers and highway users. Accordingly, research and testing programs like this one are an imperative part of that management program to ensure that structures, like our 1600 steel bridges in the State of Oklahoma, are (1) capable of meeting the expectations for performance and carrying intended loads but are also (2) safe and reliable.

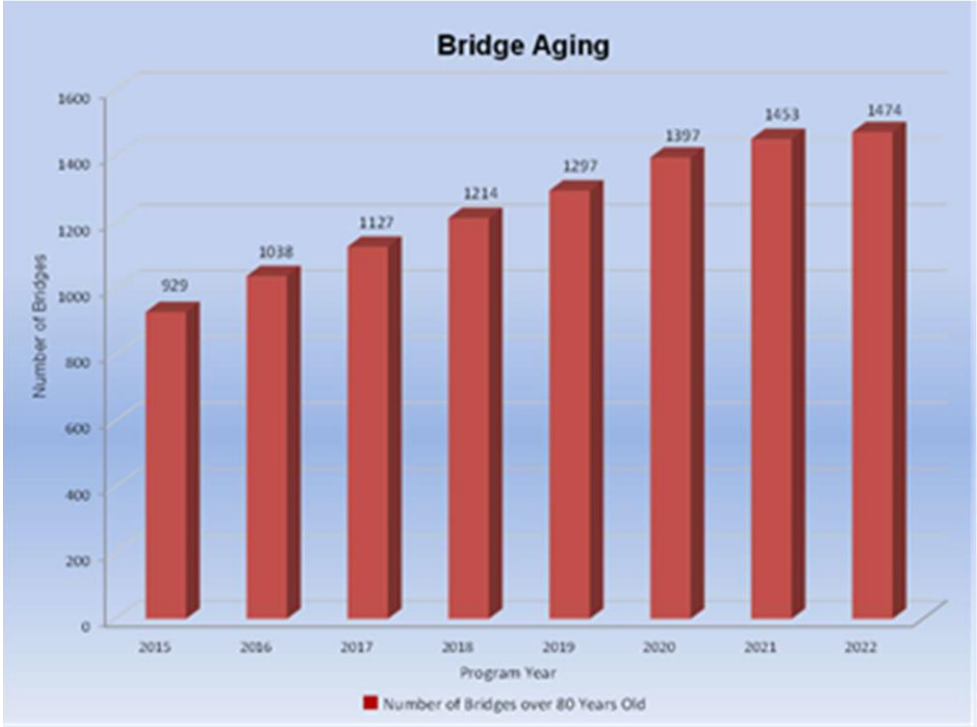

Figure 7.3: Number of ODOT Bridges over 80 years of age (Russell et al, 2015).

The following section outlines the objectives, procedures, results, and findings of an experimental study performed for the Oklahoma Department of Transportation's. ODOT has requested assistance in re-evaluating the load rating of steel girder bridge throughout the state affected by new emergency vehicle loading per a recent memo from the Federal Highway Administration (hereafter FHWA).

This chapter focuses on load rating. Load rating is defined by the American Association of State Highway and Transportation Officials' (hereafter AASHTO) Manual for Bridge Evaluation (hereafter MBE) as, the basis for determining the safe load capacity of a bridge," (AASHTO 2020).

Engineers use this procedure to ensure the general safety of bridge constructions and to lessen financial strain by extending the service life of the structure. The Load and Resistance Factor Rating (LRFR) method controls the load rating procedure. To "ensure uniform reliability in bridge load ratings, load postings, and permit determinations," this methodology was established (AASHTO 2020). This methodology consists of three procedures: design load rating, legal load rating, and permit load rating.

7.1.1. Objectives of the Research:

ODOT was tasked with re-evaluate the load ratings for all bridges affected by new emergency vehicle loading. To accomplish this goal, ODOT has reached out Oklahoma State University for assistance in rating the steel girder bridges that would be affected. FHWA has stated that all bridges on Interstates System and withing reasonable access to the interstate systems are required to be rated for the new Emergency Vehicle by December 31,2019. (Hartmann 2016)

The existing bridge in the laboratory at Oklahoma State University provides a unique opportunity to study the stresses and strains on a full load from an EV3 loading. The purpose is to apply shear and moment loads in accordance with the FAST Act EV3 loading to the existing 40 ft. span bridge structures in the Bert Engineering Cooper Laboratory. Using additional instrumentations to determine whether the LFR and the LRFR provides reasonable assurance of capacity for both shear and moment considering the larger of the axle loads.

7.2. Background

7.2.1. Existing Load and Resistance Factor Rating Procedures:

The LRFR procedure is explained in the following section. It includes the design methodology used, as well as the procedure's purpose and the various information gathered.

7.2.2. LRFR Loading Configurations:

AASHTO has developed a loading configuration based on an envelope of truck sizes to account for the potential live loads that a structure may be subjected to. Bridges must be designed in accordance with the LRFR procedure. The loading configuration for HL-93 loading consists of a nominal truck, HS20, shown in following figure, paired with a lane load of 0.64 kips per foot or a tandem truck paired with the same lane load. Bridges are then designed based on the worst-case load effects developed by either combination. The LRFR method requires that AASHOT LRFD Bridge specifications to be used to determine the capacity of structures' capacity for load rating.

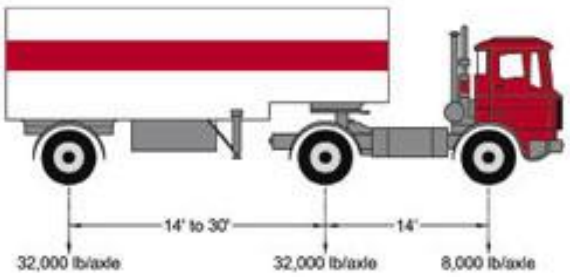

Figure 7.4: HS-20 Truck

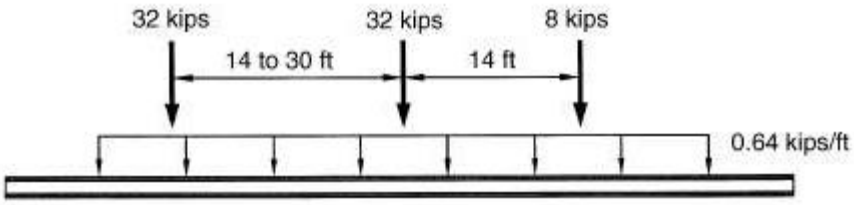

Figure 7.5: Truck and Lane Loading

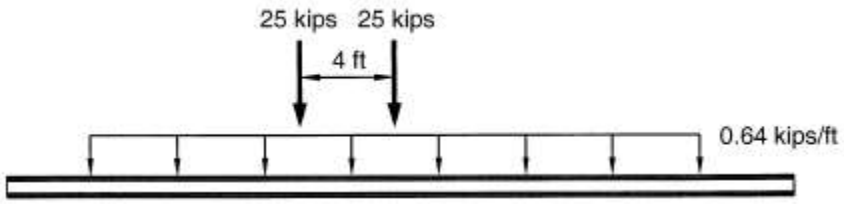

Figure 7.6: Tandem and Lane Loading

7.2.2.1. LRFR Load Rating Equation

the *AASHTO Manual for Bridge Evaluation* to determine the ***Rating Factor (RF)*** for the bridge. The equation for the ***RF*** uses the nominal strength of the bridge, the dead loads, and the live loads in its determination. The expression for the Rating Factor (RF) found in the is given:

$$RF = \frac{C - (\gamma_{DC})(DC) - (\gamma_{DW})(DW)}{(\gamma_{LL})(LL + IM)}$$

Where:

RF: Rating factor.

C: Capacity, or Nominal Strength

DC: Dead load effect due to structural components and attachments.

DW: Dead load effect due to wearing surfaces and utilities.

LL: Live load effect.

IM: Dynamic load allowance. $IM = 0.33 \times LL$

γ_{DC}: LFRD load factor for structural components and attachments (γ_{DC} *= 1.25 for Strength II).*

γ_{DW}: LFRD load factor for wearing surfaces and utilities (γ_{DC} *= 1.25 for Strength II).*

γ_{LL}: LFRD load factor for evaluation live load

γ_{DC}: load factor (γ_{DC} *= 1.35 for Strength II).*

To put it simply, the rating factor is a ratio between the capacity of a given bridge and the loads applied (Live and Dead)

Table 6A.4.2.2-1—Limit States and Load Factors for Load Rating

Bridge Type	Limit State*	Dead Load γ_{DC}	Dead Load γ_{DW}	Design Load		Legal Load	Permit Load
				Inventory	Operating		
				γ_{LL}	γ_{LL}	γ_{LL}	γ_{LL}
Steel	Strength I	1.25	1.50	1.75	1.35	Tables 6A.4.4.2.3a-1 and 6A.4.4.2.3b-1	—
	Strength II	1.25	1.50	—	—	—	Table 6A.4.5.4.2a-1
	Service II	1.00	1.00	1.30	1.00	1.30	1.00
	Fatigue	0.00	0.00	0.80	—	—	—
Reinforced Concrete	Strength I	1.25	1.50	1.75	1.35	Tables 6A.4.4.2.3a-1 and 6A.4.4.2.3b-1	—
	Strength II	1.25	1.50	—	—	—	Table 6A.4.5.4.2a-1
	Service I	1.00	1.00	—	—	—	1.00
Prestressed Concrete	Strength I	1.25	1.50	1.75	1.35	Tables 6A.4.4.2.3a-1 and 6A.4.4.2.3b-1	—
	Strength II	1.25	1.50	—	—	—	Table 6A.4.5.4.2a-1
	Service III	1.00	1.00	Table 6A.4.2.2-2	—	1.00	—
	Service I	1.00	1.00	—	—	—	1.00
Wood	Strength I	1.25	1.50	1.75	1.35	Tables 6A.4.4.2.3a-1 and 6A.4.4.2.3b-1	—
	Strength II	1.25	1.50	—	—	—	Table 6A.4.5.4.2a-1

* Defined in the *AASHTO LRFD Bridge Design Specifications*

Figure 7.7: AAASHTO 2019, Load Factors for Load Rating

7.2.3. FHWA Bridge Formula

The bridge formula that was implemented in 1975 is given as follow:

$$W = 500 \times \left[\frac{L \times N}{N-1} + 12 \times N + 36\right]$$

Where:

W: Maximum Weight (lbs) that can be carried by two or more adjacent axles

L: Spacing in feet between the outer axles being considered

N: number of axles considered

is important to note that all trucks previously used to rate bridges as legal loads, including HL-93 loading, comply with this formula. However, the new EV3 trucks' load distributions are in excess

of the limits of the formula and would not be considered as a legal load. Instead, the EV3 trucks would need to be permitted as overweight vehicles.

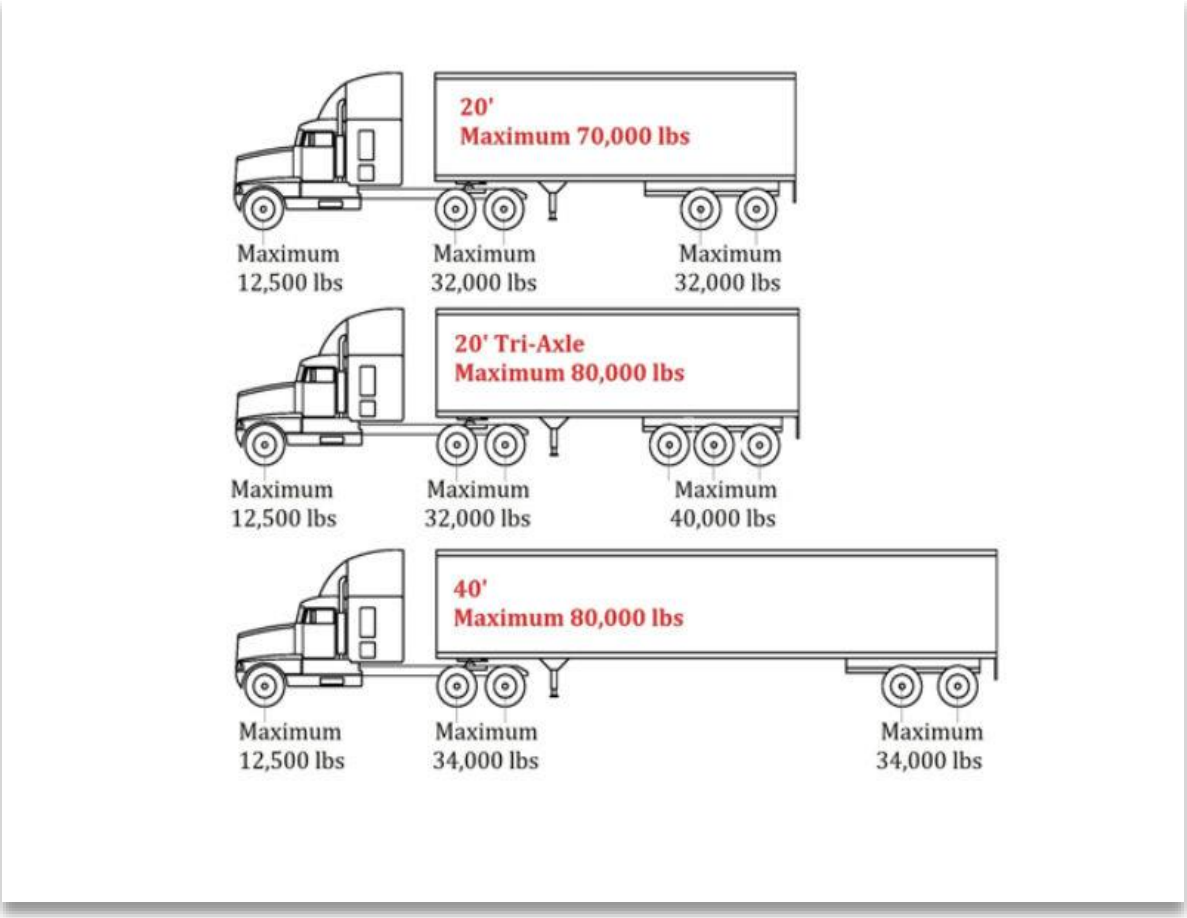

Figure 7.8: Trucks that conform the bridge Formula

Trucks conforming to the Bridge Formula, a.k.a. "FORMULA B." (Bridge formula weights, 2019):

- The Truck Configuration at the lower right with five axles and 80,000 GVW is typical.
- The Bridge Formula allows rounding of 500 lbs., so the configuration shown at lower right is 80,500 lbs.
- Axle Tandems are spaced at 4 ft. with maximum tandem weight of 34,000 lbs.

7.2.3.1. New Emergency Vehicle Load:

The new emergency vehicle (EV-3) features two 31-kip axles spaced at 4’ centers with a third axle spaced at 15 from the tandem with an axle weight of 24 kips. This gives the EV-3 a combined weight of 86 kips is significantly larger, and with smaller axle spacings than either the HS-20 truck (72 kips with 28 ft. total span) or the design tandem found in the current AASHTO LRFD Bridge Specifications.

7.2.4. EV3 Loads Compared to Current and Historical Design loads

The maximum bending moment and factor moment that is induced by the EV3 loads were computed for different span lengths. Figure 7.9 charts the Maximum Design Moments vs span length. Figure 7.10 charts the Factored Maximum Design Moments vs span length.

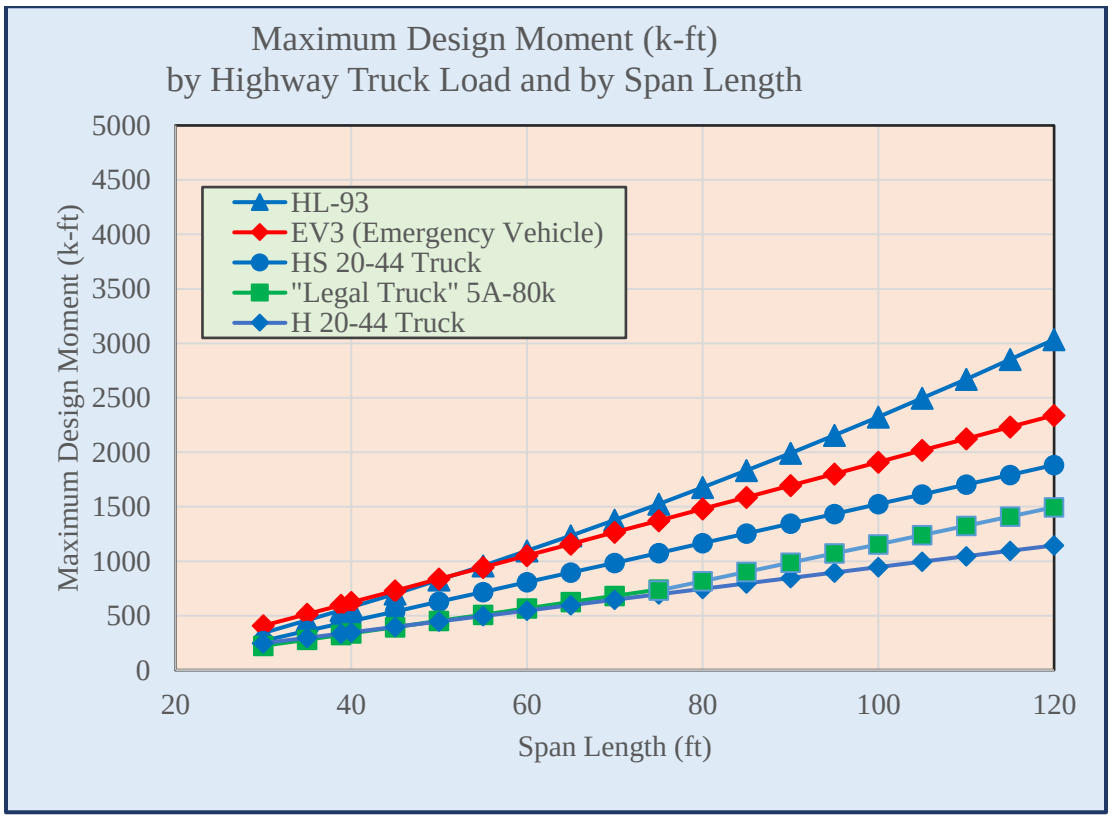

Figure 7.9: Maximum design moment by highway truck loads vs span length

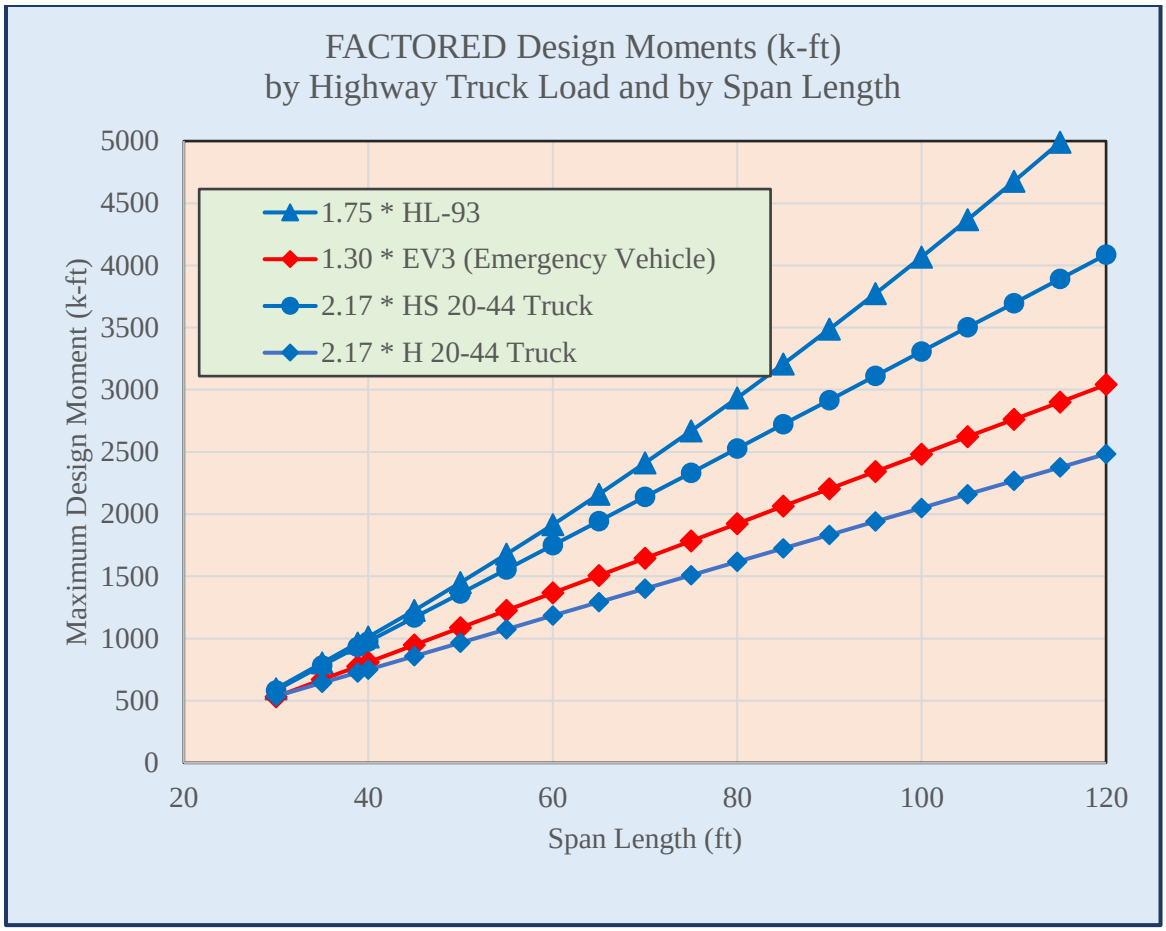

Figure 7.10: Maximum factored design moment by highway truck loads vs span length

The maximum shear force that is induced by the EV3 loads were computed for different span lengths. Figure 7.11 charts the maximum design moments vs span length. Figure 7.13 charts the factored maximum design shear force vs span length. The EV-3 produces maximum shear and maximum moment for shorter span. However, the load rating factor for emergency vehicles is 1.3 and the HL93 is 1.75. Therefore, the HL-93 produces higher shear and higher moment after being factored.

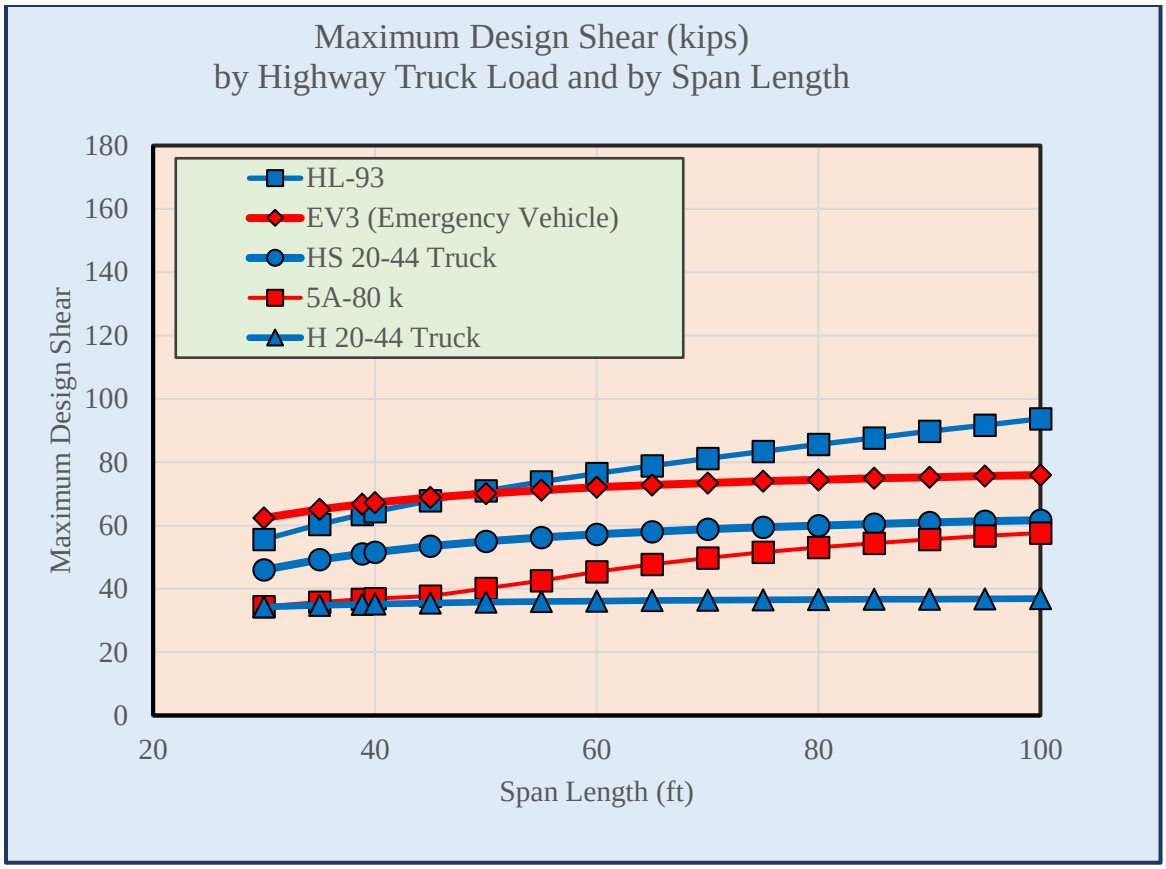

Figure 7.11: Maximum design shear by highway truck loads vs span length

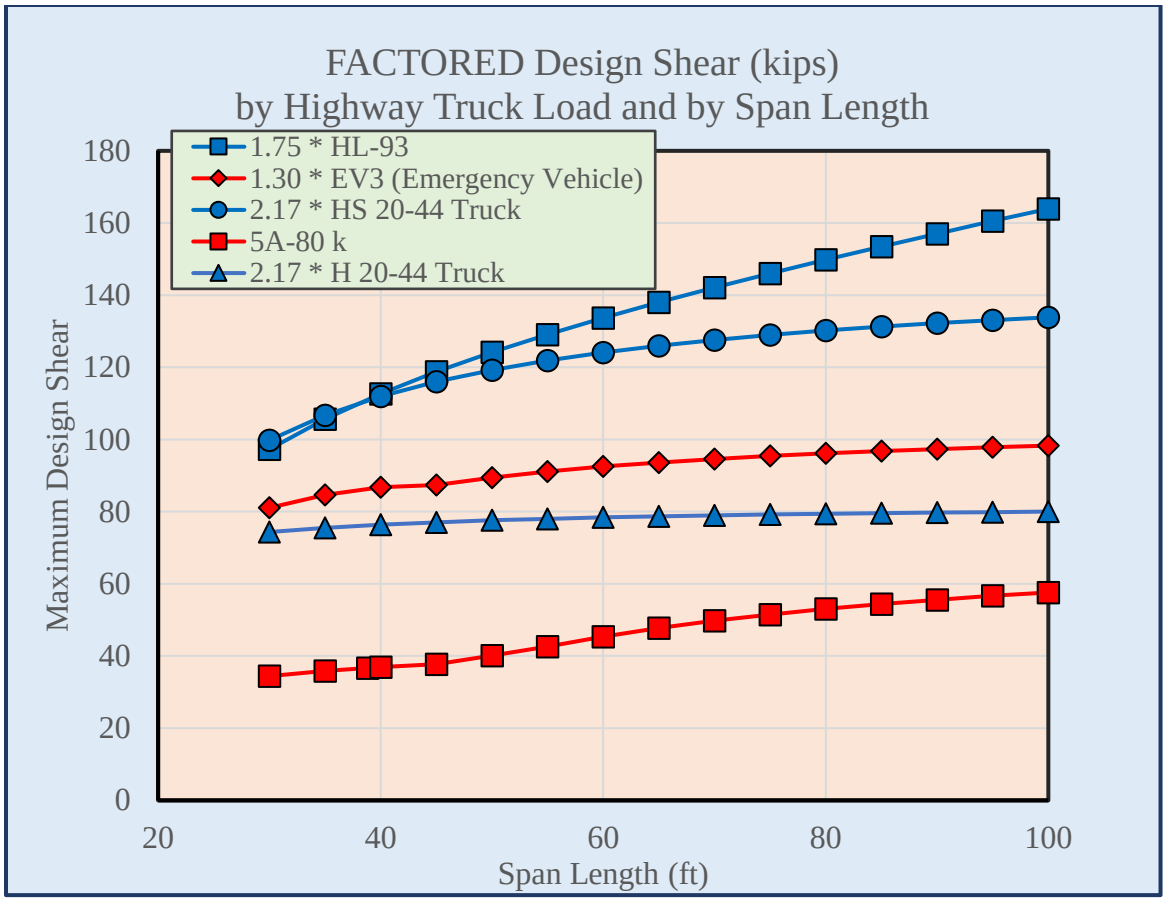

Figure 7.12: Maximum factored design shear by highway truck loads vs span length

7.3. Experimental Program

The full-scale prototype bridge was constructed at the Bert Cooper Engineering laboratory, consists of two W24x94 steel girders supporting a composite concrete deck. The bridge spans 38 ft 10 in. center to center (c/c) of the bearings. Bearings were fabricated and installed to match those found in the Eagle Chief Creek Bridge "A" in Woods Co. OK on SH 14. The concrete deck is 8 in. thick and 14 ft wide. Concrete conforms to ODOT AA concrete mixture requirements. The deck itself is 36 ft. – 0 in. in total length and is placed symmetrically on the 38.83 ft. span. The prototype bridge is shown in the following figure:

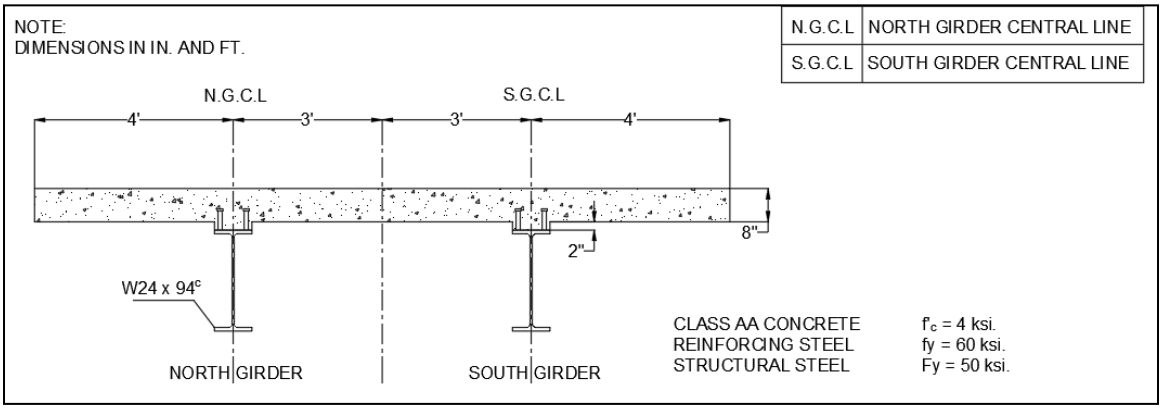

Figure 7.13: Cross Section of the lab bridge.

All together, we have installed 101 electronic gages and sensors. Their purpose was to measure and monitor concrete and steel strains, and overall bridge deflections at specific locations. Some of the instrumentations were installed prior the cast of the concrete, and some were installed later on. The instrumentation included:

1- Vibrating wire gages embedded within the concrete deck to measure strains in the hardened concrete deck.

2- Vibrating wire gages attached on the steel girders to measure strains on the steel girders.

3- Electrical resistance bonded foil gages to measure strains on the steel girders.

4- Electrical resistance bonded foil gages to measure strains on the concrete deck surface.

5- Linear variable Displacement transducers (LVDTs) to measure deflections of the bridge girders at specific locations.
6- Inclinometers to measure angle of inclination at the ends of the girders.
7- Load cells to measure the force that's applied on the spreader beams.
8- Pressure transducers, to measure the pressure that's on the hydraulic system.

Two data-loggers were used to perform the tests. The load cells and the pressure transducers and the LVDTs were wired to the CR1000X Data logger. Those sensors and data logger were programmed to record data continuously with a frequency of data collection of 1 Hz. However, all of the vibrating wire gages, and the electrical resistance gages were wired to the CR1000 Data logger. These sensors were programmed to record data continuously every minute. Because were performing a static loading. So, for each load increments, were waiting for the bridge to settle and capture a reading.

7.3.1. Load Test Scenarios:

In order to apply the EV-3 loading on the full-size prototype bridge, we have developed a testing set up. We have conducted shear tests and flexural tests on the bridge. Some of the tests were symmetric and some were eccentric (2.0 ft. offset). The targeted load for the load for both tests is shown in the table below:

Table 7.1: Targeted Load Per Load Tests

	Flexural Tests	Shear Tests
Targeted Moment or Shear for Load Rating	1134.8 kip-ft	126.5 kips
Total Load Required To be Applied	134.2 kips	156.4 kips
Load Applied per load cell	37.1 kips	78.2 kips

Flexural Tests:

The bridge was tested in four-point bending to evaluate its load deflection and its load-strain behavior. The test was conducted with an equal load applied at 16.91 ft. from the support, leaving a constant moment region of 5 ft.

Symmetric Test:

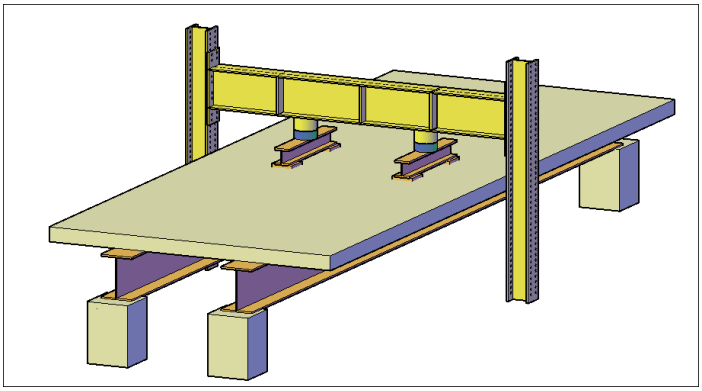

Figure 7.14: 3D view of the eccentric flexural test

Figure 7.15: Photograph of the symmetric flexural test

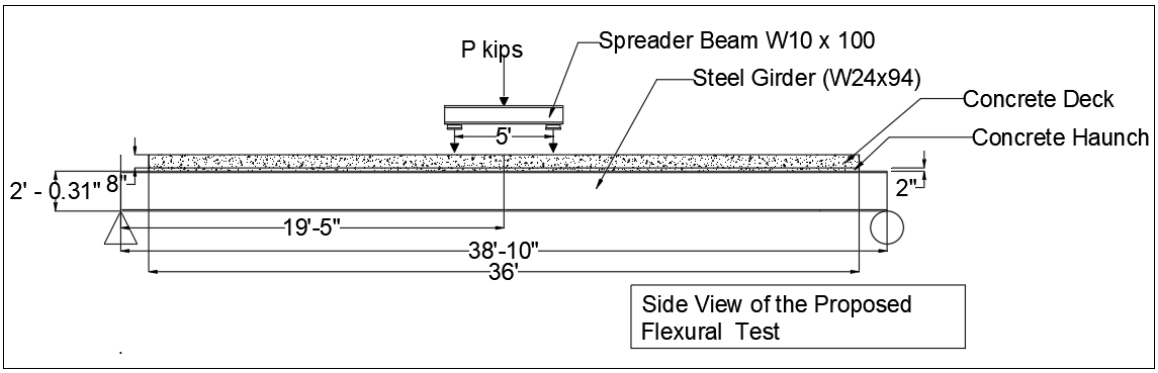

Figure 7.16: Longitudinal test schematic

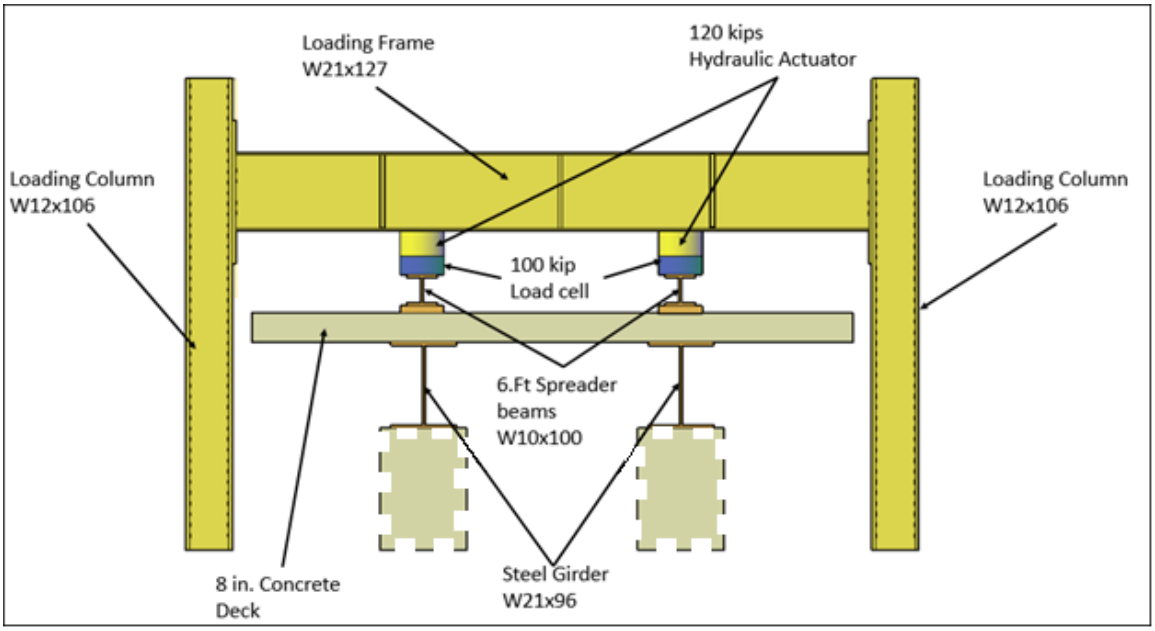

Figure 7.17: Eccentric test schematic

Eccentric Test:

In order to mimic a worst-case loading scenario for the bridge, the load was offset with 2.0 ft. from the centerline.

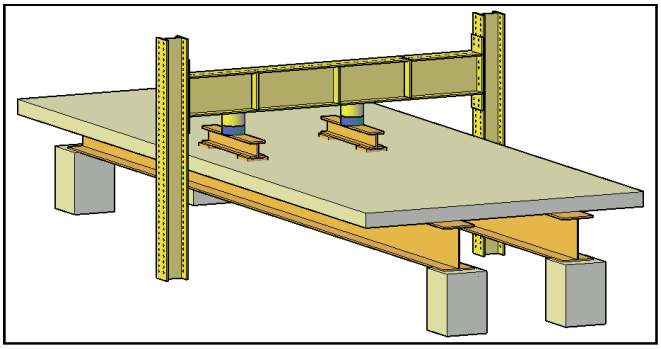

Figure 7.18: 3D schematic of the eccentric oat midspan.

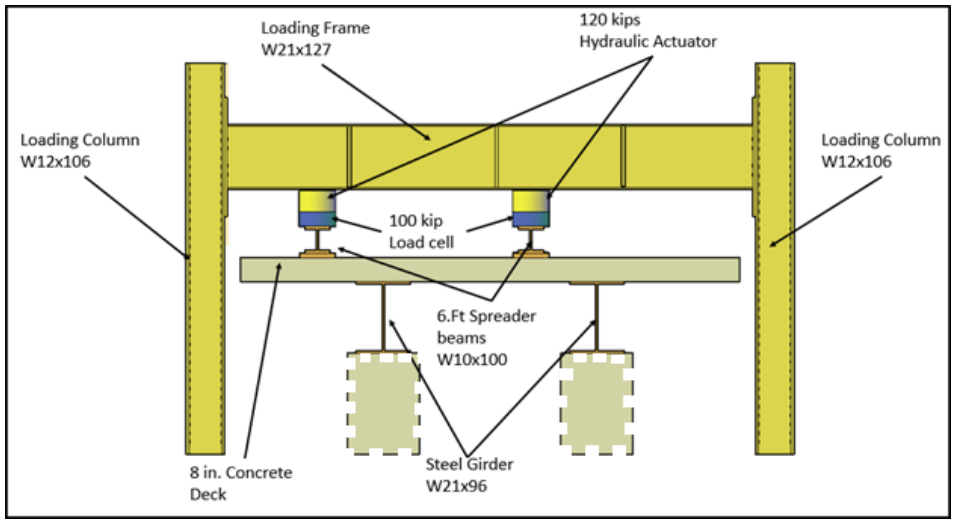

Figure 7.19: Schematic of the eccentric test at midspan.

Figure 7.20: Photograph of the eccentric flexural test

Shear Test:

Symmetric test:

The bridge was tested in four points bending to evaluate its load-deflection and its load-strain behavior. The test was conducted with an equal load on both spreader beams. The goal was to create three constant shear force regions and almost a constant bending moment region. Four-fifths of the load is applied at 77 in. from the supports, and one-fifth of the load is applied at 137 in. from the supports.

The proposed testing set-up is shown in Figure 7.21. Figure 7.22 and shows the 2D eccentric test schematic of the test.

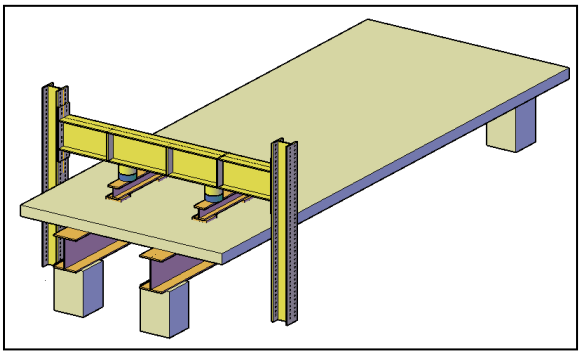

Figure 7.21 Symmetric shear test set up

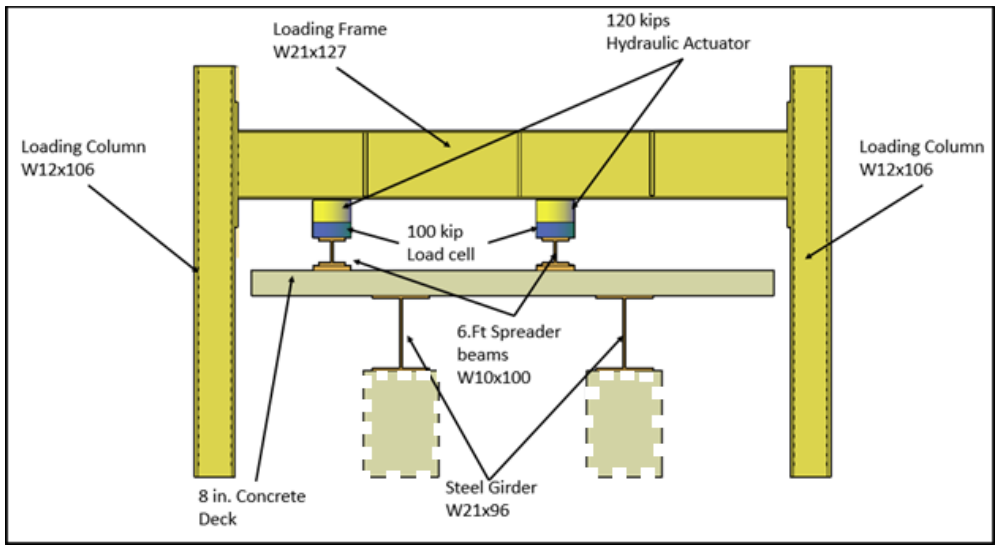

Figure 7.22: Eccentric shear test schematic

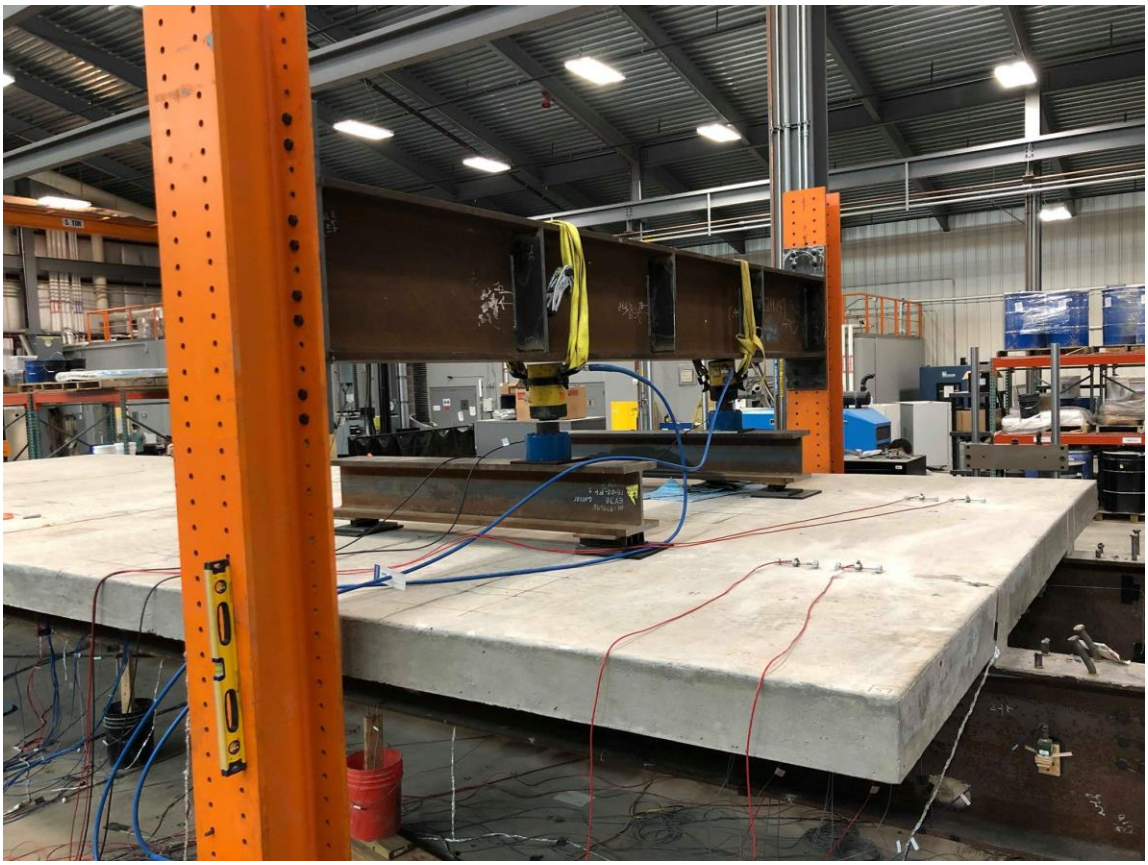

Figure 7.23: Photograph of the symmetric shear test

Eccentric test:

To simulate a worst-case loading scenario for the bridge, we decided to offset the load by 2.0 feet from the centerline. So that we may comprehend and study the transversal flexural behavior of the composite beam. The proposed testing set-up is shown in Figure 7.24. Figure 7.25 shows the 2D schematic of the test.

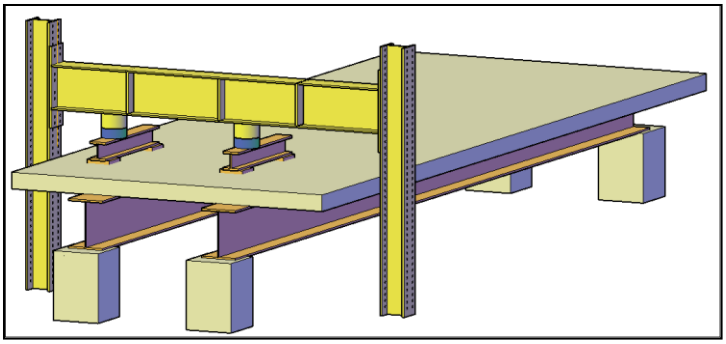

Figure 7.24: 3D Eccentric shear test set up

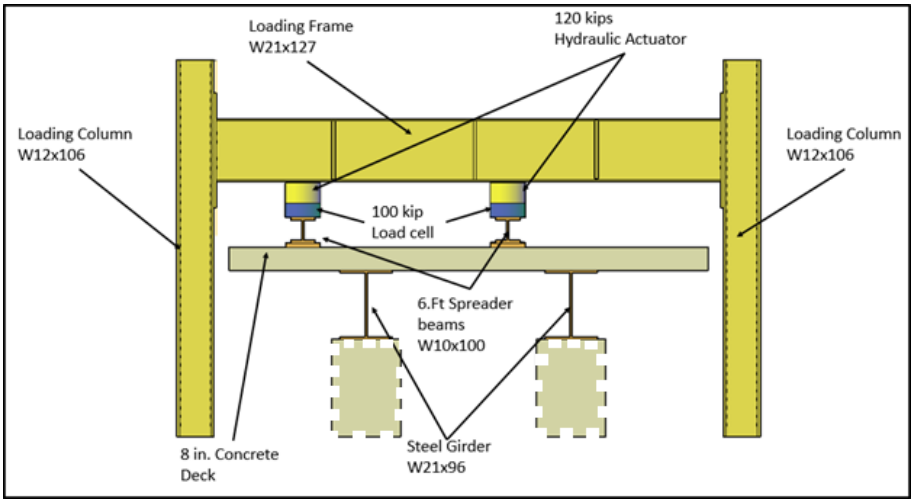

Figure 7.25: Eccentric shear test schematic

7.2. Results:

7.2.1. Flexural Tests:

Symmetric Test:

The load vs. steel girders' downward displacement at midspan is shown in Figure 7.26.. The beam behavior of the bridge seems elastic and follows the beam mechanic analysis results. The theoretical load vs. displacement curve was computed using the conjugate beam method. The load vs. deflection from the actual Loading closely matches the load vs. deflection "curve" produced from the analysis. Additionally, as the load is removed, the load vs. deflection remains substantially on the same line indicating an elastic response to the initial Loading. This figure indicates that the bridge satisfies load rating requirements under the EV-3 Loading.

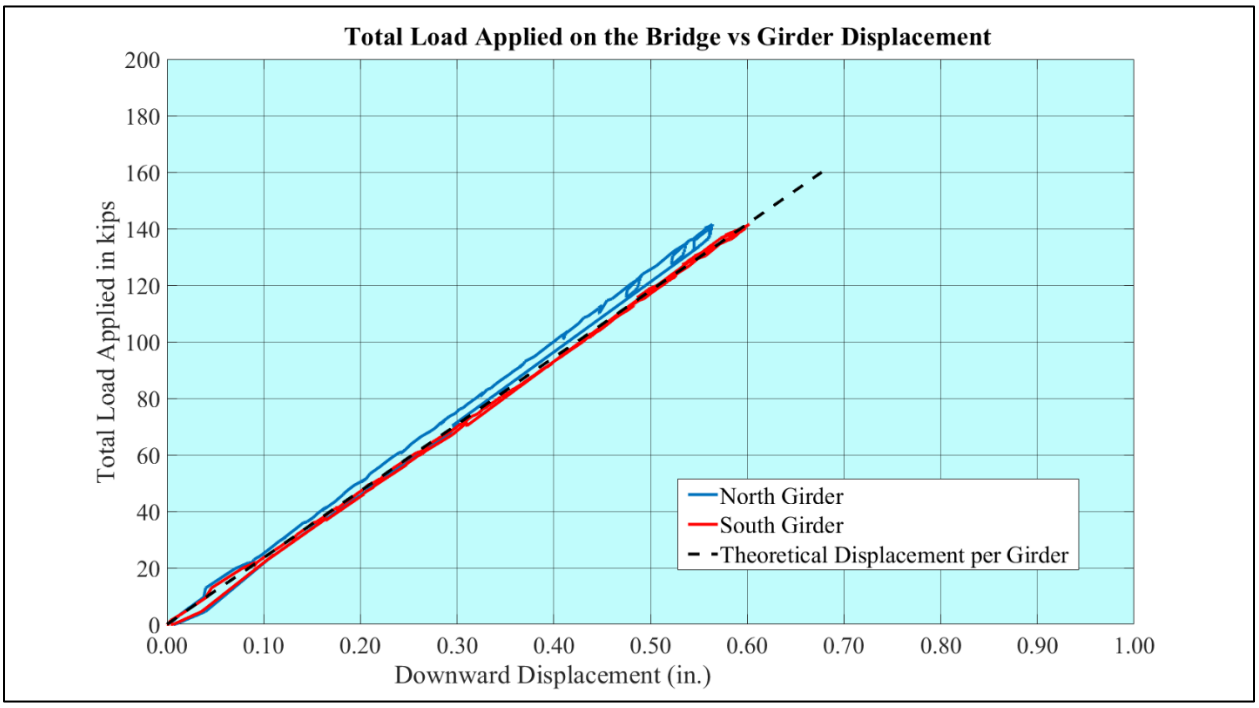

Figure 7.26: Load applied vs midspan load displacement (symmetric flexural test) Theoretical displacements were calculated using beam theory.

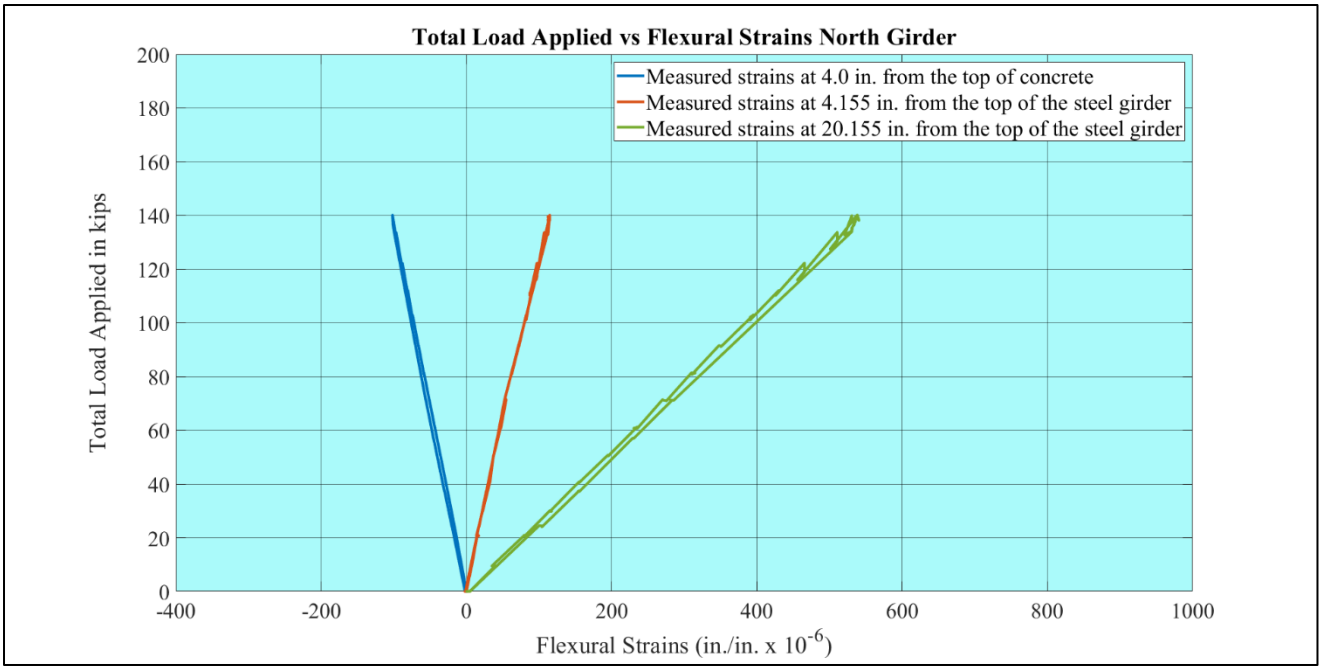

Figure 7.27: Total load applied on the bridge vs flexural strains in the north girder (symmetric flexural test)

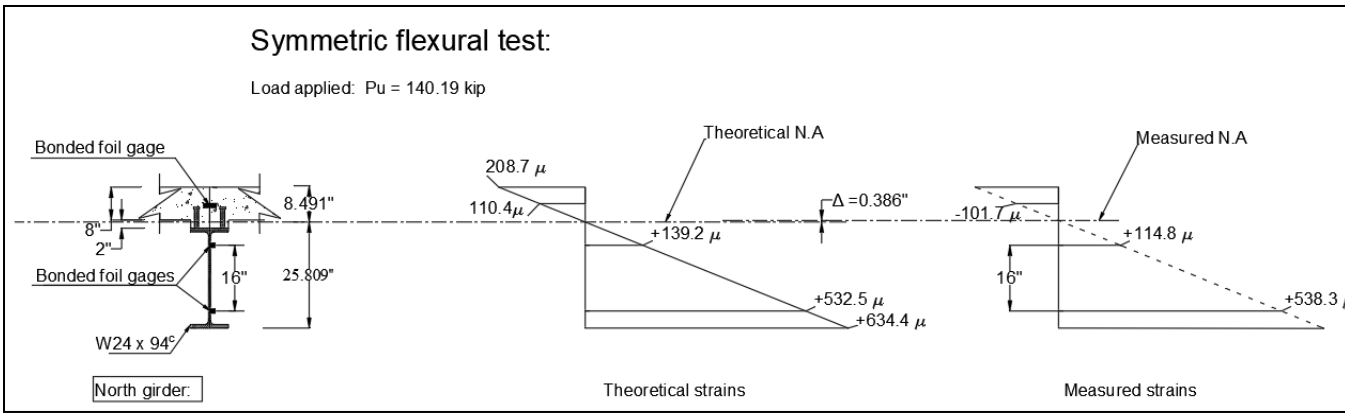

Figure 7.28: Strain profile at the mid span of the north girder (symmetric flexural test)

Figure 7.27 shows the strain profile of the composite beam at the maximum load. Strains are taken directly from gages located at various depths within the cross-section, including strains in the concrete deck and strains in the steel girder.

Concrete or steel strains are plotted vs. the “height of the beam from the bottom of the composite girder” Because the strain diagram is linear through the depth of the cross-section, this indicates

that the bridge beam is acting as a fully composite cross-section. The measured strains closely match the computed theoretical strains computed using beam mechanics. The strain data in Figure 7.28 provide strong evidence that this assumption of composite behavior through the depth of the cross-section is a good assumption for symmetric loadings that remain within the elastic limits of the materials.

Eccentric Test:

Figure 7.29 shows a sketch of the Eccentric deformed shape at the mid-span of the bridge under the maximum load. The deflection ratio of both girders is about 2/3, which differs from the beam mechanics, which is 5/6.

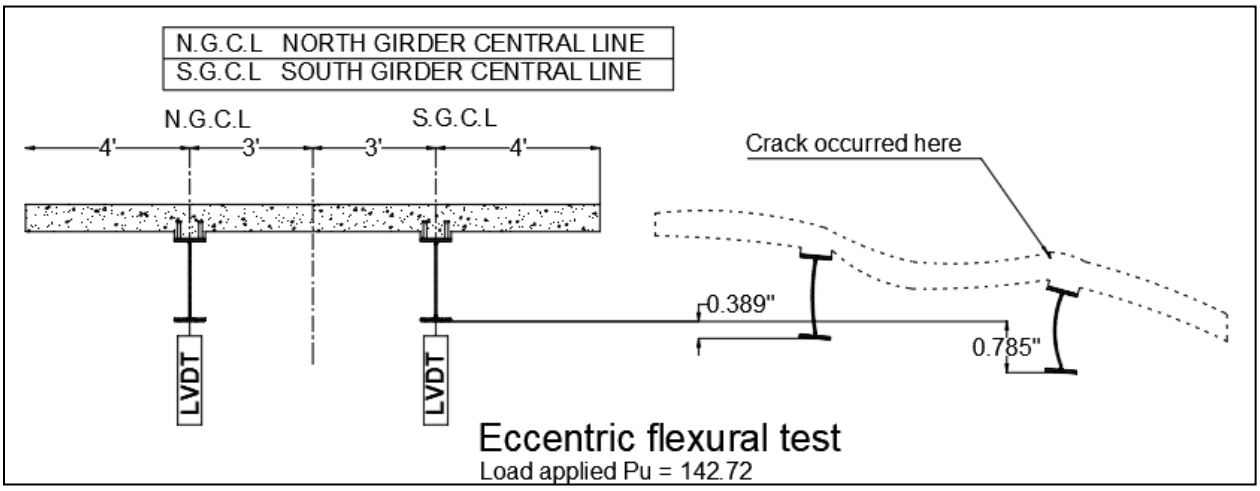

Figure 7.29: Schematic of the deflection and deformation due to 142.7 kip.

Figure 7.30 charts the load vs. steel girders' downward displacement at midspan. The bridge's beam behavior is linear elastic. Furthermore, as the load is removed, the load vs. deflection plot remains flat, indicating an elastic response to the initial loading. This figure demonstrates that the bridge meets the EV-3 Loading load rating requirements. The deflection ratio of both girders is approximately 2/3, which differs from the beam mechanics, which is 5/6.

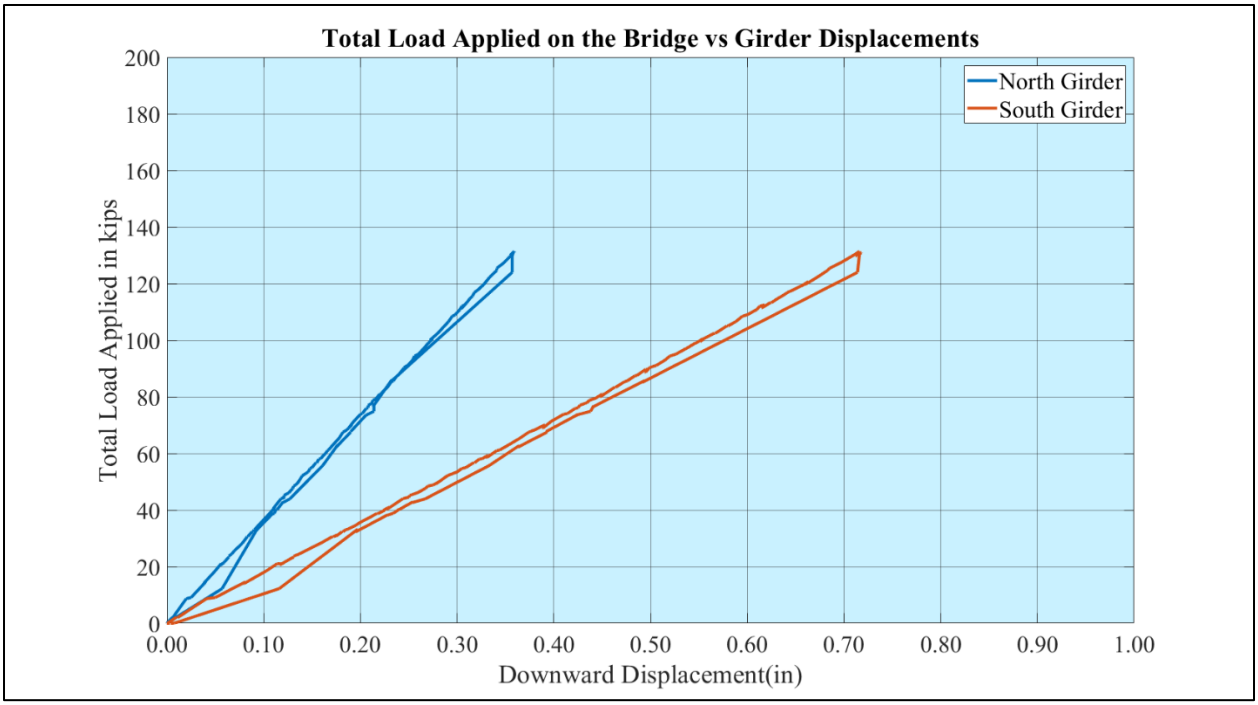

Figure 7.30: Total load applied vs midspan load displacement (eccentric flexural test)

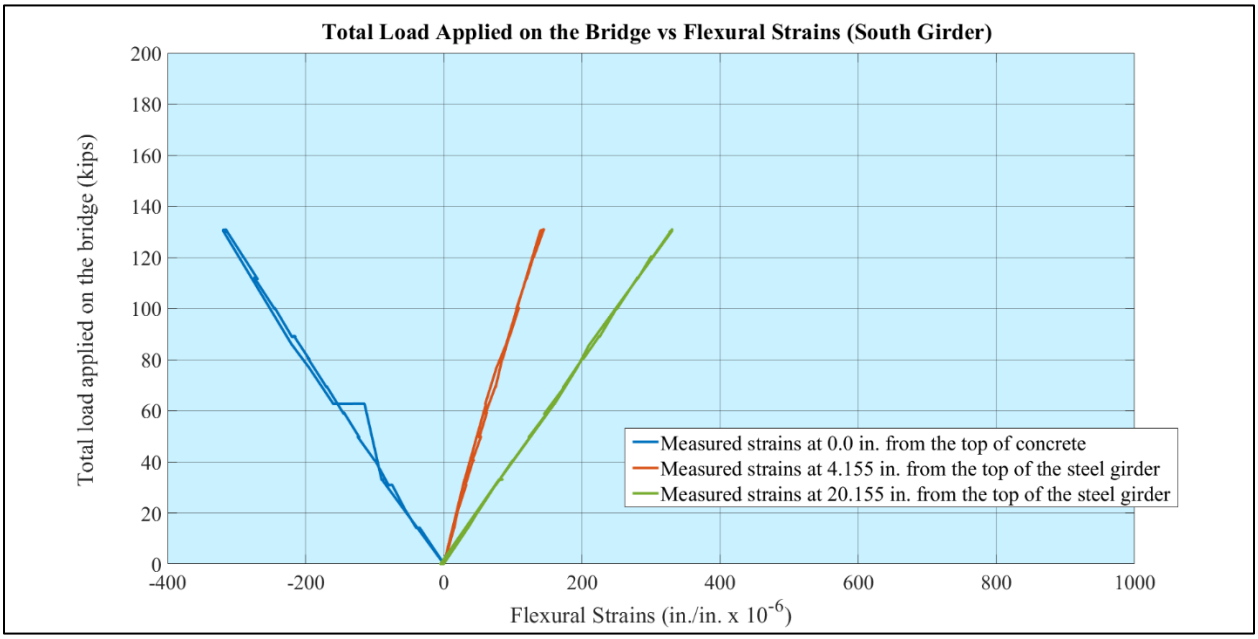

Figure 7.31: Total load applied on the bridge vs flexural strains in the south girder (eccentric flexural test)

Figure 7.31 shows the flexural strains in the south girder vs. the bending moment applied on the bridge. It appears that the changes in the strains are linear and elastic with changes in the

loadings. Additionally, when the load is removed, the strains remain substantially on the same line indicating an elastic response to the initial loading.

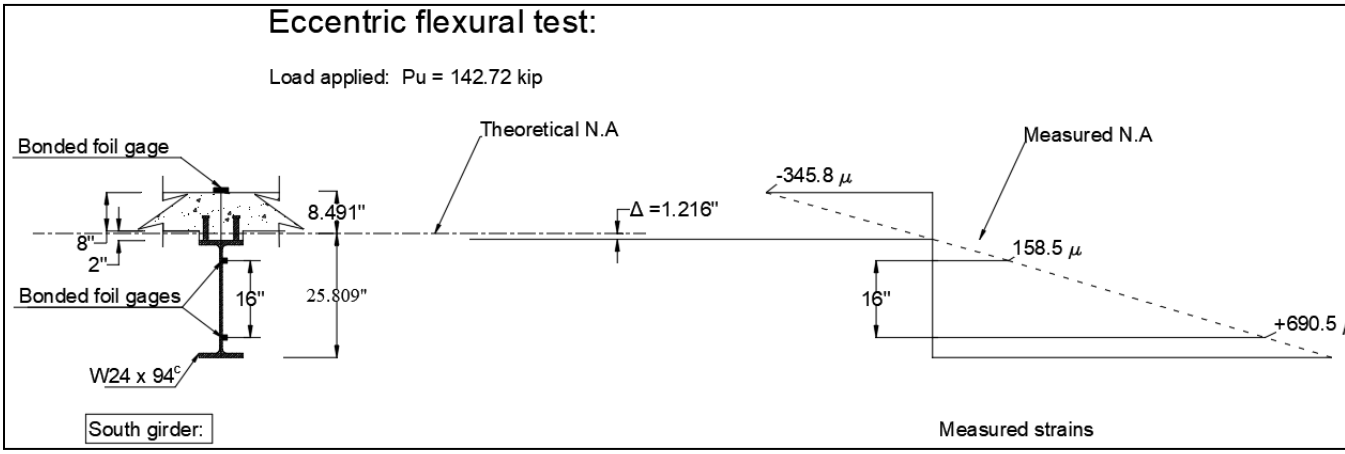

Figure 7.32: Strain profile at the mid span in the south girder (eccentric flexural test)

Figure 7.32 shows the strain profile of the south girder at mid-span. Because the strain diagram is linear through the depth of the cross-section, this indicates that the bridge beam is acting as a fully composite cross-section. It appears that the measured strains in the south girder have a ratio of 2/3 compared to the north girder. This ratio is also similar to the ratio due to the displacement.

7.2.2. Shear Tests:

Symmetric Tests:

Figure 7.33 represents the 2D schematic of the testing. Each load cell is placed underneath each actuator. To measure the load applied on the bridge from each actuator. Two LVDTs are placed under each steel girder, at 137.0 in from the support. To measure the downward displacement of each steel girder. This location corresponds to the maximum applied moment on the bridge due to this testing.

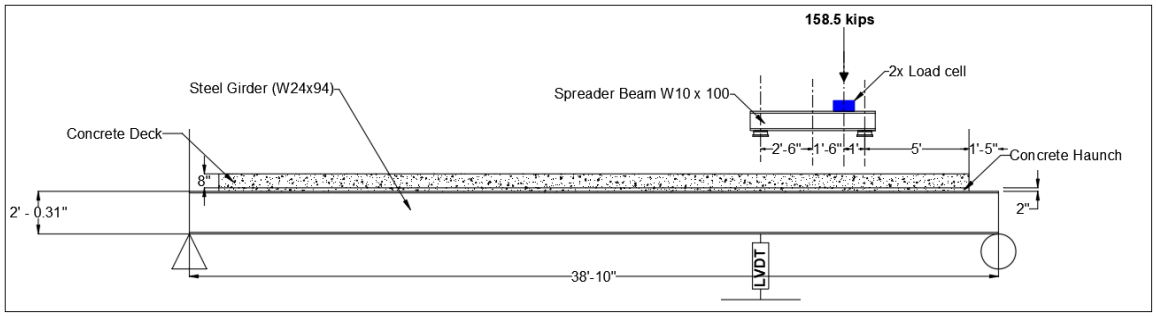

Figure 7.33: 2D schematic of the longitudinal view of the shear testing.

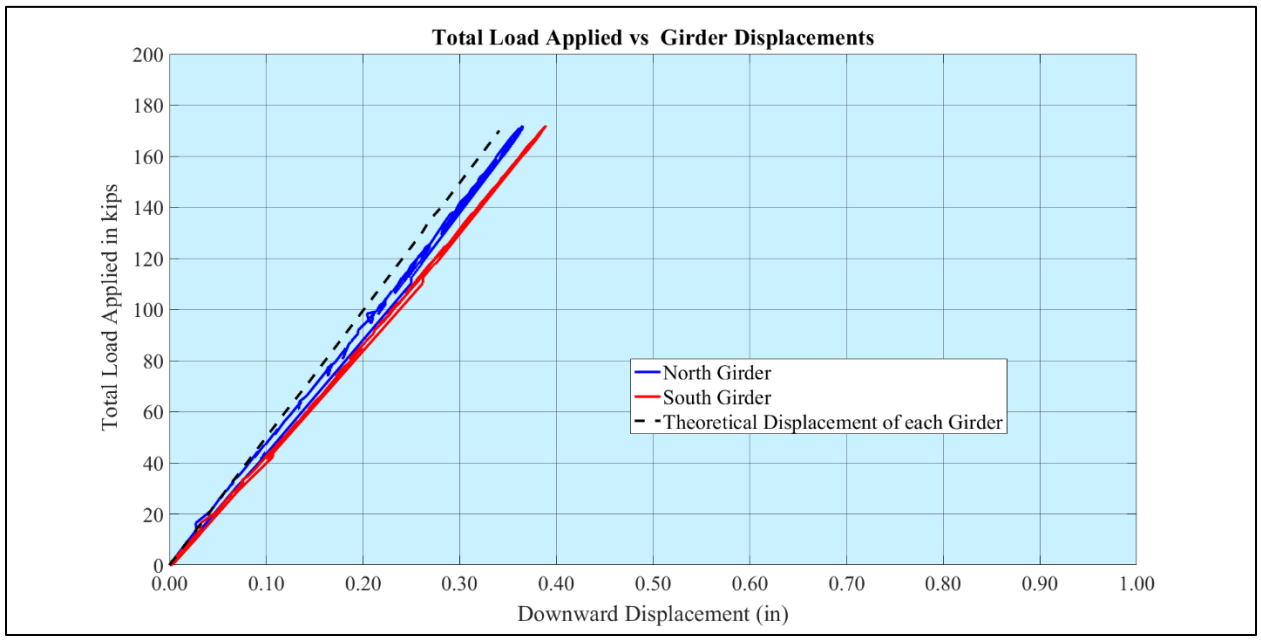

Figure 7.34: Load applied on the bridge vs downward displacement of steel girders (symmetric shear testing)

Figure 7.34 depicts the load vs. downward displacement of steel girders at midspan. The bridge's beam behavior is elastic and differs slightly from the results of the beam mechanic analysis. The conjugate beam method was used to compute the theoretical load vs. displacement curve, assuming that the bridge behaves fully compositely. Furthermore, as the load is removed, the load vs. deflection plot remains flat, indicating an elastic response to the initial loading. This figure indicates that the bridge meets the EV-3 Loading load rating requirements.

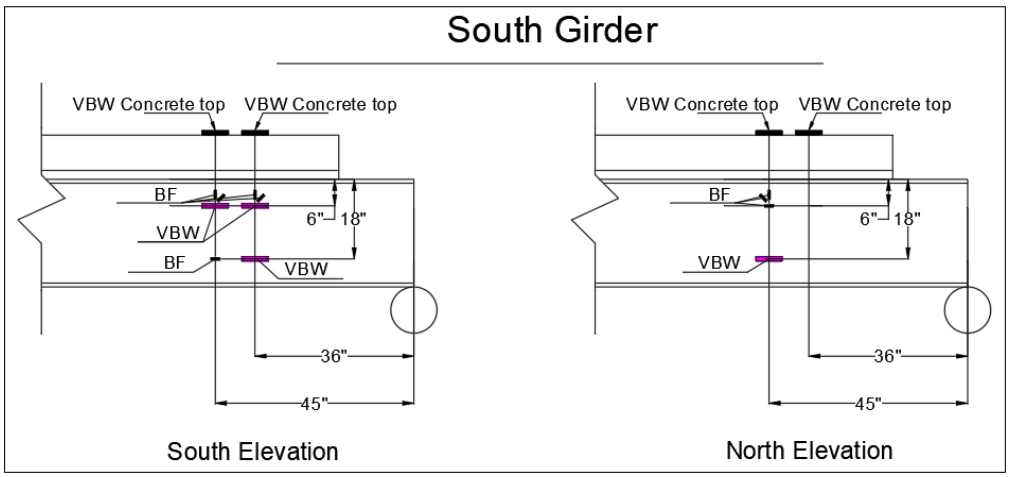

Figure 7.35: Sensors attached to south steel girder to make a rosette

Figure 7.35 represents a schematic of the location of the rosette gages on the south girder. In the south girder, a total of 16 strain gages were installed.

- 2 Vibrating wire gages were installed on top of the concrete to measure the longitudinal flexural strain.
- At 18 in. from the top of the steel girder we have attached 2 vibrating wire gages and one bonded foil gage, at 36 in. and 45 in. from the support.
- To derive the shear strain for the shear test, bonded foil and vibrating wire gages at 6 in. from the top of the steel girder were attached to measure the strains in these specific locations and at different angles.

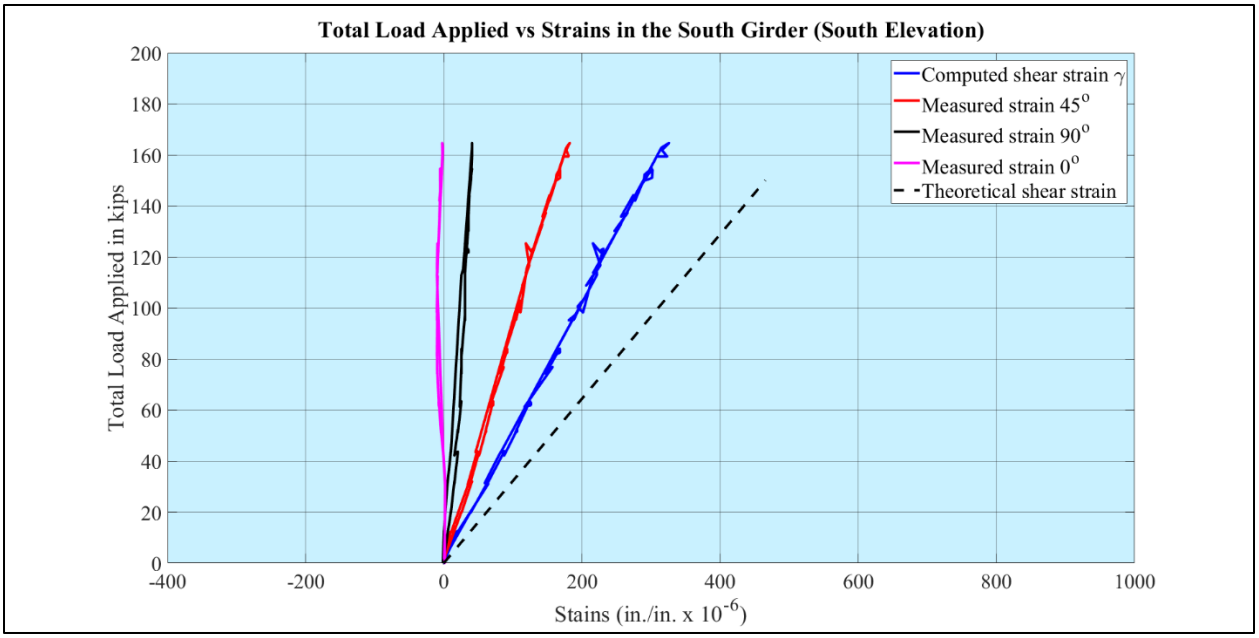

Figure 7.36: Total load applied applied on the bridge vs strains measurements at 45.0 in from the support in the south girder (south elevation) (symmetric shear testing)

Figure 7.36 shows the applied load of the bridge vs. the measured strains and the computed shear strain, and the theoretical shear strain at 45.0 in from the support location in the south girder. Our first observation is we can notice that all the strains behaved elastically. The 45° strain and the 90° strain, and the shear strains behaved linear elastic. However, the horizontal strain 0° is nonlinear. When no load is applied, the strain starts at 0μ strain, and at maximum shear force (130 kips), the strain is measured to be 0μ. But it remains elastic.

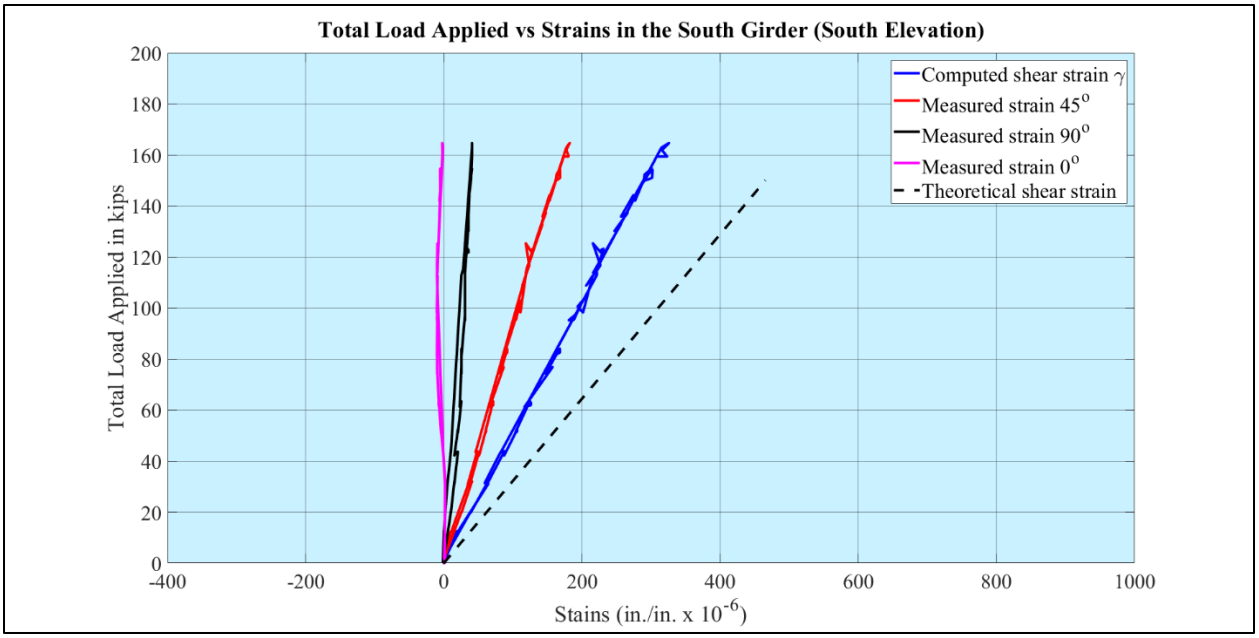

Figure 7.37: Shear applied on the bridge vs strains measurements at 45.0 in from the support in the south girder (south elevation) (symmetric shear testing)

Figure 7.37 shows the total load applied on the bridge vs the flexural strains on the south girder at 45 in. from the support (south elevation). We can notice that the changes of the strains are linear elastic with changes of the loadings in the concrete strain and in the bottom steel. Additionally, when the load is removed the strains remain substantially on the same line indicating an elastic response to the initial loading. However, the strain in the top of the steel girder seems to have a nonlinear behavior.

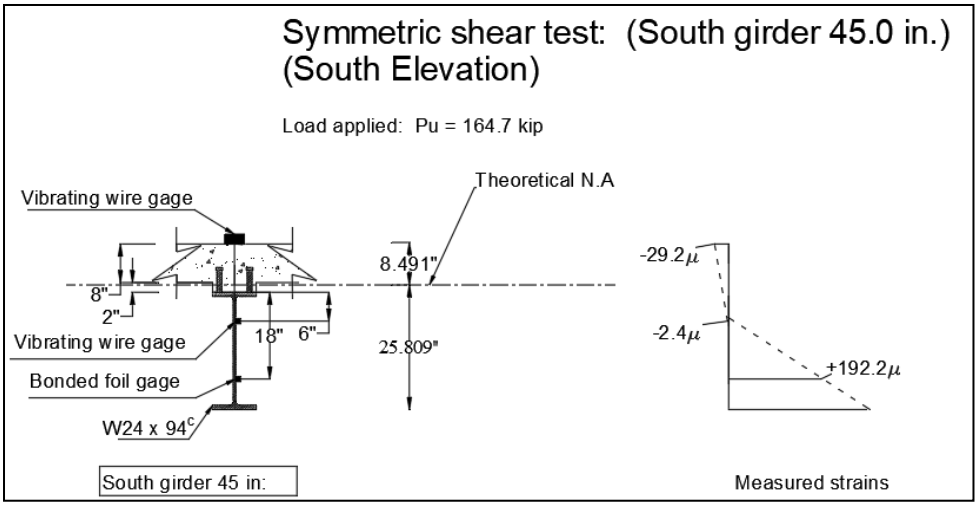

Figure 7.38: Strain profile of the south girder at 45.0 in. from the support (South Elevation)

Figure 7.38 shows the strain profile of the composite beam in the north girder. Strains are taken directly from gages located at various depths within the cross section including strains in the concrete deck and strains in the steel girder. Concrete or steel strains are plotted vs. the "height of the beam from the bottom steel girder" Because the strain diagram is not linear through the depth of the cross section, this indicates that the bridge beam is not acting as a composite cross section.

Eccentric Test

Figure 7.39 depicts the load vs. steel girders' downward displacement at the loading point. The graph shows that the load vs. deflection remains linear-elastic and that when the load is removed, the load vs. deflection retraces the loading curve. This figure indicates that the bridge meets the EV-3 Loading load rating requirements. During the loading and unloading process, cracks were discovered. Figure 7.40 depicts an idealization of deformations in the composite concrete deck as well as deformations caused by eccentric loading. It's worth noting that the applied load of 160,000 lbs. is roughly double that of the EV 3 truckloads. The deflection ratio of both girders is approximately 2/3. This is in contrast to beam mechanics, which is 5/6. During the eccentric flexural test, the same ratio was observed.

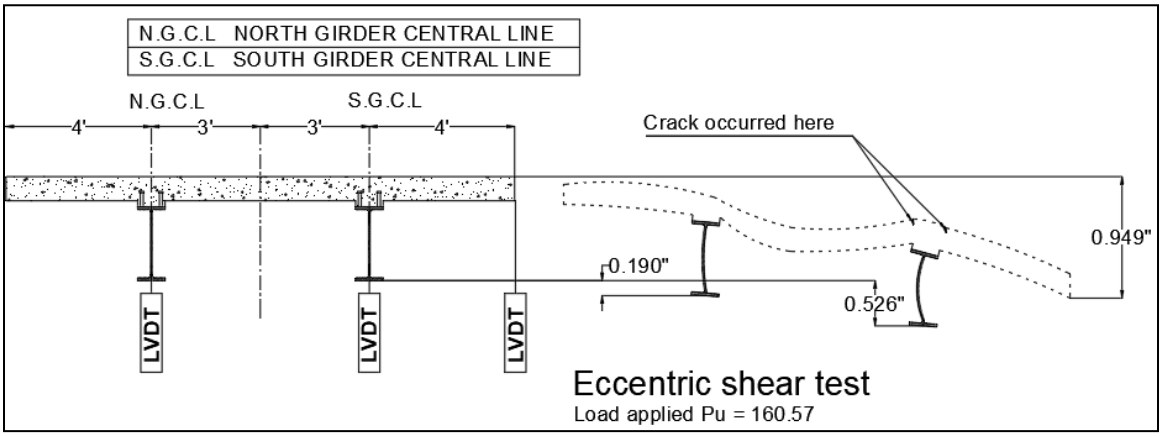

Figure 7.39: Schematic of the deflection and deformation due to 160.6 kip.

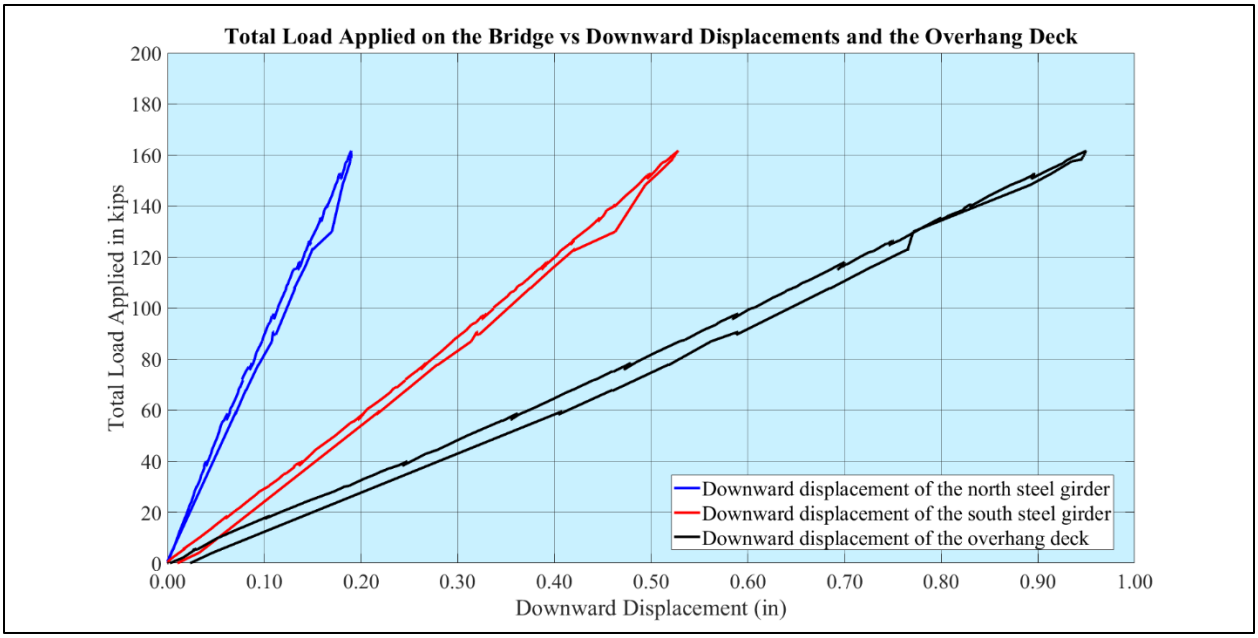

Figure 7.40: Load vs displacement (eccentric shear test)

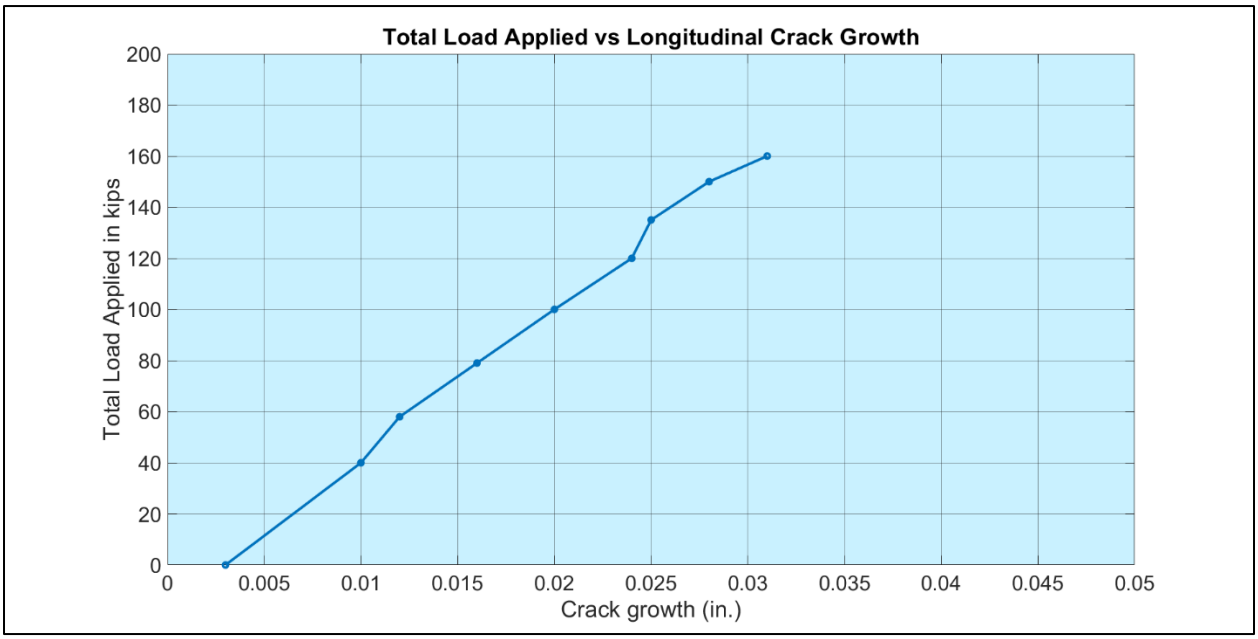

Figure 7.41: Total load applied vs a longitudinal crack growth.

Furthermore, the eccentric shear test caused the deck to crack. The primary and related secondary cracks are longitudinally or lengthwise along the deck slab. Cracking occurs in the positive moment zones that occur immediately over the steel girders. The cracks are caused directly by the eccentric loading placed outside the exterior girders (two feet from the center line girder and two

feet from the edge of the slab). As the deck cracks, readings of crack width were made. The chart in Figure 7.41 reports the crack width as a function of the applied load.

Observing that the crack propagation is linear in relation to the applied load, we can conclude that the rebars in the concrete did not yield despite the 160.6 kip applied load, and that the bridge remained elastic.

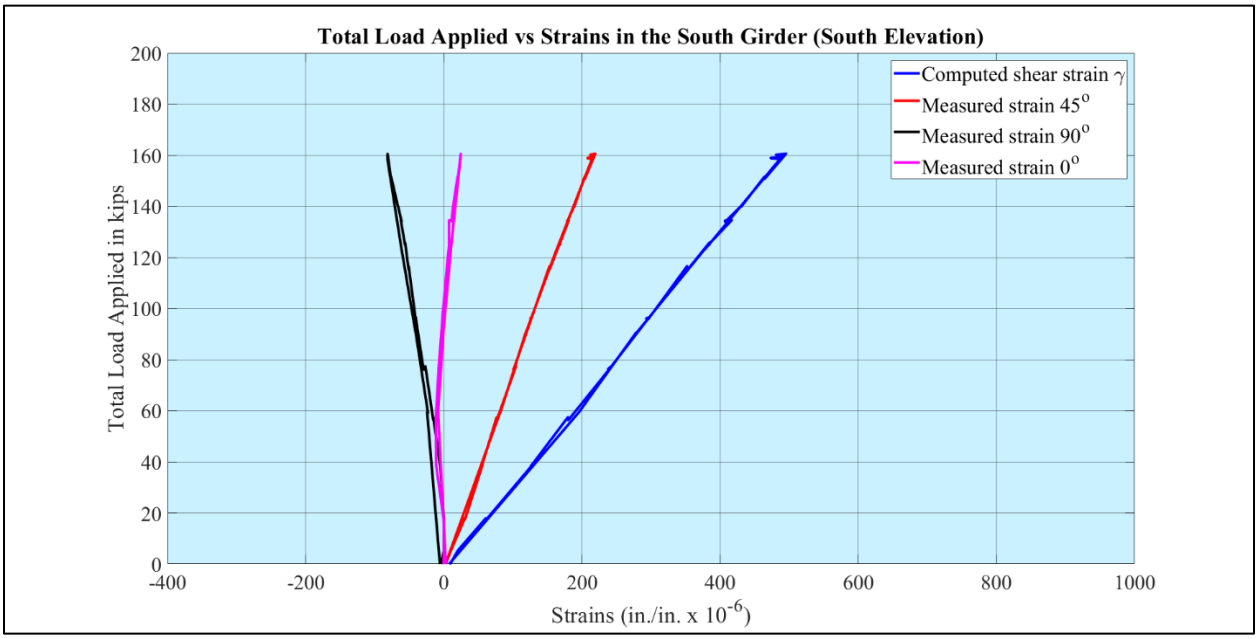

Figure 7.42: Total load applied on the bridge vs strains measurements at 45.0 in from the support in the south girder (south elevation) (eccentric shear testing)

Figure 7.42 shows the applied load on the bridge vs the measured strains and the computed shear strain and at 45.0 in from the location of the support in the south girder. Our first observation is we can notice that all the strains behaved elastically. The 45° strain and the 90° strain and the shear strains behaved linear elastic. However, the horizontal strain (0°) is nonlinear, but it remains elastic.

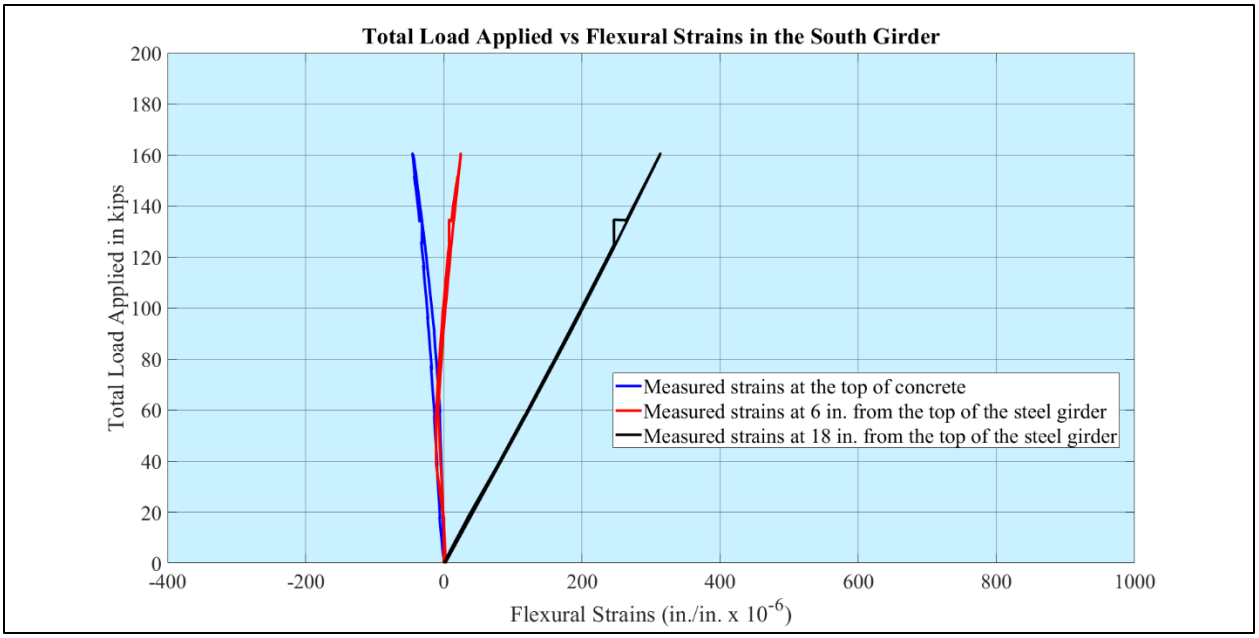

Figure 7.43: Total load applied on the bridge vs strains measurements at 45.0 in from the support in the south girder (south elevation) (eccentric shear testing)

Figure 7.43 shows the total applied load on the bridge vs. the flexural strains on the south girder at 45 in. from the support (south elevation). We can notice that the changes of the strains are linear elastic with changes of the loadings in the concrete strain and the bottom steel. Additionally, when the load is removed, the strains remain substantially on the same line indicating an elastic response to the initial loading. However, the strain on the top of the steel girder seems to have a nonlinear behavior.

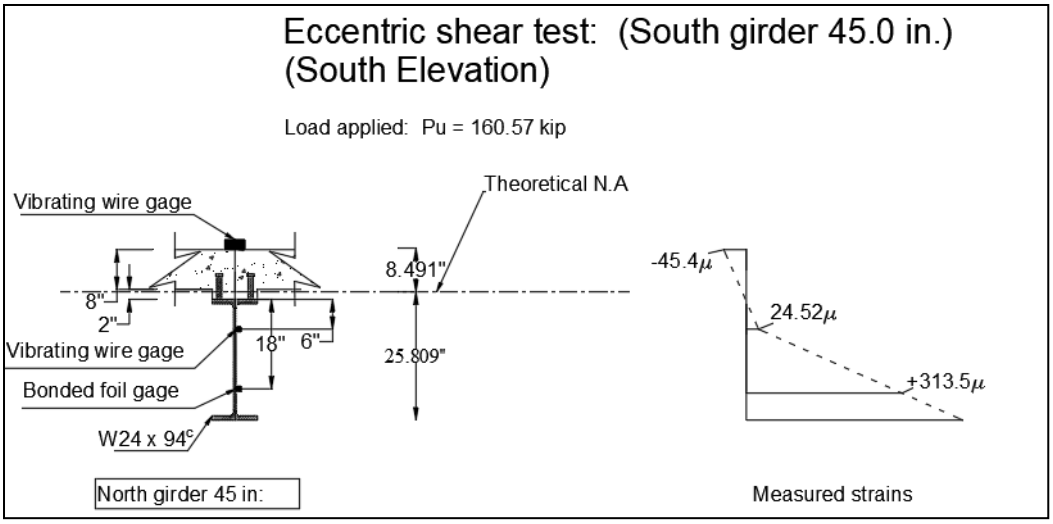

Figure 7.44: Strain profile of the south girder at 45.0 in. from the support (South Elevation)

Figure 7.44 shows the strain profile of the composite beam in the north girder. Strains are taken directly from gages located at various depths within the cross-section, including strains in the concrete deck and strains in the steel girder.

Concrete or steel strains are plotted vs. the "height of the beam from the bottom steel girder." Because the strain diagram is not linear through the depth of the cross-section, this indicates that the bridge beam is not acting as a composite cross-section.

7.3. Conclusions:

7.3.1. Conclusion from Flexural Tests:

- The beam deformations increased linearly as the flexural loads were applied. This is shown in the figures as beam deformations formed straight lines (or nearly straight lines) in plots showing deformations (whether deflections or strains) vs. load.

- Upon removal of loading, or during unloading of the bridge, the load vs. displacement charts returned to the original deflection, and the return path of the load vs. deflection chart retraced the same, or very nearly the same line, as when loading.

- This indicates that the steel and concrete materials remained elastic throughout the loading range and that the bridge did not suffer any yielding or inelastic behavior due to the factored loading from the notional EV-3 loads.

- The asymmetric flexural loading tests caused some small cracks in the slabs that resulted from tension in the top fiber of the slab as the point loads were applied at a location that caused cantilever action (tension on the top fiber) of the slab. The cracks remained small and do not affect the overall conclusions from the testing.

- Overall, a rigorous factored load (140,000 lbs.) was applied to the prototype bridge, both in symmetric loading pattern and in an asymmetric load pattern. In both sets of loads tests the bridge behaved linearly, elastically, and without yielding or significant cracking. Furthermore, the bridge demonstrated its ability to resist the EV-3 loading without compromise and demonstrates that the steel girder bridges in Oklahoma are capable, in general, of supporting the EV-3 loading as required by the federal FAST ACT.

- Bridge response to EV3 loading was predictable using Engineering Mechanics - that the material response remained linear and elastic and indicates that Basic Engineering Mechanics can be used to Load-Rate Bridges on an individual basis.

7.3.2. Conclusion from Shear Tests:

The test results indicate several key elements and findings:

- The beam deformations increased linearly as the loads were applied. This is shown in the figures as the beam deformations formed straight lines (or nearly straight lines) in plots showing deformations (whether deflections or strains) vs. load.

- Upon removal of loading, or during unloading of the bridge, the load vs. displacement charts returned to the original deflection, and the return path of the load vs. deflection chart retraced the same, or very nearly the same line, as when loading.

- Cracking appeared in asymmetric loading. No cracks were observed during symmetric loading.

- The asymmetric shear loading tests caused cracks in the slabs that resulted from tension in the top fiber of the slab as the point loads were applied at a location that caused cantilever action (tension on the top fiber) of the slab. The crack development did not affect the load distribution ratio in the two girders.

- During asymmetric shear loading, crack size increased linearly as loads were applied. This demonstrates that the reinforcement that bridged the cracks remained linear elastic and did not yield.

    - This indicates that the steel and the rebar and the concrete materials remained elastic throughout the loading range and that the bridge did not suffer any yielding or inelastic behavior due to the factored loading from the notional EV-3 loads.

- Overall, a rigorous factored load (160,000 lbs.) was applied to the prototype bridge, both in symmetric loading pattern and in an asymmetric load pattern. In both sets of loads tests the bridge behaved linearly, elastically, and without yielding or significant cracking. Furthermore, the bridge demonstrated its ability to resist the EV-3 loading without compromise and demonstrates that the steel girder bridges in Oklahoma are capable, in general, of supporting the EV-3 loading as required by the federal FAST ACT.

7.3.3. Recommendations:

- Bridge response to EV3 loading was predictable using Engineering Mechanics - that the material response remained linear and elastic and indicates that Basic Engineering Mechanics can be used to Load-Rate Bridges on an individual basis.
- During the shear test, the data shows that the bridge did not feature a composite behavior. The strains were not linear. However, the shear strain was overpredicted by beam mechanics.
    - The research recommends computing the shear capacity of the steel beam for shear for load rating.
    - More experimental, and analytical research is suggested to understand the shear behavior at the end of composite bridge girders.

CHAPTER VIII

8. CONCLUSIONS AND RECOMMENDATIONS

This research focuses, in part, on bridges and the development of structural monitoring systems used for both concrete and steel bridges. When being built, parts of two bridges were instrumented with a combination of sensors attached to a data acquisition system powered by a solar panel and battery. Data is transmitted wirelessly through cell phone technology. The research represents the first efforts to develop remote structural monitoring that is robust and reliable. The data acquisition system has proven to survive through the construction of both concrete and steel bridges. It continues to function from the beam fabrication through bridge construction and even now as the bridges have been in service for more than two years. This study aimed to present and develop a structural health monitoring program that can be used on both concrete and steel bridges. The purpose of the structural monitoring program implemented in this study is: (a) assessing the effectiveness of mild steel and fully tensioned top strands on prestress losses. (b) assessing the effectiveness of mild steel and fully tensioned top strands on mitigating and controlling camber. (c) Evaluating the effectiveness of the secondary stiffening elements and diaphragm in load distribution factors.

Additionally, part of this research tested instrumentation systems in the laboratory by performing load testing on a composite steel girder bridge. Those tests aimed to assess the genre of steel-girder bridges made composite with concrete decks and determine whether the bridge system can support heavier loads required by emergency vehicles that are proscribed in the federal law FAST-Act.

The proposed research study consisted of the following tasks to attain the objectives:

- Tasks 1: Literature Review
- Task 2: Development of a structural health monitoring program that can be used for both concrete and steel girder bridges.
- Task 3: Evaluation of Prestress Loss Prediction Models Through Real-Time Measurement of Prestress Losses
- Task 4: Evaluation of Measured Camber to Assess the effectiveness of mild steel and fully tensioned top strands.
- Task 5: Performed Static and Dynamic Load tests on the State Highway 4 bridge.
- Section 6: Load testing of a steel-girder composite bridge to evaluate the bridge behavior under emergency vehicle (EV-3) loads.

Conclusions:

Conclusions from Chapter 3:

1. The Campbell Scientific Dataloggers are appropriate for laboratory and remote applications because of its dependability, robustness, and ability to support various sensors produced by multiple manufacturers.
2. During PC Bridge Beam Fabrication, the data gathering system acquired data from a remote location. These data are helpful for both short-term and long-term structural monitoring (during fabrication, storage, handling, transportation, erection, and bridge in-service conditions).
3. The system allowed for real-time data acquisition and analysis of bridge beam performance, including evaluations of our design techniques, design decisions, and building procedures.

Conclusions from Chapter 4 and Chapter 5

1. The inclusion of mild horizontal steel as primary reinforcement reduces prestress losses by increasing the transformed section properties of the PC girders.
2. The inclusion of mild horizontal steel as primary reinforcement reduces camber by increasing the transformed section properties (short term) and reducing the cross-section curvature after prestressed release
3. Mild Steel as Primary Reinforcement reduces camber growth by increasing the transformed section properties (long term effects are magnified because of creep and shrinkage).
4. The use of fully tensioned top strands (FTTS) reduces prestress losses by reducing the total prestress moment.
5. Using fully tensioned top strands (FTTS) reduces camber by reducing the curvature caused by the prestress moments.
6. Fully Tensioned Top Strands (FTTS) help mitigate excessive camber growth.
7. The current design equations overestimate the modulus of elasticity of Self-Consolidating-Concrete. This causes the industry to underestimate elastic shortening losses.
8. The time-dependent volume changes of Self-Consolidating Concrete (SCC) are underestimated by current design equations and computational procedures used to estimate prestressed losses. Because the volume changes are underestimated, the time-dependent prestress losses like creep (CR) and shrinkage (SH) are also underestimated.

Conclusions from Chapter 6:

1. Live load Distribution Factors (DFs) for external girders are over-estimated by the lever rule method.
2. Live Load Distribution Factors are over-estimated by the AASHTO "Rigid Method."
3. Finite Element Analysis can be used to assign the Live Load Distribution Factors between girders more accurately.
4. The Inclusion of the secondary stiffening elements and Diaphragm Reduced DFs by 11.9%.

Conclusions from Chapter 7:

1. Beam Mechanics and assumed composite behavior is sufficient to analyze steel girder bridges (retrofitted with shear studs) for load rating.
2. During shear testing, with loading applied within 2d of the end region, composite behavior between the steel girder and the deck slab was not observed.
    1. The research findings recommend that the engineer use the steel girder bridge's shear capacity only for load rating.
3. The EV-3 Produces higher moments and shear forces than the HL-93 load case for shorter spans. However, the design load factor for the load rating is smaller for the emergency vehicles, 1.3 compared to the 1.75 required for HL-93.

Recommendation:

- Use Mild Steel as Primary reinforcement for prestressed girder bridges.
    - The inclusion of mild steel REDUCES camber by improving the time-dependent stiffness of the prestressed concrete bridge beam.
    - The inclusion of mild steel in the pre-compressed tensile zone helps CONTROL cambers.
    - The inclusion of mild steel in the pre-compressed tensile zone REDUCES prestressed losses.
    - The mild steel increases the flexural strength of the composite bridge section.
- Extend Mild Reinforcement to the Ends of the prestressed concrete bridges so that the reinforcement is extended over the bearing. This will increase the shear strength, and shear ductility in end regions.
- Use Fully Tensioned Top Strands in the Prestressed Girder.
    - The inclusion of fully tensioned top strand REDUCES camber by decreasing overall eccentricity of the prestressing force. This decrease the curvature of the cross section by increasing compression stresses (or reducing tension stresses) near the top of the prestressed concrete beam.
    - The inclusion of fully-tensioned top strand REDUCES TIME-DEPENDENT camber by decreasing overall eccentricity of the prestressing force. Increases in camber, over time, are largely influenced by the creep of concrete. By reducing initial curvature, the long-term camber and camber growth will also be decreased.
- Use fully-tensioned top strands and mild reinforcement in the pre-compressed tensile zones when building prestressed concrete beams from Self-Consolidating Concrete (SCC). SCC has shown to have greater shrinkage, greater creep and lower elastic

modulus than conventional concretes. Problems with camber, long-term cambers and camber growth, and prestressed losses are worsened when using SCC. These adverse effects can be offset by the inclusion of fully-tensioned top strands and mild reinforcement in the bottom flanges of prestressed concrete girder bridges.,

- Include the modulus of elasticity as required testing in QA/QC programs and use the collected data to form a database to improve understanding of the behavior and to develop more accurate estimates for elastic modulus and for creep.
- Secondary stiffening elements should be taken into consideration for calculations and prediction of the live load distribution for load rating but not for design. Secondary stiffening elements make the system more rigid and help spread the loads to the other beams.When performing load rating on prestressed concrete bridges incorporate secondary stiffening elements when calculating capacity for rating in both shear and flexure. Research shows that the stiffening elements like diaphragms and guardrails or parapets work compositely with the deck and beam systems to increase stiffness and increase the bridge's strength.
- Research showed that inclusion of full-tensioned top strands reduce cracking in end regions of prestressed concrete bridges.

REFERENCES

1. ASCE. (2021). Structurally Deficient Bridges Bridge Infrastructure *ASCE's 2021 Infrastructure Report Card*.
2. Aktan, A. E., Helmicki, A. J., & Hunt, V. J. (1998). Issues in health monitoring for intelligent infrastructure. In *Smart Materials and Structures* (Vol. 7, pp. 674-692).
3. Farrar, C. R., & Worden, K. (2007). An introduction to structural health monitoring. *Philos Trans A Math Phys Eng Sci, 365*(1851), 303-315. https://doi.org/10.1098/rsta.2006.1928
4. Jayaseelan, H. (2019). Influence of Time Dependent Properties and Temperature Effects on the Performance of Composite Bridge Girders [233]. Oklahoma State University, Stillwater, Oklahoma.
5. Tadros, M. K. (2003). *Prestress losses in pretensioned high-strength concrete bridge girders* (Vol. 496). Transportation Research Board.
6. American Association of State Highway and Transportation Officials. (2020). *AASHTO LRFD bridge construction specifications* (9th ed.). American Association of State Highway and Transportation Officials.

7. Jayaseelan, H., & Russell, B. W. (2019). Reducing Cambers And Prestress Losses By Including Fully Tensioned Top Prestressing Strands and Mild Reinforcing Steel. In *PCI Journal* (Vol. 64).A
8. AASHTO. (2018). Manual for Bridge Evaluation (3rd Edition). In *Manual for Bridge Evaluation*. Washington, DC.: American Association of State Highway and Transportation Officials AASHTO.
9. Goulet, J.-A., Texier, M., Michel, C., Smith, I. F. C., & Chouinard, L. (2014). Quantifying the Effects of Modeling Simplifications for Structural Identification of Bridges. *Journal of Bridge Engineering*, 19(1), 59-71.
10. Hernandez Ramos, E. S. (2018). *Service Response and Evaluation of Prestressed Concrete Bridges through Load Testing* ProQuest Dissertations Publishing].
11. Bao, Y., & Li, H. (2021). Machine learning paradigm for structural health monitoring. *Structural Health Monitoring* (Vol. 20, pp. 1353-1372).
12. Méndez, J. M. G. (2014). *Model of strain-related prestress losses in pretensioned simply supported bridge girders.* [University of Texas at Austin].
13. Zia, P., Preston, H. K., Scott, N. L., Workman, E. B.,. (1979). Estimating prestress losses. *Concrete International*, *1*(6), 32-38.
14. Okamura, H., & Ouchi, M. (1998). Self-compacting high performance concrete. *Progress in structural engineering and materials*, 1(4), 378-383. https://doi.org/10.1002/pse.2260010406
15. ACI Committee 237, "Self-Consolidating Concrete (ACI 237 R-04)," *American Concrete Institute*, Farmington Hills, Mi, (2007).

16. Klaus Holschemacher, Yvette Klug, “A Database for the Evaluation of Hardened Properties of SCC,” *LACER* No 7, (2002), pp 123-134.
17. Bonen, D., & Shah, S. P. (2005). Fresh and hardened properties of self-consolidating concrete. *Progress in structural engineering and materials*, *7*(1), 14-26.
18. Garcia Theran, M. M. (2009). *Experimental evaluation of the modulus of elasticity of self-consolidating concrete* [114]. University of Puerto Rico, Mayaguez (Puerto Rico), Ann Arbor.
19. Myers, John Joseph, Sells, E., Volz, J., Porterfield, K., Looney, T., Tucker, B., & Holman, K. (2012). Self-Consolidating Concrete (SCC) for Infrastructure Elements *Report A – Shear* (Issue JULY 2012). https://www.researchgate.net/publication/272417795_SCC_for_Infrastructure_Elements_Report_A%5Cnhttp://library.modot.mo.gov/RDT/reports/tryy1103/cmr13-03_C.pdf
20. Lin, T. Y., & Burns, N. H. (1981). *Design of prestressed concrete structures* (3d ed.). Wiley.
21. Videla, C., Carreira, D. J., & Garner, N. (2008). Guide for modeling and calculating shrinkage and creep in hardened concrete. *ACI report*, 209.
22. Hansen, P., Nielsen, H., Wilsky, K., Agarwal, Y., Baba, C., & Bhattacherjee, S. (1966). *Nucl. Phys.*, 76, 267. https://www.scopus.com/inward/record.uri?eid=2-s2.0-84908817226&partnerID=40&md5=854e8ff5e1c08cb7d796bbee7f1328f5
23. Troxell, G. E., Raphael, J. M., & Davis, R. E. (1958). Long-time creep and shrinkage tests of plain and reinforced concrete. *Proc. ASTM*, 58, 1101-1120.

https://www.scopus.com/inward/record.uri?eid=2-s2.0-0343360507&partnerID=40&md5=a7d0b2719f26bffd57ee493698fe9697

24. Pickett, G. (1956). Effect of aggregate on shrinkage of concrete and a hypothesis concerning shrinkage. *ACI Journal*, 52(5), 581-590. https://www.scopus.com/inward/record.uri?eid=2-s2.0-0001756807&partnerID=40&md5=1a6399b83434d9b6e61748f0857a8aaf
25. Lopez, M., Kahn, L. F., & Kurtis, K. E. (2004). Creep and shrinkage of high-performance lightweight concrete. *ACI Materials Journal, 101*(5), 391-399. https://www.scopus.com/inward/record.uri?eid=2-s2.0-7544220202&partnerID=40&md5=d31b31ed1e2e191f9d90ff5a29eaacdd
26. Alghazali, H. H., & Myers, J. J. (2020). 6 - Creep and shrinkage of SCC. In R. Siddique (Ed.), *Self-Compacting Concrete: Materials, Properties and Applications* (pp. 131-146). Woodhead Publishing. https://doi.org/https://doi.org/10.1016/B978-0-12-817369-5.00006-4
27. Wendling, A., Sadhasivam, K., & Floyd, R. W. (2018). Creep and shrinkage of lightweight self-consolidating concrete for prestressed members. *Construction and Building Materials, 167,* 205-215. https://doi.org/https://doi.org/10.1016/j.conbuildmat.2018.02.017
28. Saiidi, M., Douglas, B., & Feng, S. (1994). Prestress Force Effect on Vibration Frequency of Concrete Bridges. *Journal of structural engineering (New York, N.Y.), 120*(7), 2233-2241. https://doi.org/10.1061/(ASCE)0733-9445(1994)120:7(2233)

29. Liu, X., Wu, B., & He, C. (2014). A Novel Integrated Sensor for Stress Measurement in Steel Strand Based on Elastomagnetic and Magnetostrictive Effect. In (pp. 65-73*). Springer International Publishing*. https://doi.org/10.1007/978-3-319-09507-3_7
30. Chaki, S., & Bourse, G. (2009). Stress Level Measurement in Prestressed Steel Strands Using Acoustoelastic Effect. *Experimental mechanics*, *49*(5), 673-681. https://doi.org/10.1007/s11340-008-9174-9
31. Joint ACI-ASCE Committee 423. Guide to estimating prestress loss. Farmington Hills, MI, 2016, https://www.concrete.org/Portals/0/Files/PDF/Previews/423.10R-16_preview.pdf
32. Abdel-Jaber, H., & Glisic, B. (2018). Monitoring of long-term prestress losses in prestressed concrete structures using fiber optic sensors. *Structural Health Monitoring*, *18*(1), 254-269. https://doi.org/10.1177/1475921717751870
33. Almohammedi, A., Murray, C. D., Dang, C. N., & Hale, W. M. (2021). Investigation of measured prestress losses compared with design prestress losses in AASHTO Types II, III, IV, and VI bridge girders. *PCI Journal*, *66*(3), 32-48. https://doi.org/10.15554/pcij66.3-02
34. Hale, W. M., & Russell, B. (2006). Effect of Allowable Compressive Stress at Release on Prestress Losses and on the Performance of Precast, Prestressed Concrete Bridge Girders. *PCI Journal*, *51*(2), 14-25. https://doi.org/https://doi.org/10.15554/pcij.03012006.14.25
35. Kelly, D. J., Bradberry, T. E., & Breen, J. E. (1987). *Time dependent deflections of pretensioned beams*.

36. Storm, T. K., Rizkalla, S. H., & Zia, P. Z. (2013). Effects of production practices on camber of prestressed concrete bridge girders. *PCI Journal*, *58*(1), 96-111. https://doi.org/10.15554/pcij.01012013.96.111

37. Michaelson, G. K. (2010). *LIVE LOAD DISTRIBUTION FACTORS FOR EXTERIOR GIRDERS IN STEEL I-GIRDER BRIDGES*

38. Sanders, W. W. (1984). *NCHRP Synthesis of Highway Practice 111: Distribution of Wheel Loads on Highway Bridges.* Washington DC: Transportation Research Board.

39. Tarhini, K. M., & Frederick, G. R. (1992). Wheel Load Distribution in I-Girder Highway Bridges. *Journal of structural engineering* (New York, N.Y.), 118(5), 1285-1294. https://doi.org/10.1061/(ASCE)0733-9445(1992)118:5(1285)

40. Kim, S., & Nowak, A. S. (1997). Load Distribution and Impact Factors for I-Girder Bridges. *Journal of Bridge Engineering*, *2*(3), 97-104. https://doi.org/10.1061/(ASCE)1084-0702(1997)2:3(97)

41. Barr, P. J., Eberhard, M. O., & Stanton, J. F. (2001). Live-Load Distribution Factors in Prestressed Concrete Girder Bridges. *Journal of Bridge Engineering*, *6*(5), 298-306. https://doi.org/10.1061/(ASCE)1084-0702(2001)6:5(298)

42. Lin, C. S., & VanHorn, D. A. (1968). *The effect of midspan diaphragms on load distribution in a prestressed concrete box-beam bridge - philadelphia bridge, June 1968*.

43. Mabsout, M. E., Tarhini, K. M., Frederick, G. R., & Tayar, C. (1997). Finite-Element Analysis of Steel Girder Highway Bridges. *Journal of Bridge*

Engineering, *2*(3), 83-87. https://doi.org/10.1061/(ASCE)1084-0702(1997)2:3(83)

44. Nutt, R. V., Schamber, R. A., & Zokaie, T. (1988). *NCHRP 12-26: Distribution of Wheel Loads on Highway Bridges.* Final Report for National Cooperative Highway Research Program.
45. Conner, S., & Huo, X. S. (2006). Influence of Parapets and Aspect Ratio on Live-Load Distribution. *Journal of Bridge Engineering*, *11*(2), 188-196.
46. Hartmann, J. (2016). *Load rating for the FAST act's emergency vehicles*
47. Stansfield, N. R. (2018). *The Effects of New Emergency Vehicle Loads on the Load Rating of Concrete Culverts in Tennessee* [166]. Tennessee Technological University PP - United States -- Tennessee, Ann Arbor.
48. Office of Bridges and Structures. (2018). FAST 1410 emergency vehicles QA
49. *Bridge formula weights*. (2019). U.S. Department of Transportation, Federal Highway Administration, Office of Freight Management and Operations.
50. James, E. D., & Yarnold, M. T. (2017). Rapid Evaluation of a Steel Girder Bridge: Case Study. *Journal of Bridge Engineering, 22*(12), 05017013. https://doi.org/doi:10.1061/(ASCE)BE.1943-5592.0001151
51. Rasekh, H., Joshaghani, A., Jahandari, S., Aslani, F., & Ghodrat, M. (2020). 2 - Rheology and workability of SCC. In R. Siddique (Ed.), Self-Compacting Concrete: *Materials, Properties and Applications* (pp. 31-63). Woodhead Publishing. https://doi.org/https://doi.org/10.1016/B978-0-12-817369-5.00002-7

52. Aggarwal, P., & Aggarwal, Y. (2020). 4 - Strength properties of SCC. In R. Siddique (Ed.), *Self-Compacting Concrete: Materials, Properties and Applications* (pp. 83-115). Woodhead Publishing.

VITA

Alla Eddine Acheli

Candidate for the Degree of

Doctor of Philosophy

Dissertation: IMPLEMENTATION OF STRUCTURAL MONITORING TO ASSESS THE PERFORMANCE AND SERVICEABILITY OF CONCRETE AND STEEL GIRDER BRIDGES

Major Field: Civil Engineering

Biographical:

Education:

Completed the requirements for the Doctor of Philosophy in Civil Engineering at Oklahoma State University, Oklahoma, in May 2023.

Completed the requirements for the Master of Science in Civil Engineering at University of Houston, Houston, Texas, in August 2018.

Completed the requirements for the Master of Science in Civil Engineering at University of Science and Technology Houari Boumediene, Bab Ezzouar, Algiers, Algeria in July 2016.

Completed the requirements for the Bachelor of Science in Civil Engineering at University of Science and Technology Houari Boumediene, Bab Ezzouar, Algiers, Algeria in July 2014

Experience:

Worked as a Graduate research Assistant in the Civil Engineering Department at Oklahoma State University, Fall 2018 – Spring 2023.